IMPERIAL COLLEGE LONDON

DOCTORAL THESIS

Modelling Spatial-temporal Rainfall and Its Hydrological Impact in a Changing Climate

---

Author:

Yuting Chen

Supervisors:

Dr. Christian Onof

Dr. Athanasios Paschalis

A thesis submitted in partial fulfillment of the requirements

for the degree of Doctor of Philosophy

in the

Department of Civil and Environmental Engineering

Environmental and Water Resources Engineering research group

October 08, 2022

Declaration of Authorship

I, Yuting CHEN, declare that this thesis titled, “Modelling spatial-temporal rainfall and its hydrological impact in a changing climate” and the work presented in it are my own. I confirm that:

- This work was done wholly while in candidature for a research degree at Imperial College London.
- Where I have consulted the published work of others, this is always clearly attributed.
- Where I have quoted from the work of others, the source is always given. With the exception of such quotations, this thesis is entirely my own work.
- Where sections of this thesis are already published, I have made clear exactly what was done by myself and others.
- I have acknowledged all main sources of help.

Copyright Declaration

The copyright of this thesis rests with the author. Unless otherwise indicated, its contents are licensed under a Creative Commons Attribution 4.0 International Licence (CC BY).

Under this licence, you may copy and redistribute the material in any medium or format for both commercial and non-commercial purposes. You may also create and distribute modified versions of the work. This on the condition that you credit the author.

When reusing or sharing this work, ensure you make the licence terms clear to others by naming the licence and linking to the licence text. Where a work has been adapted, you should indicate that the work has been changed and describe those changes.

Please seek permission from the copyright holder for uses of this work that are not included in this licence or permitted under UK Copyright Law.

Abstract

Quantifying changes in future precipitation and uncertainty remains a challenge. Hydrological impacts of the changes are not fully understood either. These concerns form the research aim, which is to understand changes in the spatial-temporal structure of rainfall in a future climate so as to investigate its hydrological impact, especially in the context of catchment floods. To achieve this aim, high-resolution future precipitation is generated through a rainfall simulation tool developed in this thesis, and the hydrological impact of rainfall changes on an urban catchment is then assessed.

The first part of the thesis focuses on selecting the suitable stochastic structure used in the simulation tool. Two spatial-temporal stochastic generators are compared, not only in terms of rainfall statistics but also of their behaviour in yielding a realistic catchment runoff.

The second part concerns the evaluation of a 12-member 20-year-long convection-permitting ensemble of hourly precipitation for the British Isles, for both the current and future climates. The extensive evaluation for the current period demonstrates its added value in impact studies and its potential use for downscaling purposes. The investigation for the future climate scenario reveals future rainfall changes in more detail, in particular for high-impact events.

Building upon the identification of a realistic rainfall generator and the examination of climate model ability to simulate realistic precipitation, the third part focuses on developing a simulation tool which can well combine both sources of information. This tool is designed to provide rainfall information with a resolution suitable for urban climate impact studies. After the calibration, an extensive validation is carried out and the performance of the simulation tool for both current and future periods is evaluated.

The final part uses this simulation tool to assess the impact of rainfall changes upon the estimated future urban flood risk. Three simplifications of the rainfall input, which are usually made in engineering applications, are selected here. The effects of each simplification on the accuracy of the estimated sewer flood risk are quantified. Results highlight the estimation bias in the current risk assessment approach caused by these simplifications, and also provides valuable information for decision makers in terms of effectively reducing potential errors in sewer network designs caused by the rainfall input.

Acknowledgements

I want to express my sincere gratitude to my supervisors, Dr Christian Onof and Dr Athanasios Paschalis. You have shown me unwavering support, guidance, and expertise throughout the past four years. Without your generosity and trust, I would not have had the confidence to complete this journey. It has been an honour to work with you as a PhD student. Thank you from the bottom of my heart.

I am also grateful to my PhD examiners Dr Adrian Butler and Dr Peter Molnar for your invaluable feedback and critical evaluation of my work. Your expertise and support have played an essential role in shaping my academic development.

Thank you to Dr. Barney Dobson, Dr. Lizzie Kendon, and Dr. Nadav Peleg for your evaluable advice and collaboration, and to the financial support from FloodCitiSense and UKMO Nowcasting projects, and the amazing team members.

To all the amazing members of my research group, Lipen, Susana, Yiannis, Dekay, Zhou, and Jordi. Sincere grateful for all conversations and research discussions we have had. And to all cool folks at office 411 - you make work little less soul-sucking. You all are the glue that holds this place together.

A big shoutout to my London crew, Zishu, Zhuoyin, Zhongyao, Yaqi, Yi-chun, Yueyang, Youwen, Jieming, Kevin, Ray, Sarah, and His-kai. You were the perfect go-to team for fun travels, garden explorations, impromptu karaoke, pub nights, and bubble tea runs. You all make my life in London the best it could be! My landlord in Isleworth, Jane – your bakery sessions and pep talks kept me alive during the lockdown. Special thanks to Kelly and Yuan – for sharing all the joy and challenges of life and sending me in-person/virtual high-fives throughout my PhD journey.

I can't forget to thank my fluffy feline friend, Pudding, for the constant reminders to take breaks and the enthusiasm on napping on my keyboard. And to Mee, Wongzai, Potato, and Tapioca: the never-ending dog-cat games between you always manage to brighten my day. Finally, my deepest thanks to my family, Xuejun and Airong, for your encouragement, unconditional love, and support throughout the journey. Thanks for helping me become the not-so-messy person I am today.

Publications

Chen, Y., Paschalis, A., Kendon, E., Kim, D., & Onof, C. (2021). Changing spatial structure of summer heavy rainfall, using convection-permitting ensemble. Geophysical Research Letters, 48(3), e2020GL090903.

Chen, Y., Paschalis, A., Wang, L.-P., & Onof, C. (2021). Can we estimate flood frequency with point-process spatial-temporal rainfall models? Journal of Hydrology, 600, 126667.

Dobson, B., Jovanovic, T., **Chen, Y.**, Paschalis, A., Butler, A., & Mijic, A. (2021). Integrated modelling to support analysis of COVID-19 impacts on London's water system and in-river water quality. Frontiers in Water, 3, 641462.

Park, J., Cross, D., Onof, C., **Chen, Y.**, & Kim, D. (2021). A simple scheme to adjust Poisson cluster rectangular pulse rainfall models for improved performance at sub-hourly timescales. Journal of Hydrology, 126296.

Conferences

Chen, Y., Onof, C., & Paschalis, A. (2019). The applicability to large catchments of spatial-temporal rainfall modelling with point processes: case study of East Anglia, UK. In EGU General Assembly (Vol. 21).

Wang, L.-P., **Chen, Y.**, Lopez, C. M., & Onof, C. (2019). Characterising local rainfall cell patterns over Birmingham (UK) using 10+ years of high-resolution radar images. In EGU General Assembly (Vol. 21).

Chen, Y., Paschalis, A., & Onof, C. (2020). Evaluating the small-scale space time structure of rainfall in the Convection Permitting Model of UKCP18. In EGU General Assembly (p. 8007).

Chen, Y., Paschalis, A., Peleg, N., & Onof, C. (2021a). Generating future rainfall field at a high spatial-temporal resolution, based on a stochastic generator and an hourly-scale convection-permitting model. In AGU Fall Meeting (Vol. 2021, pp. H33I–02).

Chen, Y., Paschalis, A., Peleg, N., & Onof, C. (2021b). Reparametrizing rainfall generators with convective-permitting models to generate high-resolution rainfall for climate impact studies. In EGU General Assembly (pp. EGU21–4622).

Onof, C., **Chen, Y.**, Wang, L.-P., Jones, A., & Ochoa Rodriguez, S. (2021). A two-stage analogue model for real-time urban flood forecasting. In EGU General Assembly (pp. EGU21–15645).

Paschalis, A., Moustakis, Y., & **Chen, Y.** (2022). A global scale assessment of the intensification of rainfall extremes. In EGU General Assembly.

Wang, L.-P., Ochoa-Rodriguez, S., **Chen, Y.**, López, C. M., Scovell, R., Wright, D., et al. (2022). Uncertainty estimation for convective cell nowcasting. In STAHY2022.

List of Abbreviations

ACorr	The lag one autocorrelation
ARF	Areal reduction factor
ARMA	Autoregressive moving average
C-C	Clausius-Clapeyron
CCorr	Cross-correlation of rainfall depths between sites
CDF	Cumulative distribution function
CPMs	Convection-permitting models
CV	The coefficient of variation
CWSD	CityWat-SemiDistributed
DJF	Winter(December-January-February)
DTM	Digital terrain model
FDCs	Flow duration curves
FFCs	Flood frequency curves
GCMs	Global climate models
GEAR	Gridded estimate of areal rainfall
GHG	Greenhouse gas
GMM	The Generalized Method of Moments
IDAF	Intensity-duration-area-frequency curves
IMF	Mean areal intensity (image mean flux)
IPCC	Intergovernmental Panel on Climate Change
JJA	Summer (June-July-August)
KED	Kriging with external drift
ML	The method of the maximum likelihood
NS(s-t)	Neyman-Scott point process rainfall model
NSE	Nash-Sutcliffe efficiency
PD	The probability of dry period
RAPS	Radially averaged power spectrum
RCMs	Regional climate models
RCPs	Representative Concentration Pathways
SKEW	The coefficient of skewness
SNR	Signal-to-noise ratio
SSPs	Shared Socio-economic Pathways
STREAP	Spatial-Temporal Realisations of Areal Precipitation
STREAP-CC	Spatial-Temporal Realisations of Areal Precipitation for Climate Change impact studies
TI	Topographic index
UKBN	UK Benchmark Network
WAR	Wet area ratio
WGs	Weather generators

Table of Contents

CHAPTER 1 INTRODUCTION 1

SECTION 1.1 GENERAL BACKGROUND 1

SECTION 1.2 PRECIPITATION PROCESS 2

SECTION 1.3 PRECIPITATION UNDER CLIMATE CHANGE 4

SECTION 1.4 RESEARCH QUESTIONS AND THESIS OUTLINE 8

CHAPTER 2 STUDY AREA AND DATA DESCRIPTION 12

SECTION 2.1 UK CLIMATE 12

SECTION 2.2 RAINFALL OBSERVATION DATA 13

SECTION 2.3 CLIMATE PROJECTION DATA 17

CHAPTER 3 STOCHASTIC RAINFALL MODELS 20

SECTION 3.1 REVIEW OF STOCHASTIC RAINFALL MODELS 20

SECTION 3.2 POINT PROCESS MODEL 24

SECTION 3.3 STREAP 28

CHAPTER 4 APPLICABILITY OF STOCHASTIC MODELS FOR FLOOD-RELATED HYDROLOGICAL USE 35

SECTION 4.1 INTRODUCTION 35

SECTION 4.2 DATA 36

SECTION 4.3 METHODS 40

SECTION 4.4 RESULTS 45

SECTION 4.5 DISCUSSIONS AND CONCLUSIONS 54

CHAPTER 5 EVALUATION OF RAINFALL OUTPUT FROM CONVECTION PERMITTING ENSEMBLE 57

SECTION 5.1 INTRODUCTION 57

SECTION 5.2 DATA AND METHODS 58

SECTION 5.3 RESULTS 64

SECTION 5.4 DISCUSSIONS AND CONCLUSIONS....71

CHAPTER 6 FUTURE CHANGES IN RAINFALL PROPERTIES, USING CONVECTION-PERMITTING ENSEMBLES 73

SECTION 6.1 INTRODUCTION....73

SECTION 6.2 METHODS....75

SECTION 6.3 RESULTS....78

SECTION 6.4 DISCUSSION....84

SECTION 6.5 CONCLUSION....88

CHAPTER 7 MODELLING SPATIAL-TEMPORAL RAINFALL FOR CLIMATE IMPACT STUDIES...89

SECTION 7.1 INTRODUCTION....89

SECTION 7.2 MODEL DEVELOPMENT....90

SECTION 7.3 STUDY AREA AND VALIDATION METHOD....97

SECTION 7.4 RESULTS AND DISCUSSION....98

SECTION 7.5 CONCLUSIONS....108

CHAPTER 8 SEPARATING THE FACTORS OF RAINFALL CHANGES CONTRIBUTING TO CHANGING FUTURE URBAN FLOOD RISK....109

SECTION 8.1 INTRODUCTION....109

SECTION 8.2 DATA AND METHODS....111

SECTION 8.3 RESULTS AND DISCUSSION....118

SECTION 8.4 CONCLUSIONS....126

CHAPTER 9 CONCLUSIONS....129

SECTION 9.1 SUMMARY....129

SECTION 9.2 OUTLOOK FOR FUTURE RESEARCH....133

APPENDIX 155

List of Figures

Figure 1.1 Percentage of occurrences of disasters by disaster type (2000-2019) (van Loenhout and McClean, 2022, fig. 4). 1

Figure 1.2 Schematic illustrating factors important in determining changes in heavy precipitation and flooding (Allan et al., 2020, fig. 6). 4

Figure 2.1 Location map of rain gauges.. 13

Figure 2.2 Locations of 18 weather radar sites for the 1km composite radar rainfall data (Fairman et al., 2015). 14

Figure 2.3 A comparison of observed annual precipitation (mm/yr) (averaged amount over 2007-2018) from (a) weather radar and (b) CEH-GEAR. 16

Figure 2.4 Example of precipitation maps (at 1200 UTC on 9 July 2012) obtained from two observation datasets. (a) Radar estimates (aggregated from 5-minute radar) (b) GEAR-1hr gridded dataset. 17

Figure 2.5 Example of CPM rainfall output from different ensemble members, the value shown corresponds to the average rainfall intensity in June over the historical period (1980-2000)..18

Figure 3.1 Schematic of the point process based spatial-temporal rainfall model. 25

Figure 3.2 Schematic structure of STREAP model (Paschalis et al., 2013, fig. 1). 29

Figure 4.1 Location map of the study area, rain gauges and digital terrain model (DTM) of two experimental catchment areas. 38

Figure 4.2 Land use maps showing the land cover at the study catchments. Data source: LCM2015 datasets (Rowland et al., 2017). 39

Figure 4.3 Spatial distribution of computed soil properties (saturated water content, residual water content and saturated conductivity at the surfaces) over two catchments. 39

Figure 4.4 Comparisons of long-term flow obtained from streamflow gauges and the hydrological model, at two benchmark stations. 42

Figure 4.5 Comparisons of Hydrographs and Hyetographs in several events at Bumpstead Brook station (a,b,c panels) and at Brett station (d,e,f panels). 42

Figure 4.6 Validation of NS(s-t) model and STREAP model in terms of point rainfall statistics, including (a) the coefficient of variation; (b) the lag-1 autocorrelation; (c) the coefficient of skewness; (d) the probability of dry periods, at 1-hour and 24-hour aggregation levels..... 46

Figure 4.7 Cross-correlation of different rainfall products for all pairs of gauged sites in January and June, at an hourly scale (a, b); at a daily scale (c, d). 47

Figure 4.8 Hourly annual maximum rainfall intensity against return periods in different seasons, at MAM (a), JJA (b), SON (c) and DJF (d). 48

Figure 4.9 Same as Figure 4.8 but for extremes a 24-hr aggregation level. 48
Figure 4.10 Exceedance probability of catchment summer rainfall amount at 1-hr aggregation level (a), catchment rainfall amount at 24-hr aggregation level (b), and wet area ratio at 1-hr aggregation level (c). 49
Figure 4.11 Comparisons of FFCs from different rainfall forcings (red: observed; grey: NS generated; blue: STREAP generated) at an hourly scale (a) in summer seasons (JJA) and (b) in winter seasons (DJF). 52
Figure 4.12 Variability of simulated soil dynamics of synthetic rainfall forcing and observed rainfall forcing. 53
Figure 4.13 Comparisons of simulated soil dynamics of two rainfall forcings at Welland catchment. Each subplot shows a density plot of $\boldsymbol{\theta sim - \theta(obs)}$ in either low-flow period (summer) (a, b), or high-flow period (winter) (c, d). 54
Figure 5.1 Map of CPM simulation (1980-2000) and locations of four subregions. (a) annual mean precipitation (1980-2000) from CPM; (b) 5-year return level hourly-scale annual maximum precipitation depth. 59
Figure 5.2 Observed annual mean precipitation depths (mm/yr) from different observation datasets, including (a) HadUK-Grid, (b) CEH-GEAR and (c) C-band Radar Composite for historical periods being used in the evaluation. 60
Figure 5.3 Schematic of (a) non-clustered and (b) clustered precipitation. For the entire area, the two modes have the same spatial density (the same WAR). 63
Figure 5.4 Relative bias of the annual mean precipitation between CPM2.2 data and several observation datasets. 65
Figure 5.5 Probability distribution functions (PDFs) of several key rainfall statistics including event durations, peak WAR, 0.5 quantile WAR, peak IMF and 0.5 quantile IMF. 66
Figure 5.6 Radially averaged power spectrum (RAPS) derived from either 12-member 20-year-long CPMs or 12-year-long radar estimates. 68
Figure 5.7 Coefficient of variation of positive rain rate of spatial rainfall fields ($\boldsymbol{CVpos}$) across different aggregation levels ranging from 1 hour to 24 hours in two representative months, i.e., January (a) and June (b).. 68
Figure 5.8 Clustering features for extreme rainfall during summer, using Besag-L function at daily resolution (left panel) and hourly resolution (right panel). 69
Figure 5.9 Areal Reduction Factors (ARFs) for precipitation in southern UK. (a) 1h duration. (b) 6h duration. (c) 24h duration. 70

Figure 5.10 Exceedance probability of areal mean intensity (hourly scale) in South-West of UK (SWestUK) at different spatial scales and different seasons.....70
Figure 6.1 Separation of study region. (a) Map of summer-season average precipitation (1980–2000 period) and separation of study region; (b) Map of future change in summer-season average precipitation (2060-2080 period versus 1980-2000 period).....78
Figure 6.2 Quantile differences between the future-period and the past-period probability density functions of several heavy rainfall properties, including peak intensity ($\boldsymbol{Pmax}$) (a), size (b), storm speed (c) and total volume ($\boldsymbol{Ptotal}$) (d). 79
Figure 6.3 Relative difference of heavy rainfall features in the south UK. Relative difference in the future minus the past conditional probability of peak intensity (a), rain advection speed (b), spatial coverage(c), conditioned on areal mean intensity for all heavy rain hours. 80
Figure 6.4 Changes of the heaviest 480 summer rainfall in North-West (a), North-East (b), and South (c).....82
Figure 6.5 Relative change of areal rainfall intensity as a function of catchment scales and return levels.. 83
Figure 7.1 Flow chart of STREAP-CC calibration and validation procedures. 90
Figure 7.2 Schematic of parameter inference. The fitting curve is obtained from observation dataset and the curve is assumed to be valid for both the current-period CPM output and the future-period CPM output. 93
Figure 7.3 Comparisons of empirical cumulative distribution function (CDF) of rainfall statistics at different temporal scales (5 min and 1 hour) for the current period.....94
Figure 7.4 Comparisons of the estimated 5-min scale $\boldsymbol{CVpos}$ computed from the current-period CPM and the observed 5-min scale $\boldsymbol{CVpos}$ computed from radar measurement.....95
Figure 7.5 Linear relationship between the $\boldsymbol{CVpos}$ at 2.2 km scale and the $\boldsymbol{CVpos}$ at a 1km scale, obtained from radar measurement.....96
Figure 7.6 Scaling feature of $\boldsymbol{CVpos}$ across different time scales (from 5min to 24 hours) obtained from radar observation and the STREAP-CC estimate of 5min-$\boldsymbol{CVpos}$ for the current period and the future period at (a) January and (b) June.....99
Figure 7.7 A comparison of monthly variation of spatial variability parameters from different data sources or different climate periods. The solid lines and circles correspond to the estimates at 5min, 1km resolution and the dashed lines correspond to the estimates at 1-hour, 2.2km resolution.....99
Figure 7.8 Examples of STREAP-CC generated rainfall fields with a scale bar attached in the bottom right panel.. 100

Figure 7.9 A comparison of the mean areal statistics computed from radar estimates (Obs) and the tool-simulated mean areal statistics (Sim)..... 101
Figure 7.10 A comparison of correlation functions computed from the radar estimates (Obs), the STREAP-CC simulated (Sim) and the CPM ensemble (CPM). 102
Figure 7.11 Extreme analysis of areal mean intensity produced by different rainfall products at (a) 10-min, (b) 1-hour and (c) 6-hour aggregation levels. 103
Figure 7.12 Comparison of the parameters governing the correlation between μI and σI fitted from the radar estimation (observed) and the CPM output. 104
Figure 7.13 Exceedance probability of the precipitation depth at the point scale.. 105
Figure 7.14 Auto-correlation function of the precipitation intensity at the point scale, analysed on a seasonal basis. 106
Figure 7.15 Exceedance probability of storm arrival process (wet spells and dry spells duration) in two representative months (January and June). 107
Figure 7.16 Exceedance probability of areal statistics (wet area ratios in panels a and b; areal mean intensity in panels c and d) at two representative months. 107
Figure 8.1 Hydraulic network of the Norwich catchment with a zoom-in panel showing the details of the hydraulic system. 112
Figure 8.2 The complexity-reduced network with a zoom-in panel showing the detail of one 'compartment'. 114
Figure 8.3 Comparisons of simulated pipe flow in several pipes. Each subplot corresponds to the time series containing the seasonal peak flow of the pipe within the simulation year. 119
Figure 8.4 Comparisons of annual maximum storage volume simulated from the blanket rainfall and the one from the spatial-varying rainfall input. 120
Figure 8.5 Scatter plot of the simulated climate change signal with the blanket rainfall input versus the simulated signal with the spatially varying rainfall input..... 121
Figure 8.6 Monthly variation of catchment rainfall key statistics as shown in boxplots for each period, which are current climate (experiment 2), future climate with neglecting future changes in spatial variability (experiment 5) and the future climate with including future changes in spatial variability (experiment 4)..... 122
Figure 8.7 Similar to Fig. 8.6 but for boxplots of catchment response (compartment storage volume). 123
Figure 8.8 Changes of annual-maximum compartment storage volume as a function of the relative change in the rainfall spatial variability between experiment 4 and experiment 5 at 24 auto-selected nodes. 124

Figure 8.9 Relative bias in the baseline setting (experiment 1) due to simplifications and the contribution of each simplification to the relative bias. 125
Figure 8.10 Contribution of each simplification to the relative bias of the modelled annual variability of the compartment nodes storage, shown as a bar plot, grouped by the magnitude of the node's surface area. 126

List of Tables

Table 1.1 Summary of how the chapters match onto the proposed research questions.....10

Table 3.1 STREAP model parameters (Paschalis et al., 2013) 31

Table 4.1 Summary table of rainfall and runoff data being used in Chapter 4. 37

Table 4.2 Chosen Manning coef. and calibrated parameters of hydrological model for two catchments 41

Table 5.1 Summary of datasets used in the comparison of Chapter 5. 60

Table 5.2 Total number of spatial rainfall fields used in spectral analysis 62

Table 6.1 Rainfall occurrence of different Pmax classes [a] (unit: hour/summer season). 78

Table 7.1 Summary of how the model parameters are determined at each stage of STREAP-CC.....90

Table 8.1 Summary of all combinations of rainfall model settings and the input data resolution in the hydraulic model 115

Table 8.2 Illustration of how the designed experiments are used to partition each of selected rainfall characteristics 116

Chapter 1 Introduction

Section 1.1 General Background

Precipitation plays an important role in triggering many natural hazards such as droughts, floods, and landslides. With observed rainfall extremes intensifying (Fischer and Knutti, 2016; Guerreiro et al., 2018a; Westra et al., 2013), flooding is of particular concern. From 2000 to 2019, flooding was identified to be the highest figure for any disaster type, constituting 44% of all disaster events in the last two decades (Figure 1.1). More than 1.65 billion people have been affected by floodings (van Loenhout and McClean, 2022, fig. 9). These flooding events occur twice as frequently as in 1980. At the same time, with the population growing and prompting urbanization, impacts of such extreme events are further exacerbated. Recorded economic damage due to floods is estimated to reach over USD 651 billion in the past two decades (van Loenhout and McClean, 2022, fig. 17).

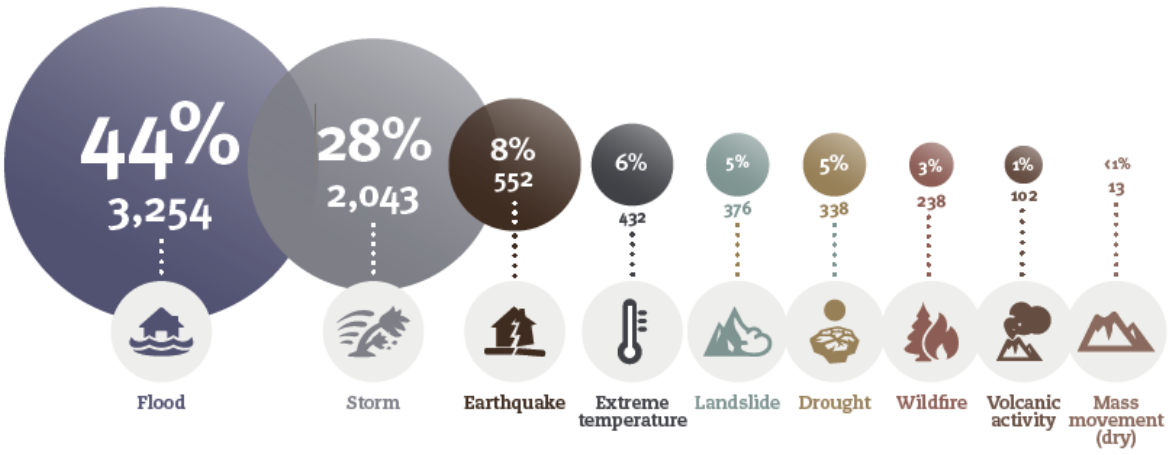


Figure 1.1 Percentage of occurrences of disasters by disaster type (2000-2019) (van Loenhout and McClean, 2022, fig. 4).

Driven by intensifying heavy rainfall, urbanization (e.g., land use changes) and changing regulations under climate change, assessment of future flood risk is becoming much more uncertain. With population increase, more people are also become more vulnerable to climate hazards such as floods. Due to substantial anthropogenic changes in the climate system, there has been a continued increase in greenhouse gas emissions. In late 2020, the global mean surface temperature reached 1.1 degrees above preindustrial levels

(Allen et al., 2018), which might continuously increase. In response to global warming, the means and extremes of precipitation patterns are also being altered. According to the Sixth Assessment Report of the United Nations Intergovernmental Panel on Climate Change (IPCC, 2022), the changing climate is bringing more intense rainfall and associated flooding. With population increase, more people are becoming more vulnerable to climate hazards such as floods. By the end of this century, there will very likely be a further increase in heavy precipitation over most of the mid-latitude temperate land regions and wet tropical regions (IPCC, 2014). For policy and decision-makers in climate change adaptation and mitigation, there is an urgent need to better understand and plan for the changing future. To achieve it, it is fundamental to understand how the physical climate risk will change.

Although the precipitation pattern is projected to be altered globally, quantifying changes in future precipitation and uncertainty remain to be a challenge. It is particularly uncertain in estimating future changes in rainfall at spatial and temporal scales suitable for flood analysis. Hydrological impacts of rainfall change are not fully understood either. These concerns form the principal aim of this thesis, which is to understand future changes in the spatial-temporal structure of rainfall so as to investigate its hydrological impact, especially in the context of floods at a catchment scale in a changing climate.

In the next section, an overview of precipitation processes and related modelling techniques will be provided, followed by introducing research questions and a thesis outline based on the research aim.

Section 1.2 Precipitation Process

1.2.1 Formation of Precipitation

As a natural process, precipitation is formed from a condensation of the water vapour from the cloud, which then drops down as water droplets with the gravitational force. The formation is a result of interaction between atmosphere, land surface and ocean, in which both large-scale (generating weather systems, related to thermodynamics of moist air and motion of air masses) and micro-scale processes (cloud microphysics) are equally important for precipitation to occur. With such a combined effect of processes from different scales, precipitation can occur in several forms, either liquid (rainfall, drizzle,

dew) or solid (snow, hail), or mixed (sleet), in different shapes of precipitation particles (drops, flakes, and hailstones). In quantitative terms, the complexity of precipitation is expressed by the variability of rainfall depth (1) in space and time; (2) across scales; (3) the intermittency and correlation across scales. The enormous variability makes precipitation difficult to understand, measure, model and predict. In this thesis, I focus on the most common form of precipitation - rainfall.

1.2.2 Link of Rainfall Extremes to Climate Systems

Rainfall extremes are of particular importance because of their high impact on human society. Driving factors of extremes can be divided into thermodynamic and dynamic contributions, while these two processes are interconnected (e.g., O'Gorman and Schneider, 2009; Shepherd, 2014).

Thermodynamic contributions (linked to temperature changes) refer to local conditions of climate systems, for example in heat, moisture, or other related quantities. Take the effect of greenhouse gas (GHG) emissions as an example: an increase in GHG emissions leads to more absorption of outgoing longwave radiation, which directly warms tropospheric air and the earth surface. Consequently, an increased moisture-holding capacity of the atmosphere leads to changes in the frequency and intensity of temperatures. The temperature changes consequently alter water vapour by increasing evaporation and water-holding capacity of the atmosphere. Following the Clausius-Clapeyron (C-C) relation (the equilibrium condition of a thermodynamic system), rainfall extremes are being affected. This mechanism is also a physical explanation of increases in precipitation extremes globally with surface warming (IPCC, 2021).

Dynamic contribution (linked to the atmospheric circulation) is another substantial governing factor of affecting rainfall extremes. The synoptic and sub-synoptic phenomena (Loriaux et al., 2016) are also governing characteristics of rainfall extremes in the future. For example, the poleward shift of frontal activity in the Southern Hemisphere and reduced frontal systems can modify the frequency and intensity of extreme precipitation (Solman and Orlanski, 2014); the El Niño–Southern Oscillation influences global precipitation variability (and extremes) particularly in tropical regions (Kurniadi et al., 2021; Li et al., 2020). In general, our understanding of dynamic processes

and their relation to rainfall extremes is still limited (Oueslati et al., 2019; Palmer, 2013; Pfahl et al., 2017).

Section 1.3 Precipitation under climate change

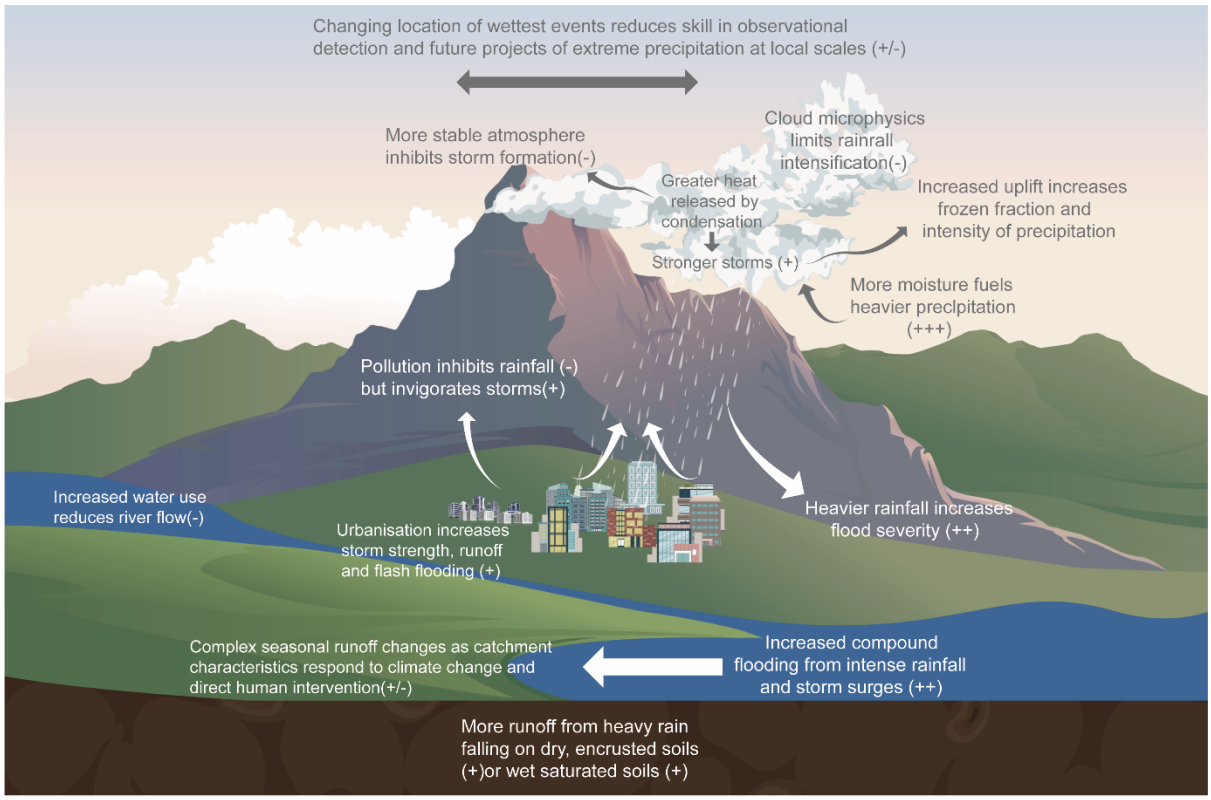


Figure 1.2 Schematic illustrating factors important in determining changes in heavy precipitation and flooding (Allan et al., 2020, fig. 6).

1.3.1 Changing Precipitation

Due to the changing thermodynamic and dynamic conditions of the atmosphere in the future climate, the stationarity of the water cycle is no longer valid (Milly et al., 2008) with strengthening hydrological cycle and increasing precipitation extremes (Xiao et al., 2016).

Increases in the frequency and intensity of extreme rainfall (primarily hourly) have been pointed out in an increasing number of observational analyses across many parts of the world (Fowler et al., 2021), for example in Australia (Guerreiro et al., 2018b), parts of China (Xiao et al., 2016), south-east Asia (Syafrina et al., 2015), Europe (Arnone et al., 2013; Madsen et al., 2009) and North America (Barbero et al., 2017). From those studies, an increase of sub-daily extremes with increasing temperatures has also been confirmed

globally (approximately following C-C rate but with a regional difference) (Fischer and Knutti, 2016; Guerreiro et al., 2018b; Scherrer et al., 2016; Westra et al., 2014). Not only on observational studies, there also have been multiple modelling studies for the future climate showing the altering precipitation patterns and increasing sub-daily rainfall extremes (Ban et al., 2015; Kendon et al., 2019b, 2014; Prein et al., 2017b).

1.3.2 How is Future Climate Being Modelled?

To understand global climate quantitively under such a complex system, global climate models (or called GCMs) are used to simulate energy transfer throughout the whole system. GCMs use a set of mathematical equations to describe physical laws governing the behaviour of the atmosphere, ocean as well as their interactions with other parts of the climate systems (such as land and ice sheets). In the model, the earth climate (the surface, ocean and atmosphere) is divided into grids with a wide range of variables being specified (such as temperature, pressure, wind and rainfall) and then to be solved numerically. Those processes for which underlying physics are not fully known or those processes occurring at scales smaller than the defined model resolution (e.g., clouds, vegetation) are represented empirically. The typical resolution of GCMs is 100-300 km while in the high-resolution GCMs developed in the recent decade the resolution can reach 25-50 km.

In GCMs, the earth system including the ocean, atmosphere and land is divided into a three-dimensional grid of cells. Each cell is represented by mathematical equations that characterize the energy transfer and interactions between those cells. After setting up the model with appropriate initial conditions, the future climate can be projected with a given scenario. The scenario is combined information on various factors that affect the amount of energy reaching and remaining in the climate system, mainly including natural radiative forcings (changes in the sun's energy output, orbital cycle, volcanic eruptions, etc) and anthropogenic radiative forcings (emissions of greenhouse gases, changes in land use, etc.). In 2011, a set of four pathways (Representative Concentration Pathways, or called RCPs) was developed to provide information on plausible future scenario regarding emissions, concentrations of greenhouse gases and air pollutants and land-use changes in future climate projections (van Vuuren et al., 2011). These four scenarios have been used in a range of climate model experiments, such as the Coupled Model Intercomparison Project Phase 5 (Taylor et al., 2012) and UK Climate Projections 2018

(Murphy et al., 2018). Recently, the Shared Socio-economic Pathways (SSPs) was developed to work combinedly with updated RCPs so as to reflect the influence of different climate policy choices on reaching the radiative forcing goal specified by an RCP. Five SSPs are defined, each of which has varying assumptions about human developments such as population, education, urbanization, economic growth, technology development etc (Riahi et al., 2017).

Through those processes, the climate model can provide us a result indicating how future climate will change in areas of interest, for example with a higher chance of a warmer or cooler climate. With developments for decades across the world, climate models have provided valuable information on changes in many climate variables, including precipitation. 'Vital details' of climate change (climate forcing at local spatial scales and fine temporal scales) are important and demanded in impact studies, while such information suitable for hydrological uses is still not available in climate models (Maraun et al., 2010). Getting detailed information on future rainfall is restricted by (1) estimation bias in its rainfall output (Sillmann et al., 2013), (2) huge computational burden, (3) different types of uncertainty (climate scenarios, model parameters, model structures, stochasticity) (Fatichi et al., 2016; Knutti, 2008; Maslin and Austin, 2012; Murphy et al., 2004).

1.3.3 Downscaling Approaches

To obtain the detailed information, downscaling methods are widely used for transferring coarse-scale biased projections from GCMs to regional/local-scale projections required in impact studies. These methods can be roughly divided into two categories: dynamical and statistical methods (Maraun and Widmann, 2018).

Dynamical approach is to use regional climate modelling (RCMs) to downscale the climate of one specific region, with the boundary conditions derived from global climate models (GCMs). The typical resolution of RCMs can be increased to tens of kilometres. In RCMs, those local processes (such as local convection) are typically represented by using empirical sub-grid parameterization schemes. Due to the parameterization scheme, estimation bias in rainfall is still found in RCMs output, such as the shifting diurnal pattern, underestimated extremes, and biased reproduction of wet/dry intermittency (Fosser et al., 2015; Prein et al., 2015; Sillmann et al., 2013).

Further reduced grid spacing (order of kilometre grid spacing) enables the model to switch off such parameterization and carry out climate projections at convection-permitting scales (convection-permitting models [CPMs]) (Prein et al., 2015; Weisman et al., 1997). Development of CPMs allows for a better representation of orography and local convection (Prein et al., 2015) where the realism of fine-scale rainfall characteristics and rainfall extremes is improved (Ban et al., 2015; Kendon et al., 2012; NAKANO et al., 2012; Rasmussen et al., 2017).

However, the huge computational burden, the estimation bias in rainfall output and the time span of projected periods still limit the applicability of CPMs for many hydrological uses. For example, in urban flood risk assessment, information on high-resolution precipitation is crucial to properly model the hydrological cycle and hydraulic dynamics. Due to the low permeability of the urban land surface and the dense hydraulic network, it is ideal to have high-resolution rainfall information at hourly/sub-hourly and kilometre scales (Ochoa-Rodriguez et al., 2019).

To get the high-resolution rainfall information for hydrological studies, the statistical downscaling approach requiring less computational burden is more widely used particularly when long-term data is needed. In statistical downscaling, a statistical model will be typically developed between the historic observed climate data and the output of the climate model (GCMs / RCMs) for the same historical period. The developed model or the statistical relationship is then used to develop the future climate data. Such downscaling methods can be classified into three categories according to the computational techniques used: weather typing approaches; regression methods; and stochastic weather generators. Among these, stochastic weather generators (WGs) are useful for impact studies in hydrology due to their capacity to generate synthetic series with an unlimited length. Additionally, WGs enable us to explicitly generate spatial fields by directly using the observations, unlike using a correction factor on the predictors (Maraun et al., 2010). The combination of information from physically based climate models (GCMs / RCMs) and the capability of WGs has been recognized as a useful tool in the last decades. Such a combination enables an impact assessment of future climate risk caused by local-scale extreme events. However, the added value of high-resolution climate models developed in the recent decade has not been fully coupled with stochastic generators.

Section 1.4 Research Questions and Thesis Outline

As mentioned, this research aims to understand future changes in the spatial-temporal structure of rainfall so as to investigate its hydrological impact, especially on catchment-scale flood risk. Recognizing the gap in terms of resolution and the necessity of having long time series of possible future rainfall depths as mentioned in Section 1.3, a combined use of high-resolution climate models and stochastic generators to simulate rainfall is fundamental in this research. The rainfall generated from the developed tool will be at hydrologically relevant scales and over time spans sufficient for hydrological design applications. The hydrological impact at catchment scale will then be assessed based on the developed simulation tool.

With a focus on flood-related applications of climate impact studies, a suitable model structure in the stochastic component becomes fundamental to represent a full picture of future rainfall changes in the developed simulation tool. Many existing stochastic rainfall models were developed with some simplifications in terms of modelled rainfall structure to meet the purpose of specific applications (Bell, 1987; Cameron et al., 2000; Cowpertwait, 1994; Over and Gupta, 1996; Schertzer and Lovejoy, 2013), to name but a few.

However, the effect of these simplifications on flood-related studies has not been well quantified in the literature. Most validations are achieved by examining rainfall statistics while only few attempt to move forward and examine its resulting catchment response for catchment modelling (Verhoest et al., 2010). This limitation defines the first research question:

Question 1: Which kind of existing model structure of spatial-temporal rainfall generator performs better in flood-related applications?

The above question will be answered in Chapter 4. After choosing an appropriate generator, the next step is to evaluate climate model output because the good performance of climate projections is fundamental to providing a credible source of information about future climate changes.

The estimation bias of rainfall output in climate models has been reduced to a large extent since the development of Convection Permitting Models (CPMs). So far, however, there

have been few studies that have evaluated climate model performance in terms of the fine-scale spatial-temporal structure of rainfall output. Evaluating this performance can help to assess to what extent this information can be used in the following tool development and impact assessment. The second research question in the thesis is to address this knowledge gap:

Question 2: Are the projections of precipitation from Convection Permitting Ensembles credible for hydrological use?

Following this, the next chapter focuses on understanding future rainfall changes based on existing climate projections. Extensive research has shown that rainfall extremes at sub-daily timescales are intensifying in many regions of the world, based on either observational studies or modelling studies on GCMs/RCMs (Ban et al., 2015; Guerreiro et al., 2018b; Kendon et al., 2019b, 2014; Lenderink and van Meijgaard, 2008; Prein et al., 2017b). However, restricted by the coarse resolution of GCMs/RCMs, the future change in their spatial structure remains very uncertain. Only a few studies have analysed the spatial rainfall features at kilometre scales for future projections (Lochbihler et al., 2019; Prein et al., 2017a). For the UK, from the literature available so far, one gains very limited insights into the changes in the spatial structure of rainfall extremes (Kendon et al., 2014). This limitation leads to the third research question:

Question 3: How will the spatial-temporal profile of extreme rainfall change in a future climate over the UK?

After answering the above three research questions, we are able to grasp a clear picture of what message we can get from physically based climate projections and what stochastic components can be essential for its downstream applications. The research then moves on to the development of a rainfall simulation tool for hydrological impact studies. As mentioned in section 1.3.3, to quantify future climate at a local scale using a statistical approach, quite a few weather generators (WGs) have been developed to generate sequences of local-scale rainfall fields with an unlimited length (Bárdossy et al., 2002; Hughes et al., 1999; Maraun and Widmann, 2018; Wheater et al., 2005; Wilks and Wilby, 1999; Yang et al., 2005).

In the literature, most WGs are designed based on the coarser-scale climate models, in which the rainfall output is not detailed enough to provide insights on its small-scale

spatial-temporal profile. Recognising the added value of Convection Permitting Models, we need a rainfall simulation tool which can incorporate projected changes from CPMs to generate more realistic future rainfall at a finer spatial-temporal resolution. This leads to the next research question:

Question 4: Can we combine the information from high-resolution climate models with stochastic rainfall generators to simulate rainfall at a finer resolution for a changing climate?

Answering the above question enables us to have a simulation tool suitable for flood analysis, which can help to quantify the impact of changing rainfall profiles on future flood risks. Both spatial and temporal variabilities have been found to play a key role in modulating responses of urban drainage systems in previous hydraulic modelling studies (Ochoa-Rodriguez et al., 2015; Peleg et al., 2017a). In terms of future flood risk, several studies have investigated the effect of rainfall intensification on resulting flood hazards based on climate models (Alfieri et al., 2017; Kay et al., 2015; Vemula et al., 2019). However, compared with the effect of rainfall intensification, the effect of changing spatial structure on the future urban catchment response has not been well identified. This defines the final research question.

Question 5: Which aspect of changes in rainfall properties contribute more to the estimated future urban flood risk?

Based on the proposed research questions, the thesis is formed through eight chapters. After the general introduction as described in the current chapter, chapter 2 gives an overview of the study area and main datasets being used in the thesis (rainfall observations and climate projections). Then, chapter 3 provides a literature review of stochastic rainfall models followed by a more detailed description of selected stochastic rainfall models used in the following investigation. The next five chapters are then aimed to answer each of research questions proposed, as summarized in Table 1.1.

Table 1.1 Summary of how the chapters match onto the proposed research questions

Chapter	*Research Question to address in the chapter*
4	Which kind of existing model structure of spatial-temporal rainfall generator performs better in flood-related applications?
5	Are the projections of precipitation from Convection Permitting Ensembles credible for hydrological use?
6	How will the spatial-temporal profile of extreme rainfall change in a future climate over the UK?

7	Can we combine the information from high-resolution climate models with stochastic rainfall generators to simulate rainfall at a finer resolution for a changing climate?
8	Which aspect of changes in rainfall properties contribute more to the estimated future urban flood risk?

Chapter 2 Study Area and Data Description

This thesis focuses on the geographic region of the UK. In this chapter, a short description of the climatology features of the area is given, followed by an overview of precipitation measurement data and climate projection data used.

The study area is selected to be within the UK because of the following reasons: (1) significant economic loss is caused by extreme rainfall events (DEFRA, 2010); (2) increasing future flooding risks are projected to happen according to climate simulations (Hirabayashi et al., 2013; Kay et al., 2015); (3) high-quality data is available for this region.

Section 2.1 UK Climate

Under the temperate maritime climate zone, the UK generally gets cool, wet winters and warm, wet summers. The spatial pattern of annual average rainfall amount is greatly affected by its geographic location, changes in land use and its altitude. Located downstream of the Atlantic storm track, the country shows a strong temporal variation in rainfall seasonality. Generally, Atlantic depressions bring a higher rainfall total during autumn and winter and a lower one over spring and summer. The seasonality also shows a regional difference. For example, far from paths of most Atlantic depressions, southern England experiences a relatively quiescent climate with generally well-distributed rainfall throughout the year.

According to monthly rainfall statistics, the UK climate can be roughly divided into the North part and the South part. The northern UK is more affected by Atlantic depressions. Most areas in the North-West UK are largely exposed to rain-bearing westerly winds, bringing a high total rainfall (e.g., annually 3200 mm in the Lake District). The area also experiences a high spatial variability due to the orographic enhancement in the west (e.g., the Eden valley in Cumbria receives less than 800mm rainfall per year). In contrast, the North-East UK generally has lower annual rainfall on average because the west to east slope of the land enables it to be sheltered from the westerly winds. In the southern UK,

there is a more varied seasonal pattern of average rainfall, particularly in the south-west where rainfall variation largely depends on altitude. Altitude has a cooling effect on moist air, producing clouds and rain locally. In the South-East, the rainfall pattern is more evenly distributed throughout the year because of the rain-shadow effect and the high frequency of convective rainfall occurrence in summer. The South-East region also suffers from the highest occurrence of mesoscale convective storms (Gray and Marshall, 1998; Lewis and Gray, 2010) resulting in record-breaking storms and drought problems at the same time (Marsh et al., 2007).

Although our study area is in the UK, for different research questions (chapters), a smaller area or a specific catchment might need to be selected (e.g., for an urban hydraulic simulation), the selection criteria are always the availability and the quality of required datasets for the research question; this will lead to using different data sets for different research questions.

Section 2.2 Rainfall Observation Data

Precipitation data used in this thesis consists of both point scale (rain gauge data) and spatial measurements (weather radar). In addition, gridded datasets interpolated from point-scale measurements are also used.

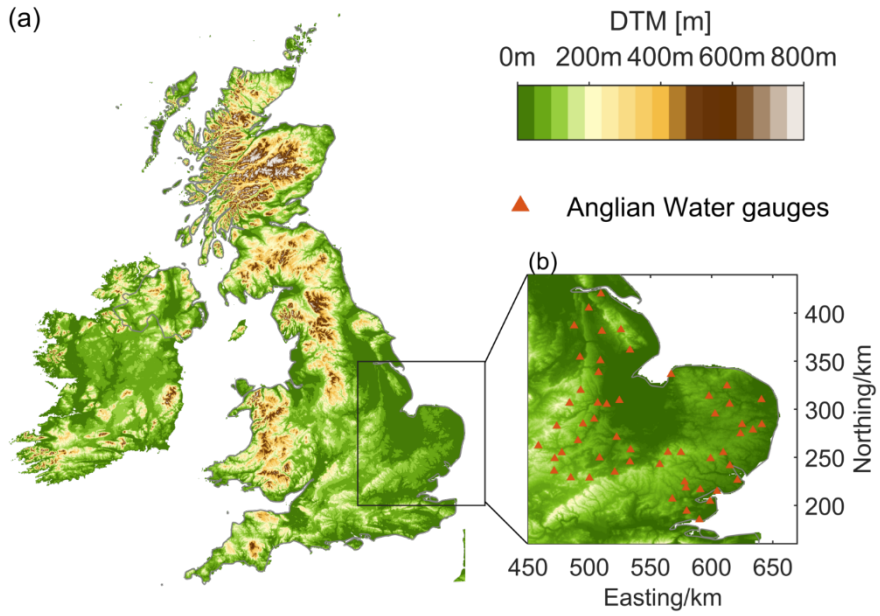


Figure 2.1 Location map of rain gauges. (a) the digital terrain model (DTM) of the UK where the DTM is obtained from Shuttle Radar Topography Mission (SRTM, 2013). (b) locations of another local-area rain gauge data collection (gauged measurements from Anglian Water).

2.2.1 Point Measurement

Point measurements used are a set of decadal-long hourly rainfall measurements across the East Anglia region (Anglian Water, 2016) (Figure 2.1.b). The hourly rain-gauge dataset used was obtained from Anglian Water. The data is available for the period from 2005 to 2016 with a resolution of 0.2 mm. This dataset provides a dense network of hourly measurements for the East Anglia region. Additional quality control has been carried out by the author for the thesis following a list of criteria proposed in a recent study (Blenkinsop et al., 2017, sec. 2) and suspect records and stations have been discarded. This dataset is used in Chapter 4 for calibrating selected stochastic models.

2.2.2 Weather Radar Data

Radar rainfall data used in this study is obtained from the operational C-band network of the UK Met Office (Met Office, 2003). It is a composite rainfall dataset consisting of measurements from 18 weather radars (Figure 2.2). The observations were taken every 5 minutes and have been generated with a grid spacing of 1km since 2006.

The radar-derived precipitation composite is retrieved from the radar reflectivity (Z) by a constant Z-R power-law relationship of $Z = 200R^{1.6}$ (Marshall and Palmer, 1948) assuming that all precipitation is liquid. The retrieved precipitation rate is then corrected to take into account orographic enhancement (Georgiou et al., 2010) and has been adjusted to match local rain gauge observations (Harrison et al., 2012).

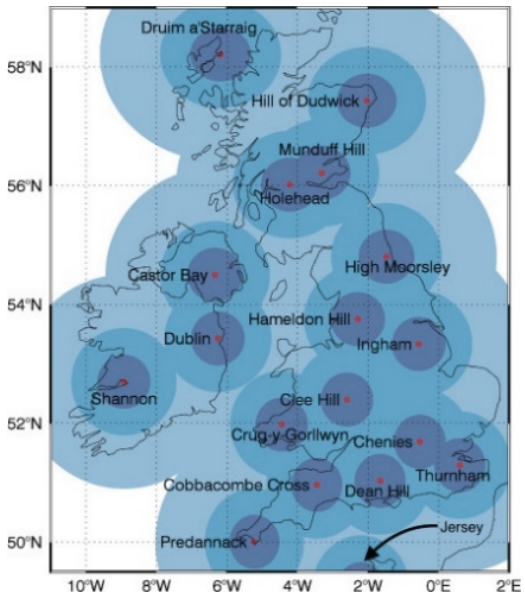


Figure 2.2 Locations of 18 weather radar sites for the 1km composite radar rainfall data (Fairman et al., 2015).

The accuracy of retrieved precipitation rate is affected by some radar data artefacts such as clutter, beam blocking (anomalous propagation) and bright band. The constant parameters used in dBZ-R conversion also limit its accuracy when the precipitation is not in liquid form (e.g., graupel, snow, hail). On average, the rainfall composite is found to overestimate by 3% the annual rainfall amounts over the UK compared with surface-gauge readings, and the measurement is less reliable in mountainous areas or places far from the radar (Fairman et al., 2015). The radar rainfall is also found to have a systematic underestimation of high intensity (Armon et al., 2020; Kendon et al., 2012). Nevertheless, the composite dataset still provides a useful depiction of the spatial distribution and temporal distribution of precipitation over the UK and has been used in many hydrological studies in the UK (Ochoa-Rodriguez et al., 2019).

2.2.3 Gridded Rainfall Datasets (GEAR)

Another observation-based data used in this study is 1 km gridded estimate of areal rainfall (GEAR) (Tanguy et al., 2019). The daily-scale GEAR data is available from 1890 to 2019. The GEAR data is derived from the Met Office database where the rain gauge network across the whole UK was used to keep the gridded estimates consistent with gauged rainfall rates at both monthly and daily scales. The natural neighbour interpolation method is used to give an estimation for those grids without gauged records (see section II.2 in Supporting document by Tanguy et al., 2019). The daily GEAR dataset also records the distance of each 1 km grid to the closest rain gauge used in the interpolation, which is an indicator of estimation quality for each grid (Figure 2.3). Due to the interpolation nature, the estimation is more reliable at places close to gauges. The GEAR data is taken as a reliable product to provide a gridded estimation of daily-scale observation rainfall and has been used in many hydrological studies over the UK (Martínez-de la Torre et al., 2019; Robinson et al., 2016; Rust et al., 2021).

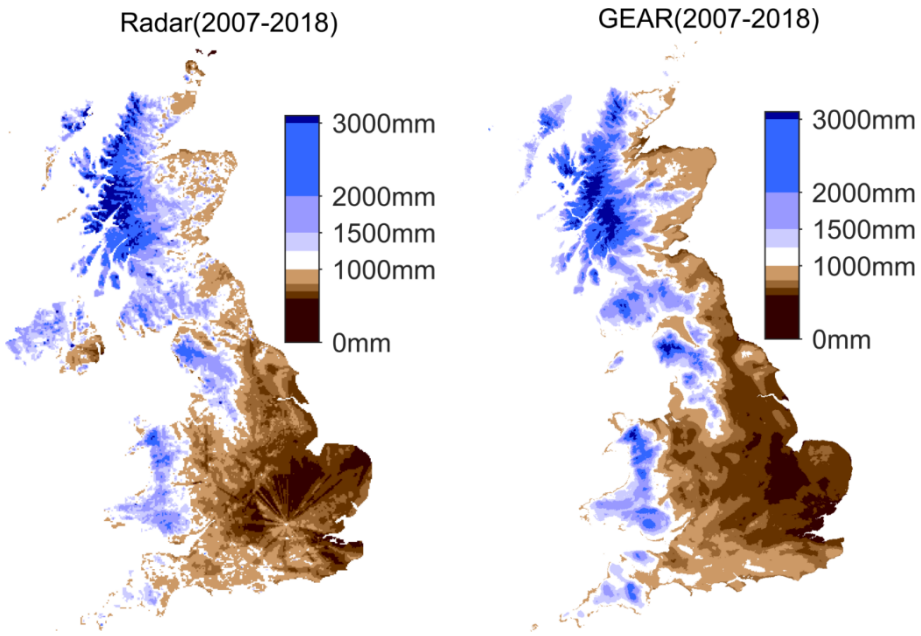


Figure 2.3 A comparison of observed annual precipitation (mm/yr) (averaged amount over 2007-2018) from (a) weather radar and (b) CEH-GEAR.

In addition to the daily GEAR data, it is worth mentioning that a disaggregated hourly version of the GEAR data (GEAR-1hr) is also made available recently (Lewis E. et al., 2022) where the data spans from 1990 to 2016. It provides useful information on hourly areal rainfall. However, the disaggregation is solely based on rain gauge measurements and the density of available rain gauges is not sufficient to provide the reliable spatial distribution of hourly rainfall (see Figure 2.4 as an example). Therefore, the GEAR-1hr dataset is only used in Chapter 5 as one of the observation references but not used in any modelling development throughout the thesis.

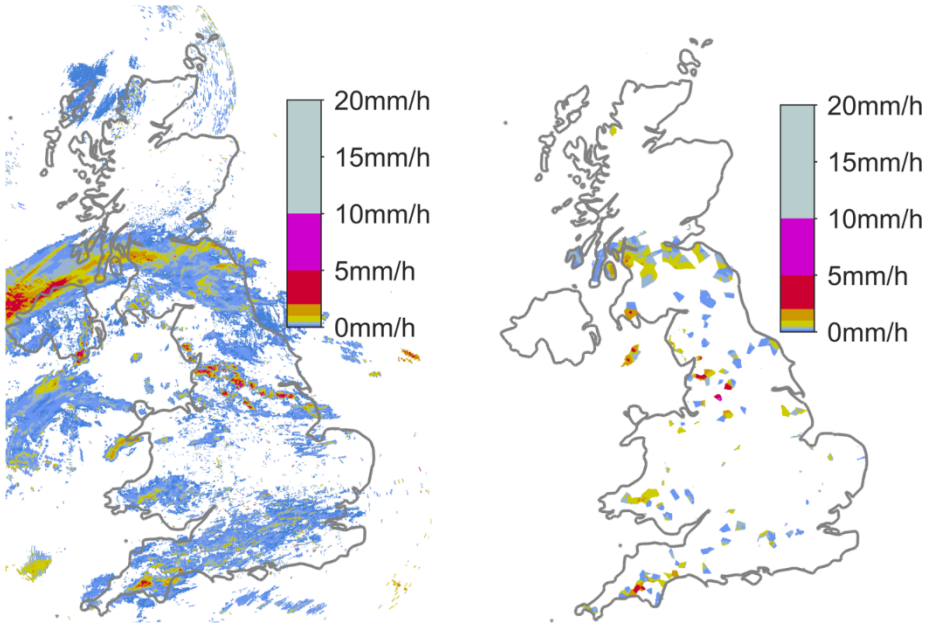


Figure 2.4 Example of precipitation maps (at 1200 UTC on 9 July 2012) obtained from two observation datasets. (a) Radar estimates (aggregated from 5-minute radar) (b) GEAR-1hr gridded dataset.

Section 2.3 Climate Projection Data

Climate projections used in this study are obtained from a 2.2km convection-permitting model (CPM) covering the British Isles (Kendon et al., 2019a; Met Office Hadley Centre, 2019), in which precipitation output is available at an hourly scale. The 12-member CPM ensemble was run in three periods (1980-2000, 2020-2040 and 2060-2080). Data for the historical (1980-2000) and future periods (2060-2080) are used in this study. For the future period, the projection is simulated under a high emission scenario RCP8.5 which assumes unmitigated greenhouse gas emissions and provides an upper estimate of expected future changes. In the model domain, horizontal grid spacing the inner region (including the UK land area) is at 2.2 km resolution and 4 km in the outer region (Kendon et al., 2019a, fig. 2.3.1).

The 2.2km CPM is driven by perturbed parameter variants of the Hadley Centre global model (HadGEN3-GC3.05) at 60 km with a 12 km RCM (HadREM3-GA705) intermediate nesting (Figure 2.5). The driving GCM ensemble contains contributions from internal variability, uncertainties from model physics and uncertainties in the global effect of carbon cycle feedback (Kendon et al., 2019a, chap. 2). The RCM nesting at 12 km provides the small-scale variability and is found to significantly reduce biases in rainfall intensity distribution and the mean summer precipitation (Fosser et al., 2019). Since the 12-member CPM samples uncertainties only through its driving GCM, parametric uncertainties in local processes and feedbacks are not well sampled, which means the uncertainty in changes at local scales is still underestimated. Nevertheless, the present ensemble is still one of the most advanced climate projections considering that previously the CPM was limited to a single model run (Kendon et al., 2014; Prein et al., 2017a), lacking any uncertainty context.

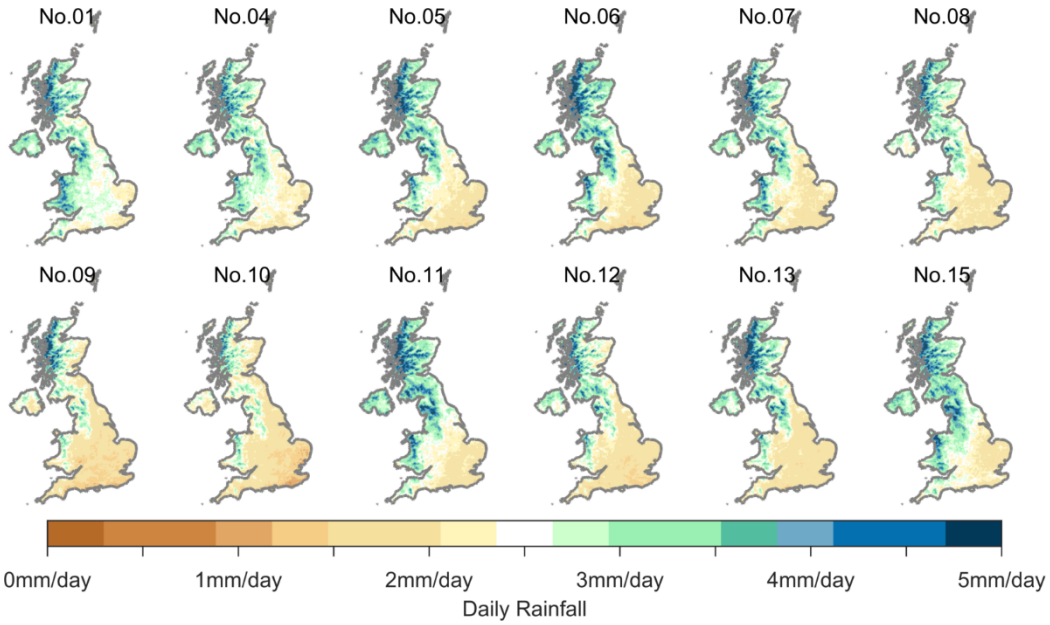


Figure 2.5 Example of CPM rainfall output from different ensemble members, the value shown corresponds to the average rainfall intensity in June over the historical period (1980-2000).

Large-scale patterns of CPM performance are strongly controlled by its driving models. For the CPM dataset used, its driving GCMs have been compared with a 13-member multi-model ensemble from CMIP5 (see the selected model name in the guidance from Met Office, 2019a, p. 16). In general, the driving GCMs perform well, particularly in reproducing UK precipitation variability, but in winter all model members show a cold bias (Murphy et al., 2018). The nested RCM and CPM output itself also has been evaluated (Kendon et al., 2019a). Its skill in representing high rainfall amounts over mountainous areas is improved substantially compared with the coarser models (Fosser et al., 2019). Notably, because of the biases inherited from driving models and systematic differences between model results and observations (such as the fact that the CPM tends to overestimate precipitation extremes) (Berthou et al., 2018; Fosser et al., 2020), there will be biases in the CPM results when moving to km-scale resolutions. According to the UKCP18 documents (Kendon et al., 2019a; Met Office, 2019b), doing bias correction (Met Office, 2019c) is recommended before using the data.

The UKCP Local (2.2 km) projections used in this thesis are obtained from the version released in late 2019. Although a graupel code error was found in the version (Kendon et al., 2020b) and an update was made by UK Met Office to improve the modelling of hourly extreme rainfall of the projections, the fully updated datasets were not available until late 2021. So, the old dataset is used throughout this thesis. For any further work, using the updated version is recommended but it is worth mentioning that future changes

projected by the UKCP are not significantly impacted (Kendon et al., 2021). Considering that the bias correction has been included in this thesis anyway, the methodology developed in this thesis for correcting and downscaling the local projections remains to be valid for both versions of the UKCP local projections and the key conclusions reported in this thesis regarding the climate change impact are still reliable.

There are also other CPM being developed for other areas such as Africa (Kendon et al., 2019b), Europe (Ban et al., 2014; Berthou et al., 2018), US (Prein et al., 2017a). Although this thesis focuses on analysis and modelling development for the UK, the developed simulation tool also can be applied to other CPM products having a similar resolution.

Chapter 3 Stochastic Rainfall Models

This chapter starts with a literature review on stochastic rainfall model development focusing on spatial-temporal models. Then, two well-established stochastic models are selected and described in detail.

Section 3.1 Review of Stochastic Rainfall Models

3.1.1 Single-site Modelling Attempts

Most of early stochastic modelling developments focus on reproducing rainfall at a single site. At daily or coarser scales, models developed were purely statistical tools based on Generalized Linear Models (Coe and Stern, 1982) and Markov chains (Hughes et al., 1999), always lacking a physical realism. For hourly scales, developed tools generally contain some physical-based concepts, such as fractal theory (Waymire and Gupta, 1993), analogue method (Lall and Sharma, 1996) or point processes (Onof et al., 2000). Further improvements based on those concepts also have shown an encouraging performance at a finer temporal scale, even down to 5 min (Kaczmarska et al., 2014). In those single-site models, spatial variability of rainfall is neglected because of lacking information in a spatial domain. Although spatial-temporal modelling goes back a long way too (Cox and Isham, 1988; Rodriguez-Iturbe et al., 1986; Wheater et al., 2000), advanced measurement technologies (such as satellite and dual-polarization doppler radars) occurring in the last few decades allow for a better understanding of the spatial rainfall profile at a kilometre scale (Hardenberg et al., 2003; Rysman et al., 2013; Seed et al., 2013) as well as more developments in spatial-temporal rainfall models.

3.1.2 Spatial Temporal Models

According to how the spatial structure is represented, spatial-temporal rainfall models can be roughly divided into following groups:

(1) Multi-site models

This type of model can be taken as an extension of single-site models. The spatial dependency is reproduced by introducing a correlation between different sites (Bárdossy and Pegram, 2009; Breinl et al., 2013; Chandler and Wheater, 2002; Mehrotra and Sharma, 2005). Model calibration is based on rain gauge networks. Temporal scales of models developed in this group have been sub-hourly (Ramesh et al., 2013) while the model does not allow for a representation of spatial field of the generated rainfall.

(2) Multi fractal models

Rainfall structure is represented through fractal theory under physical-based assumptions (scale invariance, cascade process and universality). Such an approach was widely used particularly for downscaling purposes thanks to its formal simplicity, parsimony and its ability to represent rainfall characteristics over a wide range of scales (Deidda, 2000; Over and Gupta, 1996). The 'blocking shape' problem was typically found in its generated fields (Kang and Ramírez, 2010, fig. 12; Schleiss, 2020, fig. 10), which has been addressed by using continuous cascades (Lovejoy and Schertzer, 2013). However, the realism of the synthesized spatial field is restricted by a sharp transition between rain and no-rain areas (Sapriza Azuri et al., 2013, fig. 14).

(3) Latent Gaussian field models

Under this group, rainfall fields are generated from a Gaussian field through a non-linear transformation. The advantage of this approach is the good performance in reproducing the precipitation variability. Climate factors also can be accounted for by introducing a conditional random field (Kleiber et al., 2012; Vischel et al., 2009). Most of the developed models in this group are used for event-based simulation (Benoit et al., 2018; Raut et al., 2018) or short-term prediction (Leblois and Creutin, 2013; Sigrist et al., 2012). In recent years, STREAP was developed to enable a continuous simulation based on the latent Gaussian random process and the renewal process (Paschalis et al., 2013).

STREAP model was originally developed by Paschalis (2013) and then embedded into a comprehensive weather generator including a few key climate variables (AWE-GEN-2d) (Peleg et al., 2017b). The generator has been applied to several hydrological applications, including flood studies at large rural catchments (Paschalis et al., 2014a); urban drainage modelling at smaller urbanized areas (Peleg et al., 2017a) and the investigation of landscape evolution in response to rainfall variability (Peleg et al., 2021; Skinner et al.,

2020). In general, the rainfall component of STREAP reproduces well the storm arrival processes, the temporal evolution and the spatial-temporal structure of rainstorms. For climate impact studies, there also have been attempts based on STREAP (Peleg et al., 2019). In their research, weather generator parameters are perturbed by using the "factors of change" (FC) approach (Burlando and Rosso, 1991; Kilsby et al., 2007) based on climate model outputs. However, statistics able to be re-parameterized were restricted by the spatial and temporal resolution of existing climate model outputs. A few parameters' inference in STREAP, particularly parameters governing the spatial-temporal structure over the rainfall fields, requires sub-daily and/or kilometre-scale information, which had generally not been made available in GCMs/RCMs by then.

(4) Cell-based methods

Cell-based methods are based on the concept that each storm event is a cluster of rain cells possessing a certain lifetime and extent. This concept mimics the physical process of rainfall generation and many rainfall models have been established based on this approach (McRobie et al., 2013; Moseley et al., 2019; Wheater et al., 2005). Among those developments suitable for hourly or sub-hourly scales, Poisson-cluster models are one of the most widely used. According to their clustering mechanism (Onof et al., 2000), these can be further divided into the Bartlett-Lewis and Neyman-Scott point process groups, each of which has received quite a few improvements in the past few decades from different aspects such as its temporal performance (Cowpertwait et al., 2011; Kaczmarska et al., 2014; Onof and Wang, 2020), spatial performance (Burton et al., 2010b; Leonard et al., 2008) and calibration method (Aryal and Jones, 2020; Cowpertwait et al., 2013; Jesus and Chandler, 2011; Kaczmarska et al., 2015).

Typical problems of many published versions of point process models are the lack of storm movement, the lack of statistical dependence between rainfall properties (intensity and duration) and the underestimation of rainfall extremes at fine space and time scales (Paschalis et al., 2013). To address the above limitation, Northrop (1998) introduced storm movement by increasing the detail of rainfall structure at the event scale, but generalizations to continuous-time rainfall models are not straightforward. Embedding such a structure within an additional process generating wet and dry spells, the model obtained was not parsimonious and the model calibration turned out to be quite data demanding (Wheater et al., 2006). There were also attempts to reduce the

underestimation of extremes by including some dependency between rainfall properties (Evin and Favre, 2008; Kaczmarska et al., 2014; Park et al., 2019; Paschalis et al., 2014b). Since these studies focused predominantly on single-site models they are not ready to be applied to spatial–temporal versions.

Despite the simplifications in the model structure mentioned above, one outstanding advantage of the point process models is the availability of analytical expressions for key statistics of modelled rainfall, including moment estimates up to the third-order moment, probability of dry period, autocorrelation, and spatial correlation (Cowpertwait, 1994; Leonard et al., 2008; Northrop, 1998; Onof and Wang, 2020). These key statistics can be directly included in the model calibration. Another advantage lies in the possibility of continuous rainfall simulation, which potentially overcomes the drawback of event-based simulation in long-term flood risk analysis (Verhoest et al., 2010). For climate impact studies, one recent research by Sørup (Sørup et al., 2016) has applied a point-process model (Burton et al., 2008) to urban applications by perturbing the model parameters with climate change signals. While the author already mentioned that the hourly-scale simulation might be still not sufficient in urban hydrology investigation (Ochoa-Rodriguez et al., 2019; Ochoa-Rodriguez et al., 2015), the research has shown strong potential to utilize point process models in future climate impact studies.

To decide the stochastic component used in this thesis (research question 1), two well-established stochastic tools (Cowpertwait, 2010; Paschalis et al., 2013), which are belong to the 3rd group (Latent Gaussian field models) and the 4th group (cell-based models), are taken as candidate models and described in the next two sections. These two models are selected because both are representing one of the most advanced model versions in each group and have the potential to be used as a stochastic component for future climate impact studies. Also, source code of both models has become available for this research. Scripts of the cell-based model have been replicated by the author based on publications (Cowpertwait, 2010) and available scripts for another cell-based model (Cowpertwait, 2006). The latent-gaussian field model (STREAP) is directly obtained from the model developer for this research purpose. Note, STREAP model described in this chapter refers to the version published in 2013 (Paschalis et al., 2013). All additional model improvements on STREAP achieved in this thesis are described in Chapter 7.

Section 3.2 Point Process Model

One of the most advanced point process models (Cowpertwait, 2010), a Neyman-Scott point process rainfall model (NS(s-t)), was selected for the study to answer the first research question. Compared with the earlier and more widely used version of the Neyman-Scott based space-time model (Burton et al., 2008; Cowpertwait et al., 2002), the selected version has further improved its spatial representation (Leonard et al., 2008). The model is capable of representing most key properties of point rainfall and spatial correlation at both hourly and daily resolution, and with a parsimonious structure (Cowpertwait, 2010; Cowpertwait et al., 2013). The most attractive feature of the model is that it has available analytical expressions for the moment estimates of the marginal distribution of the point rainfall depth, its temporal autocorrelation function, the probability of zero-rainfall across temporal scales, as well as the cross-correlation of rainfall depths at any temporal scales. These expressions are used for model calibration.

3.2.1 Model Structure

In the NS(s-t) tool, the rainfall field is generated in two steps: first the model generates storm arrivals and then generates the inner-storm cells.

In the storm arrival processes, storms are assumed to be independent, i.e., arrive in space and time according to a spatial-temporal Poisson process with a rate ζ_s (per unit area per unit time). A storm envelope defines the spatial extent within which rainfall can occur (Figure 3.1). The envelope has an exponentially distributed radius with parameter $\gamma_s(km^{-1})$. For each defined storm, rain cells are then generated. The number of rain cells C associated with the storm follows a Poisson distribution with a parameter ν $(-)$. The cells appear after the storm arrival time according to an exponentially distributed delay; the exponential distribution has parameter β (unit: h^{-1}).

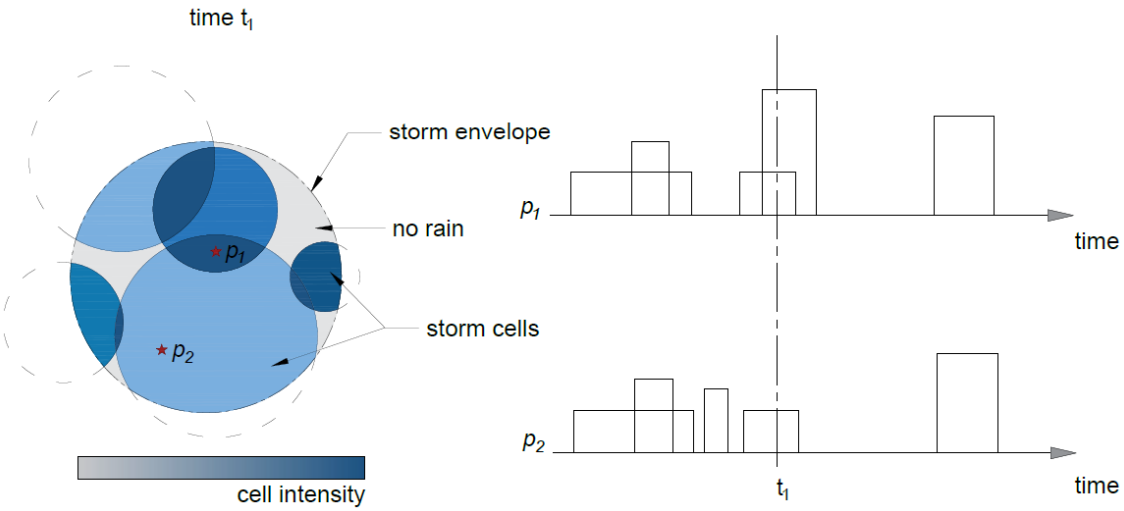


Figure 3.1 Schematic of the point process based spatial-temporal rainfall model. (left) the spatial pattern of time t_1, (right) the modelled cell occurrence at sites P_1 and P_2. The height of each rectangle represents the cell intensity. The length of each rectangle represents the cell duration.

Each rain cell is characterized by its lifetime, intensity and radius. Defined to be disc-shaped, each cell is assumed to have a constant rainfall intensity in space and time during its lifetime. The disc radius is exponentially distributed with parameter $\gamma_c(km^{-1})$. The lifetime, intensity and radius properties follow mutually independent exponential distributions, with parameters $\eta(h^{-1})$, $\xi(h \cdot mm^{-1})$ and $\gamma_c(km^{-1})$ respectively. Under the structure, the modelled rainfall at a particular location and a particular time is the superposed intensity of all cells covering that location at that moment. In the above process, the temporal rate of storms overlapping an arbitrary point $\mathbf{p} \in \mathbb{R}^2$ can be written as $\lambda = 2\pi\zeta_s\gamma_s^{-2}$.

Unlike the widely used version RainSim (Burton et al., 2008), the model also includes an additional governing random parameter z in order to capture the characteristics and the combined effect of different types of rainfall systems. The parameters mentioned above (ξ, ν) are adjusted to be functions of the additional random variable z, which is associated with storm characteristics (see equations (3.1)(3.2)). The value of z is continuously distributed according to a distribution with probability density function f_z. Same as previous studies (Cowpertwait, 2010), z is assumed to be uniform distributed over the interval $(0, 1)$. Other model parameters $\{\lambda, \beta, \eta, \gamma_c, \gamma_s\}$ are set to be independent on z.

$$\nu(z) = (1 - z)\nu_0 + z\nu_1 \tag{3.1}$$

$$\xi(z) = 1/z \tag{3.2}$$

where ν_0 and ν_1 are two model parameters.

Another significant improvement worthy to mention in the model version applied is the defined storm extent. The storm extent is included in order to achieve greater physical realism over a large area (Leonard et al., 2008). A storm envelope (defined by a randomized storm radius) is taken as a constraint so that only the part of a cell inside this envelope contributes to the storm rainfall (Figure 3.1). Hence the generated storm might only partially cover the target region of interest, which is more realistic when the study area is larger than the coverage of a typical storm. This constraint also enables the model to account for the seasonal/monthly variation of storm extent. In addition, it potentially alleviates the poor behaviour of those Neyman-Scott models (Burton et al., 2008; Cowpertwait, 2006; Cowpertwait et al., 2002) into properly capturing the fraction of wet area (Paschalis et al., 2013).

Spatial heterogeneity is also included in the model by adding a scale parameter φ_{P} to adjust ξ (the parameter governing the cell intensity) at each location site. The added scale parameter enables the model to generate a spatially varying pattern of mean rainfall intensity while keeping other dimensionless moment estimates spatially uniform. All other model parameters are valid for the whole area, and the calibration of these parameters can be undertaken for the whole available dataset (rain gauge measurements). For the model calibration, the scale parameters are obtained exclusively from the rain gauge data. When there is a need to generate gridded stochastic ensembles, additional gridded datasets (such as the GEAR product) will be used for generating gridded scale parameters.

3.2.2 Calibration

The model is calibrated by minimizing an objective function formed with the moment estimates of observed and modelled rainfall series. Included statistical properties of the modelled rainfall time series (at a certain aggregation level h hours) are the mean intensity $\mu(h)$, the coefficient of variation $\upsilon(h)$, the coefficient of skewness $\kappa(h)$, the lag 1 autocorrelation $\rho(0,1,h)$, the cross-correlation $\rho(d,0,h)$ and the probability of dry period $\varphi(\mathrm{h})$, where d is the distance between two sites (see analytical expressions in Appendix I.1). Following the previous study by Cowpertwait (2010), as shown in equation (3.1), the Poisson parameter ν is a function of variable z (z is related to rainfall types). Therefore, for each calendar month, the model parameters to optimize are

$\{\lambda, \nu_0, \nu_1, \beta, \eta, \gamma_s, \gamma_c\}$, which define vector $\boldsymbol{\theta}$. Scale parameters $\{\varphi_{\mathrm{P}}\}$ are computed based on these optimized parameters.

In the optimization, the Generalized Method of Moments (GMM) is applied to estimate the model parameters $\boldsymbol{\theta}$, which are estimated by minimization as:

$$\underset{\boldsymbol{\theta}}{argmin}\left(\sum_{i=1}^{k}\sum_{h\in H}\sum_{s=1}^{m}\left(w_{i,h,s}\left[T_{i,h,s}-\tau_{i,h}(\boldsymbol{\theta})\right]^2\right)\right) \tag{3.3}$$

where h is the time scale of aggregation, s the site, $T_{i,h,s}$ the observed estimate of statistical property number i at scale h and site s; $\tau_{i,h}(\boldsymbol{\theta})$ the modelled estimate of the same for any site (the model is spatially stationary) and $w_{i,h,s}$ is the weight assigned to this statistical property. When the hourly observation dataset is used, the set of all timescales used in calibration, H, is chosen to be $\{1,6,24\ hour\}$.

In this thesis, following statistics $\{\mu(1), \upsilon(h), \kappa(h), \rho(0,1,h), \rho(d,0,h), \varphi(24): h = 1,6,24\ hour\}$ are used in the calibration. The weights $w_{i,h,s}$ are set to the inverse of the variances of statistics (Kaczmarska et al., 2014) calculated across each of years for the selected month. In this study, the variance is computed for the statistics. Notably, in the spatial model, the $w_{i,h,s}$ and $T_{i,h,s}$ are computed for each site separately instead of pooling all sites together. This enables those sites having a larger variability of statistics (expected to have higher uncertainty) to be assigned a lower weight in the optimization.

The calibration procedure otherwise follows that in Cowpertwait (2013) and is based on the use of statistics of hourly rain gauge data. Within it, the probability distributions of the random rainfall type z and the corresponding other dependent parameters are predefined following the settings in previous research (Cowpertwait, 2010). The calibration steps are described below.

(a) The first step is to estimate the optimal set of temporal parameters θ for each calendar month, where $\theta = (\lambda, \nu_0, \nu_1, \beta, \eta)'$, $\mathrm{T} = \{\upsilon(h), \kappa(h), \rho(0,1,h), \varphi(h): h = 1,6,24\ hour\}$. Firstly, a minimisation based on a random 'multi-start' method is undertaken by using Sequential Quadratic Programming. The 'multi-start' method will return 20 local estimates based on 20 randomized starting points, and then the optimal estimate is returned so as to avoid local minima. The optimal parameter set for this calendar month is obtained from this step, denoted as θ^o.

Then, in order to obtain a smooth variation in monthly parameters, the second-round minimization is carried out for each calendar month. In this round, initial parameter guess is updated to a 3-month moving average of θ^o, and then the final parameter set θ is obtained by minimizing equation (3.3) based on the updated parameter guess.

(b) After obtaining the final temporal parameter set $\{\lambda, \nu_0, \nu_1, \beta, \eta\}$, this step is to optimize space-related parameters γ_s and γ_c by minimizing the sum of squares (Cowpertwait et al., 2013, Equation 1) using a genetic algorithm to avoid the local optimum (see the Equation (3.4)). This therefore yields a complete parameter set $\{\lambda, \nu_0, \nu_1, \beta, \eta, \gamma_s, \gamma_c\}$ for each calendar month.

$$\underset{\{\gamma_s,\gamma_c\}}{\operatorname{argmin}} \left\{ \sum_{h\in H} \sum_{d\in \mathcal{D}} \left(1 - \frac{\hat{\rho}(d,0,h)}{\rho(d,0,h)}\right)^2 + \left(1 - \frac{\rho(d,0,h)}{\hat{\rho}(d,0,h)}\right)^2 \right\} \tag{3.4}$$

where $\mathcal{D}$ is a set of distances for all pairs of gauged sites, $\rho(d,0,h)$ and $\hat{\rho}(d,0,h)$ the estimated and the sample cross-correlation at a distance of d and duration of h.

(c) The final step is to calculate the scale parameters $\{\varphi_{\mathrm{P}}\}$ (unit: mm) for calendar months (Cowpertwait, 2010). For each location p, the model parameters which are used for rainfall generation are $\{\lambda, \nu_0, \nu_1, \beta, \eta, \gamma_s, \gamma_c, \varphi_p\}$.

$$\hat{\varphi}_p = \frac{6\hat{\mu}_p(1)\hat{\eta}}{\hat{\lambda}(\hat{\nu}_0 + \hat{\nu}_1)} \tag{3.5}$$

where $\hat{\mu}_p(1)$ is the 1h sample mean for site p for the corresponding calendar month.

Section 3.3 STREAP

In the group of random field based models, STREAP was selected in our study. This section provides a brief description of STREAP model structure and calibration procedure. A detailed mathematical formulation can be found in the published research by Paschalis (2013).

3.3.1 Model Structure

STREAP model can be taken as a substantial improvement of previous work by Bell (1987) and Pegram and Clothier (2001a). The model is structured in three hierarchical stages:

(1) storm arrival process; (2) within-storm temporal evolution of mean areal statistics; (3) spatial-temporal evolution of storms (Figure 3.2).

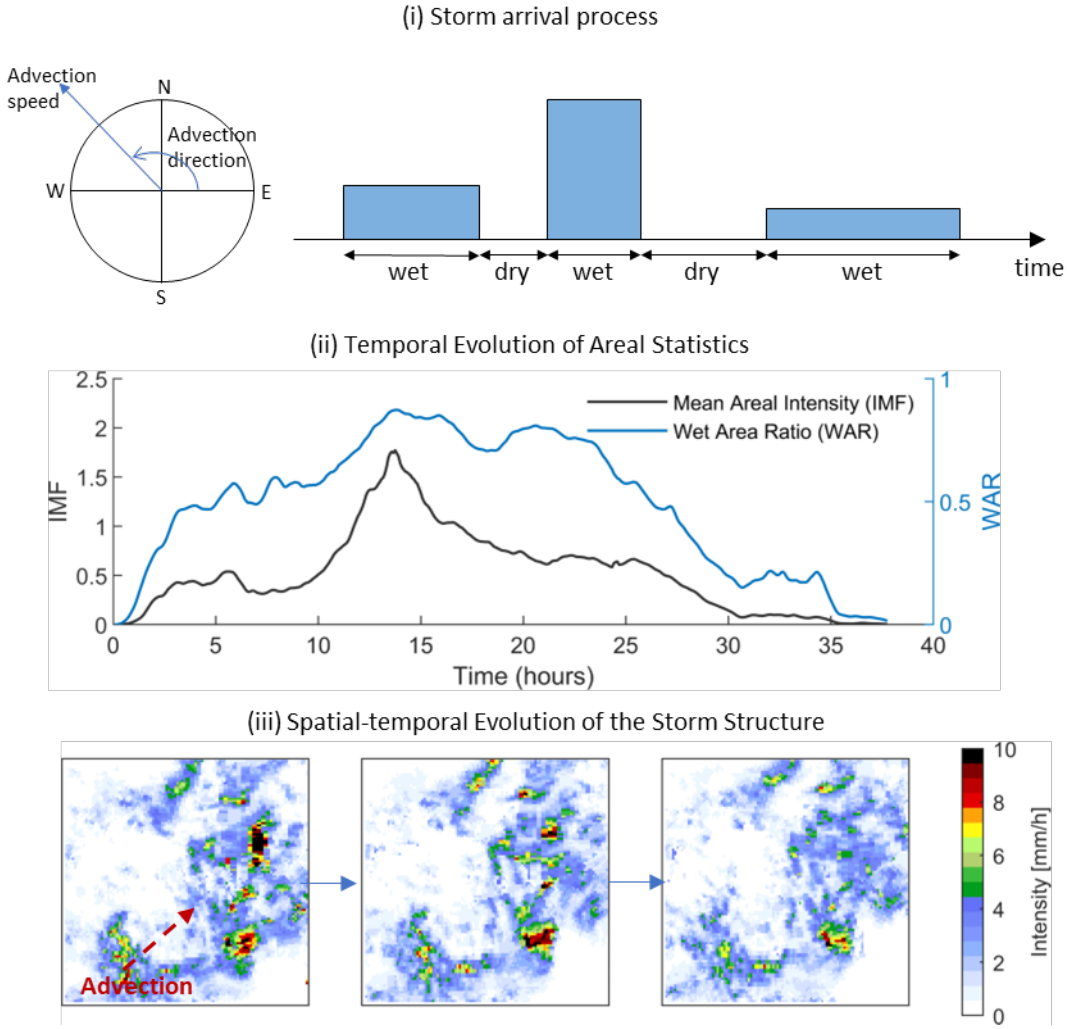


Figure 3.2 Schematic structure of STREAP model (Paschalis et al., 2013, fig. 1).

i. Storm Arrival Process

The storm arrival stage is modelled through an alternating renewal process describing a dry-wet sequence of the study area (Pegram and Clothier, 2001b). The duration of dry and wet spells is assumed to follow specific probability distributions respectively, which are mutually independent. Unlike the point process model, different probability distributions can be used for each month depending on which one fits the rainfall data better. For the spell durations, distributions normally to be considered include Generalized Pareto (e.g., Embrechts et al., 1997), Log-Normal (e.g., Papoulis, 1965) and Johnson distributions (e.g., Peleg et al., 2017b).

In addition to the dry-wet sequence, an advection speed (storm movement) is also included in the model, which is one of the key features of STREAP that differs from the point process model described in Section 3.2. For simplicity, the advection for each storm (wet spells) is assumed to be constant throughout the storm, following a normal distribution.

ii. Temporal Evolution of Areal Statistics

The next stage is to model mean areal statistics for each defined storm, mainly following the idea of the 'Strings of Beads' model (Pegram and Clothier, 2001a). Here, the mean areal statistics refer to the time series of mean areal intensity (image mean flux, abbreviate to IMF) and wet area ratio (WAR), which are considered as key characteristics of rainfall structure in determining catchment runoff.

These two time series (IMF and WAR) are assumed to be auto-correlated and cross-correlated, modelled via a bivariate Gaussian stochastic process (WAR_g, IMF_g) in STREAP. Then the generated WAR_g, IMF_g (following Gaussian distributions) are transformed into IMF series and WAR series.

The Whittle-Matérn covariance function is used to represent the bivariate process for each storm, within which the parameters are further assumed to remain invariant for all storms in each calendar month.

A Copula framework is included to preserve the variability over different storms. Five statistics, including the mean values and the standard deviation of the WAR_g and IMF_g ($\mu_W, \mu_I, \sigma_W, \sigma_I$) and storm duration T_w, are assumed to be correlated with each other. The multi-dimensional process is modelled by a t copula so as to enable a joint symmetric tail dependence (i.e., joint extreme events). Marginals of the two means are approximately Gaussian distributed and the two standard deviations are approximately Gamma distributed.

Through a distribution transformation, the WAR_g and IMF_g are then transformed into non-Gaussian WAR and IMF series, which are used in the next stage.

iii. Spatial-temporal Evolution of the Storm Structure

The third stage is to model the spatial-temporal evolution of precipitation fields based on the WAR and IMF series. The rainfall fields in space are modelled as latent Gaussian

fields (Kleiber et al., 2012), which means the modelled rainfall field is transformed from an isotropic, stationary two dimensional normally distributed random field $G(x, y)$.

The spatial correlation of the field is preserved through a one-parameter exponential autocorrelation function (Bell, 1987).

The temporal correlation of rainfall field at a point scale is also accounted for in the stage. The correlation of $G(x, y)$ is modelled as an autoregressive moving average (ARMA) process under the Lagrangian system of coordinates, i.e., following the storm motion.

As a last step, the Gaussian field is transformed into the intermittent rainfall fields, following:

$$R(x,y,t) = \begin{cases} 0, & for\ U[G(x,y,t)] < 1 - WAR(t) \\ LN^{-1}\left(\frac{U[G(x,y,t)] - 1 + WAR(t)}{WAR(t)}, \mu_r, \sigma_r\right), & for\ U[G(x,y,t)] \geq 1 - WAR(t) \end{cases} \quad (3.6)$$

Where U is the quantile function, $R(x, y, t)$ is the rainfall intensity in space and time, LN^{-1} is the inverse of the lognormal cumulative distribution with the scale parameter μ_r and the shape parameter σ_r.

3.3.2 Calibration

The calibration procedure described in this section is for general STREAP modelling purposes without a downscaling need. Calibrating STREAP requires gridded rainfall datasets (i.e., high-resolution weather radar) to provide a reliable spatial-temporal rainfall structure. All required intermediate inputs for calibration and model parameters are summarized in Table 3.1. Those changes on model structure and calibration procedure involved in the further developed tool are described in Chapter 7.

Table 3.1 STREAP model parameters (Paschalis et al., 2013)

STREAP Model Parameters	Estimated from
First Stage	
Parameters of the distribution of wet spells duration	WAR series
Parameters of the distribution of wet spells duration	WAR series
Parameters of the distribution of storm motion	Radar images
Empirical distribution of storm motion direction	Radar images
Second Stage	
Parameters of the Whittle Matérn covariance function	Normalized WAR, IMF series
Parameters of *t* copula	Normalized WAR, IMF series, storm duration
Parameters of the distribution of WAR	WAR series
Parameters of the distribution of IMF	IMF series

Third Stage	
Parameter governing the spatial correlation	Radar Images
Coefficient of variation of rainy part in space	Radar Images
Parameters of the ARMA process	Radar Images

i. Parameters in storm arrival process

In the first stage (storm arrival process), a storm separation method is applied to the spatial field to get sample data of wet spell duration and dry spell duration. In the separation, wet area fraction (WAR) >2% is taken as the spatial coverage threshold, and 2-hour consecutive dry period is taken as the temporal separation threshold (Paschalis et al., 2013). Based on the extracted spell durations, parameters of distributions are estimated using the maximum likelihood method. The best distribution with a minimal negative log-likelihood is then selected.

Parameters of storm speed and the empirical distribution of advection direction are estimated from computed time series of advection speed. The advection speed can be obtained from either reanalysis data or radar estimates. In this thesis, the advection is computed from radar data by using an optical flow based tracking algorithm (see Appendix I.2) instead of directly obtained from climate reanalysis data (i.e., ERA5). This is because the radar information is found to give a much more realistic storm speed compared with the wind component from ERA5 datasets. A comparison of storm speed from these two datasets can be found in Appendix I.3.

ii. Parameters in areal mean statistics

To estimate parameters used in the second stage, the WAR and IMF series are first transformed into normally distributed series WAR_g and $IMF_g \sim N(0,1)$. Five key statistics $(\mu_W, \mu_I, \sigma_W, \sigma_I, T_W)$ are computed for each storm and used for fitting a high-dimensional Copula, where the first four are the mean values and the standard deviation of the WAR_g and IMF_g and T_w is the storm duration. Considering that the calibration is carried out for each calendar month and that the sample size might not be large enough for less-rainy months, I use the method of the maximum likelihood (ML) instead of using an approximate ML method to estimate the linear correlation matrix of the Copula.

In the Whittle Matérn covariance process (Gneiting et al., 2010) used for representing the bivariate process, parameters needing to estimate include $\alpha_W, \alpha_I, \upsilon_W, \upsilon_I, \alpha_{WI}, \upsilon_{WI}, \rho_{WI}$. Here a parsimonious model is adopted which assumes $a_W = a_I = a_{WI}$, then, five

parameters are estimated by minimizing the mean squared error of the estimated auto-covariance (up to a 9-hour lag) and cross-covariance from the WAR_g and IMF_g.

Parameters of the distribution of IMF and WAR series are estimated using the maximum likelihood, similarly to the previous stage.

iii. Parameters in spatial-temporal fields generation

The parameter governing the spatial correlation (α_g, which is the correlation length of the exponential autocorrelation function) is estimated from binary images (rain or no-rain) following the methodologies proposed by Gutnisky (Gutnisky and Josić, 2010; Paschalis et al., 2013). The estimation is based on binary images rather than raw radar images in order to reduce the effect of radar noise on parameter inference. The binary images are obtained with a threshold of 0.1 mm/h applied to raw radar for separating rain and no rain. Spatial autocovariance is computed for each image and then the averaged autocovariance at each distance is taken as the measured autocovariance. α_g is then estimated by minimizing the squared error of measured autocovariance at all distances up to 100 km. For each calendar month, time slices with WAR larger than 0.1 are selected and the averaged value is used in the optimization.

Parameters μ_r, σ_r of the lognormal distribution (see equation (3.6)) are estimated using the methods of moments, with an assumption that the coefficient of variation of the rainy part in radar images (CV_{pos}) is only dependent on the month.

Parameters governing the temporal correlation (ARMA model parameters) are the most uncertain part in this stage. Challenges lie in the fact that the parameters are representing the correlation of Gaussian fields, which cannot be analytically obtained from the non-Gaussian intermittent rainfall fields having storm advection. To obtain suitable parameters for reproducing the temporal correlation, the radar fields in the Eulerian system need to be transformed into the Lagrangian coordinate system (which means that individual rain storms or rainfall cells are tracked, and coordinates do not vary with time) as the first step. The conversion is implemented in a much larger domain than the study area in order to eliminate the boundary effect after the transformation (see Appendix I.4 as a visual example). In the next step, since the intermittent rain field is not convertible to a Gaussian field, fitting the theoretical autocorrelation function of the ARMA process to the data is not mathematically achievable. Therefore, the ARMA parameters have to be

estimated using a trial-and-error method. In the method, a range of parameters is generated. For each parameter set, spatial fields are synthesized where the WAR and IMF series are always kept the same as the observed (for all storms lasting for at least 3 hours). Then, the autocorrelation under the non-Gaussian field is computed for each set of ARMA parameters. The parameter set giving the minimum mean squared error is then picked up as the optimal parameters.

Chapter 4 Applicability of Stochastic Models for Flood-related Hydrological Use

This chapter focuses on answering the question of which kind of existing model structure of spatial-temporal rainfall generators performs better in flood-related applications. Section 4.1 gives an introduction to existing flood estimation studies using stochastic rainfall models, followed by describing the numerical experiment designed for the research purpose. Section 4.2 describes the study area and data. Section 4.3 outlines the rainfall modelling tools, the hydrological modelling tool and all statistical analyses being used. Then, section 4.4 presents results in terms of rainfall statistics, flood responses as well as soil water dynamics over two rural catchments from different rainfall products, followed by discussions in section 4.5.

Section 4.1 Introduction

To date, both the point process model and the random field based model have been used for flood estimation studies (Brath et al., 2006; Camici et al., 2014; Moretti and Montanari, 2008; Paschalis et al., 2014a; Peleg et al., 2022, 2017a; Rulli and Rosso, 2002; Sordo-Ward et al., 2016). Long-term rainfall fields generated from the spatial-temporal stochastic generators can be taken as the rainfall-runoff modelling input for the estimation of streamflow and are particularly useful for continuous hydrological simulation. However, most of the previous research applying the models to streamflow estimation is either on ungauged basins or in areas without long-term streamflow data (Burton et al., 2010a; Cowpertwait et al., 2002; Leonard et al., 2008; Segond and Onof, 2009). The consequence is that validating a rainfall model in terms of the produced streamflow is limited to the observational data available at the study areas. Up to now, only little attention has been paid to quantifying how the estimation bias of synthesized rainfall from a stochastic model propagates to runoff estimates (Felder and Weingartner, 2016; Verhoest et al., 2010).

Besides answering the research question, this chapter also aims to investigate to what extent estimation biases in these two spatial-temporal rainfall models will propagate to the estimated streamflow. A numerical experiment is set up by calibrating two stochastic tools for the southeast of the UK and analysing the bias propagation from rainfall to catchment runoff at two medium-sized catchments within the study area. To achieve this, a fully distributed hydrological model, a dense network of hourly rain gauges and a high-resolution weather radar composite dataset were applied to the study area. Using those tools, estimation biases of the generated hourly space–time rainfall and their effect on catchment-scale dynamics are quantitatively evaluated, with an emphasis on peak flows.

The rainfall model evaluation includes two parts: analysis of synthetic rainfall fields and analysis of resulting catchment responses. After calibrating each model by using 12-years of rain gauge data and radar measurements (Table 4.1), synthetic hourly rainfall spatial fields were generated. By applying gridded scale parameters, the synthetic rainfall fields were able to preserve the observed spatial distribution of long-term annual rainfall amounts. To account for stochastic variability, 100 simulation replicates were generated for each model and then were used for validating rainfall statistics. Each replicate represents 12 years of hourly-scale spatial fields, i.e., the same length as the sample data.

Regarding the rainfall-runoff simulations, a calibrated hydrological model was used to simulate streamflow during the 2007–2015 period (9 years). The resolution of all rainfall inputs is 1 hour in time and 1 km × 1 km in space. 20 ensembles were used to represent the stochastic variability of the modelled catchment response. To evaluate how errors of the stochastic rainfall model propagate through to the catchment response, the modelled catchment response was compared with the reference runoff. Modelled soil water dynamics were also investigated to provide a further explanation of catchment response.

Section 4.2 Data

Hourly rain gauge measurements obtained from 54 stations (Figure 4.1.a) and high-resolution weather radar ($1km \times 1km$) are used in model calibration and validation, with details summarized in Table 4.1. Here, the time span used in calibrating the rainfall models is kept to 2005-2016 for all data sources. Notably, in STREAP calibration, parameters are obtained separately for three stages involved, where the parameters in

the 1st stage defines the storm arrival process, the parameters in the 2nd stage defines the areal statistics represented by a bivariate process and the parameters in the 3rd stage defines the spatial-temporal structure. Considering the discrepancy between radar measurement and rain gauge measurement in this region (Fairman et al., 2015, fig. 5a), a radar-rain gauge merged rainfall dataset is used to infer parameters in the second stage. The merging is achieved by using Kriging with the external drift (KED) method (Velasco-Forero et al., 2009). For the third stage, the raw radar is used so as to prevent destroying the spatial structure of observed radar rainfall. In addition to the rainfall data, additional datasets are required to calibrate and set up the hydrological model, which are summarized in this section.

Table 4.1 Summary table of rainfall and runoff data being used in Chapter 4.

	Model	*Details*	*Data Source*
Calibration	NS(s-t)	Model parameter sets	Hourly rain gauges
		Gridded scale parameters	GEAR
	STREAP	Parameters in the 1st stage (storm arrival)	Hourly rain gauges
		Parameters in the 2nd stage (areal statistics)	Radar - Rain gauge merged
		Parameters in the 3rd stage (spatial-temporal structure)	Radar data
		Gridded scale parameters	GEAR
Validation	NS(s-t) and STREAP	Point rainfall statistics	Hourly rain gauges
		Areal rainfall statistics	Radar
		Runoff statistics	Reference runoff
		Soil water dynamics	Simulated Soil Map

4.2.1 Site Description

The numerical experiment proposed above was carried out for two rural catchments (Figure 4.1) located in the Anglian River basin (south-east of the UK), namely the Stour and Welland catchments. The area (Anglian region) receives annual rainfall around 700 mm (Met Office, 2016), roughly spatially uniform with negligible orographic effects (Neal and Phillips, 2009). As a typical low-lying part of the country, despite the low rainfall totals, this area experiences large fluvial flooding events resulting in significant flood damages (DEFRA, 2016a, Table 7.1).

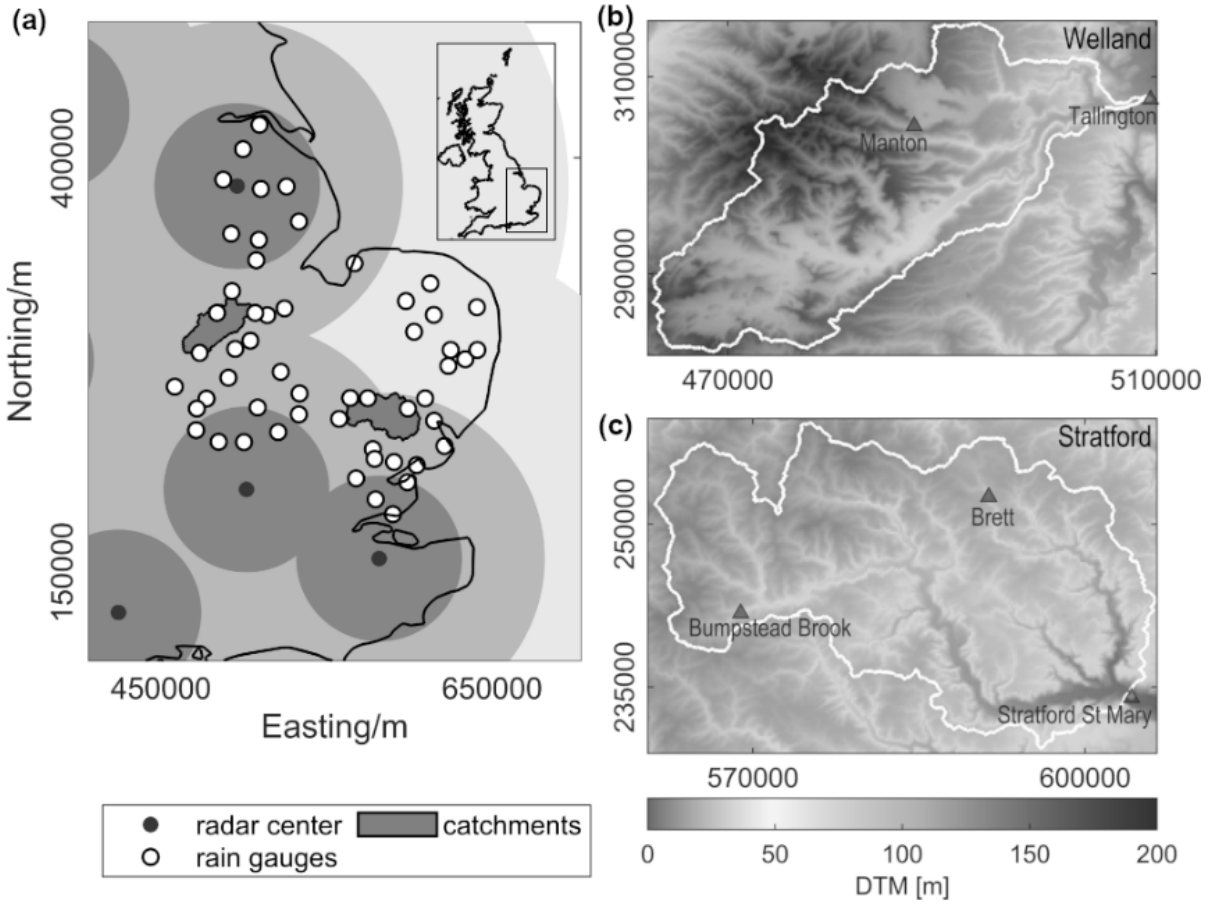


Figure 4.1 Location map of the study area, rain gauges and digital terrain model (DTM) of two experimental catchment areas. (a) locations of rain gauges, radar centre and two experimental catchment areas with the filled circles indicating distances of 50, 100 and 200 km from the radar centre; (b,c) digital terrain model (DTM) of the Welland catchment with an outlet at Tallington and the Stour catchment with an outlet at Stratford St Mary.

The Stour catchment at the Stratford (844 km^2) is located at low altitude (5.6-127.6 m), running from west to east along 75.6 km of the mainstream (Figure 4.1.c). The land cover consists mainly of arable land (75.37%) and grassland (13.94%) (NRFA, 2019a) (See Figure 4.2.a). The geology is characterized by chalk underlying clay soils, fluvial sands or gravels (Anstead and Tovey, 2017). The main flood risk is from river flooding due to soil saturation excess (DEFRA, 2016b, p. 48), while incidents of groundwater flooding are limited (DEFRA, 2009a).

The Welland catchment at the Tallington (717 km^2), compared with the Stour catchment, has a steeper topography (7.6-229.3 m) (Figure 4.1.b). The land cover (see Figure 4.2.b) is mainly arable for crop production (47.21%) and grassland (34.45%). The underlying geology is nonporous clay, with a high runoff coefficient (DEFRA, 2009b). Similarly, river flooding is the main risk in this catchment (DEFRA, 2016b, p. 133).

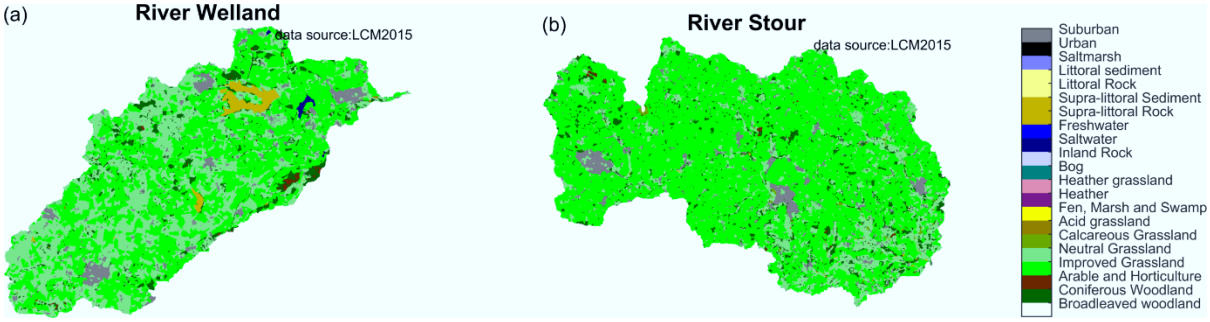


Figure 4.2 Land use maps showing the land cover at the study catchments. Data source: LCM2015 datasets (Rowland et al., 2017).

4.2.2 Site Data

Catchment data used for setting up the hydrological model includes topography, land use, soil textural properties and geology. The topography was extracted from OS Terrain 50 (Ordnance Survey, 2018) digital terrain model and regridded to 200 m × 200 m resolution. The soil textural properties (fraction of sand, clay, silt and organic matter in the first 500 mm depth) were obtained from SoilGrids (Hengl, 2018a, 2018b; Hengl and Wheeler, 2018). These soil properties were then converted to spatially distributed soil hydraulic properties (see Figure 4.3) using the Pedotransfer functions of Saxton & Rawls (2006).

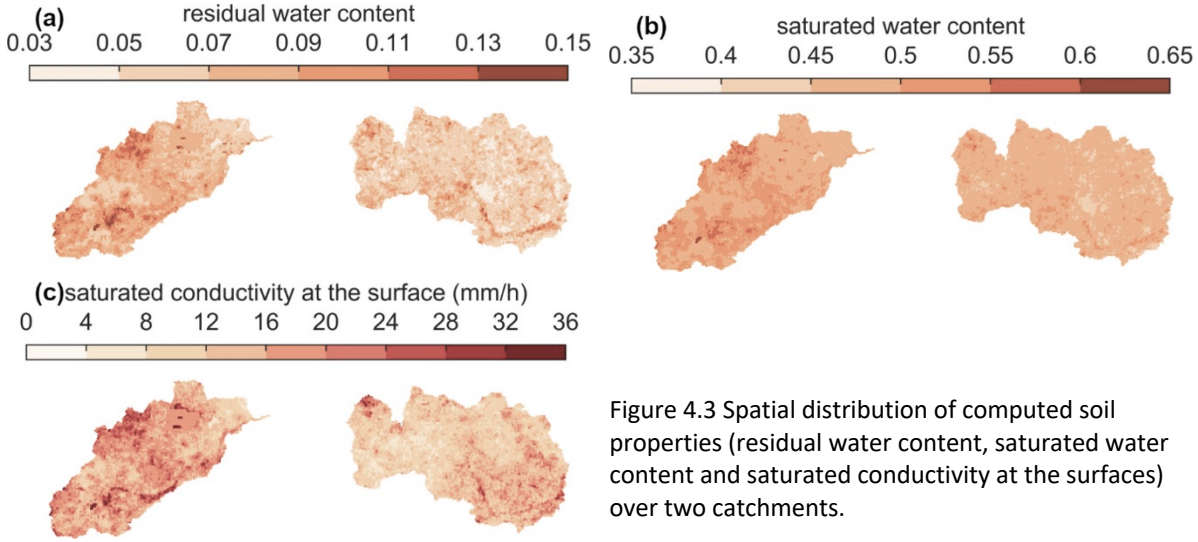


Figure 4.3 Spatial distribution of computed soil properties (residual water content, saturated water content and saturated conductivity at the surfaces) over two catchments.

Potential evapotranspiration was taken from the 1 km × 1 km gridded product (CHESS-PE), obtained from the UK Centre for Ecology and Hydrology (Robinson et al., 2016). This product contains potential evapotranspiration from 1961-2015 at a daily scale, calculated using the Penman-Monteith equation (Monteith, 1965) from the Food and Agriculture Organization of the United Nations (FAO). For the calibration of the hydrological model, gauged daily river flows at two upstream stations were used, retrieved from the UK National River Flow Archive (NRFA).

Section 4.3 Methods

4.3.1 Rainfall Modelling Tools

Following Chapter 3, a point-process-based model NS(s-t) (Cowpertwait, 2010) and a random-field-based model STREAP (Paschalis et al., 2013) are selected in this study. Details of the model structure and calibration procedures have been described in chapter 3 (see more details in Section 3.2 and Section 3.3), which will not be repeated in this chapter. How observation datasets are used to calibrate each stage and to obtain rainfall model parameters are summarized in the Table 4.1. After calibrating the two models, rainfall is then generated at 1 km spatial resolution and 1-hour temporal resolution. The generated replicates are then used for validating rainfall statistics and simulating the catchment runoff.

The catchment runoff is simulated in a continuous simulation, which is then compared with the 9-year reference runoff (i.e., simulated runoff by using observed rainfall as input). Despite stochastic models enabling the generation of rainfall fields over any timespan, the annual amount of the generated rainfall each year is purely random by default. To make sure the observed annual rainfall amount is preserved by the simulated 9-year replicates from the models for each year, a criterion is added to select the 20 most appropriate 9-year replicates as well as to determine the rank in each replicate (see details in Appendix II.1).

4.3.2 Rainfall-runoff Models

A calibrated fully distributed hydrological model is used to simulate rainfall-runoff processes in the catchments. Instead of using a lumped/semi-distributed hydrological model, the fully distributed model is selected in this study so as to analyse the impact of spatial rainfall variability on the modelled hydrological cycle. The model is the WATET model (Remondi et al., 2018) without explicit consideration of the pollutant transport as this is not relevant for this study. Briefly, the model solves hydrological fluxes on a regular grid. Soil water is solved using a simplified soil water transport model for every grid cell for computational efficiency. Similar to the grid-to-grid model by Bell (2007), surface water routing and lateral soil water flow are estimated by using a kinematic wave approximation.

To provide a more accurate representation of topographic features, the spatial resolution of the DEM is chosen to be 200 m × 200 m. Infiltration and evapotranspiration are solved at an hourly time step. Surface water is routed by using an adaptive time-step which could be as small as a few seconds, based on the Courant–Friedrichs–Lewy condition (Courant et al., 1928).

Most modelled properties are set up using the available spatially distributed catchment information (see section 4.2.2). Evapotranspiration is estimated by a potential evapotranspiration product (CHESS-PE in this study). Water stress factor β is set equal to the average effective soil moisture of the 45 cm of soil (Porporato et al., 2001). Soil hydraulic properties are estimated using a Pedotransfer function (Saxton and Rawls, 2006) based on soil textural properties obtained from SoilGrids. Groundwater flow is represented as a storage-discharge relationship $Q_{gw} = aS_{gw}^{b}$ (Benettin et al., 2015), where a, b are two empirical coefficients obtained from calibration. Urban runoff and contributions of man-made drainage networks are neglected in this study.

Aside from the available catchment data, several other parameters are required to set up the hydrological model, including the anisotropy ratio of hydraulic conductivities in different directions, the root zone depth, the maximum groundwater storage and the exponent in the storage-discharge function. Model calibration is thereby carried out to define all the parameters of this hydrological model before the numerical experiment. In the calibration, observed rainfall using the combined radar/rain gauge data is taken as rainfall input. Parameters are estimated (Table 4.2) by maximizing the Nash-Sutcliffe efficiency (NSE) (Nash and Sutcliffe, 1970) of daily streamflow at two gauging stations (Brett at Cockfield and Bumpstead Brook at Broad Green).

Table 4.2 Chosen Manning coef. and calibrated parameters of hydrological model for two catchments

Catchment property	Value
Manning Coef. – River	0.04 (McCuen, 2005, Table 3-4)
Manning Coef. – Arable	0.1 (McCuen, 2005, Table 3-4)
Anisotropy ratio	50
Root zone depth (mm)	450
Max Groundwater storage	1800
Exponent in storage-discharge function	2

These two stations are chosen because both are part of the UK Benchmark Network (UKBN), which is expected to be 'near-natural' and can be considered reasonably free from human disturbances (Harrigan et al., 2018; NRFA, 2019b). Daily streamflow measurements between 2008 and 2015 are used in calibration (see a full hydrograph in

Figure 4.4, zoom-in hydrographs and hyetographs in Figure 4.5), while the year 2007 is used for the model spin up. NSE values for the two stations are 0.68 and 0.60 for daily flows. Note, that both stations are in the Stour catchment since there are no gauged stations belonging to UKBN in the Welland catchment. At Welland, the parameters have enabled the model to broadly replicate the Welland catchment behaviour, by selecting an upstream station (Gwash South Arm at Manton), thus largely excluding the effect of built infrastructure, where the NSE value is 0.54 for daily flow.

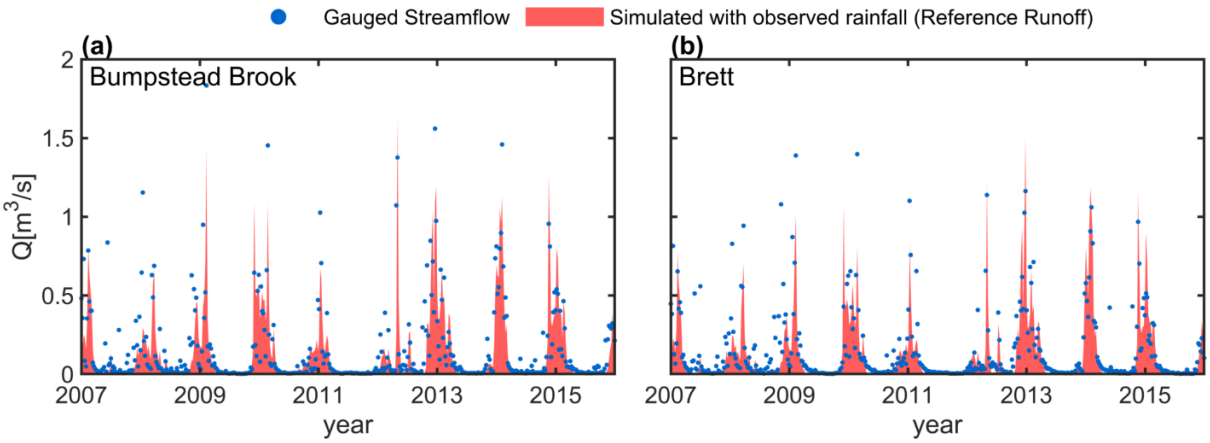


Figure 4.4 Comparisons of long-term flow obtained from streamflow gauges and the hydrological model, at two benchmark stations.

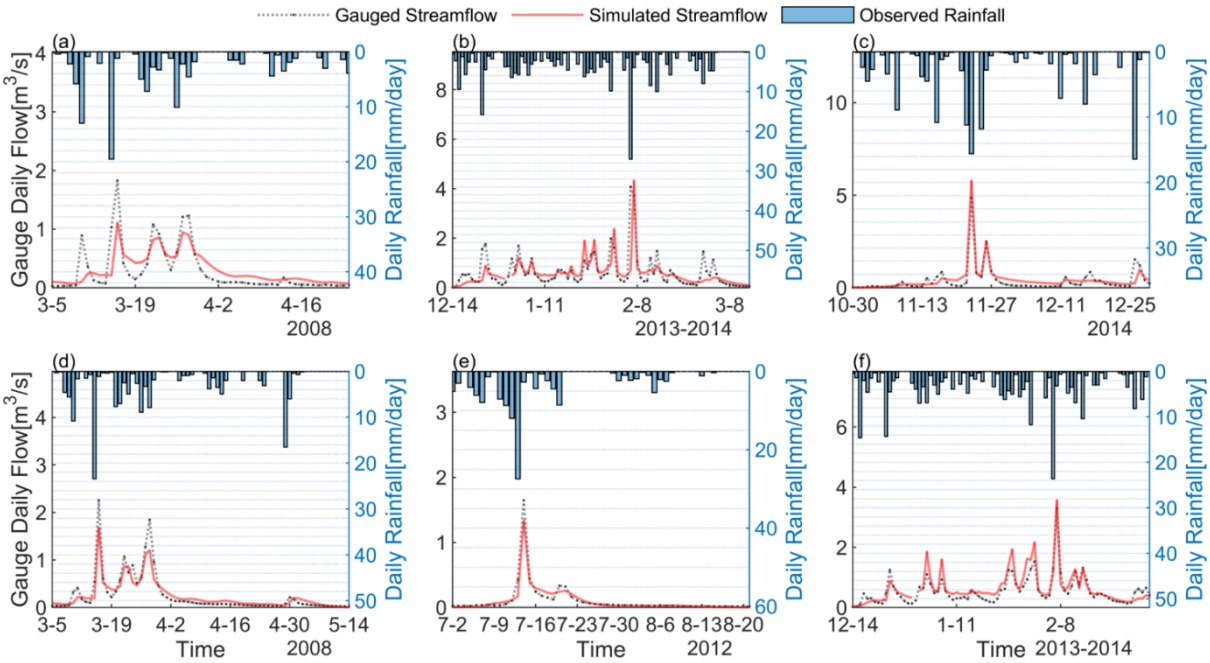


Figure 4.5 Comparisons of Hydrographs and Hyetographs in several events at Bumpstead Brook station (a,b,c panels) and at Brett station (d,e,f panels).

The calibrated model is not able to fully replicate the observed streamflow for the catchments (i.e., NSE=1) (Ritter and Muñoz-Carpena, 2013) because of simplifications

introduced by the hydrological model and uncertainty related to the observed catchment information. However, for the purpose of this study, the model performance is deemed sufficient. The 'reference runoff' used in the numerical experiment is the modelled runoff of observational rainfall forcing. All comparisons of runoff properties are made against this reference runoff. This means that the catchments we used to test the rainfall models can be regarded as virtual catchments, which are defined to be perfectly represented by the hydrological model.

4.3.3 Statistical Analysis

To make a thorough comparison, NS(s-t) modelled results and STREAP modelled results are analysed in three aspects including rainfall properties, runoff statistics and soil water dynamics. Rainfall properties are compared to evaluate the calibration performance of these two models; runoff statistics and soil water dynamics are analysed to quantify the bias propagation from rainfall input to catchment response.

i. Rainfall Properties

A range of point-scale and areal-scale rainfall statistics are analysed and compared with observational datasets. Both daily and hourly temporal scales are analysed.

Point-scale statistics computed here include the mean, the coefficient of variation (CV), the coefficient of skewness (SKEW), the lag one autocorrelation of rainfall depths at each site (ACorr), the cross-correlation of rainfall depths between sites (CCorr) and the probability of dry period at each site (PD). These statistics are not used in STREAP calibration but included in the model calibration of NS(s-t) and have been commonly used to validate point process stochastic models (Cowpertwait et al., 2013). The overall performance of these key descriptors is represented by the averaged relative bias between the fitted value and the sample value.

Extremes (annual maxima) of point rainfall are evaluated over the study area, in which 54 gauged sites are evaluated together. To visualize the spatial variability and the averaged performance in the same figure, the extreme feature is summarized in the following way: for the kth simulation of the set of 100 12-year-long simulations, the ranked annual maximum in the ith year at site s is denoted as $y_{k,i,s}$. The annual maxima are assumed sorted from largest to smallest, so that $y_{k,i,s} \geq y_{k,i+1,s}$. Let $q_{\alpha,i,k}$ be αth quantiles for the year i and the simulation k over all sites of $y_{k,i,s}$ and $m_{\alpha,i}$ be the median

over all simulations k of $q_{\alpha,i,k}$. Then, $m_{\alpha,i}$ for $\alpha = 0.10, 0.5, 0.90$ is calculated and visualized on the usual Gumbel plot. In the Gumbel plot, the horizontal axis is the Gumbel reduced variate $y(i) = -ln(-ln(1 - 1/T))$, where $T = (N + 0.12)/(i - 0.44)$ following the Gringorten formula and $N = 12$; the vertical axis is the value of $m_{\alpha,i}$. For the observational data, k = 1. Note, the spatial heterogeneity in both rainfall products has not been removed for the extreme analysis. Therefore, the range between $m_{0.1,i}$ and $m_{0.9,i}$ could then help to evaluate whether the spatial non-stationary of extremes is well represented by these two rainfall generators.

Areal statistics, including the wet area ratio (WAR) and the areal mean precipitation intensity (IMF, which is the abbreviation of Image Mean Flux), are used to evaluate simulated hourly rain fields. The wet area ratio is the fraction of wet area in the simulation domain, where grid squares having hourly rainfall depth larger than 0.2 mm are defined as 'wet' grids (1 km resolution). The areal mean precipitation intensity is computed for each time slice of the rainfall field (717 km^2). The probability distributions of WAR and IMF are used to compare the simulated rainfall with the observed.

ii. Runoff Analysis

Flow duration curves (FDCs) and flood frequency curves (FFCs) (Lamb et al., 2010) are used to evaluate the simulated runoff driven by different rainfall inputs. Both curves are derived using the continuously simulated streamflow data (at catchment outlets) of the hydrological model. FDCs are used to assess the variation of flow series. Curves for both the low flow period (June to August) and the high flow period (December to February) are plotted. FFCs are used to assess the simulated extreme streamflow, reflecting the potential risk of river flooding. A Gumbel distribution is assumed to fit the FFCs, the confidence intervals of which were estimated by employing a parametric bootstrap method (Coles, 2013). To account for seasonal variability, both curves are analysed on a seasonal basis.

iii. Soil Moisture Analysis

Analysis of soil moisture dynamics is carried out so as to shed light on how the spatial-temporal dynamics of soil moisture over the catchment will change when different rainfall products are used.

The soil moisture analysis focuses on assessing the following aspects: 1) the temporal variability of spatial-averaged S_e (the effective soil saturation) over a calendar year; 2) the spatial variability of the S_e in JJA and DJF (represented by the coefficient of variation in space at each time step); 3) for hours having at least one grid with $S_e > 0.85$, how the estimation error of $\bar{\theta}$ (single-grid soil moisture content averaged over all selected hours for each simulation year at each pixel) changes as a function of the topographic index (TI).

Both S_e and TI are obtained using the equations below:

$$S_e = \frac{\theta - \theta_r}{\theta_s - \theta_r} \tag{4.1}$$

$$\lambda = \ln\left(\frac{\alpha}{tan\beta}\right) \tag{4.2}$$

where θ is the soil moisture content, θ_s the saturated water content, θ_r the residual water content, α is the upslope contributing area per unit length of contour and $tan\beta$ the local slope of the pixel.

Section 4.4 Results

4.4.1 Stochastic Model Performance

i. Point Scale – Moment Estimates

Both models well capture the long-term annual mean precipitation (with a relative bias of less than 0.76%) and the inter-annual variability (see Appendix 0). Temporal rainfall properties, including the coefficient of variation (CV), the coefficient of skewness (SKEW), and the autocorrelation lag-1 (lag-1 ACorr) were examined at 1 h and 24 h aggregation levels in Figure 4.6. For these statistics, the NS(s-t) generally gives a better performance than STREAP, which is not surprising because those moment statistics are directly used in the model calibration of the NS(s-t) (section 3.2.2) but not in STREAP. Overall, the NS(s-t) consistently underestimates both the daily-scale lag-1 ACorr and the SKEW, while STREAP tends to overestimate quite a few statistics including the CV, daily-scale lag-1 ACorr and the hourly SKEW. This implies two models' weaknesses in capturing prolonged rainfall events, i.e., the NS(s-t) gives less prolonged rainfall events, but STREAP gives too many prolonged rainfall events.

The probability of zero rainfall hours is not used in either of the models' calibration but is also examined here (Figure 4.6.d). Compared with STREAP, the NS(s-t) produces a lower averaged error of this statistics while STREAP tends to simulate more dry hours. The overproduced dry hours can be explained by the storm arrival process of STREAP: in the modelling structure, only those hours having a rainy coverage fraction > 5% are taken as wet hours, which means, those observed rainy hours with a very small coverage fraction are taken as no-rain throughout the whole study domain. This leads to a higher probability of dry hours being modelled by STREAP at a point-scale.

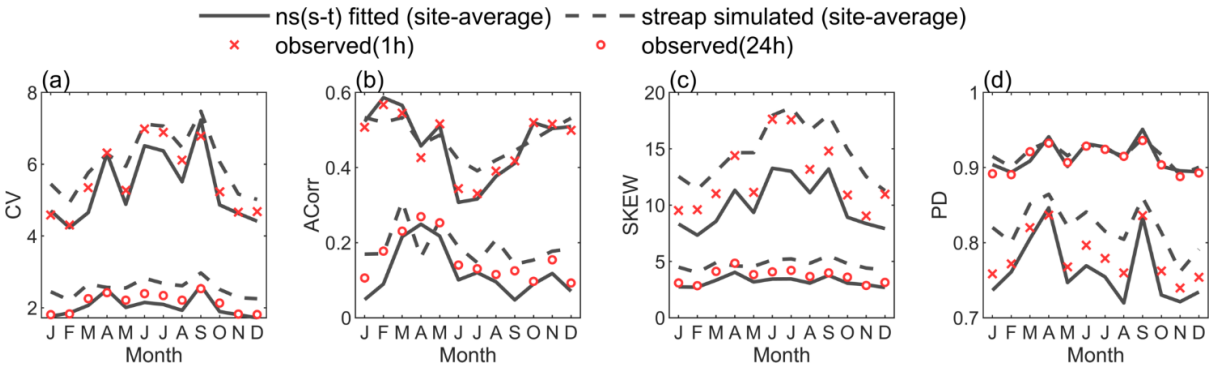


Figure 4.6 Validation of NS(s-t) model and STREAP model in terms of point rainfall statistics, including (a) the coefficient of variation; (b) the lag-1 autocorrelation; (c) the coefficient of skewness; (d) the probability of dry periods, at 1-hour and 24-hour aggregation levels.

ii. Point Scale - Spatial Correlation

The spatial correlation of synthetic series is plotted for two months, January and June, representative of winter stratiform and summer convective events respectively (Figure 4.7). The seasonal pattern of cross-correlations is well captured by both stochastic models. During the winter season, when stratiform systems with a large spatial coverage commonly occur, the 1-hour spatial correlation is well captured by both models (Figure 4.7.a). However, during summer, the NS(s-t) model tends to overestimate the 1-hour spatial correlation for distances smaller than 50 km (Figure 4.7.b), suggesting NS(s-t) is inadequate in capturing the localized features of convective summer storms. STREAP instead gives a much more realistic spatial correlation for the same distance.

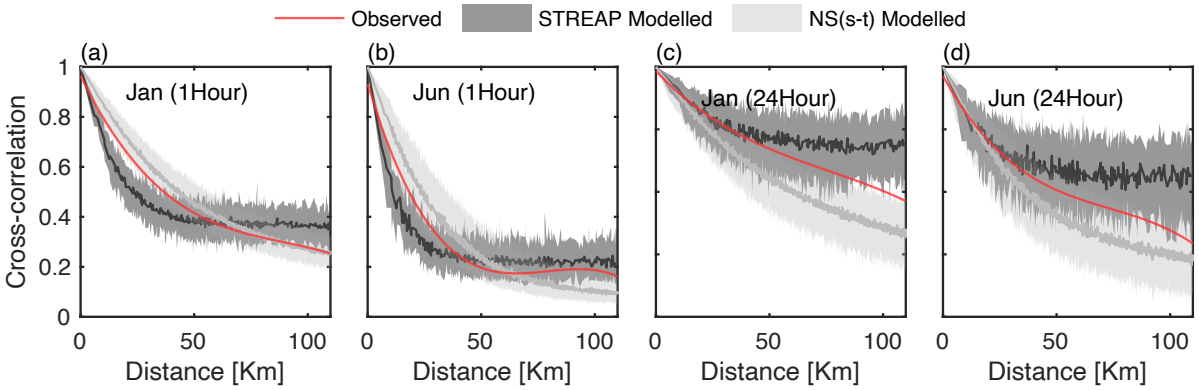


Figure 4.7 Cross-correlation of different rainfall products for all pairs of gauged sites in January and June, at an hourly scale (a, b); at a daily scale (c, d). The shaded area covers the 95th and lower 5th percentiles of 100 replicates of the rainfall model being used, which are either STREAP or NS(s-t). The two grey-colour solid lines correspond to the 50th percentile of the replicates of two models respectively. The red line corresponds to the cross-correlation estimated from all pairs of rain gauge observations.

Similar performance is found at a coarser scale (daily), in which STREAP outperforms the NS(s-t) for distances shorter than 50 km (Figure 4.7.c, d). The NS(s-t) tends to consistently overestimate the daily cross-correlation in both months, which could be explained by the assumption of non-moving storms in the NS(s-t).

iii. Point Scale – Extreme Statistics

Point-scale precipitation extremes from different rainfall products (observed, NS(s-t) simulated and STREAP simulated) are shown in Figure 4.8 (hourly scale) and Figure 4.9 (daily scale). The extremes produced by the stochastic models show an overall good agreement with observed extremes at return levels of up to 20 years.

Only a slight underestimation is found in generated hourly extremes in summer (JJA) from both models. For 20-year return levels, the NS(s-t)-modelled extremes are 2.9 mm/h lower than the observed and STREAP-modelled extremes are 0.7 mm/h lower. However, when it comes to a daily scale (Figure 4.9.b), extremes produced by the NS(s-t) tend to be systematically lower whereas the STREAP extremes are closer to the observed.

A larger discrepancy between the two models' performance occurs in winter (DJF), where the NS(s-t) largely reproduces extremes for return levels lower than 10 years. However, STREAP consistently gives a larger winter extreme. The overestimation becomes more significant at 24-hour aggregation levels (Figure 4.9.d), which can be explained by the overestimated lag-1 Acorr in the calibrated STREAP (Figure 4.6.b).

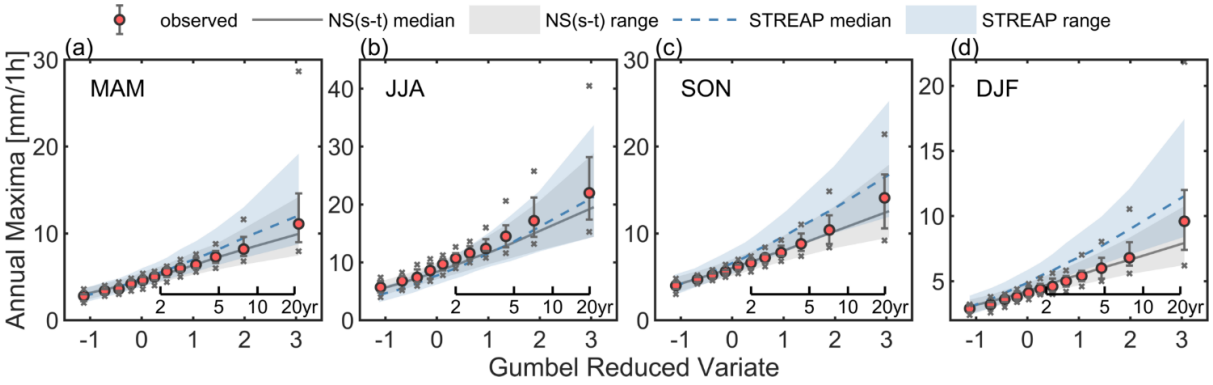


Figure 4.8 Hourly annual maximum rainfall intensity against return periods in different seasons, at MAM (a), JJA (b), SON (c) and DJF (d). The observed values are shown as quartile error bars, with upper and lower 10th percentiles shown as crosses and medians shown as circles. The solid line is an overall estimate (site-median, ensemble-median) for the simulated series ($m_{0.5,i}$). The shaded area corresponds to estimates of upper 10 percentile ($m_{0.9,i}$) and lower 10 percentile ($m_{0.1,i}$) of data (indicating the spatial variability of extremes over different sites).

In terms of the spatial variability, as represented by the shaded area (Figure 4.8), we can see that STREAP tends to give a larger range of extreme values across different sites than the NS(s-t). The larger range produced by STREAP is also more consistent with the observed variability (represented by the distance between two red crosses at each return level).

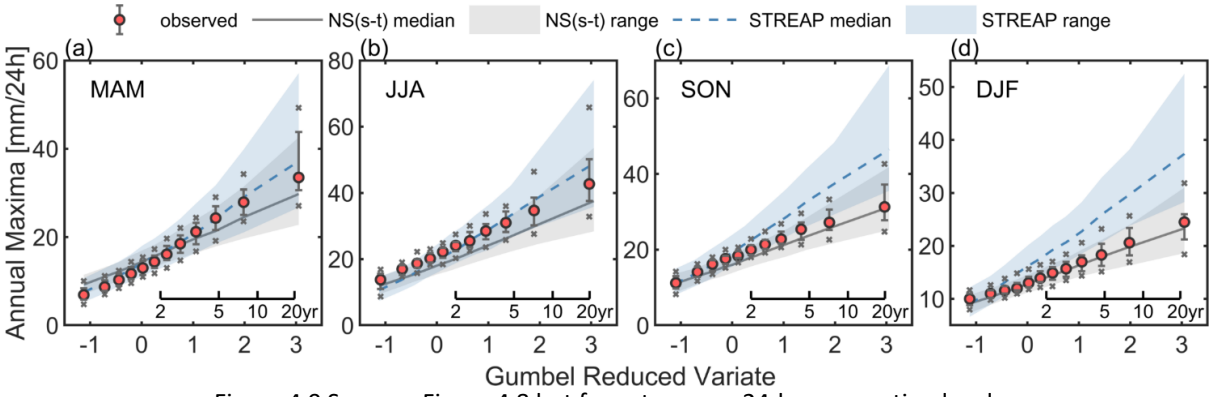


Figure 4.9 Same as Figure 4.8 but for extremes a 24-hr aggregation level.

iv. Areal Statistics

Areal statistics including the areal mean precipitation and wet area ratio are also examined on a seasonal basis. It can be seen that compared with the NS(s-t) simulated rainfall, STREAP gives a more realistic representation of the probability distribution as well as extreme values (P=0.01%) of areal mean precipitation in both seasons (Figure 4.10, and Appendix 0). The NS(s-t) tends to overestimate both hourly and daily areal extremes, which can be explained by the modelled cell structure. Firstly, the NS(s-t) model does not correctly preserve the feature of localized, short but intense rain cells. Because of the assumed independency, those very intense cells could cover a larger area

and last for a longer duration in the modelled than in the observed data. Secondly, compared to the bell-shaped rainfall cell in observations, the constant intensity throughout a modelled cell leads to a smaller coverage of wet area but a larger amount of rainfall within the wet area, thereby yielding a higher tail value. The above two features have been accounted for in STREAP model structures, which explains why STREAP outperforms NS(s-t) in the areal statistics. The only exception occurs in examining daily areal extremes during winters, where the NS(s-t) synthetic rainfall is closer to the observed while STREAP giver an overestimated daily areal extreme (Appendix 0). As mentioned, this can be explained by the calibrated STREAP parameters leading to wet spells lasting for a longer duration than the observed.

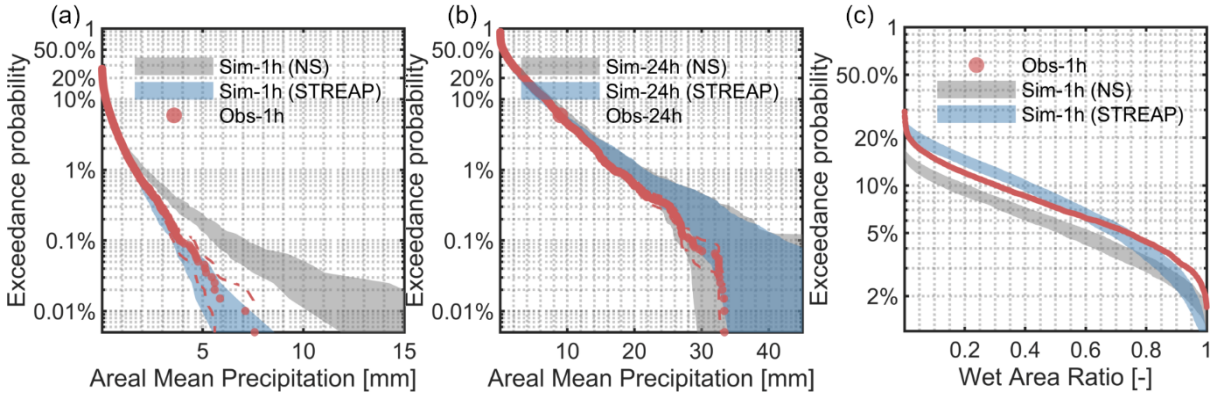


Figure 4.10 Exceedance probability of catchment summer rainfall amount at 1-hr aggregation level (a), catchment rainfall amount at 24-hr aggregation level (b), and wet area ratio at 1-hr aggregation level (c). All are computed for a medium-sized Welland catchment (717 km^2).

Compared with previous work, the bias in the mean areal intensity reported in this thesis is smaller than the bias reported in the literature (Paschalis et al., 2013) where an older version of NS(s-t) was used (Cowpertwait, 2006). The reduced bias shown here confirms the validity of the calibrated model generators and the reduction follows from the improved representation of spatial correlation in the model (Leonard et al., 2008).

On examining the spatial extent of wet spells (Figure 4.10.c), it appears that the exceedance probability of WAR produced by STREAP is overall more consistent with observed statistics. For localised summer events having a coverage fraction WAR < 0.2, occurrence frequency simulated by STREAP is more realistic while NS(s-t) underestimates the coverage by 16.31% - 31.77% on average. This is mainly due to the NS(s-t) not well representing the small-scale spatial storm structure and the temporal evolution within a rain cell. The modelled rain cells are static and cylindrical, which is a simplification of typical bell-shaped moving cells shown in radar estimates (Hardenberg

et al., 2003). Under the simplification, the simulated spatial extent of all rain cells occurring over an area at a certain duration is overall narrower than the observed area. In order to form a cylindrical shape as the model assumes, the edges having a low rain rate are therefore moved closer to the cell centre, which therefore has the effect of lowering the modelled wet area ratio. In contrast, STREAP represents the spatial structure using a latent Gaussian field instead of forcing the simulated fields to be represented by multiple cylindrical cells. This way provides the potential to better capture the wet area ratio. For wide-spreading rainfall events (i.e., WAR>0.95), both models tend to underestimate the occurrence frequency.

It is worth to mention that although STREAP calibration has directly taken IMF series and WAR series into account, these two series correspond to values computed for the whole simulation area (>10000 km^2), not for the catchment size (around 700 km^2) investigated in this section. Therefore, Figure 4.10 provides a fair validation in both models in terms of areal rainfall performance.

4.4.2 Propagation from Rainfall to Runoff

Both the flow duration curves (FDCs) and flood frequency curves (FFCs) are analysed for catchment outlets, so as to understand how the rainfall performance is propagated to catchment runoff responses. By using the calibrated hydrological model (Section 4.3.2), 9-year-long time series of simulated runoff are obtained for both observed rainfall input and each realization of stochastic rainfall (40 realizations in total) (see Appendix II.3). The hourly flow duration curves (FDCs) computed with different rainfall inputs are examined during both low flow (Summer, JJA) and high flow seasons (Winter, DJF) (see Appendix II.6). The FDCs show that the reference runoff is within the ensemble range of stochastic rainfall simulated runoff at both catchments, where there is a large range of flow values being simulated during summer seasons. It is noted that in the Stour catchment, the simulated summer flow is generally low ($\sim$0.1 m^3/s). The low value is mainly associated with the summer drought in the catchment and the omission of crop irrigation in the hydrological simulation.

Then, the flood frequency curves (FFCs) were analysed on a seasonal basis as shown in Figure 4.11. Summer (JJA) seasons show a different pattern of FFCs resulting from STREAP and NS(s-t) rainfall at an hourly scale (Figure 4.11.a). The hourly discharge of a

10-year return level (averaged over 20 ensemble simulations) produced by the NS(s-t) is 63.58 m^3/s, 163.5% higher than the reference discharge (24.13 m^3/s), while the discharge produced by STREAP model largely overlaps with the reference peak discharge. The modelled discrepancy in peak discharge is consistent with the estimation error we have seen in areal rainfall extremes (Figure 4.10.a). The highly overestimated hourly peak discharge by NS(s-t) implies that the error in representing the areal rainfall amount cannot be filtered out by the rainfall-runoff transformation for summer. In this case, spatial variability of rainfall is expected to play a vital role in modulating peak discharge. The range in flow values for the NS(s-t) model is another noticeable concern, which is too broad and could undermine the use of the model in flood prediction. This flaw is caused by overrepresented variability of areal extremes (Figure 4.10) due to the unrealistic representation of spatial structure of rainfall cells in NS(s-t) model.

During winter (DJF), the ensemble range of simulated discharges from two types of stochastic rainfall forcings overlaps with the reference runoff (Figure 4.11.b). The NS(s-t) tends to underestimate winter peak discharges by 21.6% for a 20-year return level while STREAP tends to slightly overestimate the peak by 11.1% for the same level. Daily-scale FFCs also have been analysed (see Appendix 0), both models give a reasonable daily peak discharge in summer with a relative bias of less than 40 % at a 20-year return level. For winter seasons, STREAP seems inadequate to capture the daily-scale peak discharge (see Appendix 0), which can be explained by the largely overestimated wet spell duration in STREAP replicates (Figure 4.6.b).

It is noticed that the fitting methods used for the extreme value analysis might affect to some extent the magnitude of fitted maxima, all the more so as the sample is only 9 years long. To ensure the robustness of the results, two widely used fitting methods have been tested, including generalized maximum likelihood estimation (Martins and Stedinger, 2000), and L-moment estimates. Comparison of FFCs from different rainfall forcings leads to the same conclusion for both seasons and both time scales.

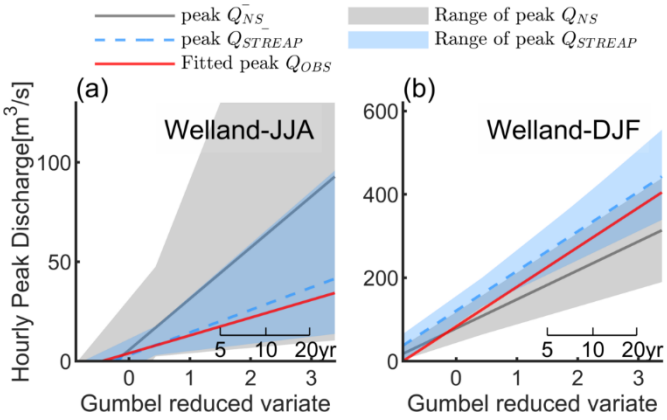


Figure 4.11 Comparisons of FFCs from different rainfall forcings (red: observed; grey: NS generated; blue: STREAP generated) at an hourly scale (a) in summer seasons (JJA) and (b) in winter seasons (DJF). Shaded area gives a range between 95th and 5th percentile of 20 ensemble simulated peak discharge (Gumbel fitted extremes).

4.4.3 Catchment Soil Water Dynamics

To understand how synthetic rainfall leads to different behaviours of hourly peak discharges, I further analysed the soil water dynamics of different rainfall forcings in this section.

i. Spatial and temporal variability of soil conditions

Figure 4.12 shows the variability of soil dynamics in two dimensions, i.e. the temporal variability over days (a) and the spatial variability of the effective saturation in summer and in winter (b, c). In terms of the spatial variability of modelled soil conditions (represented by the dimensionless coefficient of variation of S_e), both models give a similar performance (Figure 4.11.b, c). Overall, the seasonality of soil dynamics is well preserved by both models, i.e., summer seasons are expected to have a higher spatial variability of effective soil saturation than winter seasons. For winter seasons, the inadequate representation of spatial variability of rainfall seems to be larger filtered out by the rainfall-runoff transformation (Figure 4.12.c), in line with the results in flood frequency curves (Figure 4.11.b). Discrepancy in the simulated soil dynamics from the observed rainfall and the stochastic rainfall is relatively low. However, this is not the case for summer seasons, the variability of saturated soil simulated by both stochastic forcings is higher than the reference (Figure 4.12.b). This performance implies that the simulated saturated areas are too concentrated. The excess flow is able to travel faster into the river channel and results in a more intense catchment response (Paschalis et al., 2014a; Seo et al., 2012). This explains why both rainfall models lead to a higher peak discharge than the observed in summer seasons (Figure 4.11.a). The overestimation of summer peak discharges is particularly pronounced in the NS(s-t) case, which is because the NS(s-t) also gives a higher averaged S_e than the other two rainfall products. These two aspects of

modelled soil dynamics act together leading to an unrealistic summer peak discharge resulting from the NS(s-t) but a more realistic discharge from STREAP.

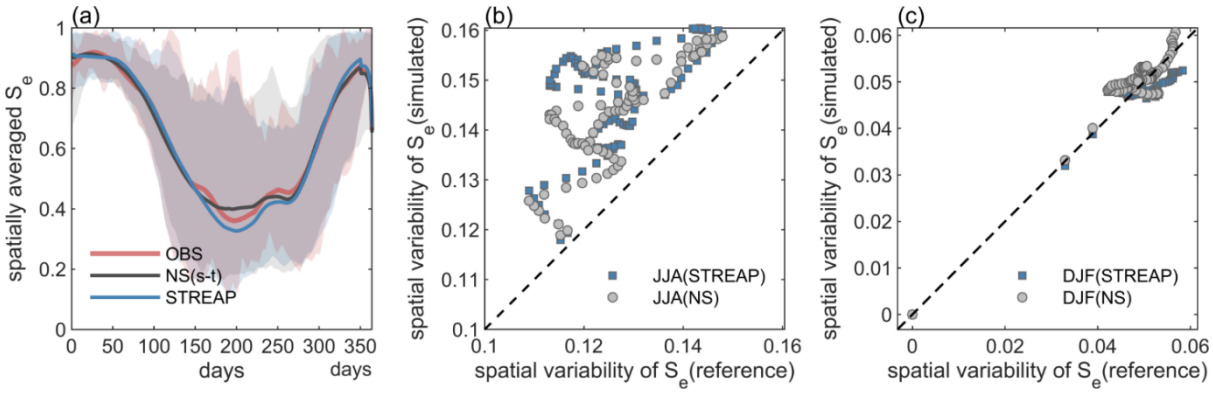


Figure 4.12 Variability of simulated soil dynamics of synthetic rainfall forcing and observed rainfall forcing, including the temporal variability of spatial-averaged effective saturation (a), the summer-season spatial variability of effective saturation (b), and the winter-season spatial variability of effective saturation (c). Soil maps used in this analysis are obtained at a daily interval. River Welland catchment is shown here for consistency, another catchment gave a similar performance.

ii. Soil dynamic condition in runoff-generation hours

Then we focus on analysing soil dynamics specifically for time steps having the potential to produce surface runoff. Since topography drives flows accumulation, topographic indexes are used to understand soil dynamics performance in different topographic areas over a catchment. How the estimation error in the simulated soil moisture content $\bar{\theta}$ changes against the topographic index (TI) is shown in Figure 4.13, on JJA and DJF respectively.

Results show that STREAP can better capture the modelled soil moisture contents than the NS(s-t) in both seasons, for most TI values. In general, the NS(s-t) modelled rainfall leads to a higher soil moisture content on average than the observed rainfall, particularly in summer. This result is consistent with previous analysis in this section (Figure 4.11) and confirms the ability of STREAP to better reproduce the spatial variability of rainfall so as to capture the soil water dynamics over the catchments.

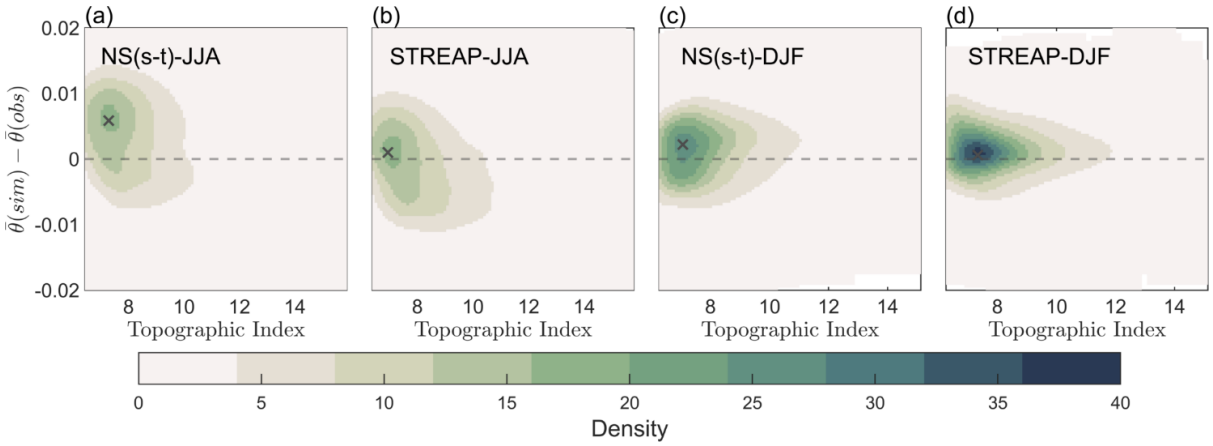


Figure 4.13 Comparisons of simulated soil dynamics of two rainfall forcings at Welland catchment. Each subplot shows a density plot of $\bar{\theta}(sim) - \bar{\theta}(obs)$ in either low-flow period (summer) (a, b), or high-flow period (winter) (c, d). $\bar{\theta}$ is the year-averaged soil moisture content calculated for each grid (year 2007 was excluded) and only those hours with at least one grid having $S_e > 0.85$ are selected.

Section 4.5 Discussions and Conclusions

In summary, this chapter focuses on comparing two spatial-temporal rainfall models (STREAP and NS(s-t)) so as to investigate which one is more suitable for flood-related analysis. In this study, not only a wide range of rainfall statistics but also their model behaviour on reproducing catchment runoff were evaluated. Results show that both rainfall models are capable of reproducing most of the key statistics of rainfall. Those statistics include long-term annual mean precipitation, moment estimates (up to the third-order) of the marginal distribution of rainfall intensity, the autocorrelation of intensities, and the decay of spatial correlation with distance at both hourly and daily scales. Summer-time point extremes are well reproduced by both models while STREAP tends to give higher daily point-scale extremes in winter seasons. In terms of spatial structure, the NS(s-t) generally overestimates the spatial correlation at short distances as well as hourly areal extremes at a spatial scale of medium-size catchments ($\sim$700 km^2) while STREAP gives more realistic areal statistics. After a non-linear rainfall-runoff transformation, the overall distribution of flow series is preserved by the generated rainfall fields in both high and low flow seasons. The hourly peak discharge during winter seasons is also captured by both models with a relative bias less than 21.6% on average at a 20-year return level in which STREAP replicates overestimate the winter-season peak discharge because it produces too many long-duration wet spells. In summer seasons, at the same return level, the NS(s-t) instead gives an unrealistic overestimation

of 163.5% in hourly peak discharge while STREAP gives a more realistic performance at both daily and hourly scales. The different performances of the two models can be further illustrated by their different resulting soil water dynamic conditions. The misrepresented effective soil saturation as well as the inadequate spatial variability of soil conditions led to a highly overestimated summer peak discharge being produced by the NS(s-t).

Regarding implications for catchment hydrological applications, these two stochastic rainfall models demonstrate the ability to infer flood frequency curves where ensemble simulations are used to represent the stochastic uncertainty. From the results, the well simulated hourly peak discharge by STREAP confirms the model's validity in inferring flood frequency curves at ungauged sites. However, the NS(s-t) is not suitable for inferring it, particularly during the summer seasons leading to a high overestimation. The overestimated summer peak discharge could lead to unnecessary investments in flood mitigation measures. Note that this study focuses on river flooding without considering the potential risks of other flooding types such as groundwater flooding.

Although the propagation results shown here are only based on one of the space-time point process models and one STREAP model, results for the NS(s-t) can be generalised. The inadequate behaviour of the NS(s-t) in representing wet area ratio and areal extremes is due to its simplified spatial structure (no storm advection, spatially constant inner-cell intensity, lack of dependency between cell radius and intensity). Although this structure could be improved by deriving analytical solutions for a new version and removing those simplified assumptions, there are only few attempts in this direction (Evin and Favre, 2008) due to the nearly intractable equations this gives rise to. Those point process models sharing the simplified spatial structure, would most likely also misrepresent the wet fraction and overestimate hourly areal extremes. Therefore, the conclusion in terms of the overestimated hourly peak discharge during summer seasons can be generalised to most existing space-time point process models sharing the same assumptions. The misrepresentation could be even greater for applications to areas experiencing more frequent localized convective events.

Unlike the NS(s-t) calibration in which multiple time scales (1, 6 and 24 hours) are used in optimization, STREAP calibration only requires one time scale (hourly in this chapter). Model performance at a coarser scale is therefore not automatically guaranteed in

STREAP but relies mostly on whether the rainfall data at the specific scale has been of good quality in representing how rainfall changes with temporal scales. As shown in the last section, although STREAP captures well the hourly-scale flood response in this study as further confirmed by the soil water dynamics, it is inadequate to reproduce daily-scale winter peak discharge due to the overestimated occurrence frequency of long-duration wet spells. The overestimated wet spells are associated with the estimation error of calibrated parameters in the storm arrival process (stage 1 in the model structure), due to the storm separation method being applied. The storm separation method applied takes a wet area fraction as the spatial coverage threshold for the definition of wet spells, and 2-hour consecutive dry periods as the temporal separation threshold between spells. Under this separation criterion, if two nearly independent storms occur in different places over the simulation domain but do have several timesteps overlapping with each other, STREAP model will identify these two storms as one continuous storm having a longer wet spells duration. Constrained by the hierarchical model structure and calibration structure of STREAP, the estimation bias in the first stage cannot be cancelled out in the following stages. This highlights the higher requirement of STREAP calibration than the NS(s-t) in well representing the storm arrival process (the first stage of STREAP).

Considering the overall model behaviours of two model structures in reproducing peak streamflow and their flexibility in being applied to climate impact studies, STREAP is selected as the stochastic component of the climate impact studies and will be further improved in this thesis.

Chapter 5 Evaluation of Rainfall Output from Convection Permitting Ensemble

This chapter focuses on answering the question of whether the climate projections of precipitation from Convection Permitting Ensembles are credible for hydrological use. Section 5.1 gives an introduction to evaluations which have been done in terms of the rainfall output from convection-permitting models (CPMs) and what is missing in the literature. Section 5.2 describes the study area, rainfall datasets and statistical analysis used for the evaluation. Section 5.3 presents evaluation results including the mean pattern, spatial-temporal statistics of rainfall and additional evaluation specifically for high impact events. Finally, the section 5.5 summarizes results obtained and discusses how this information can be used for stochastic model calibration (which is the focus of Chapter 7).

Section 5.1 Introduction

With increasing computational power, convection-permitting models (CPMs) have become more common in climate studies and have been evaluated in a few regions around the world in the recent decade (Chan et al., 2020; Kendon et al., 2019a; Prein et al., 2015). Unlike the GCMs or RCMs, convection-permitting models (CPMs) are able to represent convection processes explicitly thanks to the high spatial resolution. This feature of CPMs allows for a more realistic representation of precipitation than coarser-scale climate models which are particularly outperformed in sub-daily extremes (Kendon et al., 2014; Prein et al., 2015). The literature has reported that, at an hourly scale, CPMs give a better representation of summer-time rainfall events in terms of spatial patterns, intensities, and temperature scaling compared with coarse-scale climate models (Ban et al., 2014; Berthou et al., 2018; Steven C Chan et al., 2016; Fosser et al., 2015; Kendon et al., 2012). CPMs also have reduced biases in representing the wet-hour frequency (Ban et al., 2020), in overestimated fractional contribution of intense rainfall to total

precipitation (Berthou et al., 2018) as well as in the 'drizzle problem' in coarser models (Fosser et al., 2015).

In terms of the CPM datasets specifically used in this thesis, a technical report published by the UK Met Office has already covered extensive validation and analysis of the CPM projections (Kendon et al., 2019a). The report shows that compared to the RCM, the 12-member CPM ensemble has reduced present-day biases in all statistics being analysed (including the wet and dry frequency, the diurnal cycle of precipitation, the joint distribution of the precipitation amounts and the event duration), but the CPM tends to overestimate intensive precipitation events and hourly extremes due to the convection still not being fully resolved at a 2.2 km resolution (Kendon et al., 2019a, p. 125). Using the same model core, previous studies also have found that the simulated daily precipitation has been more realistic than coarser-scale RCMs, while in high-intensity events the spatial density and the clustering are still poorly represented (Chan et al., 2013). However, all those analyses mainly focus on assessing statistics available in both RCMs and CPMs and the properties being analysed are still not at a kilometre-scale (e.g., 5 km radar/gridded datasets were used). The small-scale structure which is not able to be assessed in RCMs has not been investigated for the CPM simulation either. This leads to the question of whether those unexplored small-scale features can be directly used in climate impact assessment.

To better understand to what extent the rainfall outputs are reliable for use in tool development for impact studies, this chapter focuses on assessing the small-scale structure of precipitation in CPMs. Simulated hourly precipitation from the CPM is compared statistically with observations. A range of statistics related to the spatial-temporal structure of rainfall is examined, including seasonality, event occurrence, wet fraction ratio, areal mean intensity, power spectral density, spatial variability, areal rainfall extremes as well as clustering feature.

Section 5.2 Data and Methods

5.2.1 Study Area

The statistical evaluation is performed over the whole UK to enable a complete assessment on the model performance. For those areal statistics which have the potential

to be directly used in calibrating the stochastic generator, four smaller areas (110 km × 110 km) are further selected for the investigation (Figure 5.1) by taking into account both the climatology and the data quality of observational radar data. To be specific, the selection in this chapter is based on the following criteria: (1) all areas are close to the weather radar location so as to ensure a good spatial representation of observed rainfall in its radar measurement; (2) considering the difference in the available data period of rainfall products (radar: 2007-2018, CPM: 1980-2000), there is no significant change found in those regions between these two periods according to a modified Mann Kendall trend test (Hamed and Ramachandra Rao, 1998) carried out on the rainfall fields; (3) the four regions represent distinct climatology features.

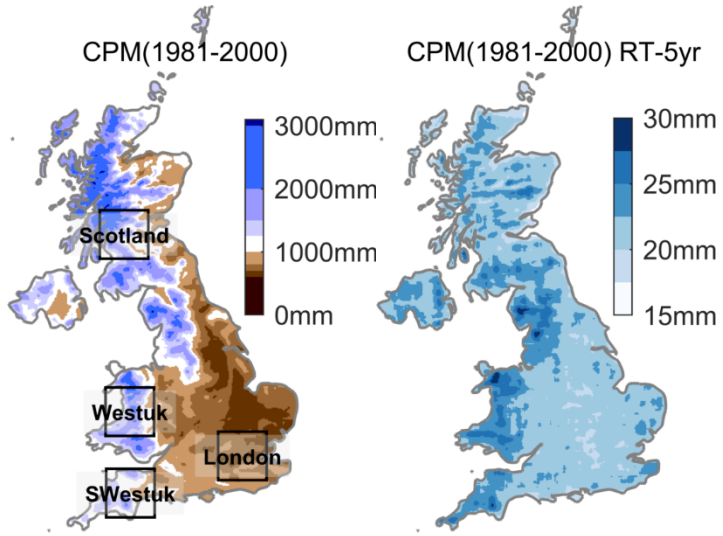


Figure 5.1 Map of CPM simulation (1980-2000) and locations of four subregions. (a) annual mean precipitation (1980-2000) from CPM; (b) 5-year return level hourly-scale annual maximum precipitation depth. Considering the product include 12 ensemble members, the median of results from model simulations was taken as a central estimate, in which all members were treated equally.

5.2.2 Data

The control period (1980-2000) of the convection-permitting ensemble (2.2km, hourly) is compared with observational datasets. Considering different pros and cons of rainfall measurements, several observational datasets are used (Figure 5.2) instead of subjectively merging these observational datasets into one for the whole UK. How those datasets are being used is summarized in Table 5.1.

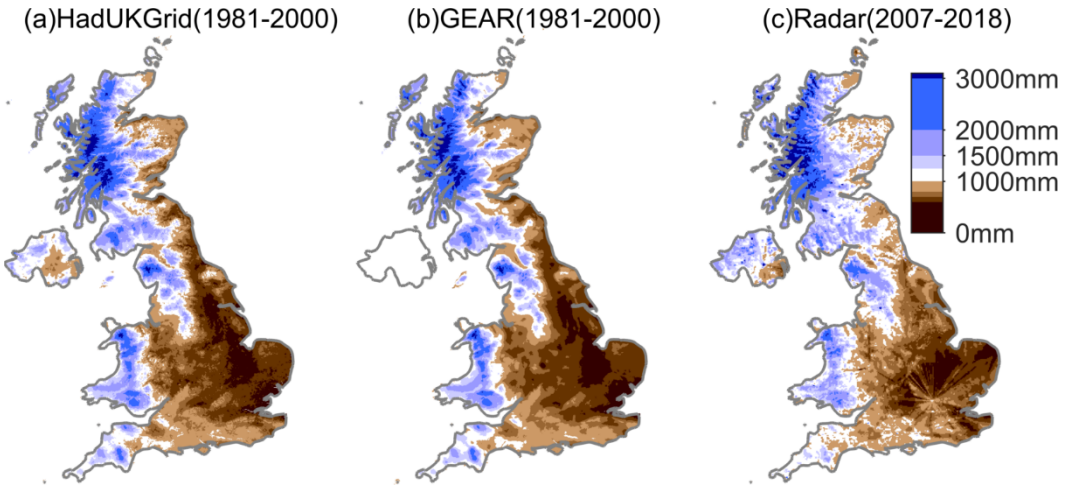


Figure 5.2 Observed annual mean precipitation depths (mm/yr) from different observation datasets, including (a) HadUK-Grid, (b) CEH-GEAR and (c) C-band Radar Composite for historical periods being used in the evaluation.

Among them, the radar estimates are used throughout all the analysis because STREAP calibration largely relies on statistics obtained from radar measurements. In addition to it, GEAR (GEAR-1hr) datasets and HadUK-Grid (Hollis et al., 2019) are used in evaluating the annual mean precipitation and the seasonality pattern so as to mitigate the potential effect of radar measurement error on representing the observed spatial pattern of long-term mean precipitation. GEAR-1hr is also used in the ARF (areal reduction factor) analysis. Because of the different resolution in the climate model output and the observational data, all observation datasets have been re-grided to a 2.2 km resolution with the total rainfall amount for each grid being preserved. Although the majority of precipitation in the UK is rainfall (liquid form), there could be some snow measurement being included particularly in Scotland during winter. In the analysis, these two forms of precipitation have not been explicitly separated.

Table 5.1 Summary of datasets used in the comparison of Chapter 5.

Category	Datasets	Period	Resolutions	Mean	Storm Arrival & Areal stats	Spatial-temporal Evolution	ARF analysis	Clustering analysis
Climate Models	CPM	1980-2000	2.2km, hourly	✓	✓	✓	✓	✓
Observation	Radar	2007-2018	1km, hourly	✓	✓	✓	✓	✓
	GEAR-1hr	1990-2014	1km, hourly				✓	
	GEAR	1981-2000	1km, daily	✓				
	HadUK-Grid	1981-2000	1km, daily	✓				

5.2.3 Evaluated Statistics

A range of key properties of spatial-temporal rainfall are being examined so as to assess the realism of the CPM for impact studies (e.g., STREAP-based stochastic model calibration). Properties being examined include the pattern of annual mean precipitation (spatial pattern and seasonality), storm arrival and areal statistics, spatial-temporal statistics of rainfall fields as well as several heavy rainfall statistics.

i. Mean Pattern

Annual mean precipitation of CPM projections is compared with the observed precipitation obtained from HadUK-Grid and GEAR datasets for the same period (1981-2000) over the whole UK. 12 ensemble members of the CPM data are treated equally, and the median is taken as CPM modelled results for each 2.2 km × 2.2 km grid.

Aside from this, monthly precipitation is calculated as long-term mean precipitation averaged over each subregion so as to provide a robust assessment of seasonal patterns for each climatologically distinct area.

ii. Storm arrival and areal Statistics

Storm arrival and areal statistics are analysed to assess their potential to be directly used in calibrating stochastic generators. Considering that the simulation domain of the generator used in this thesis (STREAP-based) is generally smaller than 128 km × 128 km (Paschalis et al., 2013), an analysis of area statistics is also carried out for each of the subregions, the size of which (110 km × 110 km) has been sufficient for most catchments of the UK. Statistics being compared here include storm duration, wet areal ratio (WAR) and areal mean intensity (IMF), which are used in the first and the second stage of STREAP model (Paschalis et al., 2013).

A storm separation method used in STREAP is also applied to the hourly spatial-temporal rainfall fields of each subregion (see details in Section 3.3.2). The probability distribution of storm duration is examined because the distribution is used in the storm arrival process and the copula framework of STREAP model structure.

For the WAR and the IMF, instead of directly comparing time series from different products, the analysis focuses on evaluating the probability distribution of several properties representing event statistics, including peak IMF, peak WAR, the median value

of IMF series (Q50 IMF) and median of WAR series (Q50 WAR) for each event. Each ensemble member is analysed separately to evaluate the ensemble uncertainty.

iii. Spatial-temporal Evolution of Rainfall Fields

Both the scaling behaviour across spatial scales and the spatial variability across temporal scales are analysed.

Scaling behaviour across spatial scales is examined for each sub-region separately considering their distinct climatology. A spatial power spectral analysis is used here to assess how the CPM product behaves at different spatial scales. The power spectrum density function has been widely used in analysing radar measurements and modelling space-time rainfall fields (de Michele and Bernardara, 2005; Seed et al., 2013). In this section, the density function is derived from radar reflectivity (dBZ) fields, which are converted from the radar rainfall rate using a constant Z-R power-law relationship (with the same parameters used by Met Office). To give an overall behaviour of the CPM product, all fields with a wet fraction exceeding 3% have been used in deriving the spatial-spectral density function, on a seasonal basis. The total number of fields extracted for each season is summarized in Table 5.2.

Table 5.2 Total number of spatial rainfall fields used in spectral analysis

	CPM (1981-2000, 12 members)		OBS (2007-2018)	
	Summer (JJA)	Winter (DJF)	Summer (JJA)	Winter (DJF)
London	109821	164945	7863	8602
SWestuk	147006	253416	10161	11644
Westuk	185583	261361	11670	13359
Scotland	234088	280764	14433	15475

The spatial variability across temporal scales is also examined. The spatial variability is represented by calculating the coefficient of variation of positive rainfall in space at each temporal aggregation level (call it CV_{pos}). This statistic is directly used in STREAP calibration (in the third stage, see details in section 3.3.2 iii). The CV_{pos} is computed for aggregation levels from 1 hour to 24 hours for each calendar month.

iv. Heavy Rainfall Statistics

Further analyses are carried out specifically for heavy rainfall, in order to assess how the CPM behaves in reproducing the spatial-temporal organization of heavy rainfall.

(1) Clustering feature

Aside from the wet area ratio and the areal mean precipitation, another important feature affecting the risk of triggering flooding is how the precipitation is clustered locally (as illustrated in Figure 5.3). To assess the model ability to correctly reproduce spatial characteristics of intense precipitation events and provide reliable information for flood studies, how the rainfall fields of high-impact events are being clustered in space is examined.

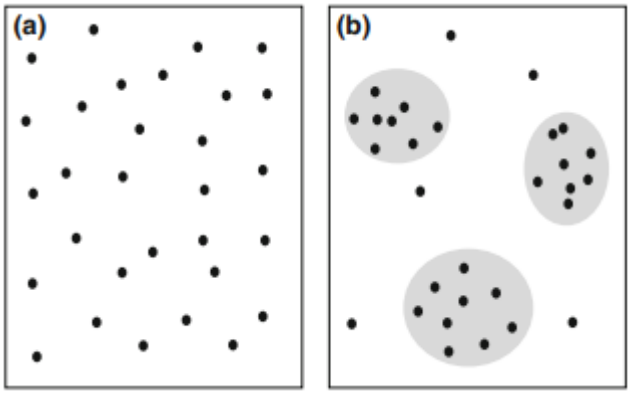


Figure 5.3 Schematic of (a) non-clustered and (b) clustered precipitation. For the entire area, the two modes have the same spatial density (the same WAR). For (a), individual grid point ''showers'' are randomly scattered, and on average spaced at regular spatial intervals. For (b), precipitation is organized into clustered ''blobs'' (represented as light grey circles). One would expect (gridded) precipitation to cluster in space across a range of spatial scales. If horizontal resolution is small enough (1 km), clustering can be caused by convective clouds occupying more than one grid point. Precipitation and clouds are also clustered on the meso- (fronts, organized convective storms, orographic precipitation), synoptic- (mid-latitude and tropical low pressure systems), and planetary scales (ITCZ, monsoon systems) (Chan et al., 2013).

The clustering is analysed by calculating the areal normalized Besag L-function at a 2.2 km horizontal scale following one of the previous studies in CPMs by Chan (2013). To remove the effect of the CPM overestimating point extremes upon how many heavy rainfall events to select, for each rainfall product, a fixed number of heaviest events is selected for each year (48 heaviest summer hours for an hourly-scale analysis; 2 heaviest summer days for a daily-scale analysis). Therefore, for the radar data, 576 slices of rainfall fields are selected, and for CPM data, 11520 slices of rainfall fields are selected. These events are required to be at least one day apart to ensure independence. Those single-grid storms are also excluded from the selection for both products. In addition to this, considering the 'drizzle problem' existing in climate models including the CPMs, all grids having intensity less than 0.1 mm/h are taken as dry.

The derived Besag L-function is then plotted against the radial distance for the summer season to represent the local increase of spatial density due to spatial clustering from

observational radar and CPM. A higher Besag L value means a higher local increase of the spatial density.

(2) Areal Extreme Feature

The Areal Reduction Factors (ARFs) are used to assess the ability of the CPM to capture how areal extremes change across different durations and different catchment scales. The Areal Reduction Factor is estimated by using the fixed-area method (Svensson and Jones, 2010). The method calculates a ratio of the point measurement when the point rainfall reaches the annual maximum to the point-measurement when a certain areal rainfall reaches the annual maximum. Multiple return periods are not considered here, which is one limitation of the fixed-area method (Bell, 1976). The ARFs computed from the observation (GEAR-1hr and radar estimates) and CPM ensemble are then compared, for durations of 1, 6 and 24 h. A larger value of ARF indicates a higher similarity between the point and the areal rain intensity.

Section 5.3 Results

5.3.1 Mean Pattern

In terms of the annual mean precipitation for the historical period (1981-2000), the 2.2km CPM gives a spatial pattern of annual mean precipitation largely consistent with its nesting RCM (Kendon et al., 2019a, figs. 3.2.3 and 3.2.4). Compared to observation datasets, the annual mean is overestimated in eastern England (Figure 5.4), particularly in winter seasons (Appendix III.1). Instead, the annual mean over western Scotland is underestimated with a relative bias of less than 30%.

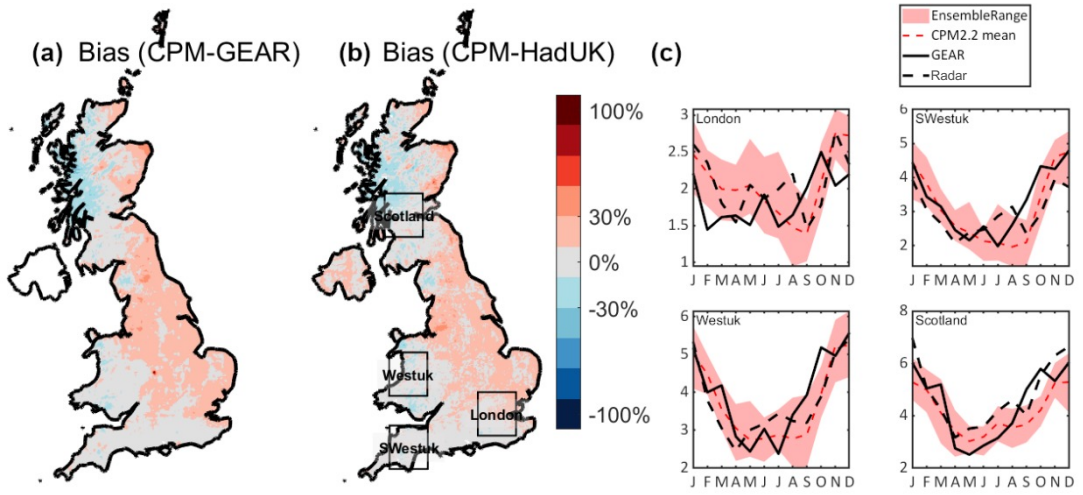


Figure 5.4 Relative bias of the annual mean precipitation between CPM2.2 data and several observation datasets. (a) relative bias between CPM2.2 and CEH-GEAR. (b) relative bias between CPM2.2 and HadUK-Grid. Non-significant difference at 5% level is shown as grey colour. (c) Averaged monthly rainfall pattern (unit: mm/day) for areas marked in (b).

For the four selected subregions, the CPM well captures the seasonal variation of total rainfall amount while it still tends to underestimate August rainfall. For the subregion in Scotland, the radar measurement is affected by the mountainous topography. The orographic enhancement of rainfall processes is not well captured by the radar, while the 2.2 km CPM successfully adds the spatial details over mountainous areas and has shown a more realistic representation of orographic precipitation (a detailed investigation can be found in the Appendix I.1). For the subregion covering London, the seasonality simulated by the CPM seems to show a larger difference from the two referenced observation datasets (the GEAR and the radar). The difference could be explained by the inadequate ability of both datasets in representing total rainfall amounts in this area. As shown in Figure 5.2.c, the radar measurement in this area has been largely affected by the beam blocking. Data quality of the GEAR rainfall is also restricted by the sparse density of available rain gauges over the large urban area.

5.3.2 Storm Arrival and Areal Statistics

The probability distribution of wet spell duration is overall captured by the 2.2 km CPM. However, the CPM tends to overestimate the occurrence frequency of events lasting for less than 12 hours and underestimate the occurrence frequency for more prolonged storm events. This inadequate performance also has been found in some previous studies in CPMs although different storm separation method was used (Ban et al., 2020; Kendon et al., 2019a).

The wet day frequency is well produced by the 2.2 km CPM with a relative bias of less than 10% in most areas over the UK (Kendon et al., 2019a, fig. 3.3.4). The average number of storm events occurring per year is well reproduced by the CPM in London and Scotland area while too many storm events are produced in the southwest and the west of the UK, as indicated in the Figure 5.5. Note, the GEAR datasets, which are interpolated purely by rain gauge data, are not used in this analysis because the storm separation method adopted in this section is based on spatial information. The weather radar data is perceived to provide a more reliable spatial information.

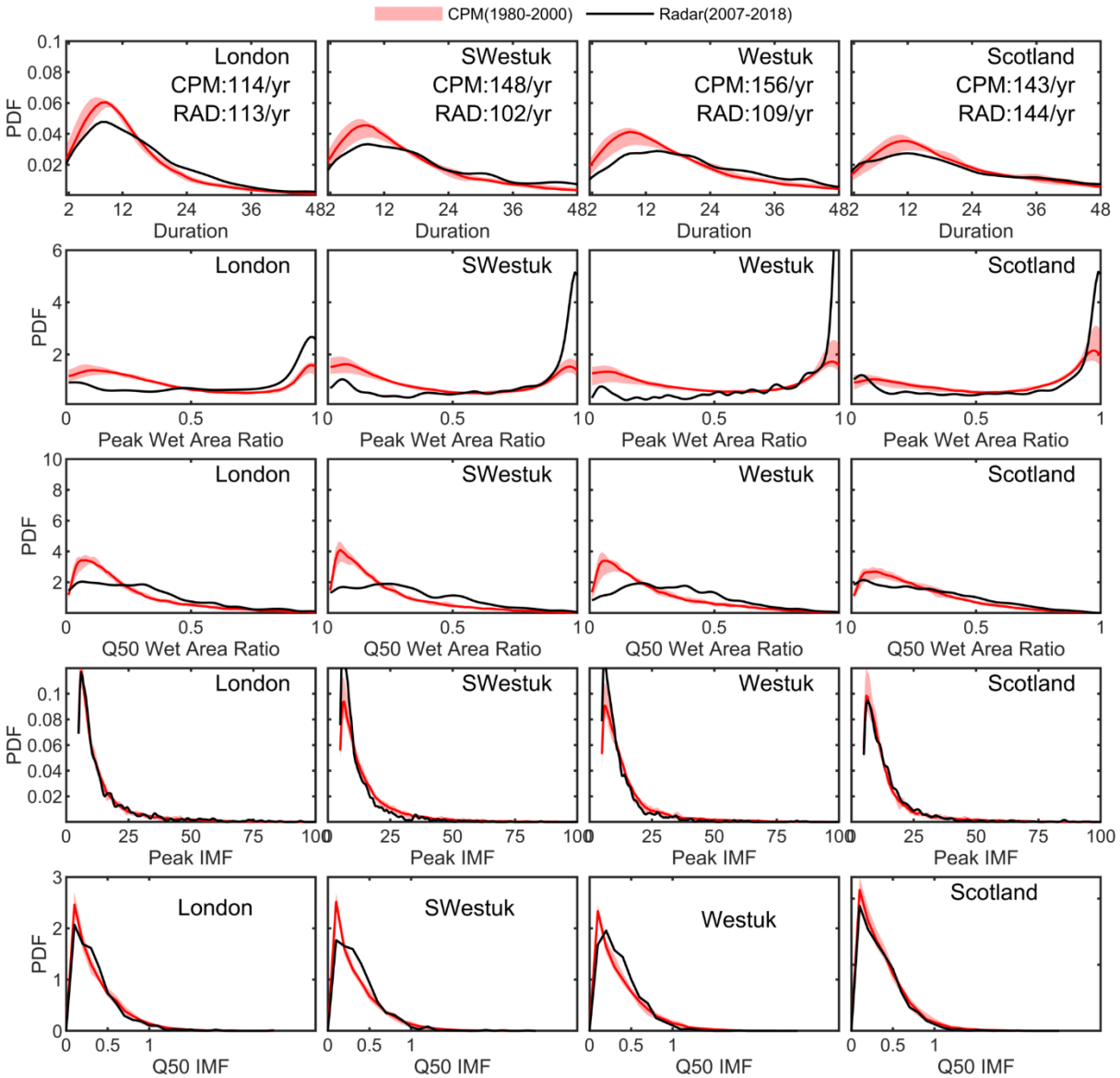


Figure 5.5 Probability distribution functions (PDFs) of several key rainfall statistics including event durations, peak WAR, 0.5 quantile WAR, peak IMF and 0.5 quantile IMF. Four selected subregions are shown respectively from the left to the right.

The inadequate performance of the CPM occurs in the distribution of peak wet area ratio of identified events. The 2.2 km CPM generally gives a smaller peak rainy fraction than the radar estimates, which is largely attributed to its tendency to produce events more localized than the radar observed particularly in summer. The Q50 wet area ratio obtained from the CPM shows a similar feature, implying that this statistic obtained from the 2.2 km CPM might not be automatically applicable in calibrating STREAP. A bias correction is needed.

Areal mean intensity (for the 110 $km \times 110\ km$ catchment scale), another key property used in the 2nd stage of STREAP calibration, is well captured by the CPM product to a large extent for all subregions investigated. A slight overestimation can be found in the occurrence of the extreme value, implying that the CPM might overestimate areal extremes. This overestimation is in line with results reported in previous studies on the same CPM (Kendon et al., 2019a, figs. 3.4.3 and 3.4.4).

5.3.3 Scaling Behaviour

In the spatial power spectral analysis (section 5.2.3.iii), both rainfall fields (the 12-member CPM and the weather radar) follow a scaling behaviour with a clear break at around 20 km scale (Figure 5.6). A similar scale break has been demonstrated in the UK (Seed et al., 2013). For scales above the break, we can see that the slope of their spectra for widespread rain (frontal rain) which is typical in winter) is generally greater than the slope of the power spectra for convective rain which is typical in summer. This is because the convection process is less organized than widespread rain on the large scale.

In all seasons, the scaling behaviour from radar estimates has been well captured by the CPMs where the behaviour of the 12 members is quite consistent. The largest discrepancy occurs on a scale of kilometres, but still, quite small.

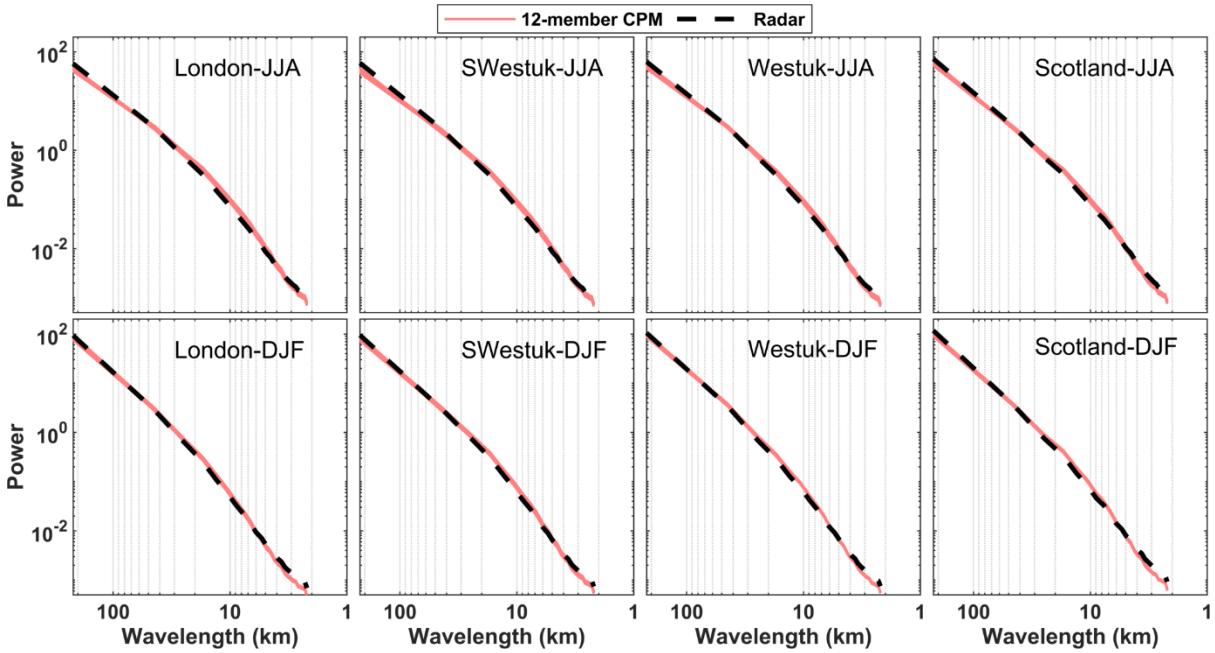


Figure 5.6 Radially averaged power spectrum (RAPS) derived from either 12-member 20-year-long CPMs or 12-year-long radar estimates. Both rainfall datasets have been converted to fields of reflectively (dBZ) at each of four subregions (110 km × 110 km per each). Upper panels correspond to results for summer (JJA) and lower panels correspond to results for winter seasons (DJF).

The spatial variability produced by the CPM also shows an overall good agreement with the radar estimates at different temporal scales (Figure 5.7). At the hourly time scale, the CPM modelled rainfall gives a slightly smaller spatial variability than the observed radar rainfall on the representative months (January and June). For a larger aggregation level (6~24 hours), the CPM instead gives a larger spatial variability in June (a representative month dominated by convective rainfall), which is because the CPMs still tend to produce more short-lived events than the observations, as shown in Figure 5.5 as well as in previous studies (Kendon et al., 2019a, fig. 3.4.8). All other months have been examined, and they show a similar pattern.

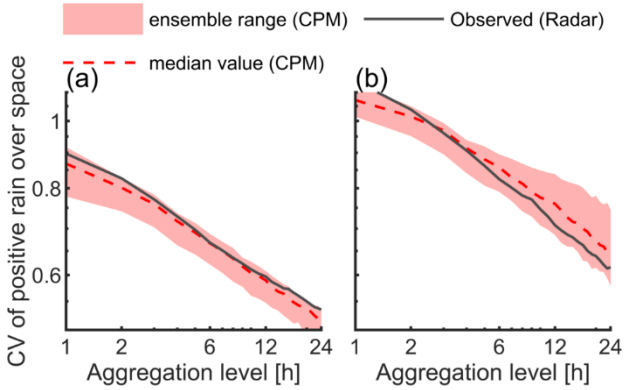


Figure 5.7 Coefficient of variation of positive rain rate of spatial rainfall fields (CV_{pos}) across different aggregation levels ranging from 1 hour to 24 hours in two representative months, i.e., January (a) and June (b). The statistic is computed at an 110 km × 110 km area in west of the UK.

5.3.4 Heavy Rainfall Pattern

i. Clustering Feature

At a daily scale, the clustering is well simulated by the 2.2 km CPM with a slight underestimation (Figure 5.8). The underestimation in the clustering is in line with one previous study on the CPM (Chan et al., 2013) where only one model run was used.

However, the hourly clustering patterns tend to exhibit larger differences. On scales of hundreds of kilometres, the local increase of spatial density due to spatial clustering produced by the CPM is 50% smaller than the observed. This hourly-scale pattern shows that the simulated rainfall fields from the CPMs tend to be smoother than the radar estimates, almost at all distances investigated ($0{\sim}400\ km$). This feature indicates the CPM data still tends to a give much smoother hourly rainfall simulation while this smoothing is largely cancelled out by the temporal aggregation at a daily scale because of the temporal evolution and advection movement of storms. Aside from this, the existing radar noise which fails to be removed in quality control of the radar composite might also contribute to the discrepancy.

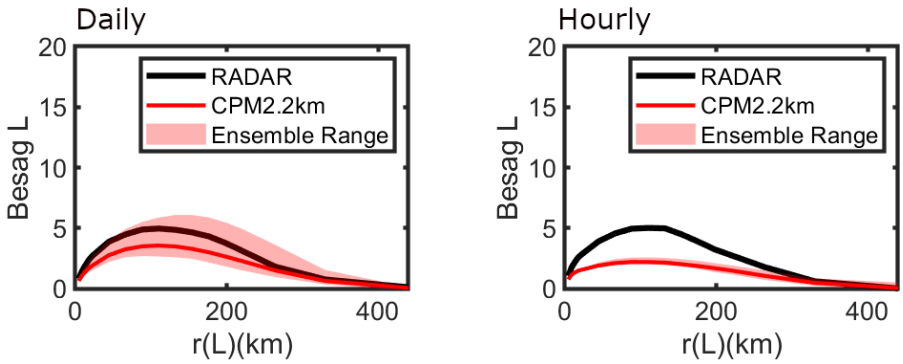


Figure 5.8 Clustering features for extreme rainfall during summer, using Besag-L function at daily resolution (left panel) and hourly resolution (right panel).

ii. Areal Extremes

Areal reduction factors (ARFs) for catchment scales ranging from several square kilometres to more than 10000 square kilometres have been computed (see Figure 5.9). Although only the 12-year radar was used for obtaining the observed factors, the reduction factors obtained here are similar to the tabulated values of ARFs presented in the Flood Studies Report (Svensson and Jones, 2010).

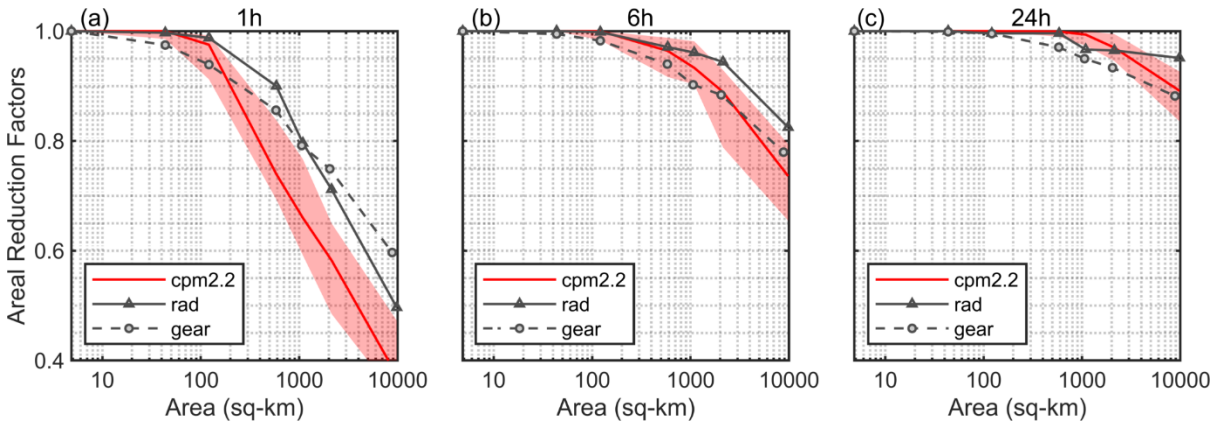


Figure 5.9 Areal Reduction Factors (ARFs) for precipitation in southern UK. (a) 1h duration. (b) 6h duration. (c) 24h duration.

Moving to the results derived from climate models, the 2.2 km CPM gives smaller ARFs particularly at an hourly scale, which can be explained by the overestimated grid-scale hourly extremes but less biased extremes at a much larger areal scale (see Figure 5.10). The overestimation in small-scale hourly extremes leads to a faster area reduction (a smaller ARFs) for large catchments (10^3~10^4 km^2).

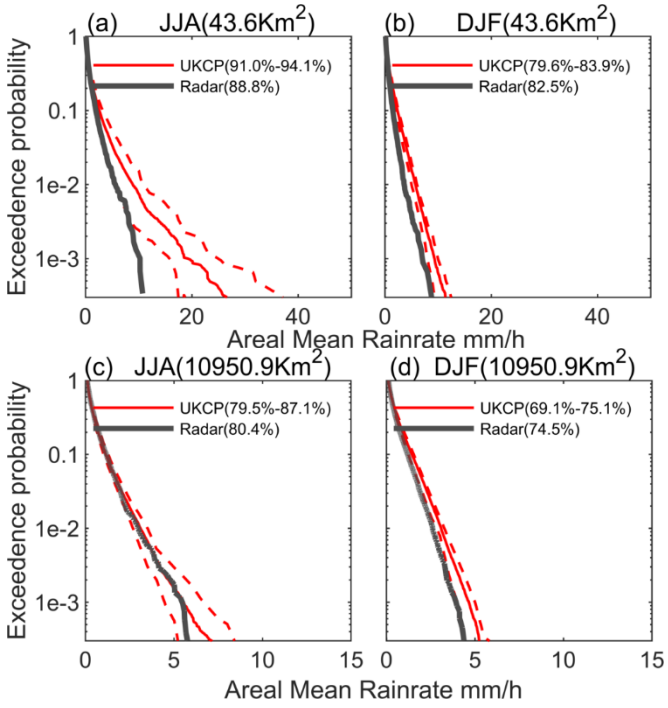


Figure 5.10 Exceedance probability of areal mean intensity (hourly scale) in South-West of UK (SWestUK) at different spatial scales and different seasons. (a, b) at a catchment scale of 43.6 km^2 (i.e., 3×3 grids of CPM outputs); (c, d) at a catchment scale of 10950.9 km^2 (i.e., around 48×48 grids). Probability of dry hours of each dataset is indicated inside the bracket of each legend.

In the comparison of two observation products, results from the GEAR-1hr observation seem to give smaller ARFs than the weather radar estimates. The discrepancy can be explained by the inadequate representation of the hourly GEAR in representing spatial organizations of storms. Notably, the GEAR dataset is interpolated by using only rain gauge data. Available rain gauge data, at an hourly scale, are not dense enough to provide

a spatial pattern of rainfall (see an example in the Section 2.2.3 Figure 2.4). This leads to an underestimated dependency of point extremes and areal extremes, therefore less reliable ARFs obtained from the GEAR datasets at the hourly timescale.

Section 5.4 Discussions and Conclusions

5.4.1 Summary

In summary, this chapter focusses on evaluating the realism of rainfall output for the latest national-wide convection-permitting ensembles. I compared the 12-member 20-year-long hourly-scale climate model outputs for the control period (1980-2000) with several quality-controlled observational rainfall datasets (Radar, GEAR, HadUK-Grid). Results show that the spatial pattern of mean annual precipitation is reasonably well captured by the CPM with a relative bias of less than 30% compared with the gridded observations. At four selected subregions which have the potential to be used for the impact studies of this thesis, seasonal variations obtained from the CPM are similar to the observed. On modelled storm durations and key areal statistics, the occurrence frequency of storm events is well reproduced by the CPM. At an area scale of $110 \times 110\ km^2$, the probability distribution of the areal mean rainfall rate is also captured in all selected subregions. Despite the considerably improved hourly precipitation variability compared to the GCMs/RCMs in previous studies (Kendon et al., 2019a), the CPM still tends to simulate too many storms having a shorter duration in time and a smaller peak coverage in space. The CPM overcorrects the bias in RCMs (too many low-intensity events) and instead gives too many moderate and intense events, as reported by Berthou et al. (2018). On spatial organization, the CPM is able to reproduce a scaling behaviour (power-law spectral density function) across spatial scales (2.2 km to 110 km) very similar to the one derived from the 12-year-long radar reflectivity fields with a clear scale break at around 20 km. The spatial variability across temporal scales (1~24 hours) also shows a similar pattern to the radar estimates. Features of high-impact events have also been examined, where the CPMs reproduce the clustering of heavy rainfall quite well at a daily scale while at an hourly scale the CPMs tend to give a smoother rainfall field in space. Areal reduction factors (of extremes) are found to be consistently lower than the radar estimates because of the overestimated grid-scale extremes in the convection-permitting model.

5.4.2 How to use CPMs-derived information in stochastic model?

In terms of the applicability of CPMs to stochastic model development for impact studies, as we can see, not all statistics can be directly used in STREAP-based model calibration. For the first stage of STREAP (storm arrival process), bias correction on dry spell durations or wet spell durations obtained from the CPM data is needed so as to make sure the calibrated model reproduces the observed probability distribution of the durations. For the second stage of STREAP (temporal evolution of mean areal statistics), CPM-modelled areal mean intensity is overall fine, but the wet area ratio needs to be bias-corrected so as to fit a reasonable probability distribution function. For the third stage (spatial-temporal evolution of the storm structure), how the spatial variability (CV_{pos}) changes across different scales is found to be well captured while at the hourly scale it is slightly underestimated.

Overall, the above statistics required for STREAP calibration are obtainable from the convection-permitting model, some of which are becoming available from climate models for the first time. Although bias correction is still recommended, the CPM model does provide valuable information to be utilized in stochastic rainfall tool development for impact studies.

Chapter 6 Future Changes in Rainfall Properties, Using Convection-permitting Ensembles

This chapter focuses on answering how the spatial-temporal statistics of extreme rainfall will change in a future climate over the UK. As in the previous chapter, the same convection permitting model is used. After an introduction in Section 6.1, Section 6.2 describes the study region and statistical methods. Section 6.3 presents projected changes in a range of characteristics of rainfall with a focus on heavy rainfall events. Then, section 6.4 provides a comparison of the results with previous studies, followed by a discussion of their potential impact on future flood risk. Section 6.5 gives a summary conclusion.

Section 6.1 Introduction

Understanding the future change of rainfall extremes is crucial to strengthen the resilience and the adaptation to natural hazards. Several studies have projected changes in daily extremes using GCMs or RCMs (Fischer and Knutti, 2015; Kharin et al., 2013; Pfahl et al., 2017). At sub-daily scales, both observational and modelling studies have shown that rainfall extremes are increasing rapidly in some regions of the world, as summarised in section 1.3.1.

The development of CPMs has improved the realism of small-scale rainfall features in future climate projections, as found in previous literature (Kendon et al., 2014, 2012) and in Chapter 5. A few modelling studies have analysed extreme hourly rainfall intensity from CPMs. In the UK, a 13-year climate simulation with a CPM shows intensifying summer downpours (Chan et al., 2018; Kendon et al., 2014). This overall trend is also found in the European Alpine region (Ban et al., 2015), Germany (Chan et al., 2020; Fosser et al., 2017), Southern France, Eastern Spain (Chan et al., 2020) and the United States

(Prein et al., 2017b). Besides the intensity, the spatial structure in the future climate also changes due to the increasing temperature and moisture availability (Lochbihler et al., 2019). A wider spatial extent can further aggravate flood risk due to increasing total rainfall amounts over a given area.

The variability of small-scale spatial structure of rainfall plays a critical role in flood generation (Paschalis et al., 2014a; Peleg et al., 2020). Only a few studies have analysed the spatial structure at kilometre scales, whether it be in observed rainfall or future projections. Those studies present some broad areas of agreement as well as conflicting results. In studies based on observations, temperature is taken as an explanatory variable to detect the trend. By analysing radar estimates from the eastern Mediterranean, Peleg et al. (2018) found that with warmer temperature, the spatial extent of rainstorms decreases whereas the areal convective rainfall increases. Wasko et al. (2016) also found a reduced spatial extent of rainstorms with increasing temperature by analysing a dense network of rain gauge data in Australia. Studies based on climate model projections do not always show consistent results with the observation-based studies: in Sydney, by analysing CPM projections, Li et al. (2015) found that the ratio of areal rainfall to point rainfall will increase at hourly scales in the future. This implicitly suggests a larger area with intense hourly rainfall extremes. Using a 4-km resolution CPM, Prein, Liu et al. (2017a) also found an increasing rainfall volume of Mesoscale Convective Systems across the USA. Using pseudo global warming simulations of 41 historic heavy rainfall events, one recent modelling study over the eastern Mediterranean region shows a decreased area of these events with global warming under the RCP8.5 scenario (Armon et al., 2022). Using a large eddy simulation, Lochbihler et al. (2019) found that the size of rain cells in the Netherlands will significantly grow along with increasing intensity due to warming. Because these modelling studies were based on a single model run, it was not plausible to assess the uncertainty related to the climate projections. For the UK, so far, from the available literature, one gains limited insights into the changes in the spatial structure of rainfall extremes. Kendon et al. (2014) found that many of the heaviest events across the southern UK in the future will be large-scale storms, highlighting the importance of unravelling details of the changes in spatial structures.

This chapter is to address the question of how the spatial profile of extreme rainfall will change in a future climate over the British Isles, by using a state-of-the-art CPM. Using a

12-member CPM ensemble, I assessed the climate change effect on hourly rainfall events during summer over the UK. Physical characteristics were extracted and compared for the past and future periods, with the uncertainty included. For hydrological use, the resulting impact of those changes was then analysed at different catchment scales, ranging from localized urban areas to large river basins.

Section 6.2 Methods

Precipitation projections are obtained from the UKCP convection-permitting ensemble (Kendon et al., 2020a, 2019a). The CPM simulation for historical (1980–2000) and future (2060–2080) periods is used. As described in previous chapters, the model has been validated with multiple observed datasets, including radar data (Met Office, 2016) and gridded rain-gauged-based rainfall estimates (Lewis E. et al., 2022; Tanguy et al., 2019). The hourly rainfall characteristics closely match observations in terms of the diurnal cycle, heavy rainfall amount, event duration, hourly extremes (Fosser et al., 2019; Kendon et al., 2019a; analysis in Chapter 5) and its spatial structure (Chan et al., 2013; Kendon et al., 2012; analysis in Chapter 5).

In this chapter, a comparison between the historical period and the future period is carried out over three subregions (land area) across the UK (Figure 6.1), with a focus on short-duration heavy rainfall. Criteria to separate regions in this chapter are different from selections in the previous chapter because here we are more focused on selecting regions having different climate features and there is no need to consider the quality of radar data at all. The three regions (North West, North East, South) are separated according to their distinct climatology (Darwish et al., 2020; Kendon et al., 2019a). Since, in most regions of the UK, 1-h annual maximum observations are highly concentrated in summer (Darwish et al., 2018), the analysis is carried out for the summer season (JJA).

i. Spatial-temporal characteristics of heavy rainstorms

Several spatial-temporal characteristics of heavy storms are extracted, and their changes are evaluated. The characteristics include rainfall advection speed, spatial coverage of heavy rain (wet area > 5 mm/h), mean areal intensity (P_{mean}, average rainfall intensity over all grid cells, also known as rain yield (Lochbihler et al., 2019) and areal rainfall

volume (P_{total}, areal rainfall amount in the sub-region within the hour (Prein et al., 2017a). The rainfall advection speed is computed by using an optical flow technique (Lucas and Kanade, 1981), same as the one used for radar data so as to keep consistent throughout the thesis (see details in Appendix I.3). Wet area (used for calculating the spatial coverage) is defined as the area having intensity (at a 2.2 km scale) greater than 0.1 mm/h, and hours with the wet area fraction > 2% are defined as "wet hours". With a focus on the high-impact events, only those heavy storms (hours having a peak intensity P_{max} >10mm/h) are extracted for in the analysis. Notably, although the fixed value (5 mm/h) is taken as a threshold to calculate the spatial coverage, considering the changing distribution of rainfall intensity, a percentile-based threshold has also been examined for ensuring the trend robustness (See Appendix I.1).

For each of those rainfall characteristics (for heavy hourly storms), their changes between the past and future periods, in their occurrence frequency and magnitude (percentile values) are evaluated. The median of results from model simulations is taken as a central estimate, in which all members are treated equally. Uncertainty is also considered in the analysis, as represented by the range of ensemble members.

ii. Spatial profile of heavy rainfall

To evaluate the spatial profile of heavy rainfall, the 480 heaviest hourly rainfalls (i.e., about two hourly events per year per ensemble member) are identified for each region. These events are hours having rainfall heavier than the 99.9th percentile hourly precipitation, which is taken as a threshold to define extreme hourly precipitation in literature (Ban et al., 2015). Other sample sizes between 120 and 840 events were also checked for statistical robustness. Those selected hours correspond to times having the heaviest peak intensity. To exclude those hours where intense rainfall occurred at a very localized area only (e.g., a single grid cell), hour selection is based on rainfall images aggregated at a 11 × 11 km^2 scale. A storm separation method (Section 3.3.2) is applied to make sure the selected hours belong to different storms (Paschalis et al., 2013). The averaged storm profile is obtained by relocating each storm profile to its respective point of maximum rainfall intensity and taking the average among all relocated profiles. The relative difference of rainfall intensity in the two periods is used to quantify changes at a certain radial distance from the storm centre. The relative differences, as well as the ensemble range of the differences are then estimated.

iii. Extreme statistics at spatial scales

Changes of extremes at different spatial scales are quantified in terms of intensity-duration-area-frequency (IDAF) curves, commonly used for hydrological design. IDAF curves are computed for the 12 ensemble members separately, by extracting annual maxima of average rainfall over a fixed area (A) and duration (D, kept being 1-hour in this analysis). The analysis follows the method of De Michele et al. (2011) in which $I_{MAX}(D, A)$ is computed according to the equations (6.1) and (6.2). In this analysis, the annual maxima analysis is undertaken for each summer season, each sub-region (Ω). Data outside UK coastline boundary is not included.

$$I_{MAX}(D, A) = MAX_{D \subset 1year,\, A \subset \Omega} \bar{\xi}_{D,A} \tag{6.1}$$

$$\bar{\xi}_{D,A}(x, y, t) = 1/DA \int_{t-D/2}^{t+D/2} \int_{x-lx/2}^{x+lx/2} \int_{y-ly/2}^{y+ly/2} \xi(\omega, \zeta, \tau) d\omega d\zeta d\tau \tag{6.2}$$

where $\bar{\xi}_{D,A}(x, y, t)$ is the rainfall intensity averaged over the space-time domain DA, centring at (x, y, t). A rectangular-shaped area (with the width and the length to be lx and ly) is selected to be the space domain A. $\xi(\omega, \zeta, \tau)$ is the gridded rainfall volume at the location (x, y, t).

Using the method of maximum likelihood, the generalized extreme value distribution is fitted to estimate $I(D, A, T)$, the T-year return precipitation in JJA at 1-h duration D and different catchment scales A. Catchment areas ranged from 4.84 to 8537.76 km^2, covering the spatial extent of rainfall events from small convective storms at a localized urban area to mesoscale convective systems influencing a much larger river basin such as River Trent (8231 km^2). The signal-to-noise ratio (SNR; Hawkins and Sutton, 2011), estimated as changes in mean value divided by the standard deviation, is estimated to quantify how large the future change is compared with the uncertainty in ensemble simulation.

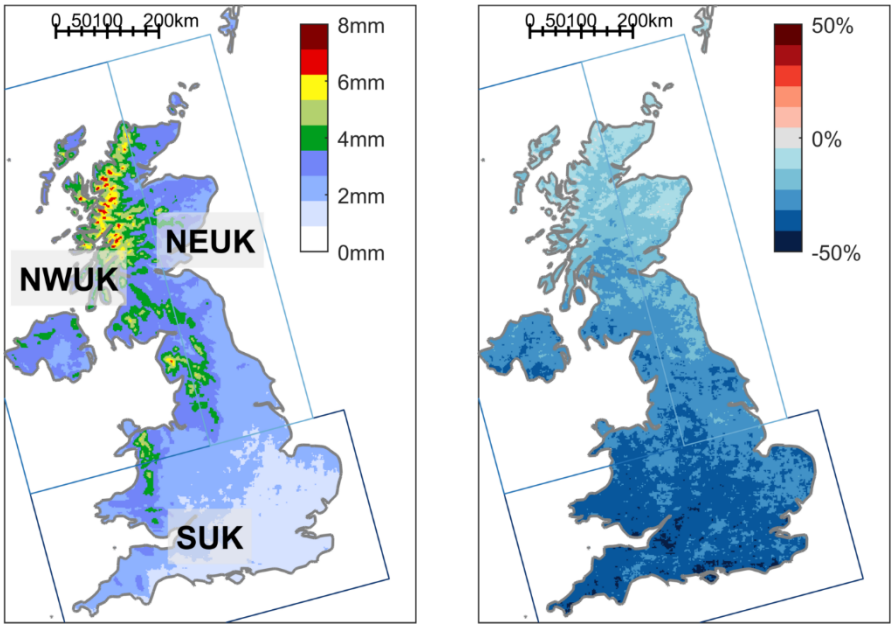


Figure 6.1 Separation of study region. (a) Map of summer-season average precipitation (1980–2000 period) and separation of study region; (b) Map of future change in summer-season average precipitation (2060-2080 period versus 1980-2000 period). For a completeness, future changes in annual mean and in winter (DJF) can be found in Appendix III.4.

Section 6.3 Results

6.3.1 Spatial-Temporal Characteristics of Heavy Rainstorms

During summer seasons, the occurrence of wet hours shows a relative decrease by 11.8%–36.2% (Table 6.1), consistent with an overall drier summer (Figure 6.1.b). However, for hours exceeding a high threshold (P_{max} > 70 mm/h, about 99.5th percentile of all hours), the occurrence frequency is projected to increase by 104.4%–139.9% in the north and 76.7% in the south.

Table 6.1 Rainfall occurrence of different Pmax classes [a] (unit: hour/summer season).

Region	*Period*	*0.1-10*	*10-30*	*30-50*	*50-70*	*>70mm/h*	*Wet hours*
NW	Past	975.43	488	106.38	40.53	12.45	1622.8
	Future	876.50	371.50	97.38	40.05	25.45	1410.9
NE	Past	1007.68	362.15	85.38	27.95	7.2	1490.4
	Future	855.15	287.28	81.23	36.2	17.28	1277.1
S	Past	549.03	319.00	72.53	23.5	8.48	972.5
	Future	317.45	197.48	60.45	26.75	14.98	617.1

[a]: calculated for all hours in each sub-region and averaged over 12 ensemble members.

Besides the occurrence frequency, trends in each heavy rainfall characteristic over various percentiles were examined. Peak intensity (P_{max}), for the 50th percentile or higher, increases by up to 15%–25% (Figure 6.2). The high percentiles of hourly spatial coverage tend to increase in all regions, reaching 30%–35% in the north. Similarly, the

mean areal intensity (P_{mean}) also shows an increase for high percentiles while a relative decrease by up to 20% for low percentiles. The increase in areal intensity accounts for a larger proportion in the north-west (about 20%) than in the south (about 10%). It is worth mentioning that it is not straightforward to compare quantile differences shown here with the Clausius-Clapeyron scaling rate, because in this analysis the calculation of quantile values is based on hours identified as 'heavy rainfall' while CC rates are calculated based on quantiles values in which all hours are included.

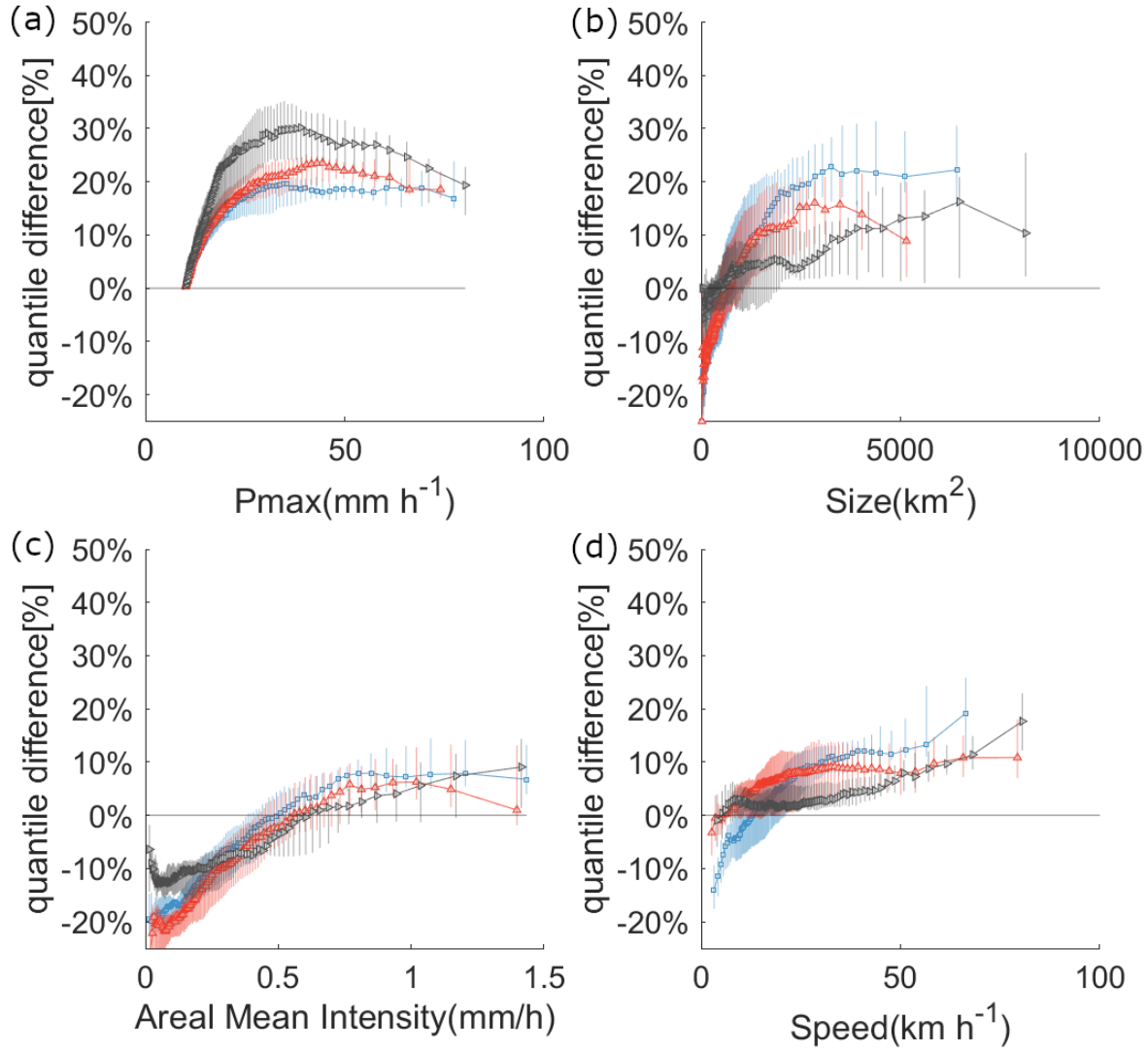


Figure 6.2 Quantile differences between the future-period and the past-period probability density functions of several heavy rainfall properties, including peak intensity (P_{max}) (a), size (b), storm speed (c) and total volume (P_{total}) (d). The difference for percentiles between 1st and 99th is shown. Each sub-region is represented by a different colour. Vertical lines represent the interquartile range based on 12 ensemble members.

The changes in peak intensity (P_{max}), advection speed and spatial coverage are not constant under different mean areal intensity (P_{mean}) conditions. In the southern UK, the shifting of P_{max} toward a higher value is more pronounced when the total areal amount

is small (P_{mean} < 0.8 mm/h) (Figure 6.3.a). Similar behaviour occurs in the north, more strongly in the north-west. As for the advection speed, the occurrence of fast-moving rainfall is projected to increase during low-intensity hours (P_{mean} < 0.5 mm/h), while no significant change is observed (p > 0.05) for the higher P_{mean} hours (Figure 6.3.b). The spatial coverage of heavy hourly rainfall (Figure 6.3.c) tends to increase regardless of the mean areal intensity. These relative differences conditioned on areal mean intensity imply that, with the same amount of areal total rainfall, future period is expected to experience a high peak intensity over the space, a higher storm speed as well as an increasing spatial coverage during the hourly heavy rains.

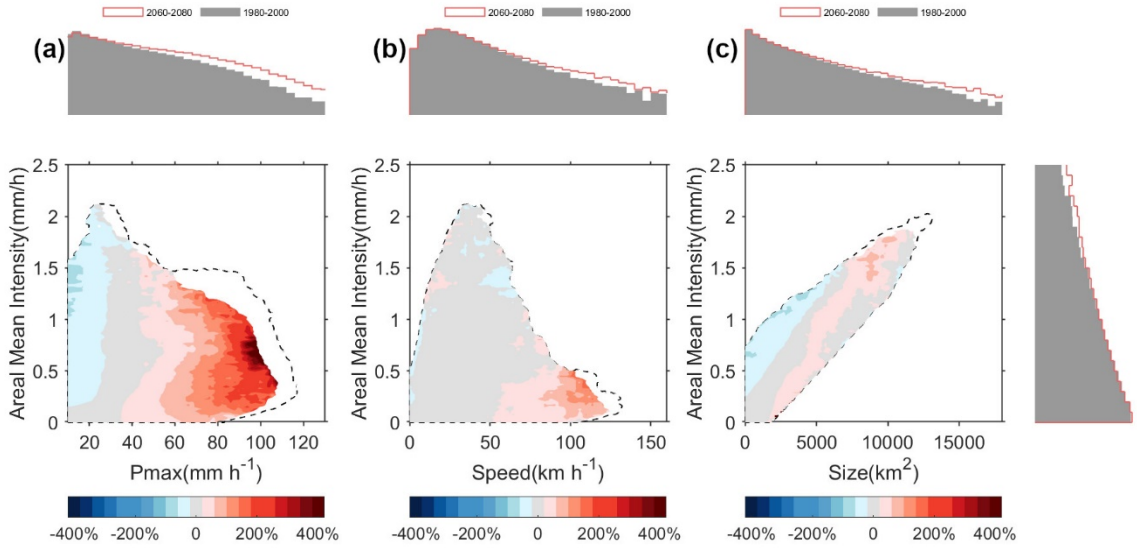


Figure 6.3 Relative difference of heavy rainfall features in the south UK. Relative difference in the future minus the past conditional probability of peak intensity (a), rain advection speed (b), spatial coverage(c), conditioned on areal mean intensity for all heavy rain hours. Filled contour shows the area with at least five heavy rain hours happening per 20 years, both in current and future climates. Gray area shows area not significantly different from zero with p < 0.05. Dashed line shows the boundary with at least five occurrences (hours) in the future. Bar charts in the upper and far right panel show the empirical density functions in a logarithmic scale for the dimension they are adjacent to.

6.3.2 Spatial Profile of Extreme Rainfall

Changes in the spatial structure of extremes in each subregion are shown in Figure 6.4. In all three subregions, the peak intensity at the centre of hourly events shows an increase, of which the relative increase is higher in the north-east (23.9%) and lower in the south (16.1%) and the north-west (14.76%).

Beyond the peak intensity, significant changes regarding their overall spatial structure are also found. The rainfall intensification tends to persist with radial distance in all three regions, particularly in the north. The north-west has its maximum intensification at 13–

30 km from the storm origin, where the relative increase is up to 53.6% (Figure 6.4.a). This increase is beyond the relative increase at its rainfall peak, confirming that the changing spatial profile is not just the manifestation of the increasing rainfall intensity at the storm centre. Correspondingly, the average spatial coverage of the storms shows an increase of 49.3% (ensemble range: 8.9%–201.7%). The south also experiences an expanding spatial coverage by up to 24.2% (ensemble range: 0.78%–66.9%), and the relative increase of intensity is about 20% for the entire spatial domain of the storms (Figure 6.4.c). Those changes in the spatial pattern of hourly events lead to an increase in areal rainfall amount (rainfall amount within a given hour focused in a 33 km radius domain around the storm centre). The average increase is 35.7% in the north-west, 15.9%–16.3% in the north-east and the south.

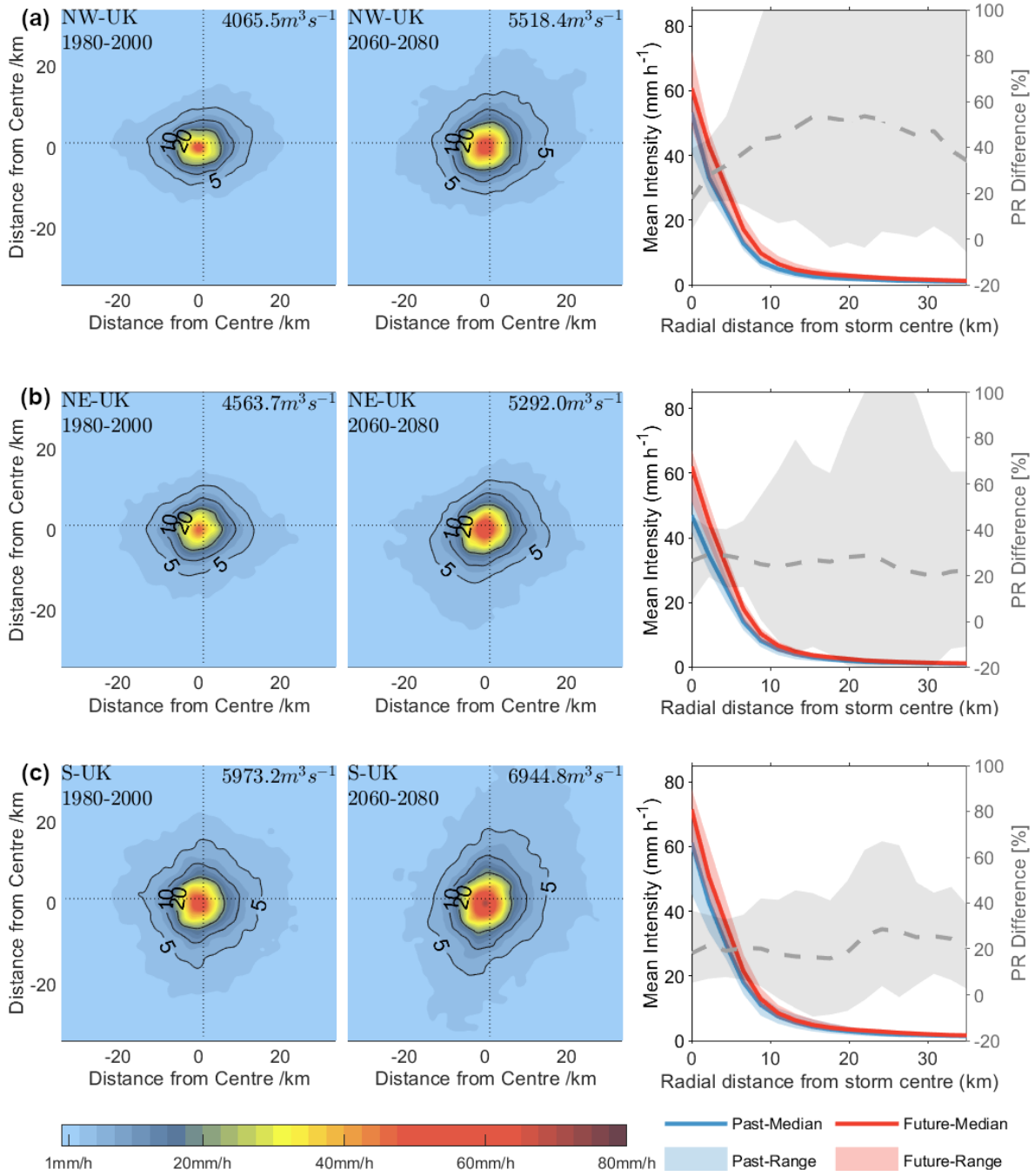


Figure 6.4 Changes of the heaviest 480 summer rainfall in North-West (a), North-East (b), and South (c). For each subregion: averaged spatial profile in 1980–2000 (left) and in 2060–2080 (middle); (right) ensemble-average rainfall rate (left side *Y*-axis) and ensemble-average relative differences of rainfall intensity (right side *Y*-axis) as a function of radial distance from the storm centre, where the corresponding filled area represents the range between the second lowest and the second highest value over the 12 ensemble members.

6.3.3 Extreme Rainfall Across Spatial Scales

Combined changes in the occurrence and the spatiotemporal dynamics of extremes can have a pronounced effect on natural hazard analysis, as quantified by IDAF curves (Figure 6.5). Extreme intensity shows an increase for almost all return periods (2–40 years) and

areas (4.84–8000 km^2) in the three subregions. The relative increase reaches 34.0% (A = 91 km^2, T = 2 years) in the north-west, 30.2% (A = 181 km^2, T = 40 years) in the north-east and 25.8% (A = 110 km^2, T = 27 years) in the south, an exception occurs in the high return levels (>10 years) at large spatial scales (>1000 km^2) over the north-west and the south, where a decrease in areal extremes was found. However, the decrease is not statistically significant.

The intensification (central estimate) of areal extremes depends on both the return period and the spatial scales. For spatial scales representative of small- and medium-sized catchments in north-eastern UK, a similar intensification is estimated for 2–40 years return levels. For the larger spatial scales and for the north-west, the intensification is higher for the lower return periods (<10 years). A typical feature found over three subregions is that the strongest increase in extremes occurs for spatial scales between 50 and 500 km^2 (Figure 6.5.d-f), while the north-west also has another peak of the relative increase occurring at a 4000 km^2 scale.

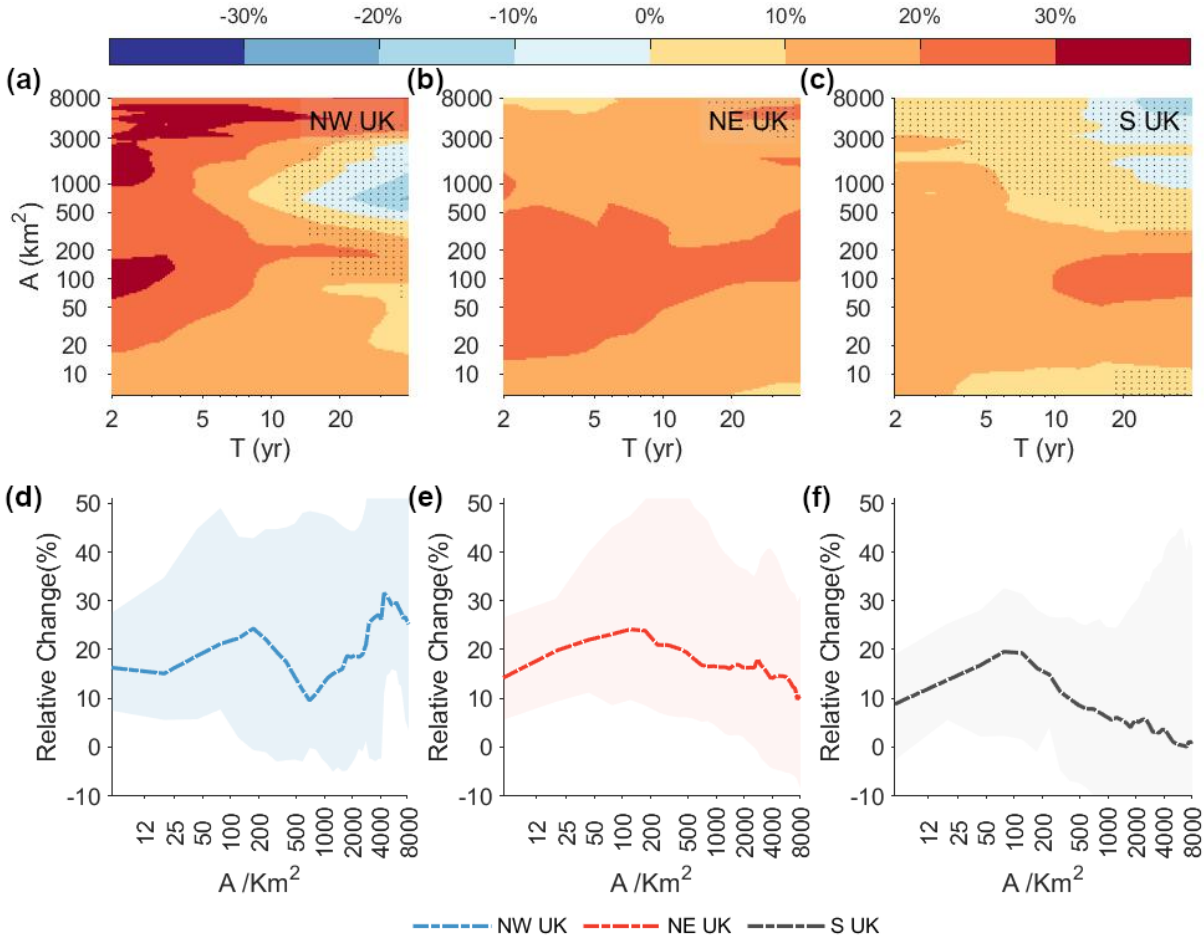


Figure 6.5 Relative change of areal rainfall intensity as a function of catchment scales and return levels. (a–c) filled contour shows an ensemble-average relative difference of $I(D, A, T)$ in the future minus the past period

(dotted area represents a nonsignificant change at $p < 0.1$) in each subregion; (d–f) relative changes of extremes in 12 ensemble members as a function of catchment scales. The filled range represents the ensemble range between the second lowest and the second highest value, with a solid line representing the median value.

The significance of the change signals tends to decrease with the catchment area enlarging, as indicated by the signal-to-noise ratio (SNR). Specifically, when the area increases from a several km^2 scale to $\sim$8000 km^2 scale, SNR drops down from 2.78 to 1.05 in the north-west, from 2.05 to 0.24 in the north-east, and from 3.03 to 1.14 in the south.

Section 6.4 Discussion

6.4.1 Intensifying Extremes Revealed by Convection-Permitting Models

The intensifying hourly extremes found in the 2.2 km CPM ensemble are qualitatively in agreement with previous findings for the UK based on convection-permitting models (Chan et al., 2018, 2020, 2014; Kendon et al., 2014). The intensification can be attributed to the increasing atmospheric moisture with warming, according to the Clausius-Clapeyron (C-C) scaling relation (Moustakis et al., 2020). The positive scaling stems from the fact that a warmer temperature can hold more moisture, which has been validated both from observations (Blenkinsop et al., 2015) and climate simulations (Chan et al., 2016) in the UK.

Projected changes of annual extremes in the north (-west) are greater than in the south, which is also consistent with the studies using a 1.5 km RCM (Chan et al., 2018; Kendon et al., 2014). Notably, there have been considerable improvements in the CPM model used in the thesis, including developments in the CPM model physics (Fosser et al., 2019), the driving GCMs (Schiemann et al., 2016) and the simulation domain (Fosser et al., 2019). Differences in results are likely related to the above improvements in the climate models themselves.

6.4.2 Expanding Spatial Extent of Rainfall Extremes

The regional difference in the spatial extent of heavy rainfall can be explained by rainfall mechanisms in each subregion. Since a threshold of minimum peak intensity (10 mm/h) is used to define heavy rainfall in this study, most of the widespread and lower-intensity

stratiform rain is filtered out (Barnolas et al., 2010). The analysed rainfall events can be regarded as a group of events formed from intense frontal rainfall, orographic rainfall, and/or convective rainfall. Extremes from those are analysed together without explicitly separating the different rainfall types. Among these, organized convective systems, which can result in large-scale extreme events mostly happen in the south UK in the present-day climate, whereas they seldom happen in the north (only one record between 1981 and 1997) (Gray and Marshall, 1998; Lewis and Gray, 2010). Such spatial variability in the occurrence of convective systems well explains the broad spatial coverage of hourly extremes in the south (the past period in Figure 6.4.c). On the contrary, the north-west experiences strong orographic influence but it is less affected by the large organized convective systems than the south-east England (Lewis and Gray, 2010). Extremes in the north-west are thereby expected to be more concentrated in specific locations (i.e., over high terrain), showing more localized events than the south.

In terms of the changes in the spatial extent, the increase in areal rainfall amount reported in this chapter (by up to 60.8%) is slightly lower than the model-based finding (80%) in the US (Prein et al., 2017a). The difference can be attributed to the fact that the US receives mesoscale organized convective storms more frequently. Also, my investigation is based on 12-member ensemble simulations while the one in the US was based on one single realization. The variability of changing spatial extent between ensemble members is large, where individual members can diverge in terms of the sign of the trend (Figure 6.4 and Figure 6.5). This discrepancy highlights that the natural variability might mask the general trend (Fatichi et al., 2016) in analysing future spatial extent of extreme rainfall.

The increasing spatial extent could be attributed to the changing thermodynamic and dynamic conditions. On the one hand, the warming temperature plays a role in changing the spatial organization of precipitation as reported by Lochbihler et al. (2019). Once the moist convection and precipitation set in, the spatial scale of areas of low-level moisture convergence and divergence becomes larger with the higher temperature (Haerter et al., 2017; Haerter and Schlemmer, 2018), thereby increasing the spatial extent of rain cells. On the other hand, the findings in the CPM are also strongly controlled by the driving GCM and its simulated large-scale circulation pattern in future climates. Dynamical changes in atmospheric circulation might result in a changing frequency of organized convective

storms. Further investigation into the corresponding weather patterns of future extremes of the UKCP simulation (McSweeney and Thornton, 2020) will help to better understand the changes of extremes for each different storm type (Marra et al., 2019). Besides, a rainstorm identification and tracking method (Chang et al., 2020) could be beneficial to segment the different rainstorms occurring at the same time in the study region; these are not separated in this study.

6.4.3 Impact of Changing Rainfall Regimes on Flood Risk

Intensification of rainfall extremes is expected to have a strong impact on the hydrological cycle. One direct consequence is the increasing potential of flood hazards, as confirmed by GCM results (Alfieri et al., 2017). Flood hazard analysis under climate change is generally assessed by downscaled GCMs (RCMs) under a certain climate scenario and hydrological models. Under the widely used delta change or quantile mapping approach (Camici et al., 2014; Kay and Jones, 2012), changes in rainfall spatial structure have not been included. As reported in this chapter, the high-resolution climate model results show that the simultaneous increase of extreme intensities and the spatial extent will yield a much higher areal rainfall amount within one hour. The small-scale feature is essential for the hydrological cycle over river basins and the peak discharge (Paschalis et al., 2014a; Peleg et al., 2020) while the current flood impact studies have not included a representation of the changing spatial structure. This fact indicates that the increasing flooding hazards in the future might be still underestimated. The related flood risk can further exceed our current expectations and impact a broader area at the same time. My study shows that it is crucial to investigate those changing rainfall regimes together in order to undertake the relevant impact studies.

IDAF analysis shows that the highest intensification occurs for the small catchment scales (20–500 km^2), corresponding to typical urban areas of the UK (e.g., Edinburgh urban area is about 119 km^2). The projected changes in extreme events at up to 30-year return levels are critical in sewer designs, provided by new build and sewerage upgrade in the UK typically happen 1 in 30 years in practice (Dale et al., 2017). The increase in rainfall hourly extremes of up to 25.8%–34% at these catchment scales implies a significant underestimation of urban flood risk in current guidance. In the contrast, the changes at the larger return period and large spatial scales (more than 1000 km^2) are not that pronounced (with the exception of north-western Scotland). Aside from the importance

of peak intensity, pluvial flooding at large scales might be less influenced than those small and urbanized areas by the changing spatial structure.

The catchment response will be also affected by other changes reported in this chapter. For example, the decreasing average rainfall amount in summer (Figure 6.1.b), and the long dry spells (consecutive hours with no rain) (see Appendix III.5) will lead to a much drier antecedent soil moisture condition; the increasing storm advection speed will affect the soil water dynamic over a catchment during the storm event. All these factors will act together to modulate the rainfall-runoff process and affect the flood hazard. The combined impact of these changes on catchment response could be quantified by coupling the CPM results with the hydrological and hydraulic tools.

Aside from the potential impact on flood risk, the increasing drought risk (Figure 6.1) in summer also implies that coping with the increasing summer-season water stress might be more challenging, particularly in the south due to the higher water demand. Adaptation strategies will be required for water supply companies to tackle the potential reduction of supply sources in the coming few decades in the UK. The drying condition of soil moisture (the lack of rain) could act together with the more frequent heatwaves, leading to unprecedented wildfire danger in the UK (Arnell et al., 2021). The altered rainfall regime also impacts agriculture and livestock production (Wilcox et al., 2017). Its direct (e.g., plant stress) and indirect (e.g., delayed agriculture activity, more irrigation water demand) impacts on agricultural yields will potentially increase the vulnerability of food production.

6.4.4 Value of CPMs and Projection Uncertainties

The convection-permitting models provide credible climate information about future precipitation at small spatial-temporal scales. The benefits of using CPMs lie in their ability to better resolve local-scale processes in the real atmosphere and consequently the changes at the small scale can be captured, such as the higher scaling relationship with increasing temperature for hourly extremes (super CC; Lenderink and van Meijgaard, 2008), and the changing spatial organization reported in this chapter. Such a high-resolution climate modelling system would be required globally in climate impact studies, but that would create a much higher computational burden. How to achieve such a much more computationally expensive simulation is still a technical challenge.

Projection uncertainty is another factor to highlight. The use of perturbed parameter ensemble improves the effectiveness of climate projections by sampling uncertainties in the assumed deterministic outputs of parameterizations (Tebaldi and Knutti, 2007). Interannual variability is also represented to some extent in the current 20-year ensemble simulation. However, the CPM ensemble only downscales Hadley Centre global models under the high-end RCP8.5 scenario. The CPM ensembles for other RCPs or the updated SSPs are currently unavailable. It does not sample uncertainties arising from the CPM model physics itself. Follow-on work for UKCP at the UK Met Office aims to address this, with a more comprehensive sampling of uncertainties at CPM scales.

Section 6.5 Conclusion

In the UK Climate Projections UKCP project, for the first time, ensemble simulations using the convection-permitting model are currently available. Using the two sets of 12-member ensemble simulations over the UK for the past and future periods, this study shows that rainfall occurs less frequently in the future summer season, but when it rains, it tends to be more intense. The increase of extremes in both peak intensity and occurrence is projected in all three subregions (North West, North East, South). The future summer rainfall is found to move faster and also has a larger spatial coverage. The increase in spatial extent and peak intensity of extremes leads to an increase in hourly areal rainfall amounts by up to 60.8% in the north-west. Such an intensification of rainfall extremes at 2–40 years return levels is projected for most of the catchment scales, reaching the highest increase at the scales with sizes 20–500 km^2. This spatial scale implies the significant underestimation of urban flood hazards in future climate in current guidance. In addition, ensemble results also indicated that, for large catchment areas (thousands of km^2) in the south, any trend may not be significant compared to variability across the 12-member ensemble.

Chapter 7 Modelling Spatial-temporal Rainfall for Climate Impact Studies

Section 7.1 Introduction

With computational power increasing, high-resolution convection-permitting models become more widely used in climate projections and related impact studies. However, as introduced in Chapter 1, the resolution of climate models is still not fine enough in both space and time and the estimation errors in its rainfall output are not negligible for hydrological applications (Kay et al., 2015). Downscaling approaches based on stochastic generators can be used to fill the gap. In the literature, most weather generators are designed for downscaling GCMs/RCMs and changes in small-scale spatial-temporal profile (see chapter 6) are not well represented by either climate model outputs or these weather generators and therefore by the downscaled rainfall products (Akhter et al., 2019; Bordoy and Burlando, 2014; Camici et al., 2014; Fowler et al., 2007; Maraun and Widmann, 2018; Sørup et al., 2016). With the development of convection-permitting models, the added value is on the combination between the strength of high-resolution CPMs and the flexibility of stochastic models to generate more realistic downscaled rainfall for climate studies, although such a tool has not been available yet.

This chapter aims at developing a simulation tool which can combine information from the most-advanced high-resolution climate models with a stochastic rainfall generator to provide a finer-resolution (5 min, $1km \times 1km$) rainfall product for climate impact studies. The calibration and validation procedures of the developed tool are summarized in Figure 7.1. Section 7.2 presents the tool developments with an emphasis on how the selected stochastic model basis (STREAP) is adapted to climate studies and how a downscaling mode is enabled. Section 7.3 then describes the study area and validation method applied to assess the tool based on climate models and radar estimates. Section 7.4 presents the calibration results of the tool as well as the validation for both the current and the future climate, followed by conclusions in section 7.5.

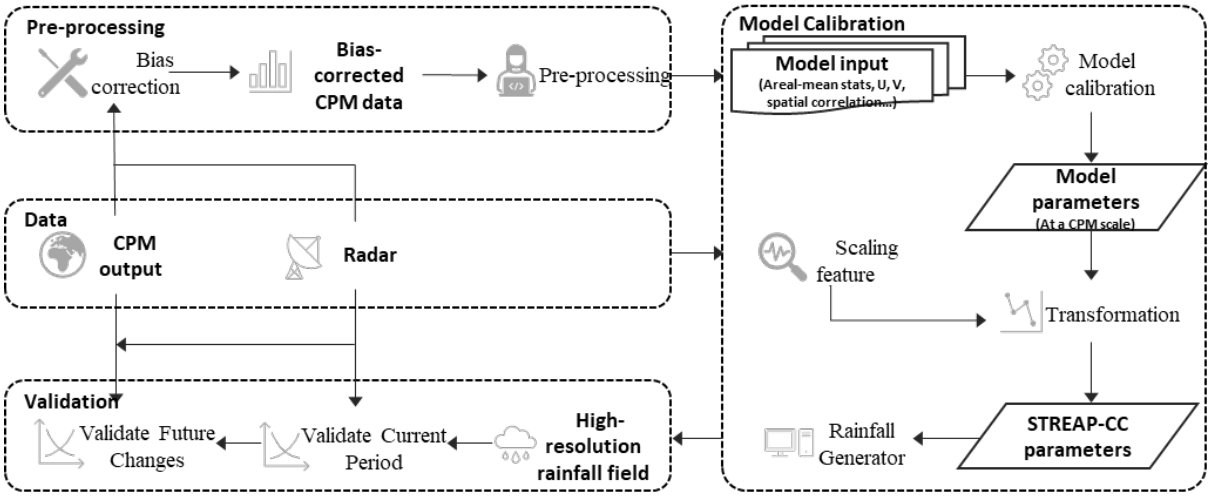


Figure 7.1 Flow chart of STREAP-CC calibration and validation procedures.

Section 7.2 Model Development

The simulation tool developed in this chapter is designed to provide rainfall information with a resolution suitable for urban applications in climate impact studies. Rainfall output from the tool is spatial-temporal rainfall fields for a specified climate period, statistically consistent with both observations and climate projections. The resolution of generated rainfall fields can reach up to 5 min in time and 1 km × 1 km in space.

In this tool, the rainfall modelling process follows the hierarchical structure used in a well-established stochastic rainfall generator STREAP (Paschalis et al., 2013), following the conclusion reached in Chapter 4. Thanks to the structure of the generator, the tool is able to generate multiple realizations of future rainfall fields, while also aiming to preserve key features projected by climate models. In order to achieve this aim, instead of calibrating the tool using rainfall observations (i.e., weather radar) like in STREAP, rainfall output from a 12-member 20-year-long convection-permitting ensemble will be used to estimate model parameters for the desired period. Before being used, the CPM rainfall output has been debiased following a bias correction recommended in the UKCP18 report (Met Office, 2019c), with details provided in Appendix IV.1.

Table 7.1 Summary of how the model parameters are determined at each stage of STREAP-CC.

Stage	*Property*	*Initial parameters obtained from*	*Corrected by (if any)*
Storm Arrival	Dry spell duration	Climate Models	Observed feature
	Wet spell duration	Climate Models	Observed feature
WAR-IMF bivariate	WAR series	Climate Models	Observed feature
	IMF series	Climate Models	Observed feature
	Copula matrix	Climate Models	-

	μ_{war_g}, μ_{imf_g}, σ_{war_g}, σ_{imf_g}	Climate Models	-
	Covariance function	Climate Models	Analytical Conversion
Spatial-temporal evolution	Spatial Variability	Climate Models	Observed feature
	Spatial correlation	Climate Models	Observed feature
	ARMA processes	Observation	-

Besides the different rainfall data being used in the general calibration procedure, the simulation tool also makes good use of the long-record of radar estimates to enable the tool to 1) generate rainfall fields having realistic fine-scale rainfall features for either current or future periods; 2) debias rainfall key properties and thereby enable unbiased model parameters to be computed from climate models; 3) improve the modelled dependency of the temporal evolution of rainfall intensity upon different spatial scales. These three features, which are new developments achieved in this thesis based on the original version of STREAP, make the simulation tool more realistic and consistent with changes projected by climate models and suitable for urban applications. To distinguish the tool from the original STREAP, the tool developed here is named STREAP-CC as an abbreviation of Spatial-Temporal Realisations of Areal Precipitation for Climate Change impact studies, with the data source of model parameters listed in Table 7.1. Since most of parameters are calibrated based on climate model output, the STREAP-CC will then include most of changes of future rainstorm profiles founds in climate models and in Chapter 6, including changes in wet/dry spell durations; changing frequency of intensity and spatial coverage; changing correlation and variability over space. The following sections will describe how the features are achieved in STREAP-CC.

7.2.1 Added Dependency of Temporal Memory Upon Scales

To improve the realism of the tool, STREAP-CC newly introduces a dependency of the ARMA coefficient upon the spatial scales. The ARMA (autoregressive moving average) process was used to represent the temporal evolution of the latent-Gaussian fields (in the Lagrangian system of coordinates), as with the model structure in STREAP (Section 3.3). In STREAP, parameters of the ARMA process were assumed to be constant across scales for the entire simulation period while in fact the low-frequency component (large-scale features, e.g., fronts) could be more correlated than the high-frequency component (small-scale features, e.g., convective cells) (Kundu and Bell, 2003; Paschalis et al., 2013). In this thesis, the AR(1) parameter ϕ_1 is set to depend on the wave number for the spatial

dimension $|k|$ ($|k| = \sqrt{k_x^2 + k_y^2}$ for the two-dimensional case, where x and y correspond to two dimensions in space), in which the dependency is newly introduced in this chapter. Here, an AR(1) process is used so as to reduce the uncertainty involved in the parameter estimation. Considering the computational burden required in calibrating the process, such a dependency is represented as a linear function (equation (7.1)) with only one parameter (slope a) needing to be calibrated. The calibration method is similar to the trial-and-error method used in optimizing the ARMA coefficients of STREAP (see details in section 3.3.2 iii). In the optimization, we are minimizing the difference between the simulated temporal correlation and the observed feature. The slope parameter a is a negative value which represents the decrease of ϕ_1 with an increasing wave number ($|k|$). Aside from this, the ϕ_1 is constrained to a value at least larger than 0.2, to prevent a negative value when the wave number is large enough

$$\phi_1(|k|) = a|k| + 1 \qquad (7.1)$$

There are also some other one-parameter based functions which potentially can be applied, for example, the half-normal function ($\exp(-|k|^2/a)$), which is similar to the dependent parameters used in one rainfall modelling study based on multi-fractals (Bowler et al., 2006, p. 2134). However, after the investigation (Appendix IV.2), the linear function is found to be sufficient to give a realistic autocorrelation at short-lags and is selected to be used in this thesis.

7.2.2 Downscaling Mode with Bias Correction

Another development made in this study is to introduce a climate change downscaling mode into the simulation tool, which also enables the bias correction at the same time. The downscaling mode is needed because the model parameters calibrated from a coarse-resolution data (i.e. CPM output) are suitable for generating rainfall fields at the same resolution but not automatically able to simulate finer-scale fields. In order to provide simulations at a finer resolution (5min, 1 km × 1 km) by using the stochastic tool and the information from CPMs (1 hour, 2.2 km × 2.2 km), a methodology to link this scale gap is needed.

To achieve it, the fine-resolution radar estimates are used to provide a reference to adjust model parameters for each period. A key assumption behind the adjustment is that how these parameters (or rainfall properties) change across different scales (in both space

and time) will remain the same in the current climate and future climate scenarios (Figure 7.2). Based on the assumption the scaling features of a few rainfall properties can be obtained from the long-term radar data and the scaling feature is then applied to derive parameters of STREAP-CC. Here, properties needing such an adjustment include (1) the probability distribution of areal statistics (areal mean intensity IMF and wet area ratio WAR); (2) the model parameter CV_{pos} governing the spatial variability of precipitation fields. In addition to this, misrepresented spell durations and parameters in the bivariate WAR-IMF process also have been adjusted, as summarized in Table 7.1. How each of these is achieved in STREAP-CC is described in what follows.

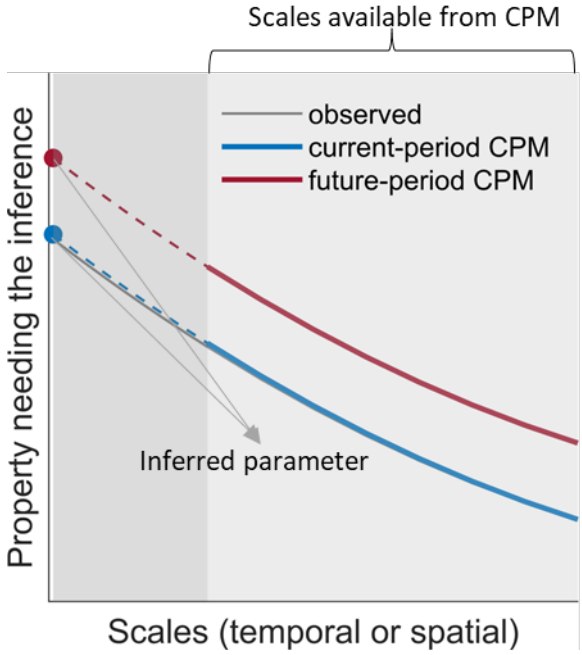


Figure 7.2 Schematic of parameter inference. The fitting curve is obtained from observation dataset and the curve is assumed to be valid for both the current-period CPM output and the future-period CPM output.

i. Downscale the probability distribution of areal statistics

As illustrated by the empirical CDFs (cumulative distribution function) of areal rainfall statistics at different scales, there is a pronounced difference between the hourly and the 5 min wet area ratio (Figure 7.3.b) while the difference of CDF curve in areal mean intensity (Figure 7.3.a) is less significant. The difference between the CDFs highlights the necessity to convert the wet area ratio computed from the hourly scale to the fitted probability distribution at a sub-hourly scale.

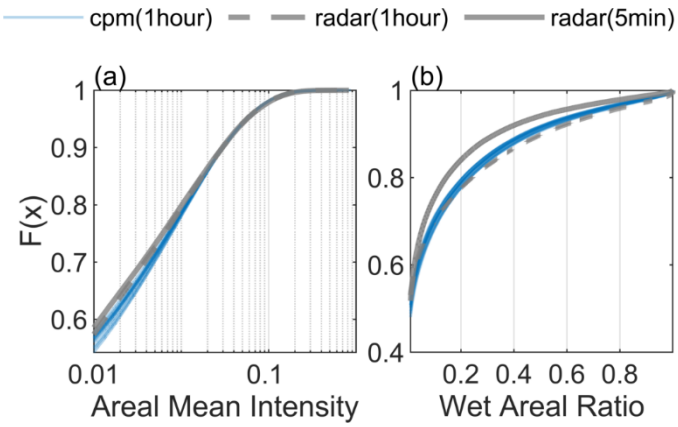


Figure 7.3 Comparisons of empirical cumulative distribution function (CDF) of rainfall statistics at different temporal scales (5 min and 1 hour) for the current period. (a) CDF of the areal mean intensity (mm/h), (b) CDF of the wet area ratio (-).

The conversion is applied to both the areal mean intensity series and wet area ratio series by using a trend-preserving quantile-mapping method for the climate period of interest (see method details in Appendix IV.1). In this method, a linear scaling approach for the long-term trend has also been added to preserve future changes projected by climate models (Met Office, 2019c). In STREAP-CC downscaling module, such a method is carried out for each calendar month separately, where samples from all ensemble members of climate model outputs are pooled together and samples corresponding to dry-spell periods (i.e., zero-rainfall or wet area ratio is smaller than 5%) are excluded in the conversion.

ii. Downscale the CV_{pos} governing the spatial variability of precipitation fields

CV_{pos} is initially obtained from climate model outputs and then further adjusted to a finer scale. Since generally both spatial and temporal scales need to be downscaled, the parameterization of CV_{pos} in STREAP-CC thereby includes three steps: first, investigate the scaling feature of CV_{pos} using radar estimates; then temporally downscale the CV_{pos} (estimate the sub-hourly CV_{pos} based on coarser-scale values), and finally spatially downscale the CV_{pos} (adjust the sub-hourly scale CV_{pos} from coarser spatial scale to get a desired spatial scale value).

In the investigation of CV_{pos} using radar estimates, how the CV_{pos} changes in spatial scales and temporal scales are analysed separately. Across temporal scales (D), a power law function ($CV_{pos} = a \times D^b$, where a and b are fitted parameters) is found to well represent changes in 2.2 km CV_{pos} on a monthly basis (Figure 7.4). This function curve is fitted by using the nonlinear least square method and is applied to the current and the future periods with parameters fitted separately. Then, the CV_{pos} at a 5 min aggregation

level (D = 1/12 hour) can be obtained based on fitted parameters for each period. Notably, here the radar estimates are only used in selecting the optimal fitting curve but not used in estimating parameters a and b for either the current period or future period. Parameters a and b are estimated based on CPM outputs. That is because the climate model used in this thesis has been found to produce slightly smoother spatial rainfall fields (Figure 5.7 in Section 5.3.3), particularly in short durations. The parameters estimated from radar estimates are thereby not suitable for a CPM-based curve. Nevertheless, the estimated CV_{pos} is still very close to the observed value at a 5-min level (Figure 7.4), implying the effectiveness of the selected function curve.

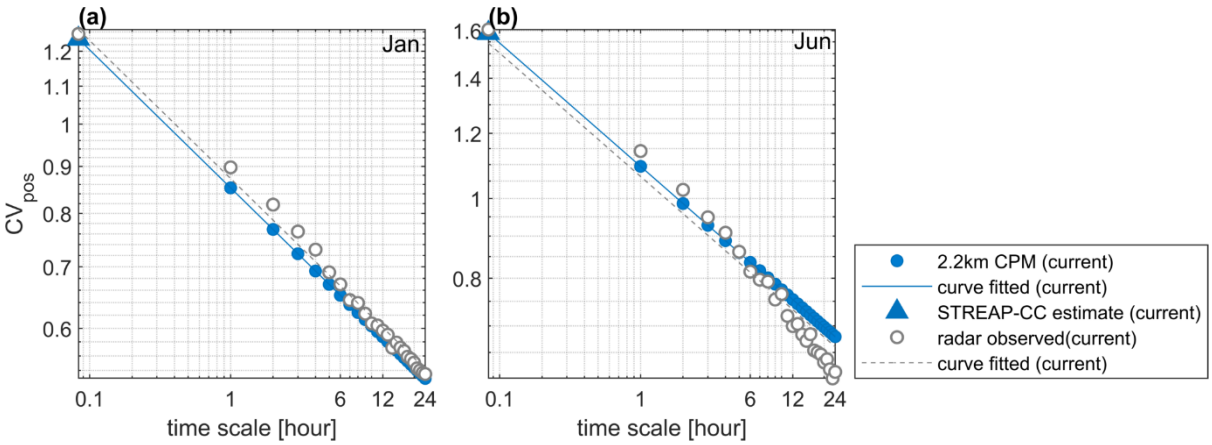


Figure 7.4 Comparisons of the estimated 5-min scale CV_{pos} computed from the current-period CPM and the observed 5-min scale CV_{pos} computed from radar measurement. Two subplots present the performance in two representative months respectively (January and June). All other months give a similar performance.

In terms of the CV_{pos} across spatial scales, a linear relationship with parameters constant over all calendar months is found to be sufficient to convert the CV_{pos} at a 2.2 km scale into the one at a 1 km scale (Figure 7.5). As mentioned, it is assumed that the linear relationship between these two spatial scales and the fitted parameters remains unchanged. The parameters are optimized by using observed data with the least-square regression model and are assumed to remain unchanged in the future period.

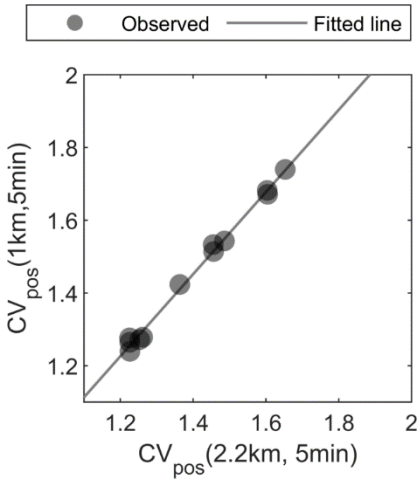


Figure 7.5 Linear relationship between the CV_{pos} at 2.2 km scale and the CV_{pos} at a 1km scale, obtained from radar measurement.

iii. Correct the probability distribution of wet or dry spells duration

Aside from obtaining model parameters required for finer-resolution stochastic rainfall generation, considering the misrepresented event spell durations (i.e., too many short duration events as shown in Figure 5.5), STREAP-CC also bias corrects the fitted probability distributions of both wet spell duration and dry spell duration. These two distributions are used in the storm arrival process stage of the model.

iv. Convert the Whittle Matérn process parameters

In addition to the above parameter inference, one parameter ($a = a_W = a_I = a_{WI}$) is analytically converted according to the equation (7.2) so as to make it suitable at a smaller time interval. The parameter a is used in the Whittle Matérn covariance function, which is the function used in representing the areal statistics bivariate process (Gneiting et al., 2010, equation 1). Similarly, in the optimization setting, the parameter constraint (the upper/lower limit of a_{W}, a_{I}, a_{WI}) and the maximum lag number for computing sample covariance (see section 3.3.2.ii) are also adjusted to preserve the consistency with the calibration settings as described in section 3.3.2.

$$a(dt_0) = a(dt_1)\frac{dt_1}{dt_0} \tag{7.2}$$

where $a(dt)$ represents the parameter at an interval of dt; dt_1 the temporal resolution of climate models (1 hour); dt_0 the desired temporal resolution of STREAP-CC output (5 min).

Besides the adjustments described above, all other processes in the STREAP-CC adopt CPM-based parameters for each period, with the only exception of the ARMA process,

which is used for representing the spatial-temporal evolution of the Gaussian-transformed precipitation field. The ARMA coefficient and the dependency function introduced in section 7.2.2 are all obtained from 5 min radar estimates instead of 1-hour climate model output. This is because an ARMA (or AR) process at a 5 min interval is not mathematically derivable from a process at a 1-hour interval. Therefore, parameters in the ARMA process are kept unchanged in the STREAP-CC.

Section 7.3 Study Area and Validation Method

The STREAP-CC tool is applied to the West Midlands of the UK, where a rectangular area having a size of 110 km × 110 km is selected. This area is selected because its observational radar data shows a good performance (Fairman et al., 2015). Meanwhile, for the data required in calibrating STREAP-CC, both radar estimates and climate model outputs in this subarea have been examined where these two datasets show an overall good consistency (Section 5.3). Following the model development described in Section 7.2, the STREAP-CC model is calibrated for this area.

To ensure the reliability of the simulation tool in impact studies, the validation of STREAP-CC includes two parts: for the current climate, generated rainfall from STREAP-CC is compared with radar observation; for the future climate, modelled changes from STREAP-CC are compared with changes projected by climate models being used. For each climate period, around 400-year-long spatial fields are generated for the validation so as to account for the stochastic variability in different realizations.

7.3.1 Validation of Control-period Rainfall

Validation of the control-period rainfall fields is achieved by quantitatively comparing generated fields by STREAP-CC (5 min, 1 km × 1 km scale) with the radar rainfall dataset. Although bias exists in climate model output, the generated fields can be directly compared to radar estimates for the current climate. This is because the STREAP-CC calibration is based on the pre-processed CPM output and properties corrected by radar information (Section 7.2.2), which enables the calibrated parameters to produce features largely consistent with observed features. Based on radar estimates, an independent validation is performed. A range of properties, different from those used for calibration, are also examined.

Similar to previous studies (Paschalis et al., 2013), rainfall properties examined here include (1) the probability distribution of areal statistics, as represented by the exceedance probability function of wet areal ratio (WAR) and areal mean intensity (IMF) of the study area; (2) the correlation of areal statistics (bivariate process), i.e., the cross-correlation (spatial correlation) and the auto-correlation (temporal correlation) of WAR and IMF; (3) the extreme analysis of IMF and (4) the probability distribution of point-scale rainfall intensity. All above statistics are computed at three temporal scales (10 min; 1 hour and 6 hours), in which 10 min is to examine how the downscaling mode behaves; 1 hour to examine how the correction on the hourly-scale CPM information performs and 6 hours to examine whether the event-scale property is well captured.

7.3.2 Assessment of Future Changes of Rainfall

Evaluation of the future-period synthetic fields is achieved by comparing future changes simulated by the STREAP-CC tool (aggregated to an hourly scale) with projected changes obtained from hourly scale climate models. Here the analysis focuses on assessing modelled changes instead of directly comparing any generated values with CPM modelled values. This is because the STREAP-CC output will have debiased most of the key features of CPM output, while the available future-period reference information which can be used in the comparison will be either raw CPM output (no bias correction) or pre-processed CPM output for calibrating STREAP-CC (only the hourly-scale intensity distribution debiased). Therefore, this part focuses on evaluating whether projected trends in key rainfall properties are well preserved by the STREAP-CC. The key properties analysed here include the spell durations which are used in the storm arrival process and the areal statistics which are used in the bivariate process. Temporal scales being analysed are 5 min and 1-hour.

Section 7.4 Results and Discussion

7.4.1 STREAP-CC Calibration Results

Calibrated parameters of STREAP-CC for the current period and the future period are listed in Appendix IV.3. In the parameterization of spatial variability, the power-law function is selected because it fits well the observational data (Figure 7.4). After applying this curve to CPM data, it is found that the power-law function also gives a good

representation in the future-period scaling feature of the spatial variability (CV_{pos}) (Figure 7.6). The goodness of fit (for the range between 1 hour and 24 hours) demonstrates the validity of the selected function.

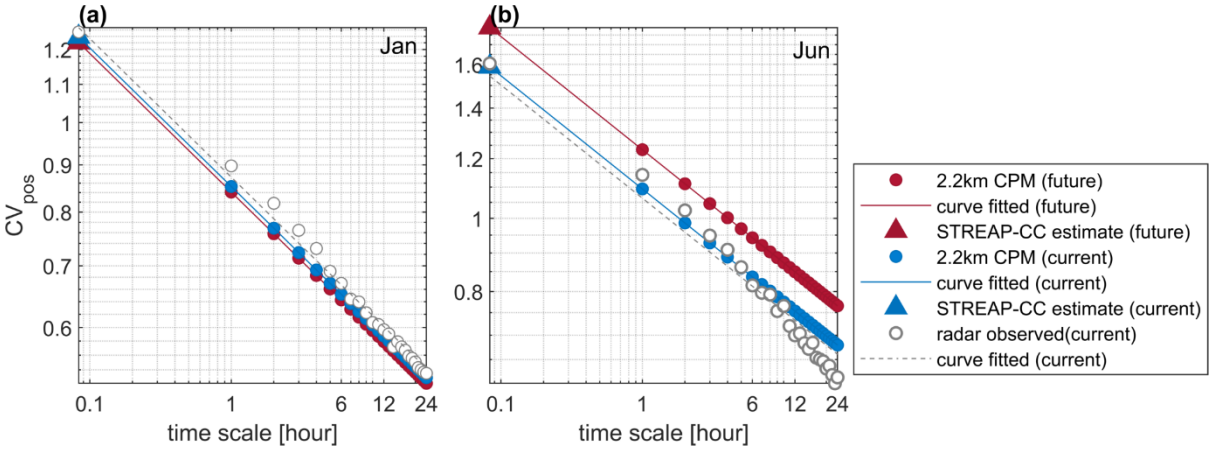


Figure 7.6 Scaling feature of CV_{pos} across different time scales (from 5min to 24 hours) obtained from radar observation and the STREAP-CC estimate of 5min-CV_{pos} for the current period and the future period at (a) January and (b) June. Each colour corresponds to different rainfall products (red colour: future-period 2.2km CPM; blue colour: current-period 2.2km CPM; black colour: radar observed). The spatial scale in this plot is kept being 2.2km for all products.

After the conversion in spatial and temporal scales, the coarse-scale spatial variability computed from climate model output will have been successfully converted into the value corresponding to a finer scale (Figure 7.7). Results show that the converted value shows good consistency with radar estimates at the same scale (5min, 1km). For the future period, the seasonal variation and the projected increase in spatial variability particularly in summer seasons are also well preserved in STREAP-CC.

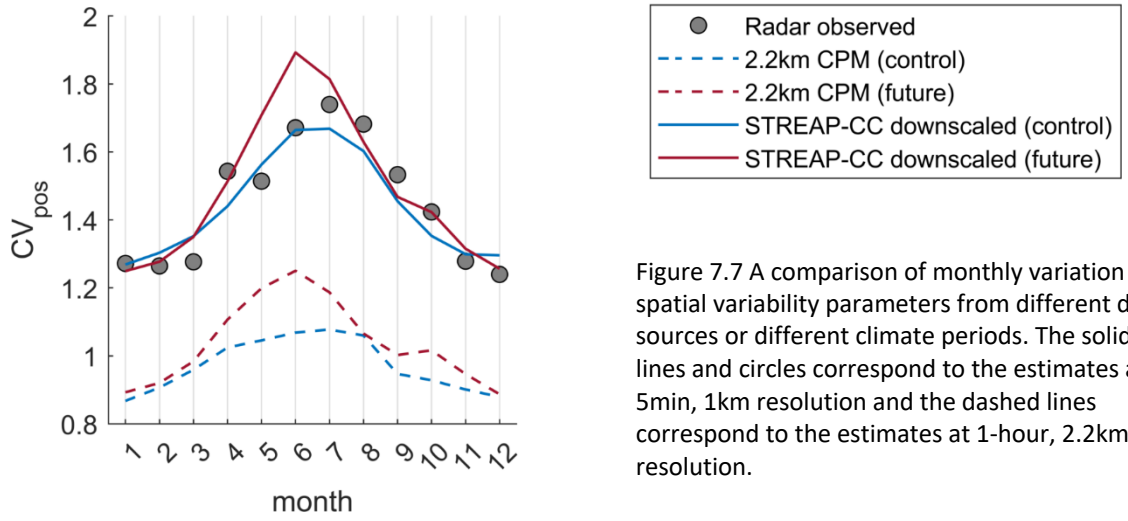


Figure 7.7 A comparison of monthly variation of spatial variability parameters from different data sources or different climate periods. The solid lines and circles correspond to the estimates at 5min, 1km resolution and the dashed lines correspond to the estimates at 1-hour, 2.2km resolution.

Based on the calibrated parameters of STREAP-CC with the adjustments (Appendix IV.3), rainfall fields can be generated for each specified period. Figure 7.8 gives a series of examples of generated rainfall fields over the study domain for the current climate. The visual inspection indicates that how the rainfall is spatially distributed appears to be similar to the rainfall fields estimated by radar. A clear storm advection also can be seen from the evolution of example snapshots. Note, although some storm evolution might partially happen outside the study domain, the evolution of the entire storms is still perceived to be well simulated because the domain size used in the STREAP-CC simulation (220 km × 220 km) is set to be much larger than the study domain of interest (110 km × 110 km).

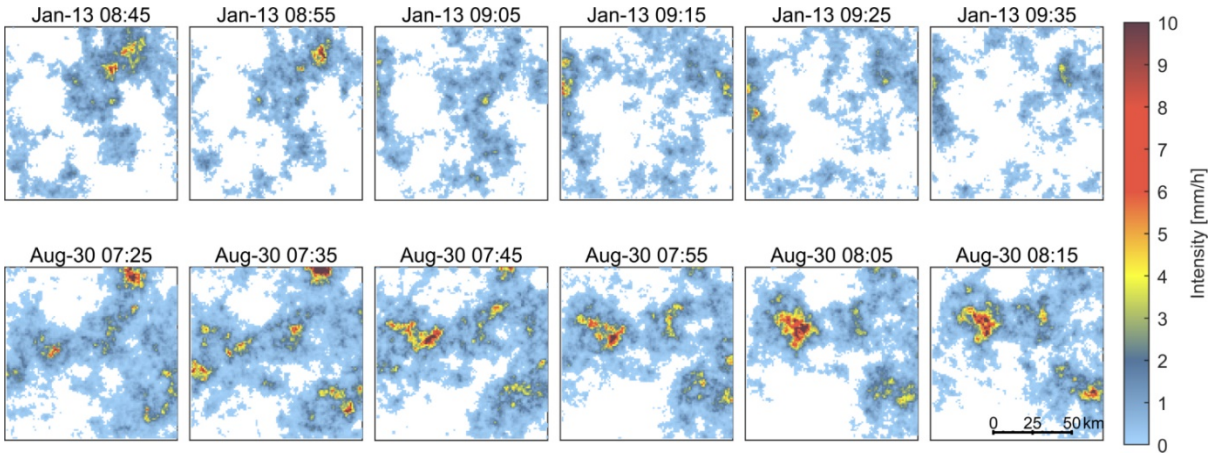


Figure 7.8 Examples of STREAP-CC generated rainfall fields with a scale bar attached in the bottom right panel. The snapshots are shown at an interval of 10 minutes.

7.4.2 Realism of the Synthetic Rainfall for the Current Climate

In this section, key statistics computed from 400-year-long synthetic rainfall fields corresponding to the current climate are compared with observed statistics computed from 12-year radar estimates. Note, the 400-year fields are stationary in terms of the represented climate period. Such a long period of data is generated so as to include the stochastic variability of synthetic rainfall.

i. Areal-scale key statistics

The distributions of areal statistics produced by STREAP-CC are shown in the exceedance probability functions (Figure 7.9). STREAP-CC well reproduces the distribution of 5min-scale area statistics because it is calibrated to do so. But the model also gives a good behaviour in capturing these distributions at aggregated scales (10-min, 1-hour and 6-hour). In the distribution of wet area ratio (Figure 7.9.a), the periods with a wet area ratio

smaller than 0.05 are not simulated at all because these periods are taken as dry periods and simulated as zero rainfall over the whole area in STREAP-CC. This threshold is set up to separate storms while a potentially negative effect is that very localized convective storms (total coverage smaller than 605 km^2) might be not included in the STREAP-CC generation. However, for the periods with the wet coverage higher than this threshold, results show that the CPM-based STREAP-CC reproduces the probability distributions of the wet area ratio and the areal mean intensity quite well. Both statistics show a very good match with the radar estimates at both the 10-min scale and 1-hour scales. Moving to a larger aggregation level (6 hours), the end tail of the areal mean intensity, corresponding to high-impact extreme events over the study area, is also reasonably reproduced by the STREAP-CC tool. This is very promising because the lower-scale probability distributions are used in the tool calibration, but the 6-h distribution is not used.

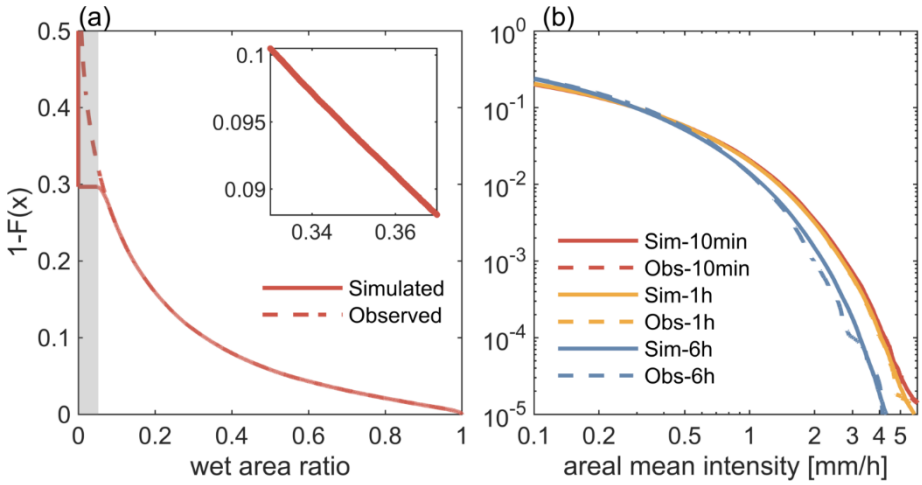


Figure 7.9 A comparison of the mean areal statistics computed from radar estimates (Obs) and the tool-simulated mean areal statistics (Sim). The radar data covers 12 years, and the STREAP-CC simulations represent the mean of 33 realizations of 12-year fields. The gray-shaded area shown in the panel (a) corresponds to the part below the WAR threshold (0.05) which was used for fitting WAR probability distribution.

The bivariate process of areal statistics is validated by examining the autocorrelation and cross-correlation functions at three representative aggregation levels (Figure 7.10). Although the correlation feature at sub-hourly scales is not included in calibrating the process and the parameters are fully based on climate models output with an analytical transformation, the autocorrelation and cross-correlation at a lag time shorter than 1-hour are still captured quite well, as shown in correlation curves at the 10-min

aggregation level. The feature highlights the reliability of directly using this information from climate models to a stochastic generator.

At a larger lag hour (>9 hours), simulated correlations are consistently larger than the radar estimates. This can be explained by the fact that (1) the CPM itself gives a correlation larger than the radar estimates at this lag time; (2) the observed feature is different from the parsimonious bivariate Whittle-Matérn model applied to represent the bivariate process (Gneiting et al., 2010, sec. 2.1). In detail, the bivariate model, also used in AWE-GEN-2D (Peleg et al., 2017b), assumes a common scale parameter (i.e., $a = a_W = a_I = a_{WI}$) and the inverse of the parameter represents the correlation length. However, for lag hours up to 9 hours (these are the lags used in finding optimal model parameters), the observed correlation length of wet area ratio is larger than the correlation length of areal mean intensity. The assumed common scale parameter a thereby leads to an intrinsic overestimation in the autocorrelation of areal mean intensity and an underestimation in the autocorrelation of wet area ratio. However, considering the fact that most events (>75% for the study area) last for less than 9 hours and the current correlations produced by the STREAP-CC have been good enough and comparable with the previous studies fully based on radar (Paschalis et al., 2013), the bivariate process remains unchanged in STREAP-CC to keep the parameter parsimony.

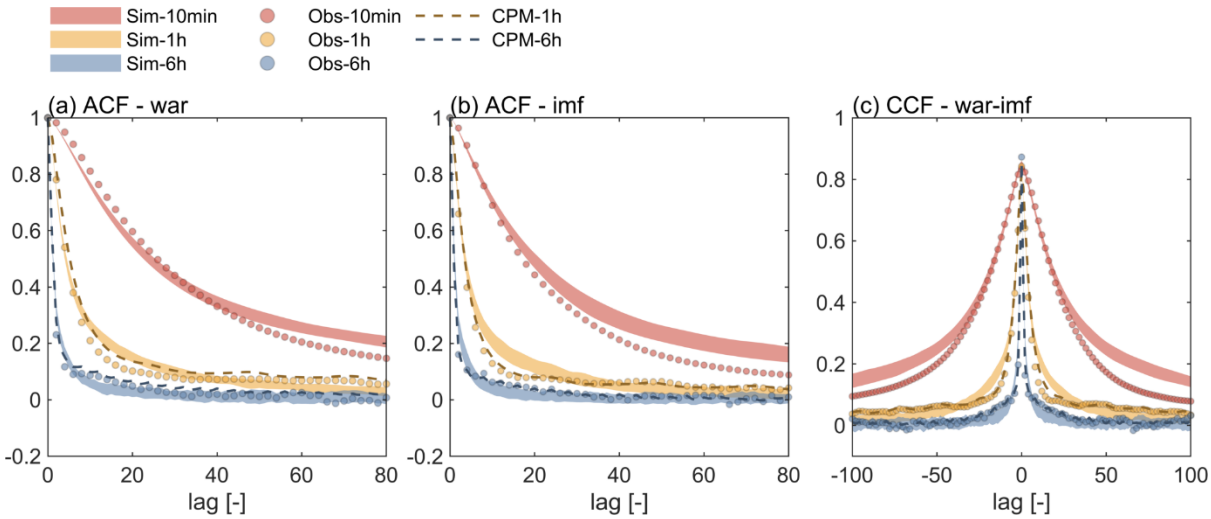


Figure 7.10 A comparison of correlation functions computed from the radar estimates (Obs), the STREAP-CC simulated (Sim) and the CPM ensemble (CPM). For the hourly-scale CPM data, 1h and 6h-scale correlations are plotted; For other two rainfall products, correlation curves at three aggregation levels (10min, 1h and 6h) are plotted. The three subplots represent (a) autocorrelation of WAR series; (b) autocorrelation of IMF series; and (c) cross-correlation between WAR series and IMF series. At each subplot and for each resolution, the shade area represents the simulation range between the upper and the lower 5th percentile of all realizations of STREAP-CC.

High-impact extreme events are also well captured by simulated fields of STREAP-CC, in particular at hourly and 6-hour scales (Figure 7.11). The behaviour indicates the strong ability of STREAP-CC to accurately reproduce the sub-daily scale (1-hour and 6-hour) precipitation fields, which can be directly used in extreme-events impact studies. Aside from this, Figure 7.11.b-c also show the effectiveness of the bias correction applied to the CPM output (Met Office, 2019c), the pre-processing required in the STREAP-CC calibration. In Figure 7.11.b, it can be seen that the overestimated extremes existing in convection-permitting models have been debiased to a large extent for return levels up to 20 years with an absolute error of less than 0.5 mm/h. The 6-hour bias-corrected CPM extremes also show a similarly good agreement with the radar estimates.

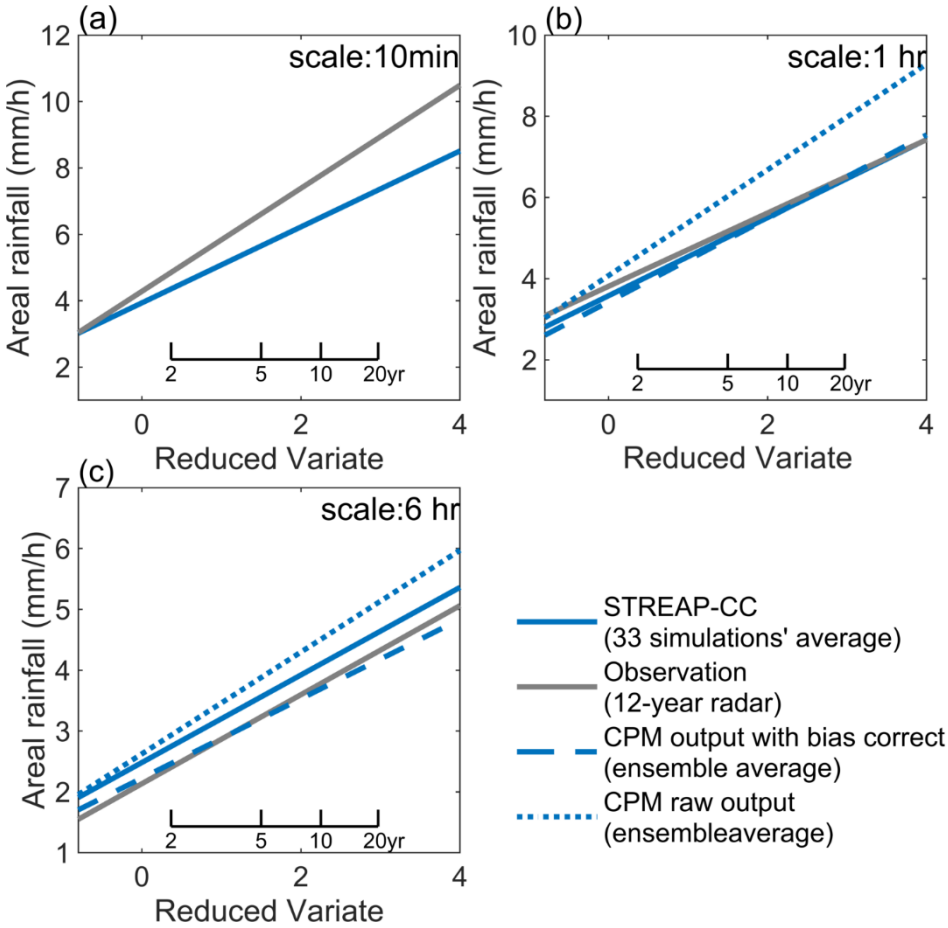


Figure 7.11 Extreme analysis of areal mean intensity produced by different rainfall products at (a) 10-min, (b) 1-hour and (c) 6-hour aggregation levels. Annual maxima are extracted and fitted to a Gumbel distribution with return periods calculated by the Gringorten formula. In STREAP-CC, around 400-year-long data are divided into 33 realizations which are fitted separately. In the bias corrected CPM output and the raw CPM output, data from each ensemble member are fitted separately. Then, for each rainfall product, the median value over realizations / ensemble members is plotted at each return level.

At a downscaled scale (10 min), generated fields from STREAP-CC seem to consistently underestimate extremes, by up to 20% at a 20-year return level (Figure 7.11.a). The

underestimation suggests the current STREAP-CC might still underestimate the temporal variability within the storm evolution, an interpretation which agrees with the overestimated autocorrelation shown in Figure 7.10.b. Another explanation of the underestimated extremes is the Copula parameters being used. The Copula parameters used for the current climate are computed from the 1-hour climate model output. There is no correction done for this correlation because the correlation is assumed to be consistent with the 5-min observed. However, Figure 7.12 shows that the correlation between μ_I (the mean value of single-event time series of gaussian transformed wet area ratio) and σ_I (the standard deviation of the series of the gaussian transformed areal mean intensity) (see details in Section 3.3.1.ii) fitted by the hourly CPM data is ~25% lower than the one fitted by the 5 min radar data. It means that in fields simulated by STREAP-CC, there is less likelihood than in the radar estimates that an event having a large areal mean intensity on average also has a large temporal variability of the areal mean intensity over time spans of the event. The inconsistency consequently leads to smaller extremes. This underestimation might be solved by updating the current copula matrix. However, considering the huge uncertainties behind the selection of a method to correct the 5×5 Copula matrix for both current climate and future climate and the model behaviour having been achieved in this chapter, this potential improvement is left for future work.

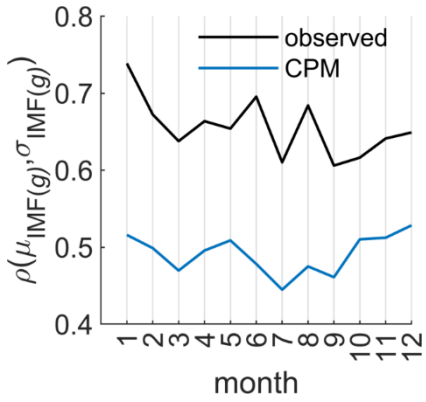


Figure 7.12 Comparison of the parameters governing the correlation between μ_I and σ_I fitted from the radar estimation (observed) and the CPM output.

ii. Point scale statistics

After examining the STREAP-CC behaviour on an areal scale (governed by the arrival process and bivariate process of areal statistics), this section focuses on examining how the 3rd stage of STREAP-CC (spatial-temporal evolution of precipitation fields) behaves in transforming the areal time series (IMF and WAR) into gridded spatial fields.

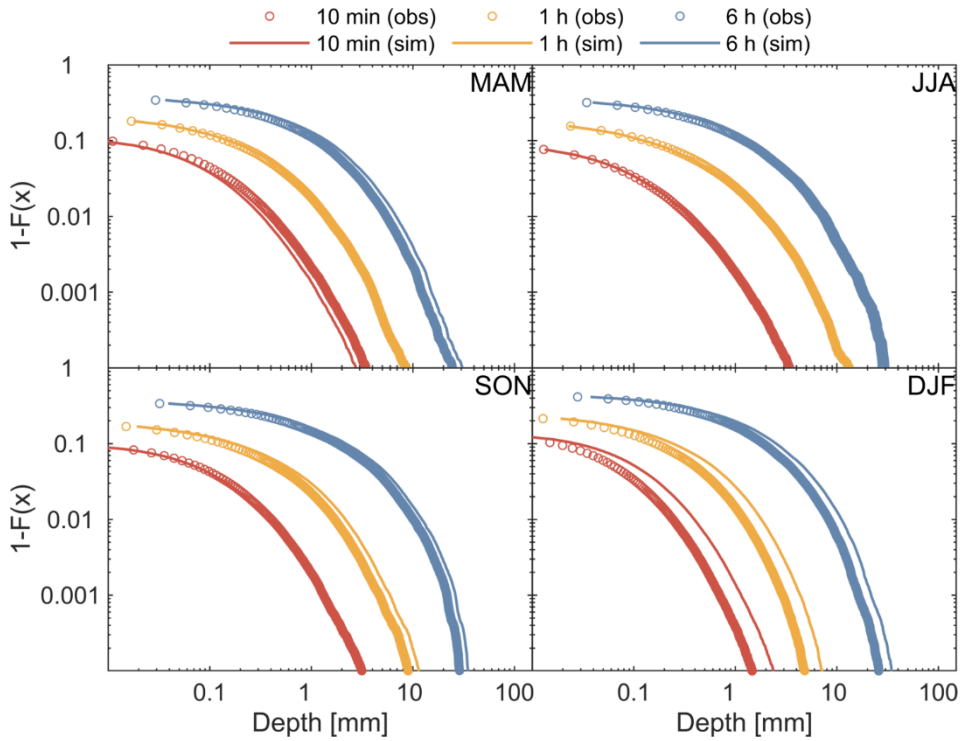


Figure 7.13 Exceedance probability of the precipitation depth at the point scale. Results show the averaged results for 50 randomly selected sites over the study area at three aggregation levels (10min, 1-hour, 6-hour) on a seasonal basis.

Figure 7.13 presents how the point-scale rainfall intensity is captured in STREAP-CC by being compared with grid measurement from radar. At all three scales (10 min, 1 hour and 6 hours), STREAP-CC developed in this chapter gives an exceedance probability function well capturing the radar estimates. Although the parameter CV_{pos} is purely computed from information from climate model output with a scaling, point-scale rainfall at sub-hourly scale is still well reproduced, which further proves that the proposed scaling method and the estimated parameters successfully transform generated Gaussian fields into precipitation fields in STREAP-CC. Nevertheless, an overestimation is found in winter, which can be explained by the slightly larger CV_{pos} obtained through the downscalling method as compared with the one computed from the radar estimates (see Figure 7.7).

The auto-correlation function shown in Figure 7.14 shows that STREAP-CC gives a much better realism of point-scale temporal correlations in all seasons, compared with previous studies in STREAP (Paschalis et al., 2013, fig. 11.a). The improvement benefits from the added dependency of temporal memory on spatial scales, which is able to assign a smaller correlation to small-scale features and a larger correlation to large-scale

features. Compared with previous studies (Paschalis et al., 2013), the overestimated correlation in most seasons has been significantly reduced.

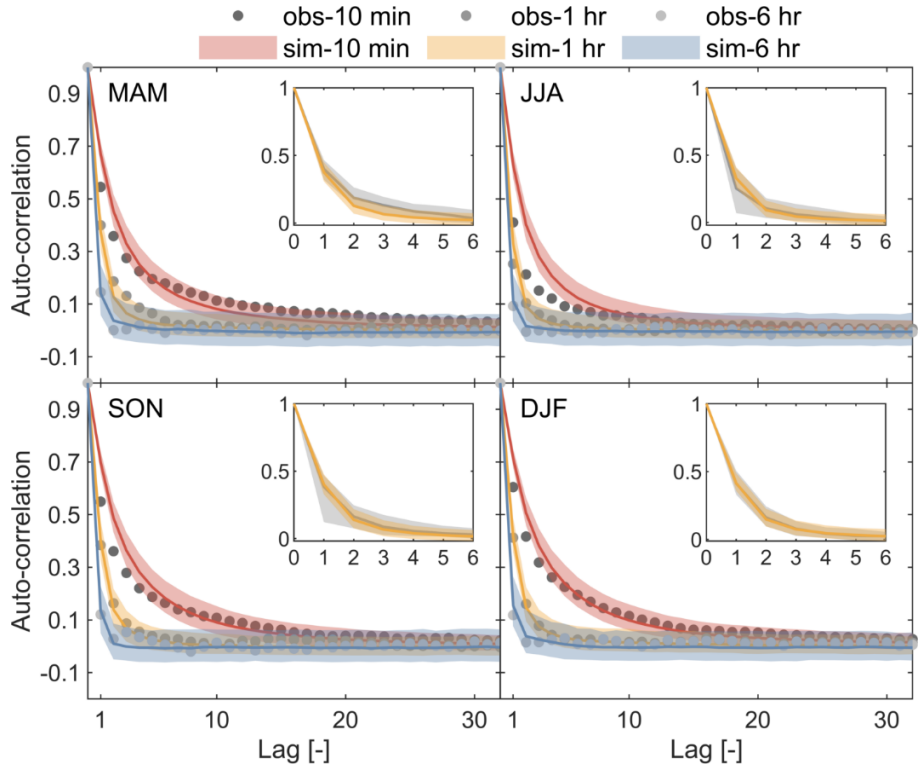


Figure 7.14 Auto-correlation function of the precipitation intensity at the point scale, analysed on a seasonal basis. Different colours represent aggregation levels of 10min, 1-hour and 6-hour respectively. The shaded area represents the range of STREAP-CC realizations with the medians shown as the solid line. The grey circles represent the radar estimates.

7.4.3 Consistency of the Synthetic Rainfall for the Future Climate

Besides validating the realism of STREAP-CC rainfall in the current climate, the realism in the future climate is also assessed so as to ensure its suitability to be directly used in climate impact studies. The assessment focuses on analysing whether the trend of changes projected by climate models is well preserved by STREAP-CC stochastic tool.

i. Changes in storm arrival process

Changes in the storm arrival process produced by STREAP-CC are compared with changes produced by the CPM output (Figure 7.15). It can be seen that both wet spell durations and dry spell durations are captured quite well by STREAP-CC in terms of future changes in their distributions. The duration distributions identified from the radar are also well preserved by the current-period STREAP-CC. Compared with the discrepancy between the CPM-produced information and the radar-estimated information, the realism of spell durations has been largely improved by using STREAP-CC tool.

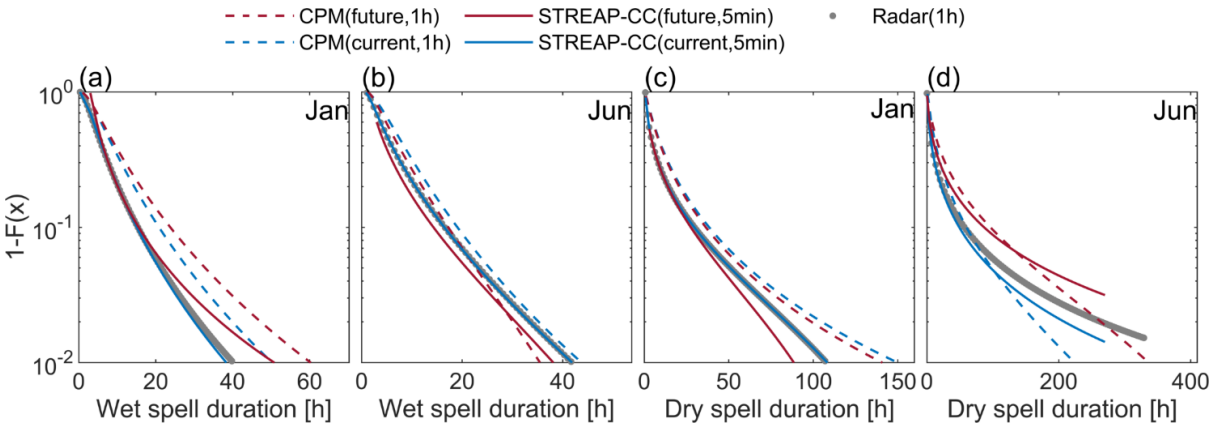


Figure 7.15 Exceedance probability of storm arrival process (wet spells and dry spells duration) in two representative months (January and June). Different colour represents different periods (current, future). Dashed lines correspond to results from the climate model (CPM) raw output; Solid lines correspond to results from STREAP-CC parameters.

ii. Changes in areal statistics

In the analysis of the wet area ratio (Figure 7.16.a-b), although current-period climate model output gives a slightly larger wet area ratio, generated fields from STREAP-CC have debiased the estimation error and are able to give a current-climate wet area ratio consistent with radar. Aside from this, the trend of future changes is well preserved in STREAP-CC for all calendar months (Figure 7.16.c-d). Similarly, the realism and the trend of changes in the areal mean intensity are also well preserved in all months. In particular, the areal extremes drastically overestimated by the raw CPM data are corrected by the STREAP-CC.

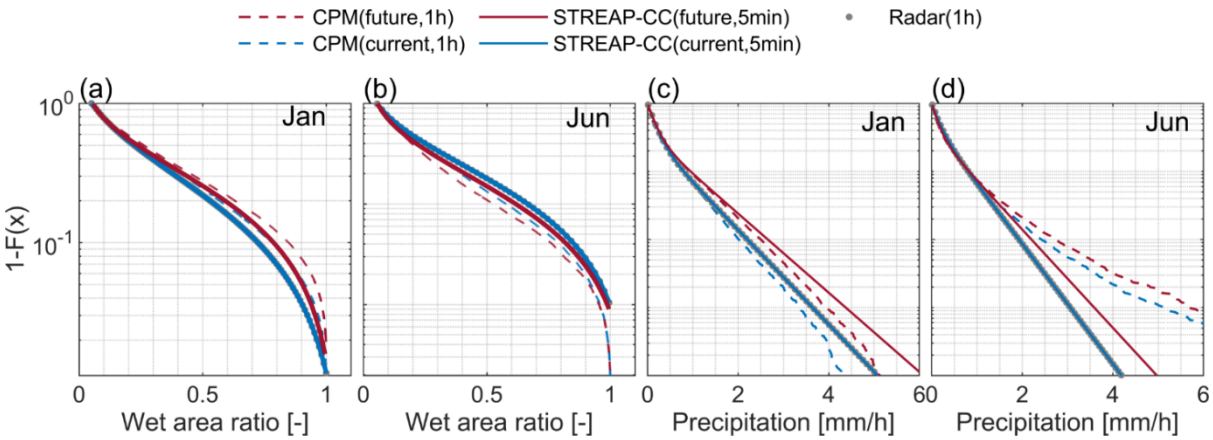


Figure 7.16 Exceedance probability of areal statistics (wet area ratios in panels a and b; areal mean intensity in panels c and d) at two representative months. Different colours represent different periods (current, future). Dashed lines correspond to results from climate model (CPM) raw output; Solid lines correspond to results from STREAP-CC.

Section 7.5 Conclusions

In summary, a fine-resolution stochastic tool STREAP-CC was developed in this chapter in order to aid climate impact studies needing high-resolution rainfall information. Based on the model structure of a well-established generator STREAP, a few more improvements also have been achieved in this chapter: (1) added a dependency function to improve the temporal autocorrelation of point rainfall; (2) calibrated the tool using climate model outputs and introduced a complete downscaling method to enable the generation of finer-scale precipitation fields, either for the current climate or future climate. (3) debiased the discrepancy between climate model output and the radar estimates in a wide range of key rainfall properties, some of which cannot be easily debiased by a statistical bias correction method.

Extensive validation is presented on the developed tool, and results show that the STREAP-CC tool is able to simulate rainfall fields largely consistent with features from observations for the current climate as well as consistent with changes projected by climate models for the future climate. The realism not only lies in the distribution of key properties (spell duration, areal statistics and point rainfall), but also in their correlation. Extreme events are also well reproduced by the tool. This tool enables users to include most changes having been found in climate models (changing wet/dry spell duration; changing frequency of intensity and spatial coverage; changing correlation and variability over space) and to output a fine-resolution rainfall.

Overall, precipitation fields produced by the STREAP-CC tool are suitable for climate impact studies in particular when spatial rainfall fields are preferred. The tool can directly provide reliable and sub-hourly rainfall information for future climate (e.g., urban drainage design needs), which is not always available in most climate models. Aside from its appealing feature in fine-scale impact studies, the tool also has advantages at an hourly scale because of the more realistic rainfall fields compared with the simple statistical bias correction method.

Chapter 8 Separating the Factors of Rainfall Changes Contributing to Changing Future Urban Flood Risk

This chapter focuses on answering the last research question of the thesis, namely, which aspect of changes in rainfall properties contributes more to the estimated future urban flood risk. To do it a stochastic simulation tool developed for current and future climates and a reduced-complexity urban hydraulic model are used for the investigation. Section 8.1 gives an introduction to current approaches and simplifications in urban hydrological impact studies of climate change. Section 8.2 describes the study catchment, the urban drainage model as well as the numerical experiment designed to achieve the quantification of the impact. Since the same rainfall model is used as in chapter 7 no more details of rainfall model are repeated in this chapter. Section 8.3 presents the urban drainage modelling results as well as the indicated sewer flood risk under different rainfall input settings, followed by a partitioned impact of the simplifications made in design methods on accurately representing future urban flood risk. Finally, section 8.4 gives a summary and concludes the achievement and limitations of this study.

Section 8.1 Introduction

In the past few decades, the further development of sewer systems has helped to facilitate urbanization and to reduce the vulnerability of cities in general. However, sewer systems are particularly vulnerable to rainfall extreme events because they lack the ability to deal with the incoming water when it exceeds the design criteria. Under the future climate, there is strong evidence that the risk of sewer flooding could further increase (Allen et al., 2018; Met Office, 2019b).

There have been some hydrological impact studies of climate change at an urban catchment scale (Mishra et al., 2012; Vemula et al., 2019; Willems et al., 2012) but these studies require high-resolution information for the future climate scenario, that is short-duration precipitation extremes (sub-hourly or at least sub-daily) on small spatial scales (usually less than 500 km^2). The climate models' output is still too coarse in space and time and not accurate enough to be used for describing precipitation extremes at a small scale. Therefore, downscaling and bias-correction methods, such as by using stochastic generators, are commonly needed in practice for the impact assessment of rainfall extremes on an urban catchment.

In the urban hydrological impact assessment, analysis of short-duration extreme rainfall statistics is required for the time period of interest, which is typically obtained from climate models. Then a downscaling (and bias correction) tool is used to produce the rainfall series for the historical period as well as the rainfall series under a certain climate change scenario. Using these two series as input of an urban drainage model, the climate change impact is then analysed by comparing two sets of corresponding urban drainage model outputs (Willems et al., 2012, fig. 2).

However, in practical applications, there are a few simplifications adopted in the above method. First, the sewer modelling is achieved on an event basis due to the computational burden related to the hydraulic of the whole sewer networks. In this event-based simulation, it is assumed that the rainfall input at a certain return period will transform into a catchment flood response at the same return level whereas the event-based simulation does not well account for the potential of compound flood hazards caused by multiple contiguous-but-less-extreme events. Secondly, the input form of rainfall typically has a blanket shape (i.e., uniform) in space in real design applications. Although the impact of spatial resolution on urban systems has been highlighted such as in one extensive analysis covering a few catchments over the Europe (Ochoa-Rodriguez et al., 2015), those studies are normally for the current climate. The impact of simplifying rainfall spatial structure to a blanket shape for the future climate has not been well investigated in literature. Thirdly, the projected changes in rainfall characteristics are always at a coarse resolution and detailed changes are therefore not fully included through using downscaling tools. For example, in the statistical downscaling method based on stochastic rainfall generators (Burton et al., 2010a; Camici et al., 2014; Peleg et

al., 2017a; Sørup et al., 2016), the generator parameters are obtained from analysis of climate model simulations. Restricted by the resolution of most climate models, the changing small-scale spatial structure reported in this thesis (see Chapter 6) is often not included in a downscaling tool because the small-scale spatial structure was always assumed unchanged in the future climate in setting up the tool.

Although the above simplifications on the urban drainage design method could potentially lead to less accurate results in supporting the design work, updating the current design process to a more complicated one requires a significant amount of effort for each of simplifications mentioned above. To help designers and water planners understand the importance of climate impact as well as impact of each simplification widely made on estimated system response so as to aid the updating of drainage systems for the future, a research question this chapter aims to answer is what aspect of rainfall properties in urban drainage design would be non-negligible for the future flood risk.

To answer this question, an urban catchment located in the south-east of the UK is taken as a study area. A newly updated stochastic simulation tool (Paschalis et al., 2013) further developed in Chapter 7 is used to downscale climate model output into rainfall products at a desired period and desired resolution. A semi-distributed sewer model is used to quantify the urban catchment response. Under a hundreds-year-long continuous simulation for each specified rainfall input, impact of following aspects of rainfall features are investigated, including the adoption of blanket rainfall, the neglecting of changing spatial structure of future rainfall and the neglecting of other changing characteristics under a future scenario. The impact of each is analysed and the impact of each simplification contributing to the total bias of the baseline setting (which is to keep all simplifications unchanged) is partitioned.

Section 8.2 Data and Methods

8.2.1 Representative Urban Catchment Geometry

An urban catchment located in the south-east of the UK is taken as a representative catchment for this study. The catchment covers the urban area of Norwich city, having a size of 98.5 km^2, which is ideal for this study because its scale is large enough to demonstrate the impact of spatially varying rainfall storms on the urban drainage system.

The chosen urban area has been under threat of flooding over recent years in particular in summer seasons (Mark Ogden, 2019). Significant impacts have been seen on the sewer network. Parts of the sewer system became overloaded and led to increased customer demand being placed across the region.

The sewer drainage network of the catchment can be taken as a representative hydraulic network, including combined, foul and storm systems. The network consists of 28891 hydraulic nodes (such as manholes) and 29470 conduits (or pipes, river links), the layout of which is shown in Figure 8.1. Considering the computational burden required to achieve a continuous simulation several hundred years long for such a large urban catchment, the drainage network is used as a basis in the hydraulic modelling and its complexity has been reduced based upon graph partitioning, as described in the next section (section 8.2.2).

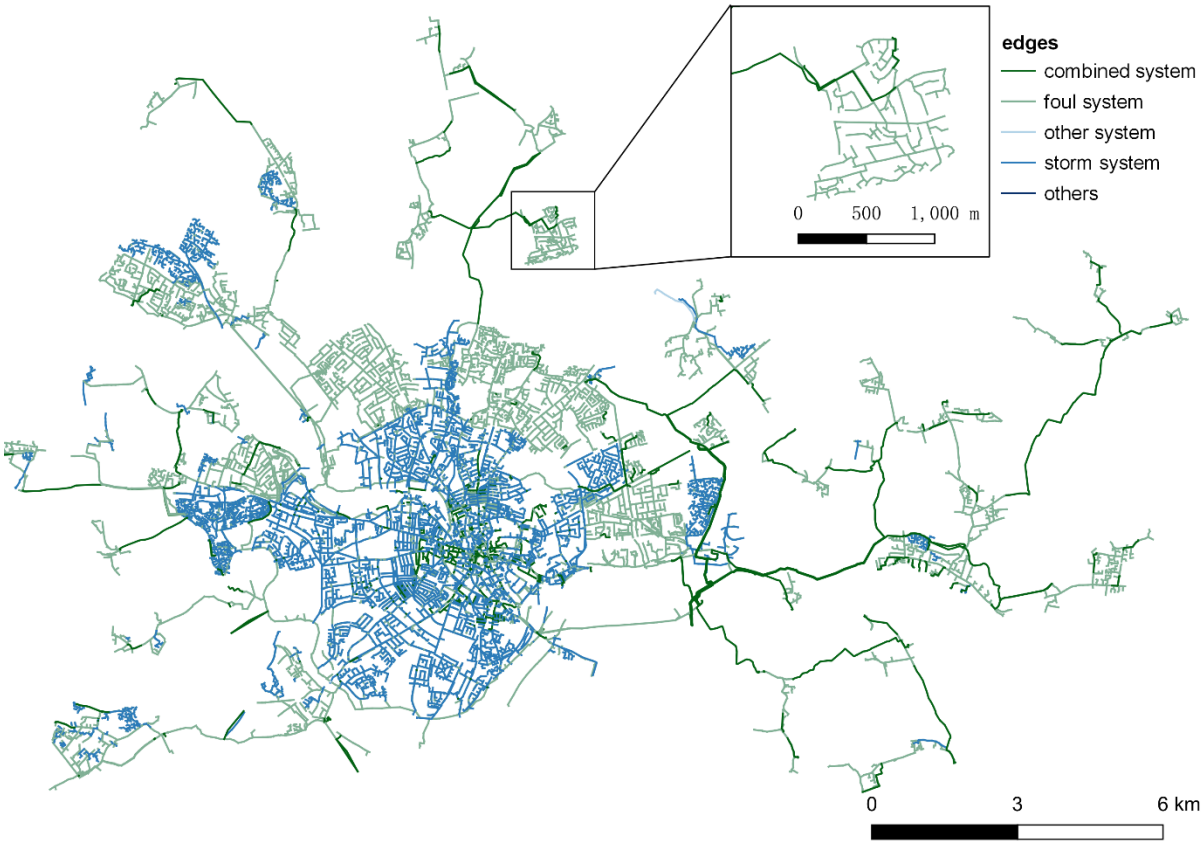


Figure 8.1 Hydraulic network of the Norwich catchment with a zoom-in panel showing the details of the hydraulic system.

8.2.2 Urban Hydraulic Modelling

A complexity-reduced sewer network model, CityWat-SemiDistributed (CWSD) (Dobson et al., 2022), is used in simulating hydrodynamics of the sewer network system. With the

flexibility to change how specific subsystems are represented, CWSD is able to facilitate simulations with a computational efficiency and complexity which suits the needs of end users. Compared with high-fidelity models existing for sewer network simulations such as InfoWorks ICM, SWMM or MIKE URBAN, the CWSD model used here can be much less expensive to set up and less computationally demanding.

In the CWSD model, a drainage network is conceptualized as a node- and arc-based system, as used in graph theory. Unlike the meaning of nodes in the original hydraulic network (Figure 8.1), the CWSD nodes can represent various elements of the water system (e.g., water treatment plants, aggregations of pipe network), each of which can be taken as a 'compartment' (sub-network) of the semi-distributed sewer network. The CWSD arcs represent paths passing the flow information between these nodes, conceptually identical to specific pipes, weirs or rivers in the high-fidelity model crossing borders between compartments. In the model used in this chapter, a range of functionalities has been enabled for the finer resolutions required for sewer network simulation including pipe travels times, variable timestep size, simplified hydraulics and time-area runoff calculations. More details about the network parameters can be found in the model development study by Dobson (2022, p. 6).

The reduced complexity modelling is performed by the graph partitioning method, which enables the model to automatically allocate sets of hydraulic nodes to sub-groups and then produce a directed graph with a smaller number of edges and nodes but having a similar connectivity as the original network. In this study, the partitioning is achieved by using an optimized Louvain parameters with spectral bisection method. This is a combined algorithm which improves the efficiency of the partitioning and the modularity score for each 'compartment' is maximized (Karypis and Kumar, 1997). At the Norwich catchment, the sewer network consisting of 28891 hydraulic nodes and 29470 edges is then reduced to the one consisting of 439 CWSD compartment nodes and 446 CWSD edges for this study. In all presented results of this study, 'nodes' being analysed always refer to compartment nodes of the complexity-reduced network. Driven by the rainfall input, the sewer model output will be a set of time series of a few key properties including flows at each edge (pipe) and storages at each node.

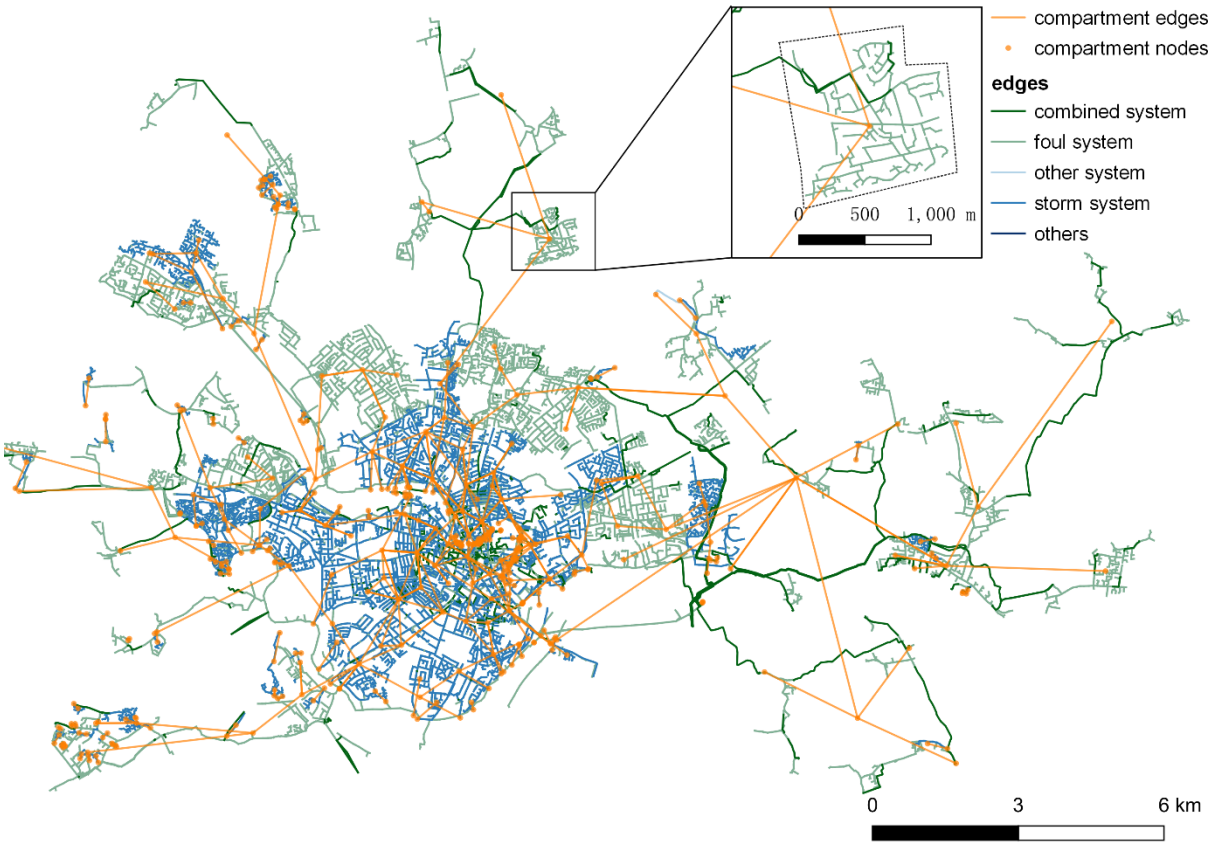


Figure 8.2 The complexity-reduced network with a zoom-in panel showing the detail of one 'compartment'.

In the sewer system modelling, rainfall is inputted as time series, representing the spatial-averaged rainfall amount flowing into the system. This time series can be either the same or varying for all partitioned compartment nodes. For this study, the rainfall input is obtained by spatial-aggregating gridded rainfall fields generated by the STREAP-CC simulation tool, parameterized for each given climate scenario and each simulated period. The spatial aggregation preserves the areal rainfall amount at each time step (5 min). In the case of spatial-varying rainfall input, for each compartment node the spatial aggregation is achieved by locating and averaging the rainfall fields over the polygon area covering all hydraulic nodes (as well as their surface area) belonging to the compartment. In the case of blanket rainfall input, the time series will be the areal-averaged time series for the whole urban catchment, keeping the same for all compartments nodes. Although the flood depth cannot be directly obtained from the complexity-reduced sewer network simulation results, it has been found in the previous study (Dobson et al., 2022) that there is a strong linear relationship between the peak value of the compartment storage and the flooded volume. Here, the annual maxima of compartment storage are therefore used to indicate the flooded volume of each compartment node.

8.2.3 Experiment Setting Up

A numerical experiment is designed to analyse the impact of future rainfall changes on the urban drainage system. The analysis is achieved by five combinations of model settings, each of which is fed into the sewer system separately and then the water dynamics resulting from each different rainfall input are analysed and compared. For each experiment ID, the rainfall input corresponds to a 400-year-long product. The product is firstly synthetised by the STREAP-CC tool with different parameter settings and then processed to have different rainfall input resolution (blanket or spatial-varying) so as to feed into the sewer system model (Table 8.1). The long-term continuous simulation is carried out to account for the stochastic variability of simulation results.

Table 8.1 Summary of all combinations of rainfall model settings and the input data resolution in the hydraulic model

ID	*STREAP-CC model setting*		*Rainfall input resolution in CWSD modelling*		*Simulation length*
	Modelled Period	*Spatial Variability consistent with the modelled period?*	*Spatial resolution*	*Temporal resolution*	
1 (baseline)	Current	Y	Blanket	5min	400-year-long continuous simulation
2	Current	Y	Spatially varying	5min	
3	Future	Y	Blanket	5min	
4	Future	Y	Spatially varying	5min	
5	Future	N	Spatially varying	5min	

In the STREAP-CC tool setting of the experiments 1-4, tool parameters are kept consistent with the modelled period as projected by the climate models (2.2 km CPM) and measured by the rainfall observation (weather radar). The parameters used here are the same as in Chapter 7 (see a full list of parameters in Appendix IV.3), with an extensive validation conducted already in the last chapter. Although experiments 1 and 2 are based on the same set of STREAP-CC synthetic rainfall, the rainfall is processed into different resolution (blanket or spatial-varying) to represent two typical ways of how rainfall is being treated as hydraulic input. Similar processes are done in experiments 3 and 4 to represent the future scenario in which most changes in rainfall properties (i.e. intensifying extremes, changing spell durations, changing spatial extent) have been well included in generated rainfall fields. In terms of setting up the experiment 5, the STREAP-CC parameters governing the spatial structure (CV_{pos}, see details in Section 3.3) are assumed to be the same as the current period, while all other parameters correspond to the future climate scenario. This experiment represents the case that most aspects of rainfall changes in the future scenario have been taken into account except for the

changing spatial structure, which can be easily neglected if any coarser-scale climate models are used as a downscaling basis.

Note, all STREAP-CC parameter sets used here are calibrated for the West Midlands of the UK, in which the STREAP-CC results have been well validated (see Chapter 7). The parameters are kept the same for the investigation of this chapter although the hydraulic network modelling is based on the Norwich catchment (located in the southeast of the UK). The STREAP-CC tool is not re-calibrated for the Norwich catchment because the radar measurements in the Midlands area are of better quality and the drainage network in the south-east area is only used as a representative template. This choice will not affect the conclusion of this study because the projected changes in these two areas are similar (Chen et al., 2021; Met Office Hadley Centre, 2019; Chapter 6) and the study focuses on investigating the summarized impact of those changes on large-sized drainage networks instead of on any specific city or any specific node.

Table 8.2 Illustration of how the designed experiments are used to partition each of selected rainfall characteristics

Experiment IDs used in comparison	*The key characteristics being partitioned*
1, 2	Impact of blanket rainfall (current climate)
3, 4	Impact of blanket rainfall (future climate)
1, 3	Simulated impact of climate change (when blanket rainfall input is used)
2, 4	Simulated impact of climate change (when spatial rainfall input is used)
4, 5	Impact of the changing spatial structure
2, 5	Impact of other changing aspects

By comparing simulated sewer network results from different experiments, the importance of different aspects of rainfall properties under the climate change can be partitioned and assessed. As shown in the Table 8.2, the modelled differences between experiments 1 and 2 represent the impact of simplifying rainfall input as the blanket form on an urban drainage network simulation. Comparing the experiment 3 with the experiment 4 will reveal the impact of a same aspect but for the future climate scenario. The difference between experiments 4 and 5 represents the impact of the changing spatial variability and the difference between the experiment 5 and experiment 2 represents the impact of other changing properties (spell duration, probability distribution of catchment rainfall, etc.) in the future climate scenario.

8.2.4 Statistical Evaluation

Evaluation of the urban drainage system dynamics focuses on the impact of each experiment setting on the resulting sewer flood. Because of the strong linear relationship between the peak value of the compartment storage and the flooded volume shown in the previous study (Dobson et al., 2022), the annual maximum compartment storage simulated by the sewer model is used for quantitatively implying the potential flooding risk, under an assumption that the linear relationship remains unchanged in all climate scenarios. Correspondingly, the difference between the two experiments in terms of the indicated flood risk is quantified by the relative difference of the year-averaged annual-maximum compartment storage simulated under each experiment setting and this difference is calculated for each compartment node separately.

After analysing the impact of rainfall properties separately (sections 8.3.1 and 8.3.2), in order to partition and analyse which simplification matters the most, the contribution of simplifications to the total bias of flood response is quantified in the following way: for each compartment node i, the relative difference between results under the baseline setting $S_i(exp1)$ and the completely future-climate setting $S_i(exp4)$ is computed in equation (8.1) and then taken as the total bias. A negative value of the total bias means an underestimated risk when the baseline setting is kept used and vice versa. Then, for each node i, the computed bias is partitioned into three parts, which are the contribution percentage from the blanket rainfall input (equation (8.2)); the percentage from the unchanged spatial variability (equation (8.3)) and the percentage from other ignored rainfall changes due to climate change (equation (8.4)). Similarly, a negative ratio corresponds to an underestimation of the risk under using this simplification, a positive value corresponds to an overestimation. In addition, how the total bias will change against the physical characteristics (the surface area directly draining into this node; the storage capacity of the node) is also assessed.

$$\Delta_i(total\ bias) = \frac{S_i(exp1) - S_i(exp4)}{S_i(exp4)} \tag{8.1}$$

$$\Delta_i(blanket\ rainfall) = \frac{S_i(exp1) - S_i(exp2)}{S_i(exp1) - S_i(exp4)} \tag{8.2}$$

$$\Delta_i(unchanged\ spatial\ variabilty) = \frac{S_i(exp5) - S_i(exp4)}{S_i(exp1) - S_i(exp4)} \quad (8.3)$$

$$\Delta_i(unchanged\ other\ climate\ signals) = \frac{S_i(exp2) - S_i(exp5)}{S_i(exp1) - S_i(exp4)} \quad (8.4)$$

To understand whether using the blanket rainfall input for climate impact studies will misrepresent future changes in the urban flood severity, the climate change impacts on urban sewer flood severity are quantified by comparing the modelled results from two types of rainfall input format. Simulated climate change signal with the blanket rainfall input is calculated as $\frac{S_i(exp3)-S_i(exp1)}{S_i(exp1)}$ and the change signal with the spatial varying rainfall input is calculated as $\frac{S_i(exp4)-S_i(exp2)}{S_i(exp2)}$.

Not only the contribution of each simplification to the bias of averaged sewer flood risk but also the contribution of each to the biased annual variability of the estimated risk is analysed. In this analysis, the annual variability is represented as the coefficient of the variation (CV) of the annual maximum compartment storage volume. For the modelled results of each experiment, the CV is calculated for each node. After getting the CVs for all experiments, the relative bias of the CVs is obtained for each assumed simplification, similar to the partitioning processes described above. Results from all nodes are then grouped by their surface drainage areas and the node-averaged relative bias is displayed for each group.

In all analysis of this chapter, results from compartment nodes including an outfall pipe to any water body (i.e., combined sewer outflows) have been excluded because the increasing storage in a combined sewer outfall does not directly link to a sewer flooding.

Section 8.3 Results and Discussion

In this section, the impact of using blanket rainfall and the impact of unchanged rainfall spatial variability on the estimated urban drainage network response are analysed in sections 8.3.1 and 8.3.2 respectively. Then those two key factors as well as other changing rainfall properties due to climate change are compared and the contribution of each to the total estimation bias is quantified in section 8.3.3.

8.3.1 Impact of Using Blanket Rainfall on Estimated Flood Risk

The impact of simplifying rainfall input into blanket-like fields on the estimated flood risk is analysed by comparing the simulation results of experiments 1 to 4. The impact of rainfall input format on the indicated sewer flood risk was investigated for the current and the future periods respectively. Results show that using the blanket rainfall as input to drive the sewer modelling will lead to a lower magnitude of sewer flooded amount as indicated by the annual maximum compartment storage volume of each node. The lowering peak volume is consistent throughout all nodes (Figure 8.4.a-b). The underestimation also can be indicated by the lower flow peaks received by the sewer network, as shown in the simulated time series of pipe flow for several selected pipes located downstream (Figure 8.3).

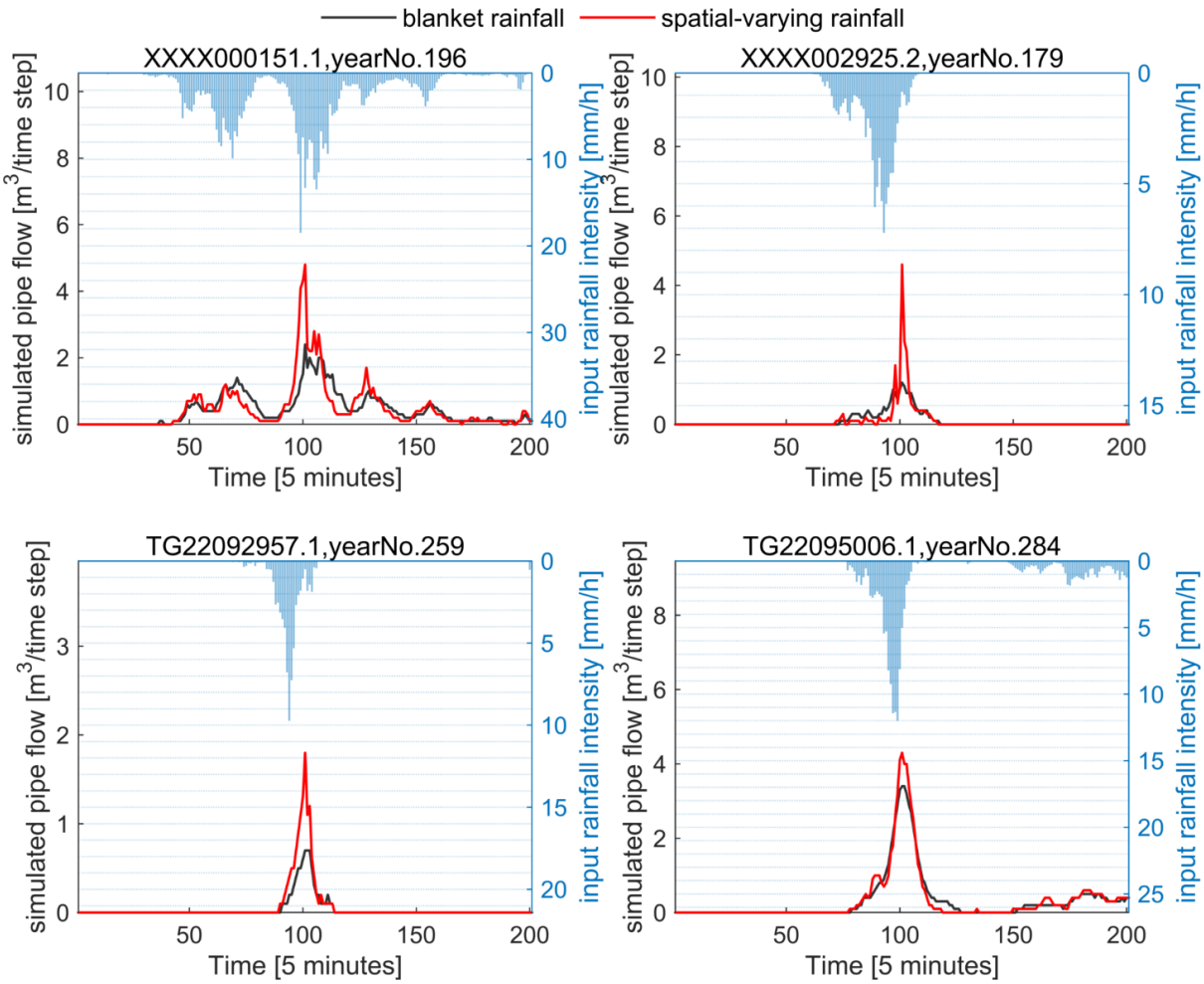


Figure 8.3 Comparisons of simulated pipe flow in several pipes. Each subplot corresponds to the time series containing the seasonal peak flow of the pipe within the simulation year. The pipe id is indicated in the subtitle, the simulation year is randomly selected for this visualization in each subplot. As indicated in the legend, the black solid line corresponds to the simulation pipe flow in experiment 1 and the red solid line corresponds to the simulated flow in experiment 2. The blue-colour bar plot corresponds to the series of 5-min rainfall intensities coming into the urban catchment.

Such an underestimation caused by blanket rainfall input holds for both current and future climate periods but to a different extent. For the current period, the annual maximum storage volume (averaged by all simulation years) could be underestimated by 42% on average. For the future climate scenario, using blanket rainfall leads to a somewhat less significant underestimation but it is still 37% lower than the case when a spatial-varying rainfall is used. The magnitude of the relative bias is not significantly dependent on either the surface area or the storage capacity of the compartment node, as indicated by Kendall correlations of -0.27 and -0.097 respectively. In the engineering design of a sewer system, the blanket design storms are commonly used to be fed into a hydraulic model. The comparison results shown here imply that the most common design method is very likely to place the drainage system at the risk of sewer floodings happening more frequently than the designed return periods. Aside from the magnitude, the variability of the storage peak volume, as represented by the difference between the highest annual peak and the lowest annual peak, is also found to be always smaller if the rainfall input is taken as a blanket shape (Figure 8.4.c), for both periods.

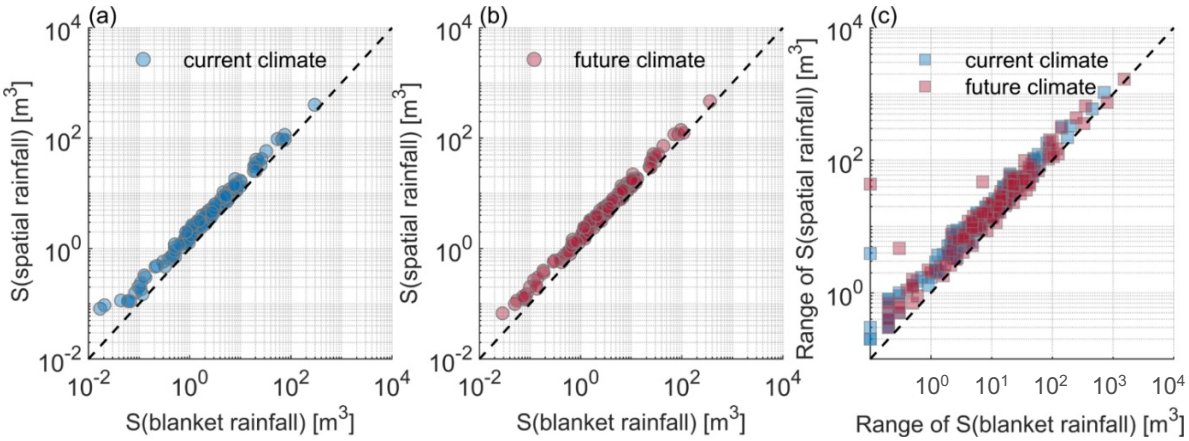


Figure 8.4 Comparisons of annual maximum storage volume simulated from the blanket rainfall and the one from the spatial-varying rainfall input. (a) scatter plot of the average annual maximum storage (S) for the current climate; (b) scatter plot of the average annual maximum storage for the future climate; (c) scatter plot of the range of annual maximum storage for both climate periods.

After assessing the impact of assuming blanket rainfall on the magnitude of the potential sewer flooding risk, this section examines whether using the blanket one for climate impact studies will misrepresent future changes in the urban flood severity by comparing the modelled climate change impact from two types of rainfall input format. From the experiment simulation results, both types of rainfall input likely to lead to an increased sewer flood risk. However, as shown in the scatter plot (Figure 8.5), while the blanket rainfall tends to give a lower magnitude of the peak storage volume, using the blanket

one will instead overestimate the relative change of sewer flooding extent almost for all sewer nodes being analysed. This implies an expected estimation bias in the future climate change adaptation for urban drainage systems while the magnitude of the bias depends on how the modelled results are being used. For example, if the estimated flooded volume (or any equivalent indicators) from future-period modelled results is directly used in redesigning the drainage network, the actual climate impact will exceed the modelled impact. However, if the relative change between two climate periods simulated by a sewer network model is taken as a key reference for updating the current drainage system, the updated design could be too conservative. In conclusion, using the blanket rainfall input in sewer modelling systems will lead to an underestimated sewer flood risk as well as an underestimated annual variability. For the future climate, this underestimation still exists and this will impact the accuracy of the modelled changes in the sewer flooded volume for climate adaptation.

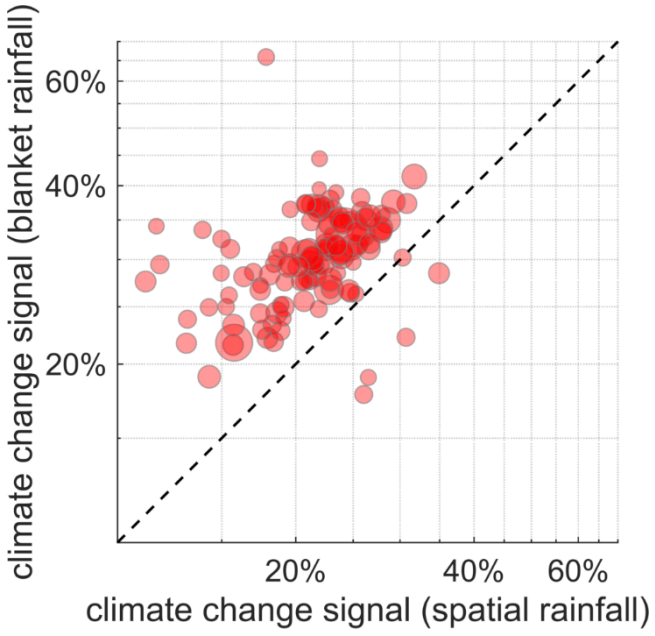


Figure 8.5 Scatter plot of the simulated climate change signal with the blanket rainfall input versus the simulated signal with the spatially varying rainfall input. Each circle represents one compartment node, with the size of the circle indicating the magnitude of the storage capacity of this node

8.3.2 Impact of Changing Spatial Structure On the Future Urban Response

Here, the effect of the changing spatial structure of future rainfall on the estimated urban response is investigated by analysing results from experiments 4 and 5, both of which are representing modelled results for the future scenario. Here, the spatial structure refers to the spatial variability of non-zero rainfall over space. As shown in the monthly variation of the average rainfall input from these two experiments (Figure 8.6.a), the

projected seasonality is well preserved in both future-period realizations. The only difference between these two types of input is the parameter used in the rainfall generator STREAP-CC. As mentioned in the method section, the parameter represents spatial variability (CV_{pos}). As projected in the climate models, the typical change of the CV_{pos} in the future scenario is the increase in summer seasons (see Figure 7.7 from Chapter 7). The projected change is included in the STREAP-CC parameters used for generating rainfall on a monthly basis in experiment 4 but not in experiment 5. Correspondingly, rainfall realizations of experiment 4 tend to give a higher magnitude of catchment extremes as well as a higher annual variability than realizations of experiment 5 (Figure 8.6.b).

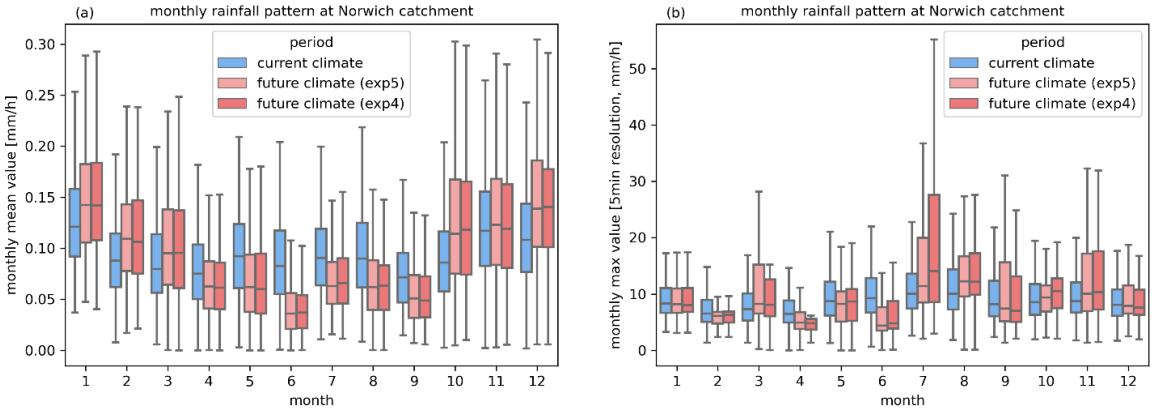


Figure 8.6 Monthly variation of catchment rainfall key statistics as shown in boxplots for each period, which are current climate (experiment 2), future climate with neglecting future changes in spatial variability (experiment 5) and the future climate with including future changes in spatial variability (experiment 4). (a) the boxplots show the variation of average rainfall intensity (mm/h) each year (b) the boxplots show the variation of maximum rainfall intensity (5min resolution, mm/h) each year, indicating the inter-annual variability of the statistics.

After feeding these two types of rainfall into the sewer network, simulation results show that future changes in the monthly variation of average storage volume can still be well preserved even though the rainfall changes in its spatial structure are not properly included. The monthly variation of projected changes in the average storage volume is also well reproduced by both types of future-climate rainfall input, as shown in the summary boxplot of the storage at one downstream compartment node (Figure 8.7.a). This is not surprising because the total amount of rainfall flowing into the sewer network and contributing to the storage volume for each calendar month remains the same for both future-climate scenarios. The annual variability of the average storage volume computed from experiment 5 is close to the variability produced in experiment 4, as shown in by the range of the boxplot, with a relative difference of ~20%, related to the

stochastic variability in the 400-year rainfall generation. However, ignoring the changing spatial structure leads to a visible impact on the annual maximum storage, indicating its effect on the estimated sewer flood extent. This impact can be shown in the monthly changes in the maximum storage volume at the same sewer node (Figure 8.7.b). Not considering future changes in the spatial structure leads to an underestimated sewer flood risk in the summer season, the season with the highest urban flooding hazard. Particularly in July and August, the simulated extent of the increasing peak storage volume in experiment 5 is 14.9-51% less than the simulated increases in experiment 4 at this downstream node in terms of the year-averaged peak value. As for the annual variability, the increasing variability in the maximum storage volume is well projected by both types of rainfall input but the projected increase by experiment 5 is less than the projected increase by experiment 4, particularly in July (~20% less). This feature shows a consistent feature with the inter-annual variability of the rainfall input as shown in the last figure (Figure 8.6.b). Other nodes roughly located downstream were also examined, showing a similar result as reported here.

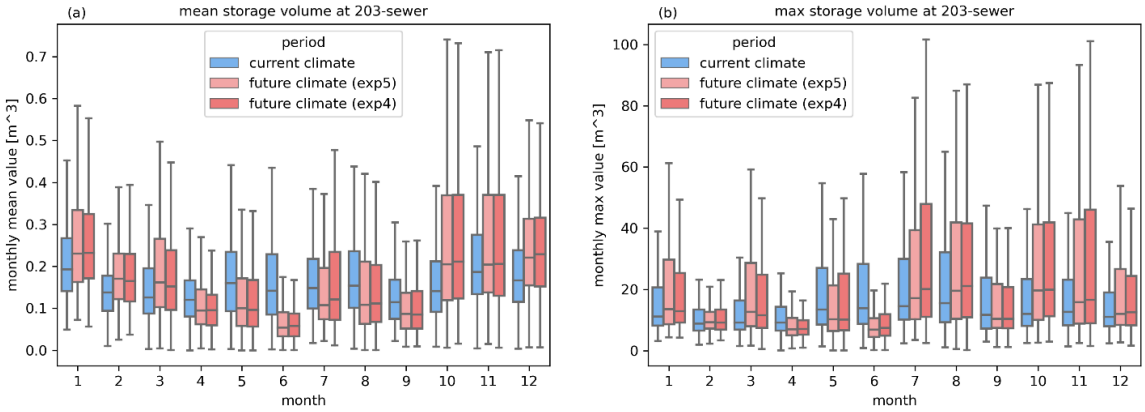


Figure 8.7 Similar to Fig. 8.6 but for boxplots of catchment response (compartment storage volume).

In order to generalize the above conclusion to see how much bias will be caused by neglecting the spatial structure changes in the modelled impact on sewer systems, the impact of changing spatial structure is further investigated by linking the changes in the maximum compartment storage (between experiment 4 and 5) to the changes in the spatial variability (CV_{pos}), on a monthly basis. More compartment nodes are selected for generalizing this conclusion. Results show that there is a clear positive correlation between the modelled change in the sewer flood risk and the change in the rainfall spatial variability between these two experiment settings (Figure 8.8). This impact is much more pronounced for those seasons having a large increase in the spatial variability, typically

in summer seasons for the UK region. This implies a potentially increasing risk in summer urban floods beyond our expectation because the increasing spatial variability is a small-scale feature which cannot be detected in most products of future climate projections.

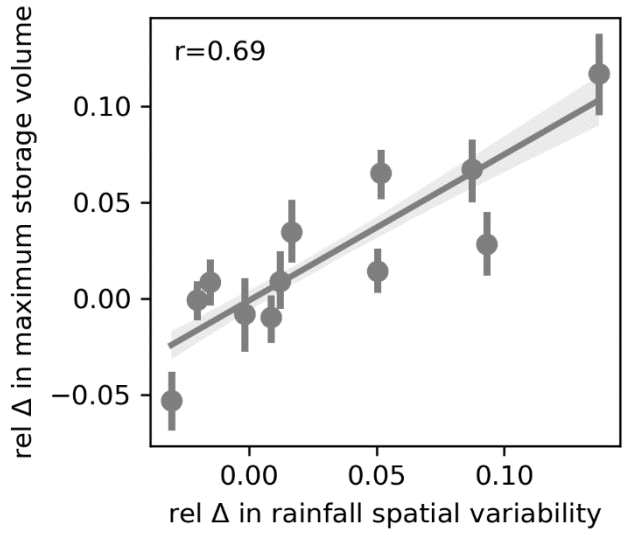


Figure 8.8 Changes of annual-maximum compartment storage volume as a function of the relative change in the rainfall spatial variability between experiment 4 and experiment 5 at 24 auto-selected nodes. These nodes are selected because they have a relatively large storage capacity. The x variable corresponds to the relative change in spatial variability, which is a discrete variable in the plot provided for each calendar month the relative change of rainfall CV_{pos} at the whole catchments (all nodes) are the same. The relative change in the maximum storage volume (y-axis) is the relative difference between the 400-year-averaged monthly-maximum storage from two experiments. The solid line with confidence level shows a linear regression model fitted from the sample data.

8.3.3 Quantifying the Contribution of Each Simplification on the Biased Future Flood Estimation

After showing the impact of different rainfall properties on modelled sewer network dynamics, this section focuses on summarizing the potential bias caused by keeping using the baseline setting (that is experiment 1, where the spatial-varying rainfall and the climate change factors are not included) on the estimated future sewer flood risk and then partitioning the contribution of each key simplification to the bias.

As shown in the computed total bias (Figure 8.9.a), keeping using the baseline setting could lead to an underestimated future flood volume by 47% on average at the urban catchment investigated. There is a significant correlation between the node's surface area and the risk being underestimated, where the linear correlation coefficient is >0.75. At those nodes representing the drainage from a smaller surface area, a larger extent of the underestimation is expected: this rises up to 60%. After partitioning the impact contributing to this correlation (Figure 8.9.b) for different groups of nodes, it can be seen that the bias of estimated risk under the baseline setting to the 'true' future risk at these nodes is largely contributed by both climate change factors and the simplified blanket-like rainfall. Instead, the effect of changing spatial variability is quite minimal. This contribution can be well explained by the increasing rainfall extremes in the future

climate scenario as well as the effect of spatial resolution on the urban catchment response. For sewer nodes having a larger drainage surface area, using the blanket rainfall input plays a much more important role in leading to the bias and hence has a greater impact upon modelled accuracy. Compared with these two simplifications, neglecting future changes in the spatial variability keeps playing a less important role, by up to 6.5% on average in modulating the catchment response. Although the changing spatial structure does affect the maximum compartment storage volume, the averaged effect of neglecting this change is relatively minimal and not significantly different from zero based on a *t* test compared to the other two simplifications.

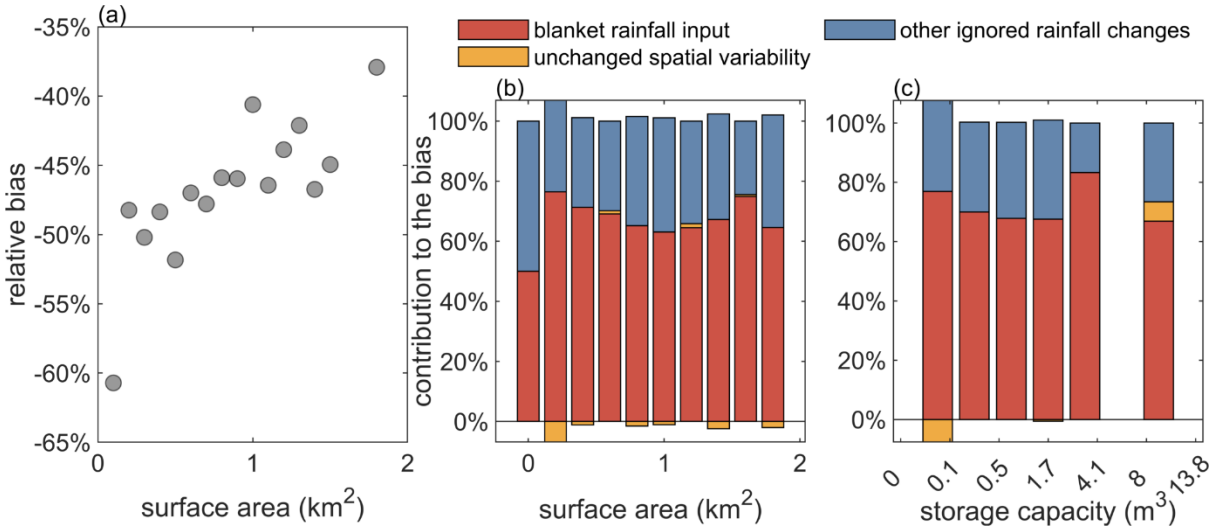


Figure 8.9 Relative bias in the baseline setting (experiment 1) due to simplifications and the contribution of each simplification to the total bias. (a) scatter plot showing the relative bias of estimated maximum compartment storage as a function of the surface drainage area to the node. All points shown in the figure are grouped summary results based on values of the surface area of the node; (b) bar plots showing the contribution of each simplification (blanket rainfall input, unchanged spatial variability, other ignored rainfall changes in future climate) to the total bias, those bars are grouped by the magnitude of node surface area. (c) similar to panel b but nodes are grouped by the magnitude of node storage capacity. In panels (b) and (c), the lengths of these bars are the percentage of contribution defined in equations (8.2) to (8.4).

However, all three simplifications lead to underestimated inter-annual variability of the modelled maximum storage volume. The node-averaged relative bias caused by each simplification in the annual variability of maximum storage volume remains a negative value, indicating a consistently underestimated annual variability in the sewer modelling (Figure 8.10) in these normally used settings. On average, the underestimation is up to 35.3% for the blanket rainfall input, 9.5% for the unchanged spatial variability and 37.9% for ignoring other rainfall changes in the future climate. The linear correlation coefficient between the bias and the surface area shows that such a bias is not significantly correlated with the drainage surface area of the node investigated.

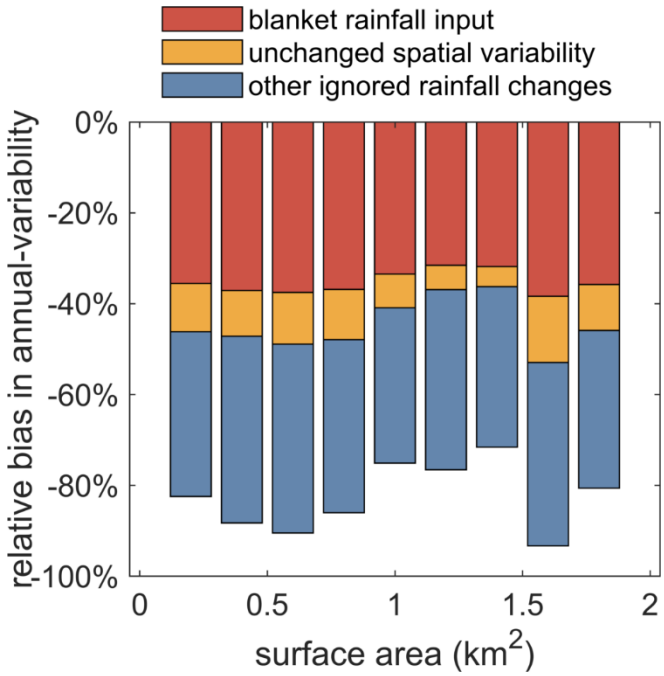


Figure 8.10 Contribution of each simplification to the relative bias of the modelled annual variability of the compartment nodes storage, shown as a bar plot, grouped by the magnitude of the node's surface area.

Section 8.4 Conclusions

In summary, this chapter analysed the impact of three key aspects of rainfall input on an urban drainage system. These three aspects refer to 1) use the spatial-varying/blanket rainfall as the sewer model input, 2) whether or not to account for the changing spatial variability under the future climate, 3) whether or not to account for other changing rainfall properties in the future climate. By using a spatial-temporal rainfall simulation tool for the climate impact studies developed in Chapter 7 of the thesis and a semi-distributed sewer model developed by Dobson (2022), I quantified the extent to which the simplification of each of these three aspects affects the accuracy of the estimated sewer flood risk and compared these effects with one another. A sizable urban catchment located in the Southeast of the UK was used for this investigation.

Numerical experiment results show that these three types of simplifications, namely (i) using blanket rainfall, (ii) not accounting for the changing spatial variability as well as (iii) not accounting for other changing rainfall properties in the future climate, will all lead to an underestimated sewer flood risk. Compared with the most comprehensive setting, which introduces no simplifications, the total underestimation can reach 47% on average. Among the underestimations, using blanket rainfall input consistently plays the most important role. For the nodes having a smaller surface drainage area, the

underestimation can be even higher, which is associated with the climate change impact. While keeping the spatial variability unchanged in the future-scenario simulation contributes less to the total bias, its impact on high-flood-risk summer seasons is not negligible. During summer seasons, ignoring this change can make the increased annual maximum storage volume up to 51% smaller than the increase simulated from the model having accounted for all three aspects. Aside from the effect on the magnitude, simplifications on all these three aspects will also misrepresent the inter-annual variability of the sewer flood risk. Model results indicate an underestimation in the variability by up to 35.3% in the simulation with a blanket rainfall input, 9.5% in the simulation with the unchanged spatial variability and 37.9% in the simulation with the ignored other future rainfall changes.

This study provides valuable information by quantitatively representing the impact of rainfall factors which are normally neglected or simplified in typical contemporary engineering applications. The partitioning studies benefit from the rainfall simulation tool developed in chapter 7 of this thesis, in particular, the downscaling mode enabling an investigation of the changing spatial structure at such a small resolution. For the climate adaptation of the urban drainage system, the analysis in this chapter highlights the necessity to pay attention to the large underestimation in the current risk assessment approach and to consider updating these three aspects of rainfall characteristics in designing the urban drainage network for the future climate. The results showing the partitioning of the impact will also help to support water managers and design engineers to decide which updates might be the most urgent one to make so as to effectively debias the potential error in the sewer network simulation caused by the rainfall input. From results shown in this study, upgrading the current drainage design approach from solely relying on blanket rainfall input to one incorporating the spatial component of the input rainfall will be essential, in fact, and surprisingly, even more so than including the impact of climate change.

While this chapter solely divides the impact of climate change factors into the changing spatial structure and other changing properties, future investigations can also be carried out to make the partitioning of the aspects of climate change effect much more detailed, for example, to analyse the separate impact of changing duration, the shifting seasonality, the changing intensity distribution etc. There are however also some limitations in this

study. Due to the structure and the extent to which the semi-distributed sewer model represents reality, the sewer simulation results does not directly show the exact value of the flooded volume in the drainage system. Instead, the compartment storage volume is used as representative of the sewer risk throughout the whole chapter, limiting the information we can obtain from the sewer modelling results. However, considering the need to carry out the long-term continuous simulation for each of experiment settings, the sewer model selected here still can be taken as a very reasonable choice and the chosen sewer model has provided valuable insights for the research focus. In addition to it, simulation results of the sewer model fully focus on the changes in rainfall characteristics while not considering other changes in the future climate for example the growing population leading to higher water consumption; a more flexible working style causing changing diurnal patterns of the domestic water usage. These changes should also be added to the design work of updating the future drainage system and potentially further increasing the load of some sewer pipes over the urbanized area.

Chapter 9 Conclusions

This study aimed to understand future changes in spatial-temporal rainfall structure and to investigate hydrological impacts under climate change. By pursuing this aim, several research questions were answered. This chapter gives a broad summary of all findings in the study and a quick outlook for future research.

Section 9.1 Summary

9.1.1 Propagation of Rainfall Estimation Bias in Rainfall-Runoff Processes

For flood-related studies, two stochastic generators of spatial-temporal rainfall (STREAP and NS(s-t)) were compared, and the model behaviour was investigated (Chapter 4). Not only rainfall statistics but also the model ability to reproduce catchment runoff was evaluated.

The results showed the ability of both rainfall models in capturing most of the key rainfall statistics, including moment estimates (up to the third-order) of the marginal distribution of rainfall intensity, the autocorrelation of intensities and the decay of spatial correlation with distance at both daily and hourly scales. However, estimation bias still exists in both models, which is due to the inherent model structure and the calibration process. STREAP tends to give higher daily extremes and the NS(s-t) generally overestimates parts of spatial correlation and hourly areal extremes. After a non-linear rainfall-runoff transformation, both types of generated rainfall fields are able to preserve the realism of the overall distribution of the flow series. The hourly peak discharge during winter seasons is also captured by both models while there is a clear discrepancy in summer seasons, i.e., the NS(s-t) gives a high overestimation in hourly peak discharges while STREAP gives a more realistic performances at both daily and hourly scales. The different performances of the two models were further illustrated by investigating the soil-water dynamic conditions simulated by these two types of rainfall.

This study provides an extensive evaluation of the stochastic model for flood studies and the investigation of how the rainfall estimation error propagates to catchment responses. This investigation provides a more direct reference for catchment hydrological applications. Both models demonstrate their ability to infer flood frequency curves at ungauged sites while STREAP performs better in the summer season while the NS(s-t) is not quite suitable in this season, particularly at an hourly scale. The overestimated summer peak discharge could lead to unnecessary investments in flood mitigation measures.

9.1.2 Added Value of CPMs in Climate Projections and Hydrological Applications

In the UK Climate Projections UKCP project, for the first time, ensemble simulations using the convection-permitting model are currently available. A 12-member 20-year-long hourly-scale convection-permitting ensemble from UKCP18 is used for evaluation.

The realism of the output for the control period (1980-2000) was evaluated by comparing climate model outputs with several quality-controlled observational rainfall datasets (Radar, GEAR, HadUK-Grid). Results (Chapter 5) show that the spatial pattern and the seasonal variation of mean precipitation are reasonably well captured by the CPM. On modelled storm durations and key areal statistics, the occurrence frequency of storm events is well reproduced by the CPM. Despite the considerably improved hourly precipitation variability compared to the GCMs/RCMs in previous studies, the CPM still tends to simulate too many storms having a shorter duration and too many moderate and intense events. As for its spatial organization, the CPM is able to reproduce a scaling behaviour (power-law spectral density function) very similar to that of radar estimates across spatial scales. The spatial variability across temporal scales up to 24 hours also shows a similar pattern to radar estimates. Features of high-impact events have also been examined, where the CPM reproduces the clustering of heavy rainfall quite well at a daily scale while tending to give smoother rainfall fields than radar estimates at an hourly scale. Areal reduction factors (of extremes) are found to be consistently lower than radar estimates because of the overestimated grid-scale extremes in the CPM outputs.

To understand the future changes in the spatial-temporal structure of rainfall, the two sets of ensemble simulations over the UK for the past and future periods were used and compared (Chapter 6). Results show that rainfall occurs less frequently in the future

summer season, but when it rains, it tends to be more intense. The increase of extremes in both peak intensity and occurrence rate is projected in all three subregions (North West, North East, and South). The future summer rainfall is found to move faster and also has a larger spatial coverage. The increase in spatial extent and peak intensity of extremes leads to an increase in hourly areal rainfall amounts by up to 60.8% in the north-west. Such an intensification of rainfall extremes at 2–40 years return levels is projected for most catchment scales, with the highest increase at the scales with sizes 20–500 km^2. This spatial scale implies a significant underestimation of urban flood hazards in future climate in the current guidance. Using the high-resolution climate model, the study exhibited further aspects of the changes in spatial-temporal features of rainfall in greater detail.

The extensive analysis of the latest convection-permitting ensembles shows that although convection-permitting models (CPMs) are not directly useful to drive hydrological processes to project future catchment responses (Kay et al., 2015), they are able to provide credible climate information, particularly at small spatial-temporal scales. Such fine-scale information shows the potential of including more vital details about the future for hydrological impact studies.

9.1.3 Modelling High-resolution Precipitation for Climate Impact Studies

Based on the examination of rainfall stochastic generators and the latest convection-permitting climate models, a fine-resolution stochastic tool STREAP-CC was developed to aid climate impact studies needing high-resolution rainfall information. Using the model structure of a well-established generator STREAP, a few more improvements also have been achieved in this research including (1) adding a dependency function to improve the temporal autocorrelation of point rainfall; (2) calibrating the tool using climate model outputs and introduced a complete downscaling method to enable the generation of finer-scale precipitation fields, either for the current climate or the future climate; (3) debiasing the discrepancy between climate model output and radar rainfall estimates in a wide range of key rainfall properties.

Validation results show the ability of the STREAP-CC tool to simulate rainfall fields largely consistent with features from observations for the current climate as well as preserving the changes projected by climate models for the future climate. The realism not only lies

in the distribution of key properties (spell duration, areal statistics and point rainfall), but also their correlations. Extreme events are also well reproduced by the tool.

The validation results show that precipitation fields produced by the STREAP-CC tool are suitable for climate impact studies particular when spatial rainfall fields are preferred. The tool can directly provide reliable and sub-hourly rainfall information for future climate (e.g., urban drainage design needs), which is not available in most climate models. Aside from its appealing feature in fine-scale impact studies, the tool also has advantages at an hourly scale because more realistic rainfall fields are generated by the STREAP-CC compared with the raw CPMs or with a simple statistical bias correction method.

9.1.4 Quantifying Contribution of Rainfall Changes to Sewer Flood Estimation

This study also investigated the impact of different aspects of rainfall inputs upon an urban drainage system by applying the developed tool STREAP-CC to an urban catchment (98.5 km^2) (Chapter 8). Three aspects, characterising simplifications normally used in drainage designs, were selected: the use of the spatial-varying/blanket rainfall as the input; whether or not to account for the changing spatial variability under the future climate; whether or not to account for other changing properties in the future climate. By using the STREAP-CC and a semi-distributed sewer model developed by Dobson (2022), the study provides a quantification of the extent to which each simplified aspect could affect the accuracy of the estimated sewer flood risk. Numerical results show that these three types of simplifications, namely (i) using blanket rainfall, (ii) not accounting for the changing spatial variability as well as (iii) not accounting for other changing rainfall properties in the future climate, will all lead to an underestimated sewer flood risk. The total underestimation caused by these simplifications reaches 47% on average. Among the underestimations, using blanket rainfall input consistently plays the dominant role. The next most important factor is the climate change impact particularly for the sewer nodes with a smaller surface drainage area. While keeping the spatial variability unchanged in the future-scenario simulation contributes less to the total bias, its impact on high-flood-risk summer seasons is not negligible. Aside from the effect on the magnitude, simplifications on all these three aspects will also misrepresent the inter-annual variability of the sewer flood risk.

This research provides valuable information by quantitatively representing the impact of rainfall factors which are normally neglected or simplified in typical contemporary engineering applications. For the climate adaptations in urban drainage systems, the analysis highlights the large underestimation in the current risk assessment approach. The partitioned impact shown in the results also helps to support water managers and design engineers to effectively reduce the potential error in the sewer network simulation caused by the rainfall input.

Section 9.2 Outlook for Future Research

As summarized above, this study has tackled various issues related to understanding and modelling future rainfall changes and filling the gap between climate model outputs and the requirements of hydrological applications. Yet there are still some future research directions which could be explored in the wake of this research.

9.2.1 Data Quality and Data Availability

High-quality observational data are essential to better understanding the rainfall pattern and assessing the impact of any future changes in it however the required measurements are not always available. The current situation in the UK is that there are a few long-term rainfall measurements which have been quality controlled. On the one hand, the discrepancy between different observational datasets themselves could be reduced in the future through data-merging methods (Ochoa-Rodriguez et al., 2019) so as to facilitate climate model evaluation and the following applications. On the other hand, such datasets having undergone good quality control are not always available in other countries, in particular for countries less developed and less urbanized. However, those countries, such as in Africa, are expected to be more vulnerable to climate change and the increasing extreme events because of the growing population and the lack of fundamental infrastructure. This is one issue which might need to be tackled in the future: how to obtain more reliable data for those places which are more vulnerable to extreme events.

For the climate projections, the one used in this study is a multi-member convection-permitting ensemble from UKCP18. The CPM is driven by a perturbed GCM to include the uncertainty related to the model parameters. Although the ensemble uncertainty and the inter-annual variability have been considered in the related analysis throughout this

thesis, results shown in this study have not included other uncertainty sources such as the uncertainty from climate model physics itself and the one from a limited number of parameter perturbation scheme. These two sources of uncertainty cannot be automatically included in the stochastic tool developed in this study. The convection-permitting ensemble for the updated scenarios (SSPs) is not available yet. To better understand the uncertainty in future climate projections, having more data available for such a scale could be essential while the computational burden behind such a large number of simulations could still be a globally technical issue in the research community.

9.2.2 Modelling Approach and its Applications

For the STREAP-CC tool developed here, there is still room for potential improvements, as follows. (1) the storm separation method used in the first stage of the model calibration could be improved. In the hierarchical structure of the STREAP-CC, the model behaviour could be sensitive to the separation method being used. In the current method, the separation is achieved by analysing the time series of two areal statistics although the approach lacks the physical justification and potentially has pitfalls in tackling the separation when storms overlap in time even though they are not correlated and might not overlap in space. Updating the current separation method could further benefit the model behaviour in reproducing rainfall extremes at scales coarser than the scale used in calibration. (2) The temporal evolution of point rainfall can be further updated. In this chapter, this evolution, represented by the ARMA process and a linear dependency function, is assumed to be unchanged in different climate periods. This can be further improved considering the changing temporal profile of sub-hourly rainfall events (S C Chan et al., 2016) which can be crucial in modulating hydrological responses of a catchment to a rainfall event. (3) Depending on the downstream applications of the STREAP-CC product, further validation might be needed on the product. The current validation of areal statistics was carried out at the areal scale used in the simulation. For potential applications in a smaller catchment, it is still suggested to choose a large domain of the same magnitude as the one used in this thesis for model parameterization. This is to make sure the storm features obtained are able to represent a complete storm evolution over space. But considering the consistency of model performance between the large simulation domain and the small catchment of interest, further investigations on a point-scale statistics might be needed.

Another improvement which could be carried out is to make the tool more targeted to applications of high-impact events. As a stochastic tool which is able to simulate long-term precipitation, the calibration is achieved by summarizing the rainfall characteristics of all wet spells instead of putting a particular focus on extreme events at all aspects. Therefore, the current tool is doing well in reproducing summary statistics but is not necessarily good at reproducing the extent of changes in extremes. One example will be the projected changes in the spatial extent as shown in Chapter 6. The model parameters governing this change are assumed to be constant for all events (on a monthly basis) while the extent of the changes could be different for storms with varying severity levels. In further research, a quantile-based parameter governing the spatial correlation can be introduced so as to better simulate changes in the spatial extent of different rainfall events since this small-scale change could play a significant role in modulating the catchment response. In addition, it will also be worthwhile to explore the model parameter uncertainties.

Aside from the purpose of flood analysis, there are further climate impact studies which could benefit from this developed tool, for example to couple this into a hyper-resolution hydrology and land surface model (Bierkens et al., 2015). Having high-resolution rainfall data for the future could further help in understanding the impact of rainfall changes in ecosystems and how different plant species will react to the changing environmental conditions. More studies could be done to explore these issues.

References

Akhter, M., Shamseldin, A., Melville, B., 2019. Comparison of dynamical and statistical rainfall downscaling of CMIP5 ensembles at a small urban catchment scale. Stochastic Environmental Research and Risk Assessment 33, 989–1012. https://doi.org/10.1007/s00477-019-01678-y

Alfieri, L., Bisselink, B., Dottori, F., Naumann, G., de Roo, A., Salamon, P., Wyser, K., Feyen, L., 2017. Global projections of river flood risk in a warmer world. Earths Future 5, 171–182. https://doi.org/10.1002/2016EF000485

Allan, R.P., Barlow, M., Byrne, M.P., Cherchi, A., Douville, H., Fowler, H.J., Gan, T.Y., Pendergrass, A.G., Rosenfeld, D., Swann, A.L.S., Wilcox, L.J., Zolina, O., 2020. Advances in understanding large-scale responses of the water cycle to climate change. Ann N Y Acad Sci 1472, 49–75. https://doi.org/10.1111/nyas.14337

Allen, M.R., O.P. Dube, W. Soleck, F. Aragón-Durand, W. Cramer, S. Humphreys, M. Kainuma, J. Kala, N. Mahowald, Y. Mulugetta, R. Perez, M.Wairiu, K. Zickfeld, 2018. Global Warming of 1.5°C. An IPCC Special Report on the impacts of global warming of 1.5°C above pre-industrial levels and related global greenhouse gas emission pathways, in the context of strengthening the global response to the threat of climate change, sustainable development, and efforts to eradicate poverty. Geneva.

Anglian Water, 2016. Anglian Water Services Limited EA Raingauge Data [WWW Document]. URL https://anglian-water.sharefile.com/Authentication/Login

Anstead, L., Tovey, N.K., 2017. Hydrological and geomorphological challenges of water transfers in East Anglia, UK in the context of climate change. International Journal of Water 11, 14. https://doi.org/10.1504/IJW.2017.081108

Armon, M., Marra, F., Enzel, Y., Rostkier-Edelstein, D., Garfinkel, C.I., Adam, O., Dayan, U., Morin, E., 2022. Reduced Rainfall in Future Heavy Precipitation Events Related to Contracted Rain Area Despite Increased Rain Rate. Earths Future 10. https://doi.org/10.1029/2021EF002397

Armon, M., Marra, F., Enzel, Y., Rostkier-Edelstein, D., Morin, E., 2020. Radar-based characterisation of heavy precipitation in the eastern Mediterranean and its representation in a convection-permitting model. Hydrol Earth Syst Sci 24, 1227–1249. https://doi.org/10.5194/hess-24-1227-2020

Arnell, N.W., Freeman, A., Gazzard, R., 2021. The effect of climate change on indicators of fire danger in the UK. Environmental Research Letters 16, 044027. https://doi.org/10.1088/1748-9326/abd9f2

Arnone, E., Pumo, D., Viola, F., Noto, L. v., la Loggia, G., 2013. Rainfall statistics changes in Sicily. Hydrol Earth Syst Sci 17, 2449–2458. https://doi.org/10.5194/hess-17-2449-2013

Aryal, N.R., Jones, O.D., 2020. Fitting the Bartlett–Lewis rainfall model using Approximate Bayesian Computation. Math Comput Simul 175, 153–163. https://doi.org/https://doi.org/10.1016/j.matcom.2019.10.018

Ban, N., Rajczak, J., Schmidli, J., Schär, C., 2020. Analysis of Alpine precipitation extremes using generalized extreme value theory in convection-resolving climate simulations. Clim Dyn 55, 61–75. https://doi.org/10.1007/s00382-018-4339-4

Ban, N., Schmidli, J., Schär, C., 2015. Heavy precipitation in a changing climate: Does short-term summer precipitation increase faster? Geophys Res Lett 42, 1165–1172. https://doi.org/10.1002/2014GL062588

Ban, N., Schmidli, J., Schär, C., 2014. Evaluation of the convection-resolving regional climate modeling approach in decade-long simulations. Journal of Geophysical Research: Atmospheres 119, 7889–7907. https://doi.org/10.1002/2014JD021478

Barbero, R., Fowler, H.J., Lenderink, G., Blenkinsop, S., 2017. Is the intensification of precipitation extremes with global warming better detected at hourly than daily resolutions? Geophys Res Lett 44, 974–983. https://doi.org/10.1002/2016GL071917

Bárdossy, A., Pegram, G.G.S., 2009. Copula based multisite model for daily precipitation simulation. Hydrol Earth Syst Sci 13, 2299–2314. https://doi.org/10.5194/hess-13-2299-2009

Bárdossy, A., Stehlík, J., Caspary, H.-J., 2002. Automated objective classification of daily circulation patterns for precipitation and temperature downscaling based on optimized fuzzy rules. Clim Res 23, 11–22. https://doi.org/10.3354/cr023011

Barnolas, M., Rigo, T., Llasat, M.C., 2010. Characteristics of 2-D convective structures in Catalonia (NE Spain): an analysis using radar data and GIS. Hydrol Earth Syst Sci 14, 129–139. https://doi.org/10.5194/hess-14-129-2010

Bell, F.C., 1976. The areal reduction factor in rainfall frequency estimation. Institute of Hydrology, Wallingford.

Bell, T.L., 1987. A space-time stochastic model of rainfall for satellite remote-sensing studies 9631.

Bell, V.A., Kay, A., Jones, R.G., Moore, R.J., 2007. Development of a high resolution grid-based river flow model for use with regional climate model output. Hydrol Earth Syst Sci 11, 532–549. https://doi.org/10.5194/hess-11-532-2007

Benettin, P., Kirchner, J.W., Rinaldo, A., Botter, G., 2015. Modeling chloride transport using travel time distributions at Plynlimon, Wales. Water Resour Res 51, 3259–3276. https://doi.org/10.1002/2014WR016600

Benoit, L., Allard, D., Mariethoz, G., 2018. Stochastic Rainfall Modeling at Sub-kilometer Scale. Water Resour Res 54, 4108–4130. https://doi.org/10.1029/2018WR022817

Berthou, S., Kendon, E.J., Chan, S.C., Ban, N., Leutwyler, D., Schär, C., Fosser, G., 2018. Pan-European climate at convection-permitting scale: a model intercomparison study. Clim Dyn. https://doi.org/10.1007/s00382-018-4114-6

Bierkens, M.F.P., Bell, V.A., Burek, P., Chaney, N., Condon, L.E., David, C.H., de Roo, A., Döll, P., Drost, N., Famiglietti, J.S., Flörke, M., Gochis, D.J., Houser, P., Hut, R., Keune, J., Kollet, S., Maxwell, R.M., Reager, J.T., Samaniego, L., Sudicky, E., Sutanudjaja, E.H., van de Giesen, N., Winsemius, H., Wood, E.F., 2015. Hyper-resolution global hydrological modelling: what is next? Hydrol Process 29, 310–320. https://doi.org/10.1002/hyp.10391

Blenkinsop, S., Lewis, E., Chan, S.C., Fowler, H.J., 2017. Quality-control of an hourly rainfall dataset and climatology of extremes for the UK. International Journal of Climatology 37, 722–740. https://doi.org/10.1002/joc.4735

Bordoy, R., Burlando, P., 2014. Stochastic downscaling of climate model precipitation outputs in orographically complex regions: 2. Downscaling methodology. Water Resour Res 50, 562–579. https://doi.org/10.1002/wrcr.20443

Bowler, N.E., Pierce, C.E., Seed, A.W., 2006. STEPS: A probabilistic precipitation forecasting scheme which merges an extrapolation nowcast with downscaled NWP. Quarterly Journal of the Royal Meteorological Society 132, 2127–2155. https://doi.org/10.1256/qj.04.100

Bowler, N.E.H., Pierce, C.E., Seed, A., 2004. Development of a precipitation nowcasting algorithm based upon optical flow techniques. J Hydrol (Amst) 288, 74–91. https://doi.org/10.1016/j.jhydrol.2003.11.011

Brath, A., Montanari, A., Moretti, G., 2006. Assessing the effect on flood frequency of land use change via hydrological simulation (with uncertainty). J Hydrol (Amst) 324, 141–153. https://doi.org/10.1016/j.jhydrol.2005.10.001

Breinl, K., Turkington, T., Stowasser, M., 2013. Stochastic generation of multi-site daily precipitation for applications in risk management. J Hydrol (Amst) 498, 23–35. https://doi.org/10.1016/j.jhydrol.2013.06.015

Burlando, P., Rosso, R., 1991. Extreme storm rainfall and climatic change. Atmos Res 27, 169–189. https://doi.org/10.1016/0169-8095(91)90017-Q

Burton, A., Fowler, H.J., Blenkinsop, S., Kilsby, C.G., 2010a. Downscaling transient climate change using a Neyman–Scott Rectangular Pulses stochastic rainfall model. J Hydrol (Amst) 381, 18–32. https://doi.org/10.1016/j.jhydrol.2009.10.031

Burton, A., Fowler, H.J., Kilsby, C.G., O'Connell, P.E., 2010b. A stochastic model for the spatial-temporal simulation of nonhomogeneous rainfall occurrence and amounts. Water Resour Res 46. https://doi.org/10.1029/2009WR008884

Burton, A., Kilsby, C.G., Fowler, H.J., Cowpertwait, P.S.P., O'Connell, P.E., 2008. RainSim: A spatial–temporal stochastic rainfall modelling system. Environmental Modelling and Software 23, 1356–1369. https://doi.org/10.1016/j.envsoft.2008.04.003

Cameron, D., Beven, K., Tawn, J., 2000. An evaluation of three stochastic rainfall models. J Hydrol (Amst) 228, 130–149. https://doi.org/https://doi.org/10.1016/S0022-1694(00)00143-8

Camici, S., Brocca, L., Melone, F., Moramarco, T., 2014. Impact of Climate Change on Flood Frequency Using Different Climate Models and Downscaling Approaches. J Hydrol Eng 19, 4014002. https://doi.org/10.1061/(ASCE)HE.1943-5584.0000959

Cannon, A.J., Sobie, S.R., Murdock, T.Q., 2015. Bias Correction of GCM Precipitation by Quantile Mapping: How Well Do Methods Preserve Changes in Quantiles and Extremes? J Clim 28, 6938–6959. https://doi.org/10.1175/JCLI-D-14-00754.1

Chan, S., Kahana, R., Kendon, E., Fowler, H., 2018. Projected changes in extreme precipitation over Scotland and Northern England using a high-resolution regional climate model. Clim Dyn 51, 3559–3577. https://doi.org/10.1007/s00382-018-4096-4

Chan, S.C., Kendon, E.J., Berthou, S., Fosser, G., Lewis, E., Fowler, H.J., 2020. Europe-wide precipitation projections at convection permitting scale with the Unified Model. Clim Dyn. https://doi.org/10.1007/s00382-020-05192-8

Chan, S.C., Kendon, E.J., Fowler, H.J., Blenkinsop, S., Ferro, C.A.T., Stephenson, D.B., 2013. Does increasing the spatial resolution of a regional climate model improve the simulated daily precipitation? Clim Dyn 41, 1475–1495. https://doi.org/10.1007/s00382-012-1568-9

Chan, S.C., Kendon, E.J., Fowler, H.J., Blenkinsop, S., Roberts, N.M., 2014. Projected increases in summer and winter UK sub-daily precipitation extremes from high-resolution regional climate models. Environmental Research Letters 9, 084019. https://doi.org/10.1088/1748-9326/9/8/084019

Chan, Steven C, Kendon, E.J., Roberts, N.M., Fowler, H.J., Blenkinsop, S., 2016. Downturn in scaling of UK extreme rainfall with temperature for future hottest days. Nat Geosci 9, 24–28. https://doi.org/10.1038/ngeo2596

Chan, S C, Kendon, E.J., Roberts, N.M., Fowler, H.J., Blenkinsop, S., 2016. The characteristics of summer sub-hourly rainfall over the southern UK in a high-resolution convective permitting model. Environmental Research Letters 11, 094024. https://doi.org/10.1088/1748-9326/11/9/094024

Chandler, R.E., Wheater, H.S., 2002. Analysis of rainfall variability using generalized linear models: A case study from the west of Ireland. Water Resour Res 38, 1192. https://doi.org/10.1029/2001WR000906

Chang, W., Wang, J., Marohnic, J., Kotamarthi, V.R., Moyer, E.J., 2020. Diagnosing added value of convection-permitting regional models using precipitation event identification and tracking. Clim Dyn 55, 175–192. https://doi.org/10.1007/s00382-018-4294-0

Chen, Y., Paschalis, A., Kendon, E., Kim, D., Onof, C., 2021. Changing Spatial Structure of Summer Heavy Rainfall, Using Convection-Permitting Ensemble. Geophys Res Lett 48, e2020GL090903. https://doi.org/10.1029/2020GL090903

Coe, R., Stern, R.D., 1982. Fitting Models to Daily Rainfall Data. Journal of Applied Meteorology 21, 1024–1031. https://doi.org/10.1175/1520-0450(1982)021<1024:FMTDRD>2.0.CO;2

Coles, S., 2013. An Introduction to Statistical Modeling of Extreme Values, Springer Series in Statistics. Springer London, Limited, London. https://doi.org/10.1007/978-1-4471-3675-0

Courant, R., Friedrichs, K., Lewy, H., 1928. Über die partiellen Differenzengleichungen der mathematischen Physik. Math Ann 100, 32–74. https://doi.org/10.1007/BF01448839

Cowpertwait, P.S.P., 2010. A spatial-temporal point process model with a continuous distribution of storm types. Water Resour Res 46, n/a. https://doi.org/10.1029/2010WR009728

Cowpertwait, P.S.P., 2006. A spatial–temporal point process model of rainfall for the Thames catchment, UK. J Hydrol (Amst) 330, 586–595. https://doi.org/10.1016/j.jhydrol.2006.04.043

Cowpertwait, P.S.P., 1994. A Generalized Point Process Model for Rainfall. Proc R Soc Lond A Math Phys Sci 447, 23–37. https://doi.org/10.1098/rspa.1994.0126

Cowpertwait, P.S.P., Kilsby, C., O'Connell, P., 2002. A space-time Neyman-Scott model of rainfall: Empirical analysis of extremes. Water Resour Res 38, 6–14. https://doi.org/10.1029/2001WR000709

Cowpertwait, P.S.P., Ocio, D., Collazos, G., de Cos, O., Stocker, C., 2013. Regionalised spatiotemporal rainfall and temperature models for flood studies in the Basque Country, Spain. Hydrol Earth Syst Sci 17, 479–494. https://doi.org/10.5194/hess-17-479-2013

Cowpertwait, P.S.P., Xie, G., Isham, V., Onof, C., Walsh, D., 2011. A fine-scale point process model of rainfall with dependent pulse depths within cells. Hydrological Sciences Journal 56, 1110–1117. https://doi.org/10.1080/02626667.2011.604033

Cox, D.R., Isham, V., 1988. A Simple Spatial-Temporal Model of Rainfall. Proceedings of the Royal Society of London. A. Mathematical and Physical Sciences 415, 317–328. https://doi.org/10.1098/rspa.1988.0016

Dale, M., Luck, B., Fowler, H.J., Blenkinsop, S., Gill, E., Bennett, J., Kendon, E., Chan, S., 2017. New climate change rainfall estimates for sustainable drainage. Proceedings of the Institution of Civil Engineers - Engineering Sustainability 170, 214–224. https://doi.org/10.1680/jensu.15.00030

Darwish, M.M., Fowler, H.J., Blenkinsop, S., Tye, M.R., 2018. A regional frequency analysis of UK sub-daily extreme precipitation and assessment of their seasonality. International Journal of Climatology 38, 4758–4776. https://doi.org/10.1002/joc.5694

Darwish, M.M., Tye, M.R., Prein, A.F., Fowler, H.J., Blenkinsop, S., Dale, M., Faulkner, D., 2020. New hourly extreme precipitation regions and regional annual probability estimates for the UK. International Journal of Climatology n/a. https://doi.org/10.1002/joc.6639

de Michele, C., Bernardara, P., 2005. Spectral analysis and modeling of space-time rainfall fields. Atmos Res 77, 124–136. https://doi.org/10.1016/j.atmosres.2004.10.031

de Michele, C., Zenoni, E., Pecora, S., Rosso, R., 2011. Analytical derivation of rain intensity–duration–area–frequency relationships from event maxima. J Hydrol (Amst) 399, 385–393. https://doi.org/https://doi.org/10.1016/j.jhydrol.2011.01.018

DEFRA, 2016a. Anglian river basin district flood risk management plan, Department for Environment, Food and Rural Affairs. Environment Agency.

DEFRA, 2016b. Anglian River Basin District Flood Risk Management Plan 2015 - 2021 PART B – Sub Areas in the Anglian River Basin District, Department for Environment, Food and Rural Affairs.

DEFRA, 2010. The costs of the summer 2007 floods in England. Environment Agency.

DEFRA, 2009a. North Essex: Catchment Flood Management Plan, Department for Environment, Food and Rural Affairs. Environment Agency.

DEFRA, 2009b. River Welland: Catchment flood management plan, Department for Environment, Food and Rural Affairs. Environment Agency.

Deidda, R., 2000. Rainfall downscaling in a space-time multifractal framework. Water Resour Res 36, 1779–1794. https://doi.org/10.1029/2000WR900038

Dobson, B., Watson-Hill, H., Muhandes, S., Borup, M., Mijic, A., 2022. A Reduced Complexity Model With Graph Partitioning for Rapid Hydraulic Assessment of Sewer Networks. Water Resour Res 58. https://doi.org/10.1029/2021WR030778

Embrechts, P., Klüppelberg, C., Mikosch, T., 1997. Modelling Extremal Events. Springer Berlin Heidelberg, Berlin, Heidelberg. https://doi.org/10.1007/978-3-642-33483-2

Evin, G., Favre, A.-C., 2008. A new rainfall model based on the Neyman-Scott process using cubic copulas. Water Resour Res 44. https://doi.org/10.1029/2007WR006054

Fairman, J.G., Schultz, D.M., Kirshbaum, D.J., Gray, S.L., Barrett, A.I., 2015. A radar-based rainfall climatology of Great Britain and Ireland. Weather 70, 153–158. https://doi.org/10.1002/wea.2486

Fatichi, S., Ivanov, V.Y., Paschalis, A., Peleg, N., Molnar, P., Rimkus, S., Kim, J., Burlando, P., Caporali, E., 2016. Uncertainty partition challenges the predictability of vital details of climate change. Earths Future 4, 240–251. https://doi.org/10.1002/2015EF000336

Felder, G., Weingartner, R., 2016. An approach for the determination of precipitation input for worst-case flood modelling. Hydrological Sciences Journal 61, 2600–2609. https://doi.org/10.1080/02626667.2016.1151980

Fischer, E.M., Knutti, R., 2016. Observed heavy precipitation increase confirms theory and early models. Nat Clim Chang 6, 986–991. https://doi.org/10.1038/nclimate3110

Fischer, E.M., Knutti, R., 2015. Anthropogenic contribution to global occurrence of heavy-precipitation and high-temperature extremes. Nat Clim Chang 5, 560–564. https://doi.org/10.1038/nclimate2617

Fosser, G., Kendon, E., Chan, S., Lock, A., Roberts, N., Bush, M., 2019. Optimal configuration and resolution for the first convection-permitting ensemble of climate projections over the United Kingdom. International Journal of Climatology n/a. https://doi.org/10.1002/joc.6415

Fosser, G., Kendon, E.J., Stephenson, D., Tucker, S., 2020. Convection-Permitting Models Offer Promise of More Certain Extreme Rainfall Projections. Geophys Res Lett 47. https://doi.org/10.1029/2020GL088151

Fosser, G., Khodayar, S., Berg, P., 2017. Climate change in the next 30 years: What can a convection-permitting model tell us that we did not already know? Clim Dyn. https://doi.org/10.1007/s00382-016-3186-4

Fosser, G., Khodayar, S., Berg, P., 2015. Benefit of convection permitting climate model simulations in the representation of convective precipitation. Clim Dyn 44, 45–60. https://doi.org/10.1007/s00382-014-2242-1

Fowler, H.J., Blenkinsop, S., Tebaldi, C., 2007. Linking climate change modelling to impacts studies: recent advances in downscaling techniques for hydrological modelling.

International Journal of Climatology 27, 1547–1578. https://doi.org/10.1002/joc.1556

Fowler, H.J., Lenderink, G., Prein, A.F., Westra, S., Allan, R.P., Ban, N., Barbero, R., Berg, P., Blenkinsop, S., Do, H.X., Guerreiro, S., Haerter, J.O., Kendon, E.J., Lewis, E., Schaer, C., Sharma, A., Villarini, G., Wasko, C., Zhang, X., 2021. Anthropogenic intensification of short-duration rainfall extremes. Nat Rev Earth Environ 2, 107–122. https://doi.org/10.1038/s43017-020-00128-6

Georgiou, S., Gaussiat, N., Lewis, H.W., 2010. Dynamic modelling of the orographic enhancement of precipitation in the UK.

Gneiting, T., Kleiber, W., Schlather, M., 2010. Matérn Cross-Covariance Functions for Multivariate Random Fields. J Am Stat Assoc 105, 1167–1177. https://doi.org/10.1198/jasa.2010.tm09420

Gray, M.E.B., Marshall, C., 1998. Mesoscale convective systems over the UK, 1981–97. Weather 53, 388–396. https://doi.org/10.1002/j.1477-8696.1998.tb06352.x

Guerreiro, S.B., Fowler, H.J., Barbero, R., Westra, S., Lenderink, G., Blenkinsop, S., Lewis, E., Li, X.-F., 2018a. Detection of continental-scale intensification of hourly rainfall extremes. Nat Clim Chang 8, 803–807. https://doi.org/10.1038/s41558-018-0245-3

Guerreiro, S.B., Fowler, H.J., Barbero, R., Westra, S., Lenderink, G., Blenkinsop, S., Lewis, E., Li, X.-F., 2018b. Detection of continental-scale intensification of hourly rainfall extremes. Nat Clim Chang 8, 803–807. https://doi.org/10.1038/s41558-018-0245-3

Gutnisky, D.A., Josić, K., 2010. Generation of Spatiotemporally Correlated Spike Trains and Local Field Potentials Using a Multivariate Autoregressive Process. J Neurophysiol 103, 2912–2930. https://doi.org/10.1152/jn.00518.2009

Haerter, J.O., Berg, P., Moseley, C., 2017. Precipitation onset as the temporal reference in convective self-organization. Geophys Res Lett 44, 6450–6459. https://doi.org/10.1002/2017GL073342

Haerter, J.O., Schlemmer, L., 2018. Intensified Cold Pool Dynamics Under Stronger Surface Heating. Geophys Res Lett. https://doi.org/10.1029/2017GL076874

Hamed, K.H., Ramachandra Rao, A., 1998. A modified Mann-Kendall trend test for autocorrelated data. J Hydrol (Amst) 204, 182–196. https://doi.org/10.1016/S0022-1694(97)00125-X

Hardenberg, J. v, Ferraris, L., Provenzale, A., 2003. The shape of convective rain cells. Geophys Res Lett 30, 2280-n/a. https://doi.org/10.1029/2003GL018539

Harrigan, S., Hannaford, J., Muchan, K., Marsh, T.J., 2018. Designation and trend analysis of the updated UK Benchmark Network of river flow stations: the UKBN2 dataset. Hydrology Research 49, 552–567. https://doi.org/10.2166/nh.2017.058

Harrison, D.L., Norman, K., Pierce, C., Gaussiat, N., 2012. Radar products for hydrological applications in the UK. Proceedings of the Institution of Civil Engineers - Water Management 165, 89–103. https://doi.org/10.1680/wama.2012.165.2.89

Hawkins, E., Sutton, R., 2011. The potential to narrow uncertainty in projections of regional precipitation change. Clim Dyn 37, 407–418. https://doi.org/10.1007/s00382-010-0810-6

Hengl, T., 2018a. Clay Content In % (Kg / Kg) At 6 Standard Depths (0, 10, 30, 60, 100 And 200 Cm) At 250 M Resolution (Version v0.2). https://doi.org/10.5281/zenodo.1476855

Hengl, T., 2018b. Sand Content In % (Kg / Kg) At 6 Standard Depths (0, 10, 30, 60, 100 And 200 Cm) At 250 M Resolution (Version v0.2). https://doi.org/10.5281/zenodo.1476852

Hengl, T., Wheeler, I., 2018. Soil Organic Carbon Content In X 5 G / Kg At 6 Standard Depths (0, 10, 30, 60, 100 And 200 Cm) At 250 M Resolution (Version v0.2). https://doi.org/10.5281/zenodo.1475458

Hirabayashi, Y., Mahendran, R., Koirala, S., Konoshima, L., Yamazaki, D., Watanabe, S., Kim, H., Kanae, S., 2013. Global flood risk under climate change. Nat Clim Chang 3, 816–821. https://doi.org/10.1038/NCLIMATE1911

Hollis, D., McCarthy, M., Kendon, M., Legg, T., Simpson, I., 2019. HadUK-Grid—A new UK dataset of gridded climate observations. Geosci Data J 6, 151–159. https://doi.org/10.1002/gdj3.78

Hughes, J.P., Guttorp, P., Charles, S.P., 1999. A non-homogeneous hidden Markov model for precipitation occurrence. J R Stat Soc Ser C Appl Stat 48, 15–30. https://doi.org/10.1111/1467-9876.00136

IPCC, 2022. Climate Change 2022: Mitigation of Climate Change. Contribution of Working Group III to the Sixth Assessment Report of the Intergovernmental Panel on Climate Change. Cambridge University Press, Cambridge, UK and New York, NY, USA. https://doi.org/10.1017/9781009157926

IPCC, 2021. Climate Change 2021: The Physical Science Basis. Contribution of Working Group I to the Sixth Assessment Report of the Intergovernmental Panel on Climate Change. Cambridge University Press, Cambridge, United Kingdom and New York, NY, USA. https://doi.org/10.1017/9781009157896

IPCC, 2014. Climate Change 2014: Synthesis Report. IPCC, Geneva, Switzerland.

Jesus, J., Chandler, R.E., 2011. Estimating functions and the generalized method of moments. Interface Focus 1, 871–885. https://doi.org/10.1098/rsfs.2011.0057

Kaczmarska, J., Isham, V., Onof, C., 2014. Point process models for fine-resolution rainfall. Hydrological Sciences Journal 59, 1972–1991. https://doi.org/10.1080/02626667.2014.925558

Kaczmarska, J.M., Isham, V.S., Northrop, P., 2015. Local generalised method of moments: an application to point process-based rainfall models. Environmetrics 26, 312–325. https://doi.org/10.1002/env.2338

Kang, B., Ramírez, J.A., 2010. A coupled stochastic space-time intermittent random cascade model for rainfall downscaling. Water Resour Res 46, 2008WR007692. https://doi.org/10.1029/2008WR007692

Karypis, G., Kumar, V., 1997. METIS: A Software Package for Partitioning Unstructured Graphs, Partitioning Meshes, and Computing Fill-Reducing Orderings of Sparse Matrices.

Kay, A., Jones, R.G., 2012. Comparison of the use of alternative UKCP09 products for modelling the impacts of climate change on flood frequency. Clim Change 114, 211–230. https://doi.org/10.1007/s10584-011-0395-z

Kay, A., Rudd, A., Davies, H., Kendon, E., Jones, R., 2015. Use of very high resolution climate model data for hydrological modelling: baseline performance and future flood changes. Clim Change 133, 193–208. https://doi.org/10.1007/s10584-015-1455-6

Kendon, E.J., Chris Short, James Pope, Steven Chan, Jonathan Wilkinson, Simon Tucker, Phil Bett, Glen Harris, 2021. Update to UKCP Local (2.2km) projections [WWW Document].

Kendon, E.J., Fosser, G., Murphy, J., Chan, S., Clark, R., Harris, G., Lock, A., Lowe, J., Martin, G., Pirret, J., Roberts, N., Sanderson, M., Tucker, S., 2019a. UKCP Convection-permitting model projections: Science report [WWW Document]. URL https://www.metoffice.gov.uk/pub/data/weather/uk/ukcp18/science-reports/UKCP-Convection-permitting-model-projections-report.pdf

Kendon, E.J., Roberts, N.M., Fosser, G., Martin, G.M., Lock, A.P., Murphy, J.M., Senior, C.A., Tucker, S.O., 2020a. Greater future UK winter precipitation increase in new convection-permitting scenarios. J Clim. https://doi.org/10.1175/JCLI-D-20-0089.1

Kendon, E.J., Roberts, N.M., Fowler, H.J., Roberts, M.J., Chan, S.C., Senior, C.A., 2014. Heavier summer downpours with climate change revealed by weather forecast resolution model. Nat Clim Chang 4, 570–576. https://doi.org/10.1038/nclimate2258

Kendon, E.J., Roberts, N.M., Senior, C.A., Roberts, M.J., 2012. Realism of Rainfall in a Very High-Resolution Regional Climate Model. J Clim 25, 5791–5806. https://doi.org/10.1175/JCLI-D-11-00562.1

Kendon, E.J., Steven Chan, Hayley Fowler, Fai Fung, Jason Lowe, James Murphy, Cath Senior, Christopher Short, Simon Tucker, Jonathan Wilkinson, 2020b. Technical note: Issue with UKCP Local (2.2km) simulation data.

Kendon, E.J., Stratton, R.A., Tucker, S., Marsham, J.H., Berthou, S., Rowell, D.P., Senior, C.A., 2019b. Enhanced future changes in wet and dry extremes over Africa at convection-permitting scale. Nat Commun 10, 1794. https://doi.org/10.1038/s41467-019-09776-9

Kharin, V. v, Zwiers, F.W., Zhang, X., Wehner, M., 2013. Changes in temperature and precipitation extremes in the CMIP5 ensemble. Clim Change 119, 345–357. https://doi.org/10.1007/s10584-013-0705-8

Kilsby, C.G., Jones, P.D., Burton, A., Ford, A.C., Fowler, H.J., Harpham, C., James, P., Smith, A., Wilby, R.L., 2007. A daily weather generator for use in climate change studies. Environmental Modelling and Software 22, 1705–1719. https://doi.org/10.1016/j.envsoft.2007.02.005

Kleiber, W., Katz, R.W., Rajagopalan, B., 2012. Daily spatiotemporal precipitation simulation using latent and transformed Gaussian processes. Water Resour Res 48. https://doi.org/10.1029/2011WR011105

Knutti, R., 2008. Should we believe model predictions of future climate change? Philosophical Transactions of the Royal Society A: Mathematical, Physical and Engineering Sciences 366, 4647–4664. https://doi.org/10.1098/rsta.2008.0169

Kundu, P.K., Bell, T.L., 2003. A stochastic model of space-time variability of mesoscale rainfall: Statistics of spatial averages. Water Resour Res 39. https://doi.org/10.1029/2002WR001802

Kurniadi, A., Weller, E., Min, S.-K., Seong, M.-G., 2021. Independent ENSO and IOD impacts on rainfall extremes over Indonesia. International Journal of Climatology 41, 3640–3656. https://doi.org/https://doi.org/10.1002/joc.7040

Lall, U., Sharma, A., 1996. A Nearest Neighbor Bootstrap For Resampling Hydrologic Time Series. Water Resour Res 32, 679–693. https://doi.org/10.1029/95WR02966

Lamb, R., Faulkner, D., Zaidman, M., 2010. Fluvial Design Guide, Environment Agency. Environment Agency, UK.

Leblois, E., Creutin, J.-D., 2013. Space-time simulation of intermittent rainfall with prescribed advection field: Adaptation of the turning band method. Water Resour Res 49, 3375–3387. https://doi.org/10.1002/wrcr.20190

Lenderink, G., van Meijgaard, E., 2008. Increase in hourly precipitation extremes beyond expectations from temperature changes. Nat Geosci. https://doi.org/10.1038/ngeo262

Leonard, M., Lambert, M.F., Metcalfe, A. v, Cowpertwait, P.S.P., 2008. A space-time Neyman-Scott rainfall model with defined storm extent. Water Resour Res 44. https://doi.org/10.1029/2007WR006110

Lewis E., Quinn, N., Blenkinsop S., Fowler H.J., Freer J., Tanguy M., Hitt O., Coxon G., Bates P., Woods R., Fry M., Chevuturi A., Swain O., White S M, 2022. Gridded estimates of hourly areal rainfall for Great Britain 1990-2016 [CEH-GEAR1hr] v2. https://doi.org/10.5285/fc9423d6-3d54-467f-bb2b-fc7357a3941f

Lewis, M.W., Gray, S.L., 2010. Categorisation of synoptic environments associated with mesoscale convective systems over the UK. Atmos Res. https://doi.org/https://doi.org/10.1016/j.atmosres.2010.04.001

Li, J., Sharma, A., Johnson, F., Evans, J., 2015. Evaluating the effect of climate change on areal reduction factors using regional climate model projections. J Hydrol (Amst). https://doi.org/https://doi.org/10.1016/j.jhydrol.2015.06.067

Li, X.-F., Blenkinsop, S., Barbero, R., Yu, J., Lewis, E., Lenderink, G., Guerreiro, S., Chan, S., Li, Y., Ali, H., Villalobos Herrera, R., Kendon, E., Fowler, H.J., 2020. Global distribution of the intensity and frequency of hourly precipitation and their responses to ENSO. Clim Dyn 54, 4823–4839. https://doi.org/10.1007/s00382-020-05258-7

Lochbihler, K., Lenderink, G., Siebesma, A.P., 2019. Response of Extreme Precipitating Cell Structures to Atmospheric Warming. Journal of Geophysical Research: Atmospheres. https://doi.org/10.1029/2018JD029954

Loriaux, J.M., Lenderink, G., Siebesma, A.P., 2016. Peak precipitation intensity in relation to atmospheric conditions and large-scale forcing at midlatitudes. Journal Of Geophysical Research-Atmospheres 121. https://doi.org/10.1002/2015JD024274

Lovejoy, S., Schertzer, D., 2013. The Weather and Climate: Emergent Laws and Multifractal Cascades. Cambridge University Press, Cambridge. https://doi.org/10.1017/CBO9781139093811

Lucas, B.D., Kanade, T., 1981. An iterative image registration technique with an application to stereo vision. Vancouver.

Madsen, H., Arnbjerg-Nielsen, K., Mikkelsen, P.S., 2009. Update of regional intensity–duration–frequency curves in Denmark: Tendency towards increased storm intensities. Atmos Res 92, 343–349. https://doi.org/10.1016/j.atmosres.2009.01.013

Maraun, D., Wetterhall, F., Ireson, A.M., Chandler, R.E., Kendon, E.J., Widmann, M., Brienen, S., Rust, H.W., Sauter, T., Themeßl, M., Venema, V.K.C., Chun, K.P., Goodess, C.M., Jones, R.G., Onof, C., Vrac, M., Thiele-Eich, I., 2010. Precipitation downscaling under climate change: Recent developments to bridge the gap between dynamical models and the end user. Reviews of Geophysics 48. https://doi.org/10.1029/2009RG000314

Maraun, D., Widmann, M., 2018. Statistical Downscaling and Bias Correction for Climate Research. Cambridge University Press, Cambridge. https://doi.org/10.1017/9781107588783

Mark Ogden, 2019. Investigation Report into the flooding in Norwich Urban Area: 2016 to 2018 [WWW Document].

Marra, F., Zoccatelli, D., Armon, M., Morin, E., 2019. A simplified MEV formulation to model extremes emerging from multiple nonstationary underlying processes. Adv Water Resour 127, 280–290. https://doi.org/https://doi.org/10.1016/j.advwatres.2019.04.002

Marsh, T., Cole, G., Wilby, R., 2007. Major droughts in England and Wales, 1800–2006. Weather 62, 87–93. https://doi.org/10.1002/wea.67

Marshall, J.S., Palmer, W.M.K., 1948. The distribution of raindrops with size. Journal of Meteorology 5, 165–166. https://doi.org/10.1175/1520-0469(1948)005<0165:TDORWS>2.0.CO;2

Martínez-de la Torre, A., Blyth, E.M., Weedon, G.P., 2019. Using observed river flow data to improve the hydrological functioning of the JULES land surface model (vn4.3) used for regional coupled modelling in Great Britain (UKC2). Geosci Model Dev 12, 765–784. https://doi.org/10.5194/gmd-12-765-2019

Martins, E.S., Stedinger, J.R., 2000. Generalized maximum-likelihood generalized extreme-value quantile estimators for hydrologic data. Water Resour Res 36, 737–744. https://doi.org/https://doi.org/10.1029/1999WR900330

Maslin, M., Austin, P., 2012. Climate models at their limit? Nature 486, 183–184. https://doi.org/10.1038/486183a

McRobie, F.H., Wang, L.-P., Onof, C., Kenney, S., 2013. A spatial-temporal rainfall generator for urban drainage design. Water Sci Technol 68, 240–249. https://doi.org/10.2166/wst.2013.241

McSweeney, C., Thornton, H., 2020. UKCP European Circulation Indices: Weather Patterns. UKCP Factsheet.

Mehrotra, R., Sharma, A., 2005. A nonparametric nonhomogeneous hidden Markov model for downscaling of multisite daily rainfall occurrences. Journal of Geophysical Research - Atmospheres 110, D16108. https://doi.org/10.1029/2004JD005677

Met Office, 2019a. UKCP18 Guidance: Data availability, access and formats [WWW Document]. URL https://www.metoffice.gov.uk/binaries/content/assets/metofficegovuk/pdf/research/ukcp/ukcp18-guidance-data-availability-access-and-formats.pdf (accessed 6.7.22).

Met Office, 2019b. UKCP18 Factsheet: UKCP Local (2.2km) Projections [WWW Document]. URL https://www.metoffice.gov.uk/binaries/content/assets/metofficegovuk/pdf/research/ukcp/ukcp18-factsheet-local-2.2km.pdf

Met Office, 2019c. UKCP18 Guidance: Bias correction [WWW Document]. URL https://www.metoffice.gov.uk/binaries/content/assets/metofficegovuk/pdf/research/ukcp/ukcp18-guidance---how-to-bias-correct.pdf (accessed 6.7.22).

Met Office, 2016. Technical note: Issue with UKCP Local (2.2km) simulation data [WWW Document]. URL https://www.metoffice.gov.uk/binaries/content/assets/metofficegovuk/pdf/weather/learn-about/uk-past-events/regional-climates/eastern-england_-climate---met-office.pdf (accessed 10.2.20).

Met Office, 2003. Met Office Rain Radar Data from the NIMROD System. NCAS British Atmospheric Data Centre [WWW Document].

Met Office Hadley Centre, 2019. UKCP18 Convection-Permitting Model Projections for the UK at 2.2km resolution [WWW Document]. URL http://catalogue.ceda.ac.uk/uuid/ad2ac0ddd3f34210b0d6e19bfc335539

Milly, P.C.D., Betancourt, J., Falkenmark, M., Hirsch, R.M., Kundzewicz, Z.W., Lettenmaier, D.P., Stouffer, R.J., 2008. Stationarity Is Dead: Whither Water Management? Science (1979) 319, 573–574. https://doi.org/10.1126/science.1151915

Mishra, V., Dominguez, F., Lettenmaier, D.P., 2012. Urban precipitation extremes: How reliable are regional climate models? Geophys Res Lett 39. https://doi.org/10.1029/2011GL050658

Monteith, J.L., 1965. Evaporation and environment. Symp Soc Exp Biol 19, 205—234.

Moretti, G., Montanari, A., 2008. Inferring the flood frequency distribution for an ungauged basin using a spatially distributed rainfall-runoff model. Hydrol Earth Syst Sci 12, 1141–1152. https://doi.org/10.5194/hess-12-1141-2008

Moseley, C., Henneberg, O., Haerter, J.O., 2019. A Statistical Model for Isolated Convective Precipitation Events. J Adv Model Earth Syst 11, 360–375. https://doi.org/10.1029/2018MS001383

Murphy, J.M., Harris, G.R., Sexton, D.M.H., Kendon, E.J., Bett, P.E., Clark, R.T., Eagle, K.E., Fosser, G., Fung, F., Lowe, J.A., McDonald, R.E., McInnes, R.N., McSweeney, C.F., Mitchell, J.F.B., Rostron, J.W., H.E. Thornton, Tucker, S., Yamazaki, K., 2018. UKCP18 Land Projections: Science Report.

Murphy, J.M., Sexton, D.M.H., Barnett, D.N., Jones, G.S., Webb, M.J., Collins, M., Stainforth, D.A., 2004. Quantification of modelling uncertainties in a large ensemble of climate change simulations. Nature 430, 768–772. https://doi.org/10.1038/nature02771

NAKANO, M., KATO, T., HAYASHI, S., KANADA, S., YAMADA, Y., KURIHARA, K., 2012. Development of a 5-km-Mesh Cloud-System-Resolving Regional Climate Model at the Meteorological Research Institute. Journal of the Meteorological Society of Japan. Ser. II 90A, 339–350. https://doi.org/10.2151/jmsj.2012-A19

NASA Shuttle Radar Topography Mission (SRTM), 2013. Shuttle Radar Topography Mission (SRTM) Global.

Nash, J.E., Sutcliffe, J. v, 1970. River flow forecasting through conceptual models part I — A discussion of principles. J Hydrol (Amst) 10, 282–290. https://doi.org/10.1016/0022-1694(70)90255-6

Neal, R.A., Phillips, I.D., 2009. Summer daily precipitation variability over the East Anglian region of Great Britain. International Journal of Climatology 29, 1661–1679. https://doi.org/10.1002/joc.1826

Norfolk County Council, 2015. Investigation Report into the flooding within the Norwich Urban Area during the summer of 2014.

Northrop, P., 1998. A clustered spatial-temporal model of rainfall. Proceedings of the Royal Society of London. Series A: Mathematical, Physical and Engineering Sciences 454, 1875–1888. https://doi.org/10.1098/rspa.1998.0238

NRFA, 2019a. Stour at Stratford St Mary [WWW Document]. URL https://nrfa.ceh.ac.uk/data/station/info/36001

NRFA, 2019b. Gauged Daily Flow Data [WWW Document]. URL https://nrfa.ceh.ac.uk

Ochoa-Rodriguez, S., Wang, L. -P., Willems, P., Onof, C., 2019. A Review of Radar-Rain Gauge Data Merging Methods and Their Potential for Urban Hydrological Applications. Water Resour Res 55, 6356–6391. https://doi.org/10.1029/2018WR023332

Ochoa-Rodriguez, S., Wang, L.-P., Gires, A., Pina, R.D., Reinoso-Rondinel, R., Bruni, G., Ichiba, A., Gaitan, S., Cristiano, E., van Assel, J., Kroll, S., Murlà-Tuyls, D., Tisserand, B., Schertzer, D., Tchiguirinskaia, I., Onof, C., Willems, P., ten Veldhuis, M.-C., 2015. Impact of spatial and temporal resolution of rainfall inputs on urban hydrodynamic modelling outputs: A multi-catchment investigation. J Hydrol (Amst) 531, 389–407. https://doi.org/10.1016/j.jhydrol.2015.05.035

O'Gorman, P.A., Schneider, T., 2009. The physical basis for increases in precipitation extremes in simulations of 21st-century climate change. Proceedings of the National Academy of Sciences 106, 14773–14777. https://doi.org/10.1073/pnas.0907610106

Onof, C., Chandler, R., Kakou, A., Northrop, P., Wheater, H., Isham, V., 2000. Rainfall modelling using Poisson-cluster processes: a review of developments. Stochastic Environmental Research and Risk Assessment 14, 384. https://doi.org/10.1007/s004770000043

Onof, C., Wang, L.-P., 2020. Modelling rainfall with a Bartlett–Lewis process: new developments. Hydrol Earth Syst Sci 24, 2791–2815. https://doi.org/10.5194/hess-24-2791-2020

Ordnance Survey, 2018. OS MasterMap Topography Layer - OS Terrain 50 [WWW Document]. URL https://digimap.edina.ac.uk/roam/download/os

Oueslati, B., Yiou, P., Jézéquel, A., 2019. Revisiting the dynamic and thermodynamic processes driving the record-breaking January 2014 precipitation in the southern UK. Sci Rep 9, 2859. https://doi.org/10.1038/s41598-019-39306-y

Over, T.M., Gupta, V.K., 1996. A space-time theory of mesoscale rainfall using random cascades. Journal of Geophysical Research: Atmospheres 101, 26319–26331. https://doi.org/10.1029/96JD02033

Palmer, T.N., 2013. Climate extremes and the role of dynamics. Proceedings of the National Academy of Sciences 110, 5281–5282. https://doi.org/10.1073/pnas.1303295110

Papoulis, A., 1965. Probability, Random Variables and Stochastic Processes.

Park, J., Onof, C., Kim, D., 2019. A hybrid stochastic rainfall model that reproduces some important rainfall characteristics at hourly to yearly timescales. Hydrol Earth Syst Sci 23, 989–1014. https://doi.org/10.5194/hess-23-989-2019

Paschalis, A., Fatichi, S., Molnar, P., Rimkus, S., Burlando, P., 2014a. On the effects of small scale space–time variability of rainfall on basin flood response. J Hydrol (Amst) 514, 313–327. https://doi.org/10.1016/j.jhydrol.2014.04.014

Paschalis, A., Molnar, P., Fatichi, S., Burlando, P., 2014b. On temporal stochastic modeling of precipitation, nesting models across scales. Adv Water Resour 63, 152–166. https://doi.org/10.1016/j.advwatres.2013.11.006

Paschalis, A., Molnar, P., Fatichi, S., Burlando, P., 2013. A stochastic model for high-resolution space-time precipitation simulation. Water Resour Res 49, 8400–8417. https://doi.org/10.1002/2013WR014437

Pegram, G.G.S., Clothier, A.N., 2001a. High resolution space–time modelling of rainfall: the "String of Beads" model. J Hydrol (Amst) 241, 26–41. https://doi.org/10.1016/S0022-1694(00)00373-5

Pegram, G.G.S., Clothier, A.N., 2001b. Downscaling rainfields in space and time, using the String of Beads model in time series mode. Hydrol Earth Syst Sci 5, 175–186. https://doi.org/10.5194/hess-5-175-2001

Peleg, N., Ban, N., Gibson, M.J., Chen, A.S., Paschalis, A., Burlando, P., Leitão, J.P., 2022. Mapping storm spatial profiles for flood impact assessments. Adv Water Resour 166, 104258. https://doi.org/10.1016/j.advwatres.2022.104258

Peleg, N., Blumensaat, F., Molnar, P., Fatichi, S., Burlando, P., 2017a. Partitioning the impacts of spatial and climatological rainfall variability in urban drainage modeling. Hydrol Earth Syst Sci 21, 1559–1572. https://doi.org/10.5194/hess-21-1559-2017

Peleg, N., Fatichi, S., Paschalis, A., Molnar, P., Burlando, P., 2017b. An advanced stochastic weather generator for simulating 2-D high-resolution climate variables. J Adv Model Earth Syst 9, 1595–1627. https://doi.org/10.1002/2016MS000854

Peleg, N., Marra, F., Fatichi, S., Molnar, P., Morin, E., Sharma, A., Burlando, P., 2018. Intensification of Convective Rain Cells at Warmer Temperatures Observed from High-Resolution Weather Radar Data. J Hydrometeorol 19, 715–726. https://doi.org/10.1175/JHM-D-17-0158.1

Peleg, N., Molnar, P., Burlando, P., Fatichi, S., 2019. Exploring stochastic climate uncertainty in space and time using a gridded hourly weather generator. J Hydrol (Amst) 571, 627–641. https://doi.org/10.1016/j.jhydrol.2019.02.010

Peleg, N., Skinner, C., Fatichi, S., Molnar, P., 2020. Temperature effects on the spatial structure of heavy rainfall modify catchment hydro-morphological response. Earth Surface Dynamics 8, 17–36. https://doi.org/10.5194/esurf-8-17-2020

Peleg, N., Skinner, C., Ramirez, J.A., Molnar, P., 2021. Rainfall spatial-heterogeneity accelerates landscape evolution processes. Geomorphology 390, 107863. https://doi.org/10.1016/j.geomorph.2021.107863

Pfahl, S., O'Gorman, P.A., Fischer, E.M., 2017. Understanding the regional pattern of projected future changes in extreme precipitation. Nat Clim Chang 7, 423–427. https://doi.org/10.1038/nclimate3287

Porporato, A., Laio, F., Ridolfi, L., Rodriguez-Iturbe, I., 2001. Plants in water-controlled ecosystems: active role in hydrologic processes and response to water stress: III. Vegetation water stress. Adv Water Resour 24, 725–744. https://doi.org/10.1016/S0309-1708(01)00006-9

Prein, A.F., Langhans, W., Fosser, G., Ferrone, A., Ban, N., Goergen, K., Keller, M., Tölle, M., Gutjahr, O., Feser, F., Brisson, E., Kollet, S., Schmidli, J., Lipzig, N.P.M., Leung, R., 2015. A review on regional convection-permitting climate modeling: Demonstrations, prospects, and challenges. Reviews of Geophysics 53, 323–361. https://doi.org/10.1002/2014RG000475

Prein, A.F., Liu, C., Ikeda, K., Trier, S.B., Rasmussen, R.M., Holland, G.J., Clark, M.P., 2017a. Increased rainfall volume from future convective storms in the US. Nat Clim Chang 7, 880–884. https://doi.org/10.1038/s41558-017-0007-7

Prein, A.F., Rasmussen, R.M., Ikeda, K., Liu, C., Clark, M.P., Holland, G.J., 2017b. The future intensification of hourly precipitation extremes. Nat Clim Chang 7, 48–52. https://doi.org/10.1038/nclimate3168

Ramesh, N.I., Thayakaran, R., Onof, C., 2013. Multi-site doubly stochastic Poisson process models for fine-scale rainfall. Stochastic Environmental Research and Risk Assessment 27, 1383–1396. https://doi.org/10.1007/s00477-012-0674-x

Rasmussen, K.L., Prein, A.F., Rasmussen, R.M., Ikeda, K., Liu, C., 2017. Changes in the convective population and thermodynamic environments in convection-permitting regional climate simulations over the United States. Clim Dyn. https://doi.org/10.1007/s00382-017-4000-7

Raut, B.A., Seed, A.W., Reeder, M.J., Jakob, C., 2018. A Multiplicative Cascade Model for High-Resolution Space-Time Downscaling of Rainfall. Journal of Geophysical Research: Atmospheres 123, 2050–2067. https://doi.org/10.1002/2017JD027148

Remondi, F., Kirchner, J.W., Burlando, P., Fatichi, S., 2018. Water Flux Tracking With a Distributed Hydrological Model to Quantify Controls on the Spatiotemporal

Variability of Transit Time Distributions. Water Resour Res 54, 3081–3099. https://doi.org/10.1002/2017WR021689

Riahi, K., van Vuuren, D.P., Kriegler, E., Edmonds, J., O'Neill, B.C., Fujimori, S., Bauer, N., Calvin, K., Dellink, R., Fricko, O., Lutz, W., Popp, A., Cuaresma, J.C., KC, S., Leimbach, M., Jiang, L., Kram, T., Rao, S., Emmerling, J., Ebi, K., Hasegawa, T., Havlik, P., Humpenöder, F., da Silva, L.A., Smith, S., Stehfest, E., Bosetti, V., Eom, J., Gernaat, D., Masui, T., Rogelj, J., Strefler, J., Drouet, L., Krey, V., Luderer, G., Harmsen, M., Takahashi, K., Baumstark, L., Doelman, J.C., Kainuma, M., Klimont, Z., Marangoni, G., Lotze-Campen, H., Obersteiner, M., Tabeau, A., Tavoni, M., 2017. The Shared Socioeconomic Pathways and their energy, land use, and greenhouse gas emissions implications: An overview. Global Environmental Change 42, 153–168. https://doi.org/10.1016/j.gloenvcha.2016.05.009

Ritter, A., Muñoz-Carpena, R., 2013. Performance evaluation of hydrological models: Statistical significance for reducing subjectivity in goodness-of-fit assessments. J Hydrol (Amst) 480, 33–45. https://doi.org/10.1016/j.jhydrol.2012.12.004

Robinson, E.L., Blyth, E., Clark, D.B., Comyn-Platt, E., Finch, J., Rudd, A.C., 2016. Climate hydrology and ecology research support system potential evapotranspiration dataset for Great Britain (1961-2015) [CHESS-PE]. https://doi.org/10.5285/8baf805d-39ce-4dac-b224-c926ada353b7

Rodriguez-Iturbe, I., Cox, D.R., Eagleson, P.S., 1986. Spatial Modelling of Total Storm Rainfall. Proceedings of the Royal Society of London. A. Mathematical and Physical Sciences 403, 27–50. https://doi.org/10.1098/rspa.1986.0002

Rowland, C.S., Morton, R.D., Carrasco, L., McShane, G., O'Neil, A.W., Wood, C.M., 2017. Land Cover Map 2015 (25m raster, GB), NERC Environmental Information Data Centre.

Rulli, M.C., Rosso, R., 2002. An integrated simulation method for flash-flood risk assessment: 1. Frequency predictions in the Bisagno River by combining stochastic and deterministic methods. Hydrol Earth Syst Sci 6, 267–284. https://doi.org/10.5194/hess-6-267-2002

Rust, W., Cuthbert, M., Bloomfield, J., Corstanje, R., Howden, N., Holman, I., 2021. Exploring the role of hydrological pathways in modulating multi-annual climate teleconnection periodicities from UK rainfall to streamflow. Hydrol Earth Syst Sci 25, 2223–2237. https://doi.org/10.5194/hess-25-2223-2021

Rysman, J.-F., Verrier, S., Lemaître, Y., Moreau, E., 2013. Space-time variability of the rainfall over the western Mediterranean region: A statistical analysis. Journal of Geophysical Research: Atmospheres 118, 8448–8459. https://doi.org/10.1002/jgrd.50656

Sapriza Azuri, G., Jódar, J., Carrera, J., Gupta, H. v., 2013. Stochastic Simulation of Nonstationary Rainfall Fields, Accounting for Seasonality and Atmospheric Circulation Pattern Evolution. Math Geosci 45, 621–645. https://doi.org/10.1007/s11004-013-9467-0

Saxton, K.E., Rawls, W.J., 2006. Soil Water Characteristic Estimates by Texture and Organic Matter for Hydrologic Solutions. Soil Science Society of America Journal 70, 1569. https://doi.org/10.2136/sssaj2005.0117

Scherrer, S.C., Fischer, E.M., Posselt, R., Liniger, M.A., Croci-Maspoli, M., Knutti, R., 2016. Emerging trends in heavy precipitation and hot temperature extremes in Switzerland. Journal of Geophysical Research: Atmospheres 121, 2626–2637. https://doi.org/10.1002/2015JD024634

Schertzer, D., Lovejoy, S., 2013. Physical Modeling and Analysis of Rain and Clouds by Anisotropic Scaling Multiplicative Processes. pp. 9693–9714. https://doi.org/10.1002/9781118782071.ch16

Schiemann, R., Demory, M.-E., Shaffrey, L.C., Strachan, J., Vidale, P.L., Mizielinski, M.S., Roberts, M.J., Matsueda, M., Wehner, M.F., Jung, T., 2016. The Resolution Sensitivity of Northern Hemisphere Blocking in Four 25-km Atmospheric Global Circulation Models. J Clim 30, 337–358. https://doi.org/10.1175/JCLI-D-16-0100.1

Schleiss, M., 2020. A new discrete multiplicative random cascade model for downscaling intermittent rainfall fields. Hydrol Earth Syst Sci 24, 3699–3723. https://doi.org/10.5194/hess-24-3699-2020

Seed, A.W., Pierce, C.E., Norman, K., 2013. Formulation and evaluation of a scale decomposition-based stochastic precipitation nowcast scheme. Water Resour Res 49, 6624–6641. https://doi.org/10.1002/wrcr.20536

Segond, M.-L., Onof, C., 2009. Modelling of space–time rainfall for three UK regions. Proceedings of the Institution of Civil Engineers - Water Management 162, 147–158. https://doi.org/10.1680/wama.2009.162.2.147

Seo, Y., Schmidt, A.R., Sivapalan, M., 2012. Effect of storm movement on flood peaks: Analysis framework based on characteristic timescales. Water Resour Res 48, n/a. https://doi.org/10.1029/2011WR011761

Shepherd, T.G., 2014. Atmospheric circulation as a source of uncertainty in climate change projections. Nat Geosci 7, 703–708. https://doi.org/10.1038/ngeo2253

Sigrist, F., Künsch, H.R., Stahel, W.A., 2012. A dynamic nonstationary spatio-temporal model for short term prediction of precipitation. Ann Appl Stat 6. https://doi.org/10.1214/12-AOAS564

Sillmann, J., Kharin, V. v, Zhang, X., Zwiers, F.W., Bronaugh, D., 2013. Climate extremes indices in the CMIP5 multimodel ensemble: Part 1. Model evaluation in the present climate. Journal of Geophysical Research: Atmospheres 118, 1716–1733. https://doi.org/10.1002/jgrd.50203

Skinner, C.J., Peleg, N., Quinn, N., Coulthard, T.J., Molnar, P., Freer, J., 2020. The impact of different rainfall products on landscape modelling simulations. Earth Surf Process Landf 45, 2512–2523. https://doi.org/10.1002/esp.4894

Solman, S.A., Orlanski, I., 2014. Poleward Shift and Change of Frontal Activity in the Southern Hemisphere over the Last 40 Years. J Atmos Sci 71, 539–552. https://doi.org/10.1175/JAS-D-13-0105.1

Sordo-Ward, A., Bianucci, P., Garrote, L., Granados, A., 2016. The Influence of the Annual Number of Storms on the Derivation of the Flood Frequency Curve through Event-Based Simulation. Water (Basel) 8, 335. https://doi.org/10.3390/w8080335

Sørup, H.J.D., Christensen, O.B., Arnbjerg-Nielsen, K., Mikkelsen, P.S., 2016. Downscaling future precipitation extremes to urban hydrology scales using a spatio-temporal

Neyman–Scott weather generator. Hydrol Earth Syst Sci 20, 1387–1403. https://doi.org/10.5194/hess-20-1387-2016

Svensson, C., Jones, D.A., 2010. Review of methods for deriving areal reduction factors. J Flood Risk Manag 3, 232–245. https://doi.org/10.1111/j.1753-318X.2010.01075.x

Syafrina, A.H., Zalina, M.D., Juneng, L., 2015. Historical trend of hourly extreme rainfall in Peninsular Malaysia. Theor Appl Climatol 120, 259–285. https://doi.org/10.1007/s00704-014-1145-8

Tanguy, M., Dixon, H., Prosdocimi, I., Morris, D.G., Keller, V.D.J., 2019. Gridded estimates of daily and monthly areal rainfall for the United Kingdom (1890-2017) [CEH-GEAR]. https://doi.org/10.5285/ee9ab43d-a4fe-4e73-afd5-cd4fc4c82556

Taylor, K.E., Stouffer, R.J., Meehl, G.A., 2012. An Overview of CMIP5 and the Experiment Design. Bull Am Meteorol Soc 93, 485–498. https://doi.org/10.1175/BAMS-D-11-00094.1

Tebaldi, C., Knutti, R., 2007. The use of the multi-model ensemble in probabilistic climate projections. Philosophical Transactions of the Royal Society A: Mathematical, Physical and Engineering Sciences 365, 2053–2075. https://doi.org/10.1098/rsta.2007.2076

Ulbrich, U., Fink, A.H., Klawa, M., Pinto, J.G., 2001. Three extreme storms over Europe in December 1999. Weather 56, 70–80. https://doi.org/10.1002/j.1477-8696.2001.tb06540.x

van Loenhout, J., McClean, D., 2022. human cost of disasters, An overview of the last 20 years 2000-2019. Belgium.

van Vuuren, D.P., Edmonds, J., Kainuma, M., Riahi, K., Thomson, A., Hibbard, K., Hurtt, G.C., Kram, T., Krey, V., Lamarque, J.-F., Masui, T., Meinshausen, M., Nakicenovic, N., Smith, S.J., Rose, S.K., 2011. The representative concentration pathways: an overview. Clim Change 109, 5–31. https://doi.org/10.1007/s10584-011-0148-z

Velasco-Forero, C.A., Sempere-Torres, D., Cassiraga, E.F., Jaime Gómez-Hernández, J., 2009. A non-parametric automatic blending methodology to estimate rainfall fields from rain gauge and radar data. Adv Water Resour 32, 986–1002. https://doi.org/10.1016/j.advwatres.2008.10.004

Vemula, S., Raju, K.S., Veena, S.S., Kumar, A.S., 2019. Urban floods in Hyderabad, India, under present and future rainfall scenarios: a case study. Natural Hazards 95, 637–655. https://doi.org/10.1007/s11069-018-3511-9

Verhoest, N.E.C., Vandenberghe, S., Cabus, P., Onof, C., Meca-Figueras, T., Jameleddine, S., 2010. Are stochastic point rainfall models able to preserve extreme flood statistics? Hydrol Process 24, 3439–3445. https://doi.org/10.1002/hyp.7867

Vischel, T., Lebel, T., Massuel, S., Cappelaere, B., 2009. Conditional simulation schemes of rain fields and their application to rainfall–runoff modeling studies in the Sahel. J Hydrol (Amst) 375, 273–286. https://doi.org/10.1016/j.jhydrol.2009.02.028

Wasko, C., Sharma, A., Westra, S., 2016. Reduced spatial extent of extreme storms at higher temperatures. Geophys Res Lett 43, 4026–4032. https://doi.org/10.1002/2016GL068509

Waymire, E.C., Gupta, V.K., 1993. A statistical analysis of mesoscale rainfall as a random cascade. Journal of Applied Meteorology 32, 251–267. https://doi.org/10.1175/1520-0450(1993)032%3C0251:ASAOMR%3E2.0.CO;2

Weisman, M.L., Skamarock, W.C., Klemp, J.B., 1997. The Resolution Dependence of Explicitly Modeled Convective Systems. Mon Weather Rev 125, 527–548. https://doi.org/10.1175/1520-0493(1997)125<0527:TRDOEM>2.0.CO;2

Westra, S., Alexander, L., Zwiers, F., 2013. Global increasing trends in annual maximum daily precipitation. J Clim 26. https://doi.org/10.1175/JCLI-D-12-00502.1

Westra, S., Fowler, H.J., Evans, J.P., Alexander, L. v, Berg, P., Johnson, F., Kendon, E.J., Lenderink, G., Roberts, N.M., 2014. Future changes to the intensity and frequency of short-duration extreme rainfall. Reviews of Geophysics 52, 522–555. https://doi.org/10.1002/2014RG000464

Wheater, H., Chandler, R., Onof, C., Isham, V., Bellone, E., Yang, C., Lekkas, D., Lourmas, G., Segond, M.-L., 2005. Spatial-temporal rainfall modelling for flood risk estimation. Stochastic Environmental Research and Risk Assessment 19, 403–416. https://doi.org/10.1007/s00477-005-0011-8

Wheater, H., Isham, V.S., Chandler, R.E., Onof, C.J., Stewart, E.J., 2006. Improved methods for national spatial-temporal rainfall and evaporation modelling for BSM. Defra.

Wheater, H., Isham, V.S., Cox, D.R., Chandler, R.E., Kakou, A., Northrop, P.J., Oh, L., Onof, C., Rodriguez-Iturbe, I., 2000. Spatial-temporal rainfall fields: modelling and statistical aspects. Hydrol Earth Syst Sci 4, 581–601. https://doi.org/10.5194/hess-4-581-2000

Wilcox, K.R., Shi, Z., Gherardi, L.A., Lemoine, N.P., Koerner, S.E., Hoover, D.L., Bork, E., Byrne, K.M., Cahill, J., Collins, S.L., Evans, S., Gilgen, A.K., Holub, P., Jiang, L., Knapp, A.K., LeCain, D., Liang, J., Garcia-Palacios, P., Peñuelas, J., Pockman, W.T., Smith, M.D., Sun, S., White, S.R., Yahdjian, L., Zhu, K., Luo, Y., 2017. Asymmetric responses of primary productivity to precipitation extremes: A synthesis of grassland precipitation manipulation experiments. Glob Chang Biol 23, 4376–4385. https://doi.org/10.1111/gcb.13706

Wilks, D.S., Wilby, R.L., 1999. The weather generation game: a review of stochastic weather models. Progress in Physical Geography: Earth and Environment 23, 329–357. https://doi.org/10.1177/030913339902300302

Willems, P., Arnbjerg-Nielsen, K., Olsson, J., Nguyen, V.T.V., 2012. Climate change impact assessment on urban rainfall extremes and urban drainage: Methods and shortcomings. Atmos Res 103, 106–118. https://doi.org/10.1016/j.atmosres.2011.04.003

Xiao, C., Wu, P., Zhang, L., Song, L., 2016. Robust increase in extreme summer rainfall intensity during the past four decades observed in China. Sci Rep 6, 38506. https://doi.org/10.1038/srep38506

Yang, C., Chandler, R.E., Isham, V.S., Wheater, H., 2005. Spatial-temporal rainfall simulation using generalized linear models. Water Resour Res 41. https://doi.org/10.1029/2004WR003739

Appendix
I. Appendices to Chapters 1-3

I.1. Moment estimates of the rainfall generator

For the model having a continuous storm type, several typos (Cowpertwait, 2010, Equation 10 and 11) are spotted in the equations of covariance and skewness and it was reformulated. The statistics have been validated through a comparison with the discrete version (Cowpertwait et al., 2013). Other moment estimates referring to Cowpertwait' s research (Cowpertwait, 1994,Cowpertwait, 1995,Cowpertwait, 2010) are also listed below.

Let $S_{\mathrm{P},i}(h)$ to be the rainfall time series aggregated into a time interval of h at $\mathrm{P} \in \mathbb{R}^2$, for a continuous storm type, we have

$$\mu_{\mathrm{P}}(h) = E\left[S_{\mathrm{P},i}(h)\right] = 2\pi\varphi_{\mathrm{P}} h \int_z \frac{\nu(z)\zeta_s f_z(z)}{\gamma_s^2(z)\eta(z)\xi(z)}\,dz$$

$$\begin{aligned}\Phi_{\mathrm{P}}(h,l) &= \mathrm{cov}\left[S_{\mathrm{P},i}(h), S_{\mathrm{P},i+l}(h)\right] \\ &= 2\pi\varphi_{\mathrm{P}}^2 \int_z \frac{\nu(z)\zeta_s f_z(z)}{\gamma_s^2(z)\xi^2(z)} \\ &\cdot [A(z,h,l)\eta(z)^{-3}\{4+\beta(z)^2\nu(z)\{\beta(z)^2-\eta(z)^2\}^{-1}\} \\ &- B(z,h,l)\nu(z)\{\beta(z)(\beta(z)^2-\eta(z)^2)\}^{-1}]dz\end{aligned}$$

$$\begin{aligned}\Psi_{\mathrm{P}}(h) &= E\left[\left\{S_{\mathrm{P},i}(h), S_{\mathrm{P},i+l}(h)\right\}^3\right] \\ &= 2\pi\varphi_{\mathrm{P}}^3 \int_z \frac{\nu(z)\zeta_s f_z(z)}{\gamma_s^2(z)\eta^4(z)\xi^3(z)}\Big[36h\eta(z) - 72 + 72e^{-h\eta(z)} + 36h\eta(z)e^{-\eta(z)h} \\ &+ 3\nu(z)Q_1(\eta(z),\beta(z),h)\beta(z)^{-1}\cdot(\beta(z)^2-\eta(z)^2)^{-2} \\ &+ \upsilon(z)^2 Q_2(\eta(z),\beta(z),h) \\ &\cdot\left\{2\beta(z)(\eta(z)^2-\beta(z)^2)\big(\eta(z)-\beta(z)\big)\right. \\ &\cdot\left.\big(2\beta(z)+\eta(z)\big)\big(\beta(z)+2\eta(z)\big)\right\}^{-1}\Big]\,dz\end{aligned}$$

$$\begin{aligned}\Phi_{\mathrm{a,b}}(h,l) &= \mathrm{cov}\left[S_{\mathrm{a},i}(h), S_{\mathrm{b},i+l}(h)\right] \\ &= \varphi_{\mathrm{a}}\varphi_{\mathrm{b}}\varphi_{\mathrm{P}}^2\Phi_{\mathrm{P}}(h,l) \\ &- 8\pi\varphi_{\mathrm{a}}\varphi_{\mathrm{b}}\int_z \frac{\nu(z)\kappa_{\mathrm{a,b}}[\gamma_s(z)]\zeta_s f_z(z)\{1-\kappa_{\mathrm{a,b}}[\gamma_c(z)]\}A(z,h,l)}{\gamma_s^2(z)\eta^3(z)\xi^2(z)}\,dz\end{aligned}$$

where Q_1 and Q_2 are high-order polynomials (Cowpertwait,1998, equations 2.10 and 2.11).

Probability of dry period (Cowpertwait, 2010):

$$P\left[S_{\mathrm{P},i}(h)=0\right]=\exp\left[-2\pi\int_z \frac{\zeta_s f_z(z)}{\gamma_s^2(z)}\left\{\int_0^\infty\{1-p(z,h,t)\}dt+\int_0^h\{1-p(z,t,0)\}dt\right\}dz\right]$$

where $p(z,h,t)=\exp\left[-\nu(z)+\nu(z)e^{-\beta(z)(t+h)}+\omega(z,t)\nu(z)\left\{1-e^{-\beta(z)t}\right\}\right]$, and $\omega(z,t)=1-\beta(z)\left\{e^{-\beta(z)t}-e^{-\eta(z)t}\right\}/\left[\{\eta(z)-\beta(z)\}\{1-e^{-\beta(z)t}\}\right]$. Hence, $p(z,t,0)=\exp\left[-\nu(z)+\nu(z)e^{-\beta(z)t}\right]$.

Given the analytical statistics, dimensionless statistics applied to fit the NS(s-t) are:

Coefficient of variation (CV): $\upsilon(h)=\Phi_{\mathrm{P}}^{1/2}(h,0)\mu_{\mathrm{P}}(h)^{-1}$

Coefficient of skewness (SKEW): $\kappa(h)=\Psi_{\mathrm{P}}(h)\Phi_{\mathrm{P}}^{-3/2}(h,0)$

Lag l autocorrelation (ACorr): $\rho(l,h)=\Phi_{\mathrm{P}}(h,l)\Phi_{\mathrm{P}}^{-1}(h,0)$

Cross correlation (CCorr): $\rho\left(\left\|\mathrm{P}_i-\mathrm{P}_j\right\|,0,h\right)=\Phi_{\mathrm{P}_i,\mathrm{P}_j}(h,0)\Phi_{\mathrm{P}_i}^{-1/2}(h,0)\Phi_{\mathrm{P}_j}^{-1/2}(h,0)$

Probability of dry period (PD): $\varphi(h)=P\left[S_{\mathrm{P},i}(h)=0\right]$

Cowpertwait, P.S.P., 2010. A spatial-temporal point process model with a continuous distribution of storm types. Water Resources Research. 46, n/a. https://doi.org/10.1029/2010WR009728.

Cowpertwait, P.S.P., 1995. A Generalized Spatial-Temporal Model of Rainfall Based on a Clustered Point Process. Proceedings of the Royal Society of London. Series A: Mathematical and Physical Sciences. 450, 163-175. https://doi.org/10.1098/rspa.1995.0077.

Cowpertwait, P.S.P., 1994. A Generalized Point Process Model for Rainfall. Proceedings of the Royal Society of London. Series A: Mathematical and Physical Sciences. 447, 23-37. https://doi.org/10.1098/rspa.1994.0126.

Cowpertwait, P.S.P, Ocio, D., Collazos, G., de Cos, O., Stocker, C., 2013. Regionalised spatiotemporal rainfall and temperature models for flood studies in the Basque Country, Spain. Hydrology and Earth System Sciences. 17, 479-494. https://doi.org/10.5194/hess-17-479-2013.

I.2. Comparison of radar-derived speed and ERA5 wind speed

Here the wind speed from ERA5 u/v component at 500hPa are compared with the tracked storm velocity obtained from weather radar. The West Midlands area is chosen and all slides between 2000 and 2018 are used in the scatter plots for each component (easting or northing direction).

From the figure we can see there is a clear correlation between storm advection speed obtained from these two data sources where the ERA5 500 hPa wind component tends to give a greater value than the radar-derived one.

Taking the maximum recorded storm speed in the UK (around 120 km/h, equivalent to 33.3 m/s) as a reference (Ulbrich et al., 2001). we can see that the radar derived speed outperforms the ERA5 wind component in reproducing the magnitude of the advection speed. It justifies the reason why we choose radar-derived storm speed in the thesis.

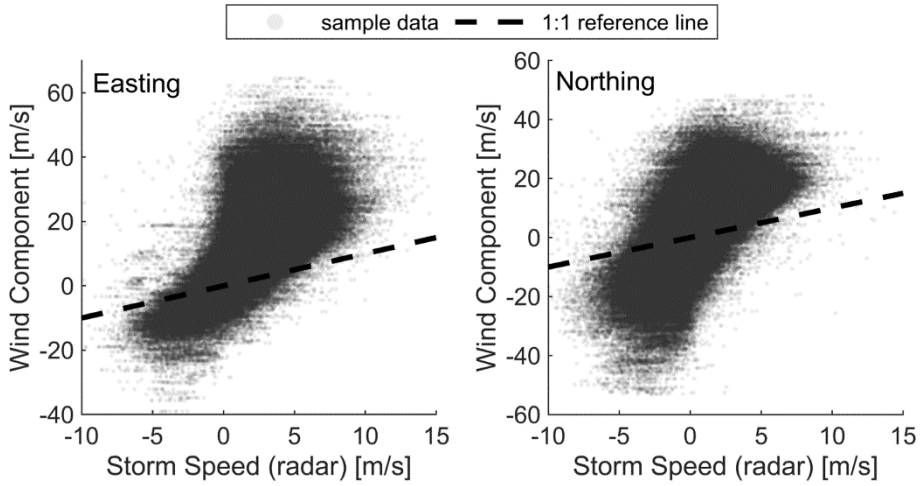


Figure I.2.1. Comparisons of Radar-based speed and ERA5-based speed with the easting component and northing component shown in two panels respectively.

I.3. Method to compute storm advection speed based on radar

The storm movement between each time slice is diagnosed with an optical flow technique, where Lucas-Kanade algorithm is used (Lucas and Kanade, 1981). Prior to implementing optical flow, each rainfall image is smoothed by a squared box kernel and then the transformed reflectively field (based on Marshall-Palmer relationship) is used for estimation. The size of the box kernel is defined to be 120 $km/h \times \Delta t$ so as to make sure that the method is able to detect the movement not quicker than 120 km/h along one direction (Bowler et al., 2004). The 120km/h is chosen in the thesis as it is close to the maximum advection speed of rainfall objects (Ulbrich et al., 2001).

I.4. Transforming radar images from Eulerian system to the Lagrangian system

A radar domain of 500 km × 500 km is used for the coordinate system transformation. Advection is assumed to be constant throughout the fields.

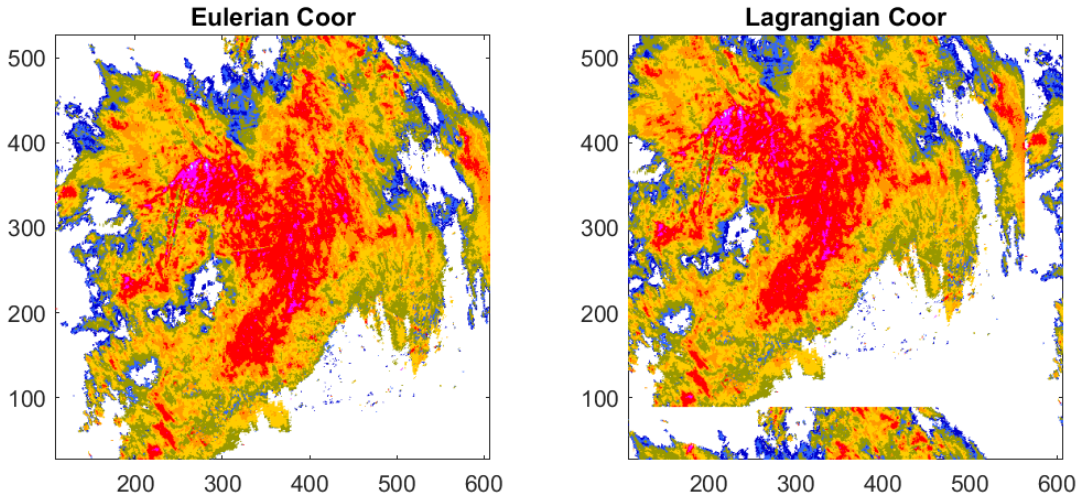


Figure II.4.1 Comparisons of raw radar field (Eulerian coordinate system) and converted rainfall fields in Lagrangian coordinate system

I.5. Data Use Agreement

CCC Marketplace™

This is a License Agreement between Yuting Chen ("User") and Copyright Clearance Center, Inc. ("CCC") on behalf of the Rightsholder identified in the order details below. The license consists of the order details, the Marketplace Order General Terms and Conditions below, and any Rightsholder Terms and Conditions which are included below.

All payments must be made in full to CCC in accordance with the Marketplace Order General Terms and Conditions below.

Order Date	30-Sep-2022	Type of Use	Republish in a thesis/dissertation
Order License ID	1274702-1		
ISSN	1749-6632	Publisher	NEW YORK ACADEMY OF SCIENCES
		Portion	Image/photo/illustration

LICENSED CONTENT

Publication Title	Annals of the New York Academy of Sciences	Publication Type	e-Journal
		Start Page	49
Article Title	Advances in understanding large-scale responses of the water cycle to climate change. : Expected water cycle response to climate change	End Page	75
		Issue	1
		Volume	1472
		URL	http://books.google.com/books?id=GY4G4RpFHxwC
Author/Editor	New York Academy of Sciences., HighWire Press.		
Date	01/01/1877		
Language	English		
Country	United States of America		
Rightsholder	John Wiley & Sons - Books		

REQUEST DETAILS

Portion Type	Image/photo/illustration	Distribution	U.K. and Commonwealth (excluding Canada)
Number of images / photos / illustrations	1	Translation	Original language of publication
Format (select all that apply)	Electronic	Copies for the disabled?	No
Who will republish the content?	Academic institution	Minor editing privileges?	Yes
		Incidental promotional use?	No
Duration of Use	Life of current edition		
Lifetime Unit Quantity	Up to 499	Currency	GBP
Rights Requested	Main product		

NEW WORK DETAILS

Title	Modelling spatial-temporal rainfall and its hydrological impact in a changing climate	Institution name	Imperial College London
		Expected presentation date	2022-12-05
Instructor name	Christian Onof; Athanasios Paschalis		

ADDITIONAL DETAILS

CCC Marketplace™

This is a License Agreement between Yuting Chen ("User") and Copyright Clearance Center, Inc. ("CCC") on behalf of the Rightsholder identified in the order details below. The license consists of the order details, the Marketplace Order General Terms and Conditions below, and any Rightsholder Terms and Conditions which are included below.

All payments must be made in full to CCC in accordance with the Marketplace Order General Terms and Conditions below.

Order Date	30-Sep-2022	Type of Use	Republish in a thesis/dissertation
Order License ID	1274701-1		
ISSN	0043-1656	Publisher	ROYAL METEOROLOGICAL SOCIETY.
		Portion	Image/photo/illustration

LICENSED CONTENT

Publication Title	Weather	Rightsholder	John Wiley & Sons - Books
Article Title	A radar-based rainfall climatology of Great Britain and Ireland	Publication Type	Journal
		Start Page	153
Author/Editor	ROYAL METEOROLOGICAL SOCIETY (GREAT BRITAIN)	End Page	158
		Issue	5
Date	01/01/1946	Volume	70
Language	English		
Country	United Kingdom of Great Britain and Northern Ireland		

REQUEST DETAILS

Portion Type	Image/photo/illustration	Distribution	U.K. and Commonwealth (excluding Canada)
Number of images / photos / illustrations	1	Translation	Original language of publication
Format (select all that apply)	Electronic	Copies for the disabled?	No
Who will republish the content?	Academic institution	Minor editing privileges?	No
		Incidental promotional use?	No
Duration of Use	Life of current edition		
Lifetime Unit Quantity	Up to 499	Currency	GBP
Rights Requested	Main product		

NEW WORK DETAILS

Title	Modelling spatial-temporal rainfall and its hydrological impact in a changing climate	Institution name	Imperial College London
		Expected presentation date	2022-12-05
Instructor name	Christian Onof; Athanasios Paschalis		

ADDITIONAL DETAILS



Open Government Licence

for public sector information

delivered by

THE | NATIONAL | ARCHIVES

Back to The National Archives

You are encouraged to use and re-use the Information that is available under this licence freely and flexibly, with only a few conditions.

Using Information under this licence

Use of copyright and database right material expressly made available under this licence (the 'Information') indicates your acceptance of the terms and conditions below.

The Licensor grants you a worldwide, royalty-free, perpetual, non-exclusive licence to use the Information subject to the conditions below.

This licence does not affect your freedom under fair dealing or fair use or any other copyright or database right exceptions and limitations.

You are free to:

copy, publish, distribute and transmit the Information;

adapt the Information;

exploit the Information commercially and non-commercially for example, by combining it with other Information, or by including it in your own product or application.

You must (where you do any of the above):

acknowledge the source of the Information in your product or application by including or linking to any attribution statement specified by the Information Provider(s) and, where possible, provide a link to this licence;

If the Information Provider does not provide a specific attribution statement, you must use the following:

Contains public sector information licensed under the Open Government Licence v3.0.

If you are using Information from several Information Providers and listing multiple attributions is not practical in your product or application, you may include a URI or hyperlink to a resource that contains the required attribution statements.

II. Appendices to Chapter 4

II.1. Rainfall replicates selection criteria

The criteria are for selecting the most suitable 20 9-year-long rainfall replicates. This selection is carried out for each calendar month.

For each calendar month, 400 simulations (400×24×~30×~170×~238 values) are generated for the stochastic generator (either STREAP or NS(s-t)), those simulated are divided into 400/9 groups with each group including 9-year data. No additional sorting is needed because of the stationarity of the simulations. Each group is then sorted to give an annual variability closest to the observed order, as the relation shown below:

$$\mu_{y_1} \leq \mu_{y_2} \leq \cdots \leq \mu_{y_9}$$

$$\mu_{m_1} \leq \mu_{m_2} \leq \cdots \leq \mu_{m_9}$$

Where μ_{y_i} is the monthly mean of observed data, μ_{m_i} the monthly mean of simulated data, $\{y_i | i = 1,2, \dots ,9\}$ the observed series containing 9 years ranging from 2007 to 2015, where the order is sorted according to its observed monthly rainfall amount. Similarly, $\{m_i | i = 1,2, \dots ,9\}$ corresponds to the order in simulated group.

After this sorting, we start to select 20 groups. Those groups include at least one scaling factor far from 1 are first excluded, then the first 20 groups which give an averaged scaling factor closer to 1 will then be selected. Note, those 20 groups will be ordered back to keep it same as the observed rainfall when being fed into the hydrological simulation.

II.2. Rainfall annual mean value and variability

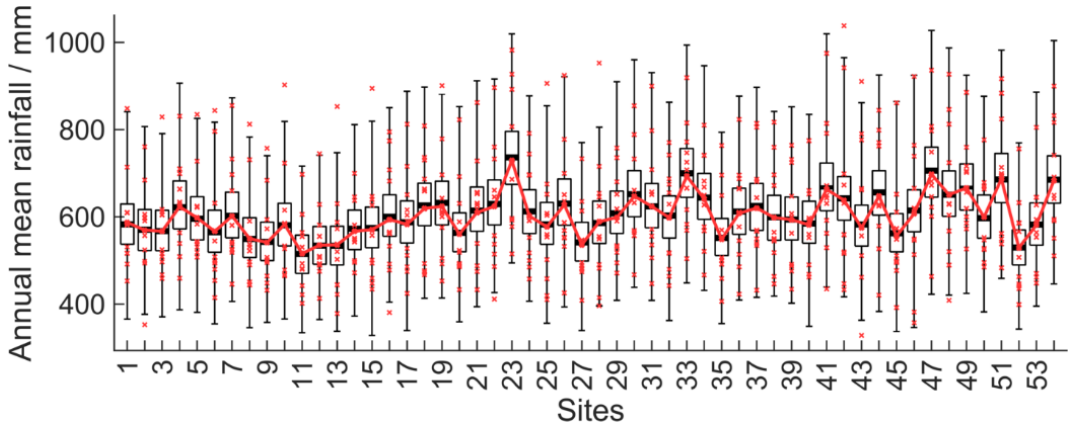


Figure II.2.1 Annual variability of point-scale mean rainfall at 54 gauges

II.4. Time series of simulated streamflow at river Stour outlet

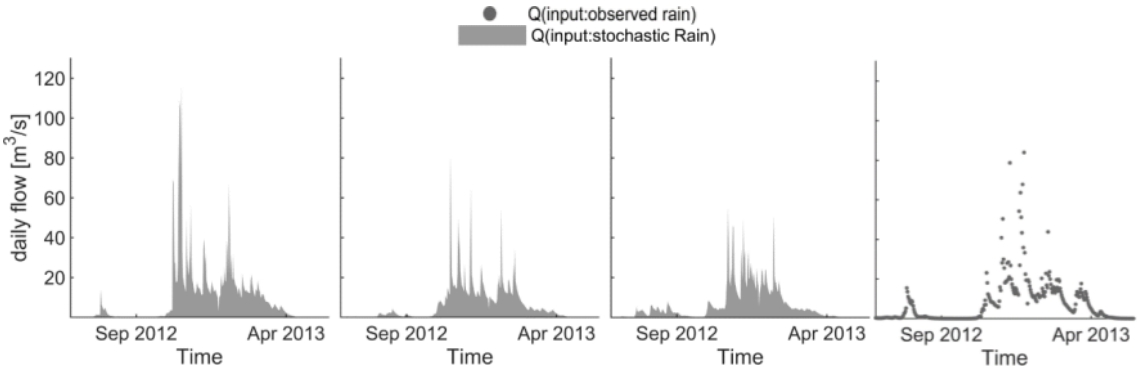


Figure II.3.1. Time series of simulated streamflow at river Stour outlet. (left three panels): the shaded area shows the simulated streamflow with one realization of stochastic rainfall as input; (right panel): dots show the simulated streamflow with observed rainfall as input (i.e. the reference runoff).

II.5. Exceedance probability functions of areal statistics in winter (DJF)

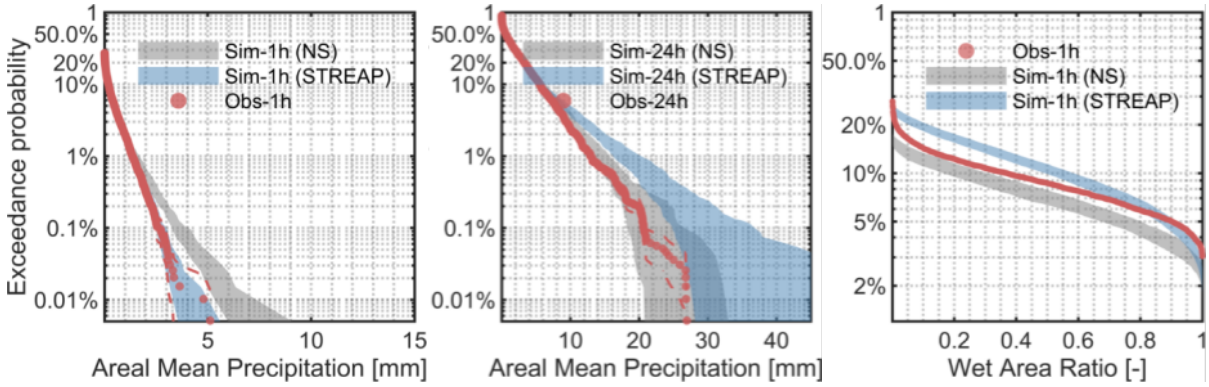


Figure II.4.1 same as Figure 4.10 but for winter (DJF)

II.6. Comparisons of flow duration curves at two catchments

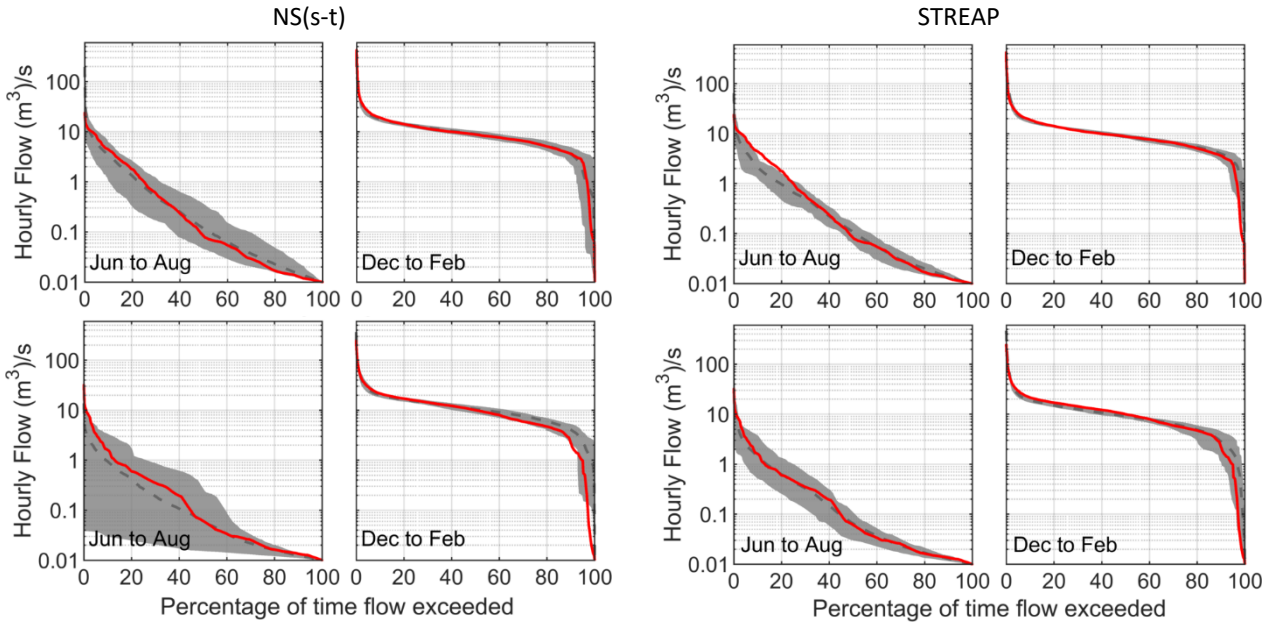


Figure II.5.1. Comparison of flow duration curves between the reference runoff (simulation of observed rainfall forcing) and simulations of stochastic rainfalls at River Welland (upper panels) and River Stour (lower panels) catchments.

II.7. Flow frequency curves at a daily scale

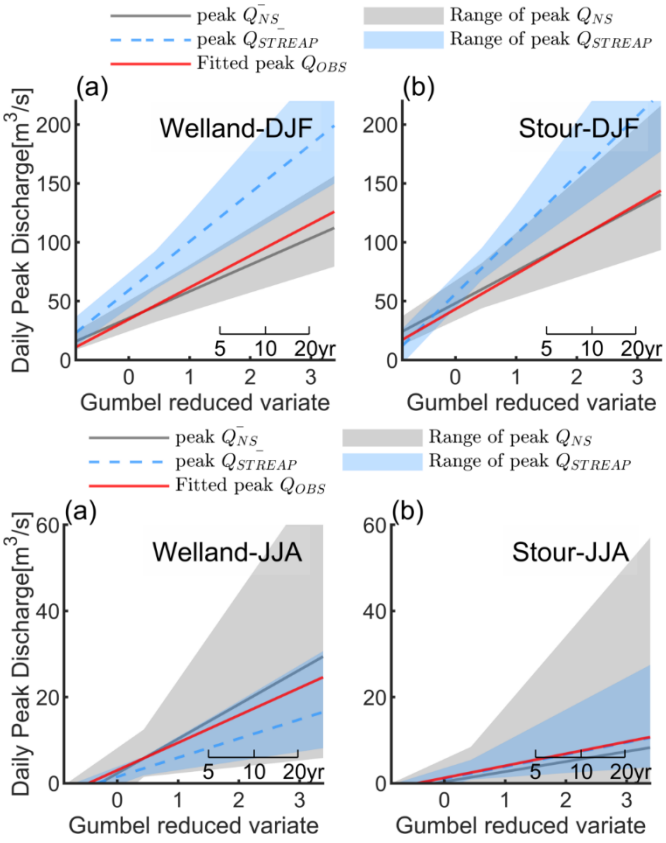


Figure II.6.1. Similar to the figure above but for winter-season FFCs at a daily scale.

Figure II.6.2. Similar to the figure above but for summer-season FFCs at a daily scale.

III. Appendices to Chapter 5 and 6

III.1. CPM vs OBS bias in winter and in summer

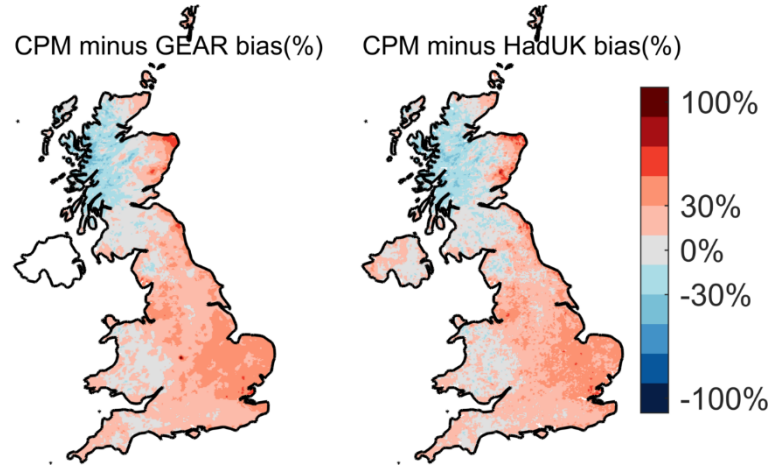


Figure III.1.1. Observed and simulated winter mean precipitation

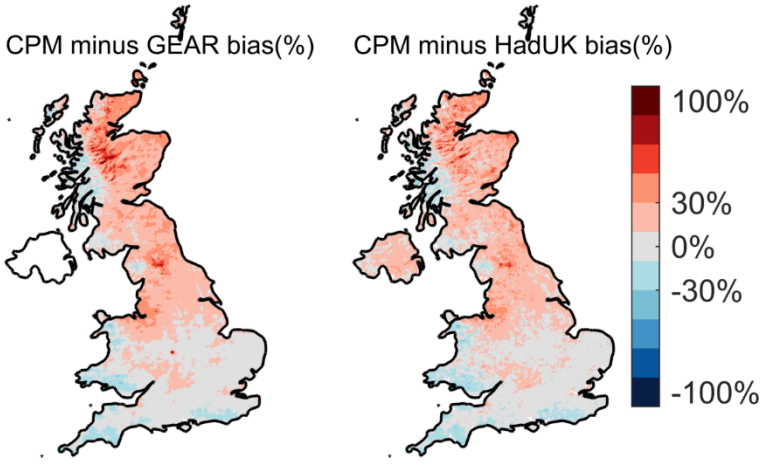


Figure III.1.2. Observed and simulated summer mean precipitation

III.2. Product behaviour in representing the orographic enhancement of rainfall

A cross section located in the north of the UK (as indicated by the red line in Figure III.2.1) is selected to investigate how each of rainfall products behaves in representing the orographic enhancement of rainfall. In total, 68 gridded locations (2.2 km ×2.2 km grid) with the elevation ranging from 6 m to 812.9 m are analysed. The elevation information used here is obtained from OS Terrain 50 digital terrain model (50m grid spacing) (Ordnance Survey, 2018). For two representative months (January and June), scatter plots are used to show how the annual mean rainfall will change over the DTM of each gridded location (Figure III.2.2). The solid line indicates a fitted linear model based on the scatter points. For the CPM product, the 12 ensemble members (20 years for each) are fitted separately. 12 years data are included for the radar product and 20 years data are included for the GEAR product.

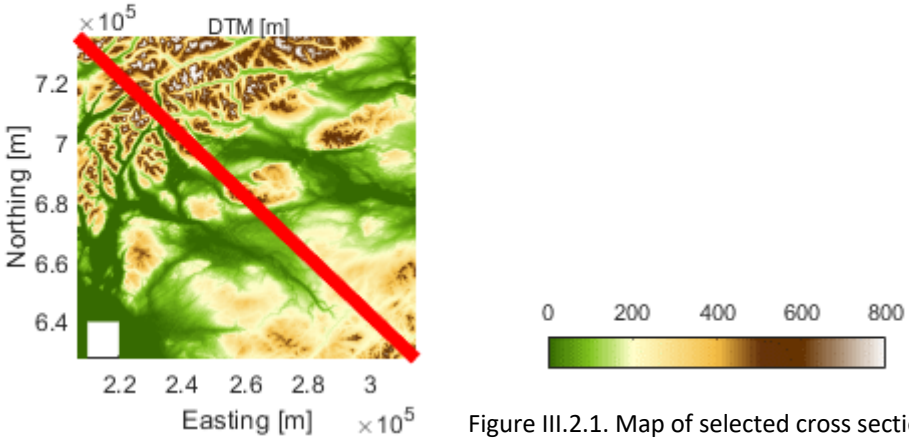


Figure III.2.1. Map of selected cross section

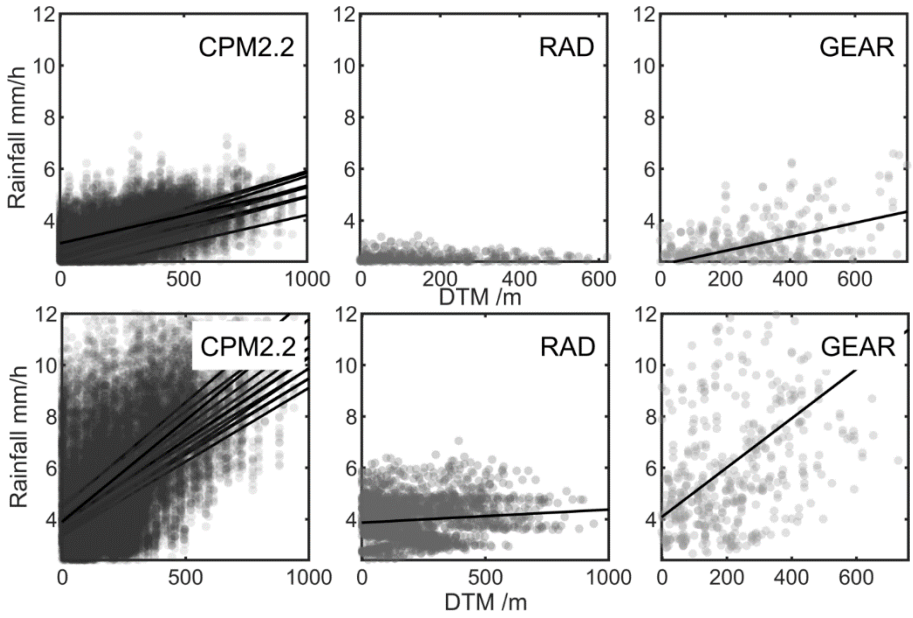


Figure III.2.2. Changes of annual rainfall amount obtained from different rainfall products as a function of elevation in January (upper panels) and in June (lower panels).

III.3. Robustness of the increase in the spatial extent

In order to confirm that the increase in the spatial extent is an additional change on top of the increase in the peak intensity, I re-examined the change of spatial coverage where a percentile-based approach is applied. In detail, instead of using a fixed $5mm\,h^{-1}$ to calculate spatial coverage, I redefine the area larger than the 99.9th percentile value of all hours as the spatial coverage. The 99.9th percentile value is obtained for each subregion (land area), each period, and each ensemble member separately. Here I selected the 99.9th percentile value because it is close to $5\ mm\,h^{-1}$, and the rainfall having an intensity above this percentile value is defined as a typical rainy area, which plays a crucial role on hydrological processes.

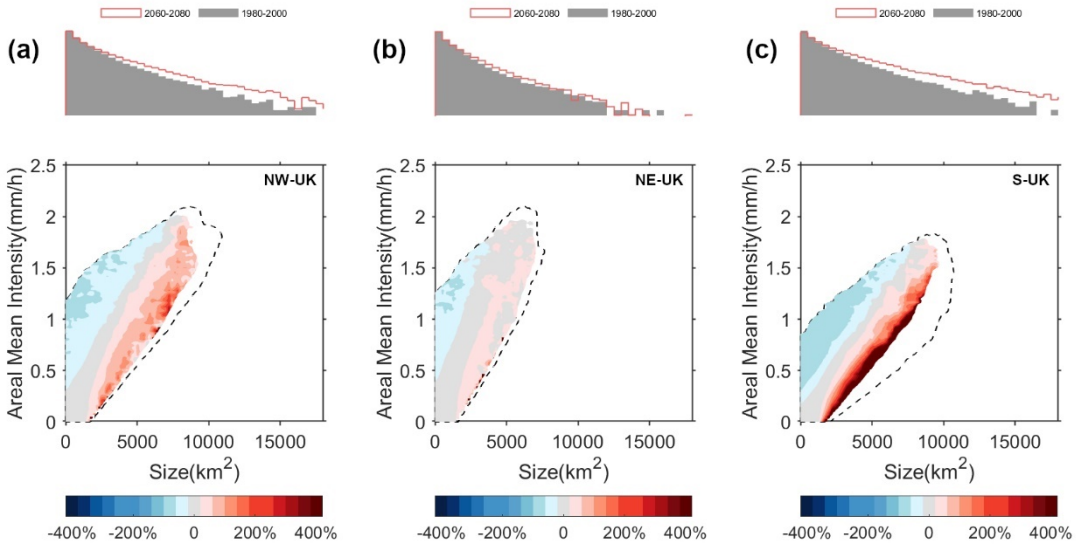


Figure III.3.1. Changes in spatial coverage of heavy precipitation conditioned on areal mean intensity at three regions, where a percentile-based threshold is applied to define the 'heavy' part of a rainy area

III.4. Annual mean precipitation and projected changes in future period (2060-2080) during winter season

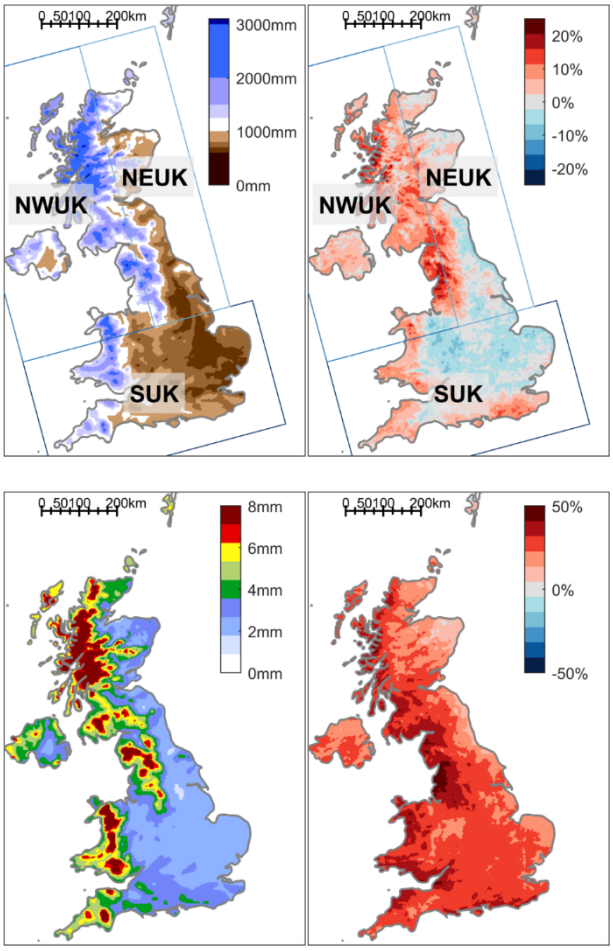


Figure III.4.1 Same as Figure 6.1 but for annual mean (upper two) and for winter season (DJF) (lower two panels)

III.5. Projected changes in wet spell duration and dry spell duration

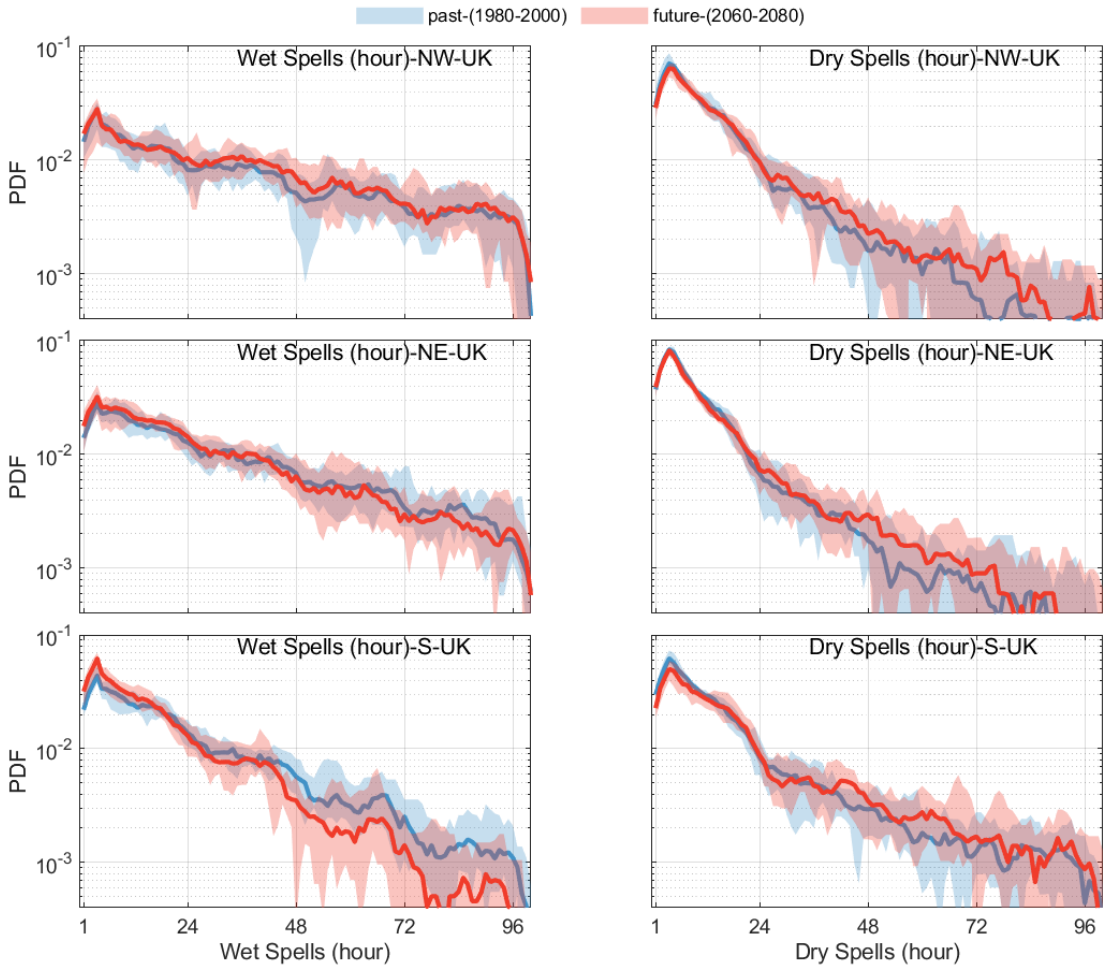


Figure III.5.1 Probability density function of Wet spell duration and dry spell duration for three sub-regions over the UK. Solid line and the shaded area represent the central estimate and the ensemble range

IV. Appendices to Chapter 7

IV.1. Bias correction method

The quantile delta mapping (QDM) method is applied to raw CPM output, which is one of recommended method in the UKCP18 (Met Office, 2019c) and widely used in processing climate model rainfall output. In detail, the bias-corrected future projection at time t is given by multiplying the relative change Δ by the historical bias-corrected value (Cannon et al., 2015) as shown in the equation.

$$\hat{x}_{m,p}(t) = \hat{x}_{o:m,h:p}(t) \cdot \Delta_m(t)$$

$$\hat{x}_{o:m,h:p}(t) = F_{o,h}^{-1}[F_{m,p}^{(t)}\{x_{m,p}(t)\}]$$

$$\Delta_m(t) = \frac{x_{m,p}(t)}{F_{m,h}^{-1}[F_{m,p}^{(t)} \cdot \{x_{m,p}(t)\}]}$$

where the variable used for bias correction is rainfall output data in this thesis. $\hat{x}_{o:m,h:p}(t)$ is the bias corrected data for the historical period; $\hat{x}_{m,p}(t)$ the bias corrected data for the future period and the $\Delta_m(t)$ is the relative change data between the historical and future periods obtained from the climate model.

IV.2. Comparisons of decay functions used in defining AR1 parameters

Two types of curve functions are investigated: a linear function ($\phi_{|k|} = A|k| + 1$ as described in the main text) and the Gaussian-curved function ($\phi_{|k|} = \exp\left(\frac{-|k|^2}{a}\right)$). For the linear function, the parameter is optimized through a trial-and-error method. For the Gaussian curve, the parameter is estimated according to the previous study (Bowler et al., 2006, p. 2134).

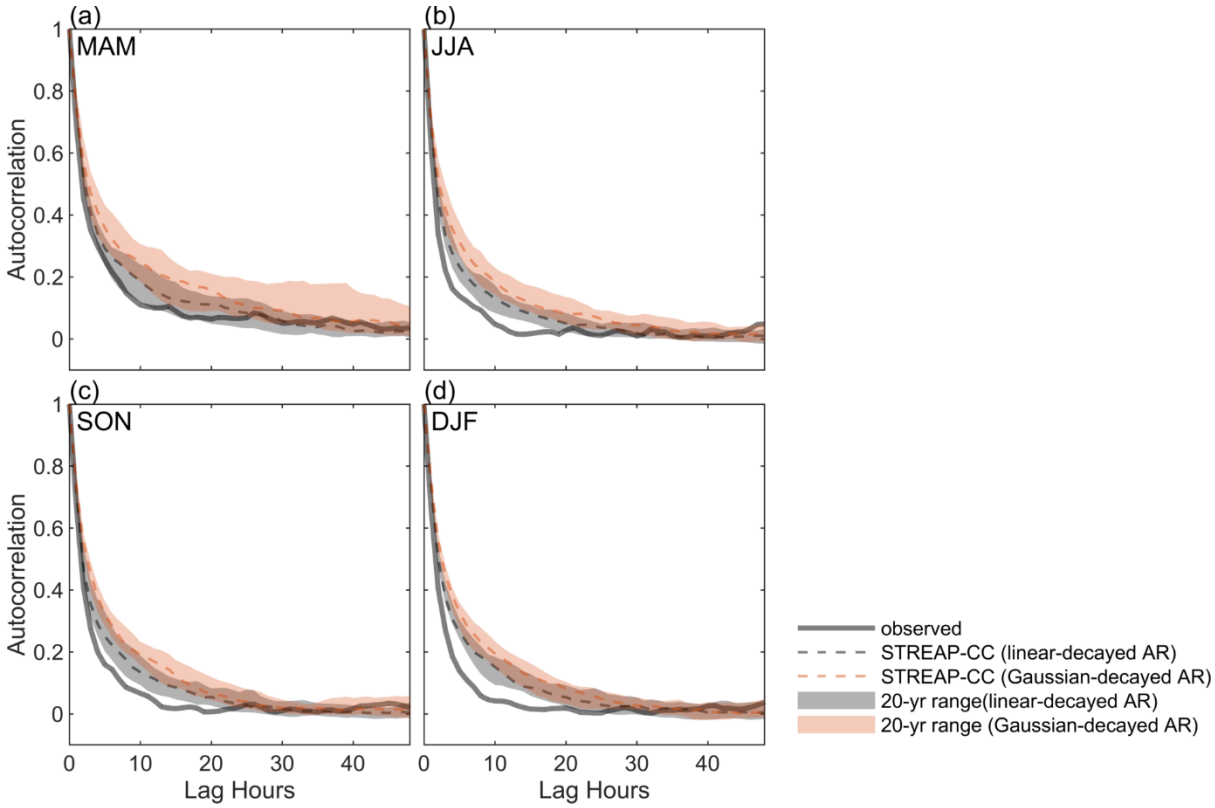


Figure IV.2.1 Impact of curve function on the simulation autocorrelation of STREAP-CC.

IV.3. STREAP-CC model parameters

Calibrated model parameters for the current and the future period are displayed in following tables (Table IV.2.1 – IV.2.7)

Table IV.2.1 1st stage model parameters of the STREAP-CC tool for the current period, where the listed parameters of the Johnson distribution are $\gamma, \delta, \xi, \lambda$ respectively, the parameters for the Lognormal distribution are μ, σ respectively. Parameters of the U and V component of the advection speed correspond to the fitted normal distribution

month	Distribution of wet spells [min]					Distribution of dry spells [min]					Advection speed [m/s]			
	Distribution	Parameters				Distribution	Parameters				U		V	
Jan	Johnson	-3.7	0.8	158.4	1.0	Johnson	2.2	0.5	34.4	11038.0	2.9	2.6	0.3	2.4
Feb	Johnson	1.9	0.8	34.7	2910.0	Johnson	3.0	0.6	46.3	36569.7	2.4	2.6	0.2	2.5
Mar	Johnson	2.5	0.8	59.0	5266.7	Lognormal	5.5	1.8	-	-	1.7	2.7	0.5	2.5
Apr	Johnson	4.5	1.0	31.0	22792.9	Lognormal	5.6	1.9	-	-	1.3	2.6	0.6	2.4
May	Johnson	4.1	1.1	-22.2	13837.7	Lognormal	5.6	1.9	-	-	1.0	2.9	0.8	2.4
Jun	Johnson	3.1	0.9	34.4	8557.5	Lognormal	5.7	1.9	-	-	1.9	2.3	1.1	2.1
Jul	Lognormal	5.7	0.9	-	-	Lognormal	6.2	1.0	-	-	2.4	2.1	1.3	2.3

Aug	Johnson	2.8	0.9	38.3	4996.7	Lognormal	5.7	1.7	-	-	2.7	2.0	1.2	2.3
Sep	Johnson	2.4	1.0	0.0	3759.5	Johnson	2.4	0.5	37.3	24069.8	2.5	2.2	0.4	2.4
Oct	Johnson	2.4	0.9	12.5	3530.9	Lognormal	5.5	1.9	-	-	2.3	2.3	0.9	2.7
Nov	Johnson	2.0	0.8	30.9	2854.8	Lognormal	5.2	1.9	-	-	2.6	2.6	0.6	2.7
Dec	Johnson	2.6	0.9	40.3	5009.3	Lognormal	5.4	1.9	-	-	3.2	2.5	0.3	2.3

Table IV.2.2 Same as Table IV.2.1 but for the future period

month	Distribution of wet spells [min]					Distribution of dry spells [min]					Advection speed [m/s]			
	Distribution	Parameters				Distribution	Parameters				U		V	
Jan	Johnson	-3.9	0.8	170.2	1.0	Johnson	2.1	0.5	20.0	8604.3	2.9	2.6	0.3	2.4
Feb	Johnson	2.0	0.8	14.4	3826.8	Johnson	2.8	0.6	80.1	26938.0	2.4	2.6	0.2	2.5
Mar	Johnson	2.8	0.8	44.9	7345.3	Lognormal	5.6	1.8	-	-	1.7	2.7	0.5	2.5
Apr	Johnson	5.4	1.0	29.3	50520.5	Lognormal	5.8	1.8	-	-	1.3	2.6	0.6	2.4
May	Johnson	4.1	1.0	-17.0	16348.3	Lognormal	6.1	1.8	-	-	1.0	2.9	0.8	2.4
Jun	Johnson	2.5	0.7	74.4	4875.6	Lognormal	6.0	2.0	-	-	1.9	2.3	1.1	2.1
Jul	Johnson	2.8	0.9	43.1	4792.3	Lognormal	6.8	1.2	-	-	2.4	2.1	1.3	2.3
Aug	Johnson	2.3	0.8	67.3	2765.8	Lognormal	6.4	1.8	-	-	2.7	2.0	1.2	2.3
Sep	Johnson	2.9	1.1	-13.9	4098.3	Johnson	6.5	1.7	-	-	2.5	2.2	0.4	2.4
Oct	Johnson	2.4	0.9	9.2	3455.2	Lognormal	5.9	1.7	-	-	2.3	2.3	0.9	2.7
Nov	Johnson	1.9	0.8	32.2	2917.2	Lognormal	5.3	1.9	-	-	2.6	2.6	0.6	2.7
Dec	Johnson	2.3	0.8	44.8	4793.4	Lognormal	5.4	1.8	-	-	3.2	2.5	0.3	2.3

Table IV.2.3 2nd stage model parameters (Whittle-Matérn covariance function) of the STREAP-CC tool for the current (control) and the future (projected) period

month	Current period					Future period				
	ν_W	ν_I	α	ν_{WI}	ρ_{WI}	ν_W	ν_I	α	ν_{WI}	ρ_{WI}
Jan	0.75	0.69	0.03	0.72	0.91	0.84	0.75	0.03	0.79	0.92
Feb	0.74	0.66	0.03	0.70	0.91	0.82	0.70	0.03	0.76	0.91
Mar	0.80	0.66	0.03	0.73	0.89	0.85	0.68	0.03	0.77	0.89
Apr	0.86	0.69	0.03	0.75	0.86	0.83	0.65	0.03	0.73	0.86
May	0.95	0.74	0.03	0.76	0.84	0.75	0.62	0.02	0.67	0.84
Jun	1.05	0.79	0.03	0.79	0.81	0.69	0.57	0.02	0.63	0.83
Jul	1.00	0.77	0.03	0.78	0.81	0.66	0.53	0.02	0.60	0.85
Aug	0.93	0.76	0.03	0.76	0.82	0.66	0.54	0.02	0.60	0.87
Sep	0.84	0.71	0.03	0.71	0.84	0.63	0.56	0.02	0.60	0.88
Oct	0.83	0.71	0.03	0.76	0.88	0.68	0.65	0.02	0.66	0.90
Nov	0.85	0.75	0.03	0.80	0.90	0.80	0.74	0.03	0.77	0.91
Dec	0.87	0.77	0.03	0.82	0.91	0.80	0.76	0.03	0.78	0.92

Table IV.2.4 2nd stage model parameters (Multi-variate Copula) of the STREAP-CC tool for the current period[1]

month	P_c					ν_c	month	P_c					ν_c	month	P_c					ν_c
	1.00	0.63	0.45	0.58	0.41			1.00	0.63	0.45	0.58	0.41			1.00	0.63	0.45	0.58	0.41	
	0.63	1.00	0.60	0.92	0.55			0.63	1.00	0.60	0.92	0.55			0.63	1.00	0.60	0.92	0.55	
Jan	0.45	0.60	1.00	0.56	0.85	17.2	Feb	0.45	0.60	1.00	0.56	0.85	17.4	Mar	0.45	0.60	1.00	0.56	0.85	18.6
	0.58	0.92	0.56	1.00	0.52			0.58	0.92	0.56	1.00	0.52			0.58	0.92	0.56	1.00	0.52	
	0.41	0.55	0.85	0.52	1.00			0.41	0.55	0.85	0.52	1.00			0.41	0.55	0.85	0.52	1.00	
	1.00	0.63	0.45	0.58	0.41			1.00	0.63	0.45	0.58	0.41			1.00	0.63	0.45	0.58	0.41	
	0.63	1.00	0.60	0.92	0.55			0.63	1.00	0.60	0.92	0.55			0.63	1.00	0.60	0.92	0.55	
Apr	0.45	0.60	1.00	0.56	0.85	16.0	May	0.45	0.60	1.00	0.56	0.85	18.2	Jun	0.45	0.60	1.00	0.56	0.85	19.8
	0.58	0.92	0.56	1.00	0.52			0.58	0.92	0.56	1.00	0.52			0.58	0.92	0.56	1.00	0.52	
	0.41	0.55	0.85	0.52	1.00			0.41	0.55	0.85	0.52	1.00			0.41	0.55	0.85	0.52	1.00	
	1.00	0.63	0.45	0.58	0.41			1.00	0.63	0.45	0.58	0.41			1.00	0.63	0.45	0.58	0.41	
	0.63	1.00	0.60	0.92	0.55			0.63	1.00	0.60	0.92	0.55			0.63	1.00	0.60	0.92	0.55	
Jul	0.45	0.60	1.00	0.56	0.85	28.7	Aug	0.45	0.60	1.00	0.56	0.85	25.8	Sep	0.45	0.60	1.00	0.56	0.85	28.1
	0.58	0.92	0.56	1.00	0.52			0.58	0.92	0.56	1.00	0.52			0.58	0.92	0.56	1.00	0.52	
	0.41	0.55	0.85	0.52	1.00			0.41	0.55	0.85	0.52	1.00			0.41	0.55	0.85	0.52	1.00	

	0.58	0.92	0.56	1.00	0.52			0.58	0.92	0.56	1.00	0.52			0.58	0.92	0.56	1.00	0.52	
	0.41	0.55	0.85	0.52	1.00			0.41	0.55	0.85	0.52	1.00			0.41	0.55	0.85	0.52	1.00	
	1.00	0.63	0.45	0.58	0.41			1.00	0.63	0.45	0.58	0.41			1.00	0.63	0.45	0.58	0.41	
	0.63	1.00	0.60	0.92	0.55			0.63	1.00	0.60	0.92	0.55			0.63	1.00	0.60	0.92	0.55	
Oct	0.45	0.60	1.00	0.56	0.85	20.0	Nov	0.45	0.60	1.00	0.56	0.85	17.9	Dec	0.45	0.60	1.00	0.56	0.85	89.0
	0.58	0.92	0.56	1.00	0.52			0.58	0.92	0.56	1.00	0.52			0.58	0.92	0.56	1.00	0.52	
	0.41	0.55	0.85	0.52	1.00			0.41	0.55	0.85	0.52	1.00			0.41	0.55	0.85	0.52	1.00	

[1] P_c is the linear correlation matrix of the Copula framework where the five variables correspond to $T, \mu_W, \sigma_W, \mu_I, \sigma_I$.

Table IV.2.5 Same as the Table IV.2.4, but for the future period.

month	P_c					ν_c	month	P_c					ν_c	month	P_c					ν_c
	1.00	0.65	0.51	0.60	0.45			1.00	0.64	0.49	0.60	0.45			1.00	0.65	0.47	0.61	0.45	
	0.65	1.00	0.65	0.93	0.57			0.64	1.00	0.60	0.93	0.54			0.65	1.00	0.55	0.91	0.52	
Jan	0.51	0.65	1.00	0.60	0.83	19.5	Feb	0.49	0.60	1.00	0.55	0.84	20.4	Mar	0.47	0.55	1.00	0.50	0.83	17.4
	0.60	0.93	0.60	1.00	0.55			0.60	0.93	0.55	1.00	0.51			0.61	0.91	0.50	1.00	0.49	
	0.45	0.57	0.83	0.55	1.00			0.45	0.54	0.84	0.51	1.00			0.45	0.52	0.83	0.49	1.00	
	1.00	0.65	0.46	0.61	0.46			1.00	0.70	0.50	0.61	0.50			1.00	0.69	0.46	0.64	0.47	
	0.65	1.00	0.51	0.87	0.53			0.70	1.00	0.54	0.83	0.55			0.69	1.00	0.44	0.85	0.44	
Apr	0.46	0.51	1.00	0.44	0.82	14.3	May	0.50	0.54	1.00	0.45	0.79	17.2	Jun	0.46	0.44	1.00	0.42	0.78	15.9
	0.61	0.87	0.44	1.00	0.47			0.61	0.83	0.45	1.00	0.49			0.64	0.85	0.42	1.00	0.44	
	0.46	0.53	0.82	0.47	1.00			0.50	0.55	0.79	0.49	1.00			0.47	0.44	0.78	0.44	1.00	
	1.00	0.68	0.44	0.66	0.44			1.00	0.66	0.44	0.66	0.44			1.00	0.65	0.43	0.63	0.41	
	0.68	1.00	0.41	0.88	0.39			0.66	1.00	0.41	0.90	0.40			0.65	1.00	0.41	0.91	0.40	
Jul	0.44	0.41	1.00	0.40	0.78	15.5	Aug	0.44	0.41	1.00	0.41	0.80	16.8	Sep	0.43	0.41	1.00	0.43	0.79	14.7
	0.66	0.88	0.40	1.00	0.39			0.66	0.90	0.41	1.00	0.38			0.63	0.91	0.43	1.00	0.38	
	0.44	0.39	0.78	0.39	1.00			0.44	0.40	0.80	0.38	1.00			0.41	0.40	0.79	0.38	1.00	
	1.00	0.67	0.47	0.61	0.46			1.00	0.65	0.47	0.58	0.43			1.00	0.63	0.48	0.58	0.43	
	0.67	1.00	0.51	0.89	0.50			0.65	1.00	0.61	0.92	0.55			0.63	1.00	0.64	0.93	0.58	
Oct	0.47	0.51	1.00	0.49	0.81	19.8	Nov	0.47	0.61	1.00	0.58	0.82	18.5	Dec	0.48	0.64	1.00	0.60	0.84	23.0
	0.61	0.89	0.49	1.00	0.48			0.58	0.92	0.58	1.00	0.55			0.58	0.93	0.60	1.00	0.55	
	0.46	0.50	0.81	0.48	1.00			0.43	0.55	0.82	0.55	1.00			0.43	0.58	0.84	0.55	1.00	

Table IV.2.6 2nd stage model parameters of the STREAP-CC tool for the current (control) and the future (projected) period, where μ_W and μ_W follow the Normal distribution and σ_W and σ_I follow the Gamma distribution

month	Current period								Future period							
	μ_W		σ_W		μ_I		σ_I		μ_W		σ_W		μ_I		σ_I	
	μ	σ	α	β	μ	σ	α	β	μ	σ	α	β	μ	σ	α	β
Jan	-0.30	0.76	4.45	0.16	-0.30	0.73	4.64	0.15	-0.32	0.79	3.87	0.19	-0.33	0.75	4.41	0.15
Feb	-0.28	0.72	4.85	0.15	-0.29	0.71	4.96	0.14	-0.29	0.75	4.45	0.16	-0.29	0.72	4.81	0.14
Mar	-0.29	0.71	5.28	0.13	-0.29	0.72	5.08	0.13	-0.31	0.73	4.84	0.14	-0.31	0.72	5.04	0.13
Apr	-0.29	0.70	5.39	0.13	-0.29	0.71	5.09	0.13	-0.31	0.71	5.25	0.13	-0.30	0.73	5.01	0.13
May	-0.31	0.70	5.52	0.13	-0.28	0.74	4.96	0.14	-0.37	0.72	5.23	0.13	-0.34	0.76	4.31	0.15
Jun	-0.32	0.70	5.72	0.12	-0.26	0.76	4.65	0.14	-0.37	0.70	5.51	0.12	-0.37	0.77	4.56	0.13
Jul	-0.30	0.69	5.66	0.12	-0.25	0.73	4.48	0.14	-0.37	0.69	5.66	0.11	-0.38	0.76	4.83	0.13
Aug	-0.30	0.71	5.37	0.12	-0.25	0.76	4.14	0.15	-0.37	0.67	5.88	0.11	-0.40	0.72	4.97	0.13
Sep	-0.28	0.72	5.13	0.13	-0.26	0.74	4.61	0.14	-0.35	0.70	5.15	0.13	-0.36	0.76	4.47	0.14
Oct	-0.31	0.75	4.74	0.15	-0.29	0.75	4.58	0.14	-0.34	0.73	4.76	0.14	-0.33	0.75	4.35	0.15
Nov	-0.29	0.76	4.31	0.17	-0.30	0.73	4.61	0.15	-0.33	0.77	4.41	0.16	-0.32	0.78	4.56	0.14
Dec	-0.27	0.75	4.49	0.16	-0.28	0.72	4.73	0.15	-0.31	0.78	3.94	0.18	-0.31	0.76	4.11	0.16

Table IV.2.7 3rd stage parameters of the STREAP-CC for the current (control) and the future (projected) period

month	Current period		Future period	
	correlation length [km]	coefficient of variation [-]	correlation length [km]	coefficient of variation [-]
	α_g	CV_{pos}	α_g	CV_{pos}

Jan	20	1.27	18	1.25
Feb	20	1.30	18	1.28
Mar	17	1.35	17	1.35
Apr	15	1.44	16	1.51
May	16	1.56	19	1.71
Jun	15	1.66	19	1.89
Jul	15	1.67	14	1.81
Aug	17	1.60	13	1.63
Sep	18	1.45	18	1.47
Oct	20	1.35	19	1.42
Nov	20	1.30	19	1.32
Dec	19	1.30	20	1.26
AR(1) model with a dependent coef. $\phi_1(\lvert k \rvert) = -0.0067\lvert k \rvert + 1$				